University of Alberta

MOUTH–THROAT DEPOSITION WITH NON-BALLISTIC PHARMACEUTICAL AEROSOL INHALATION DEVICES

by

Wesley Hugh DeHaan

A thesis submitted to the Faculty of Graduate Studies and Research in partial fulfillment of the requirements for the degree of **Doctor of Philosophy**.

Department of Mechanical Engineering

Edmonton, Alberta
Fall 2002

National Library
of Canada

Acquisitions and
Bibliographic Services

395 Wellington Street
Ottawa ON K1A 0N4
Canada

Bibliothèque nationale
du Canada

Acquisitions et
services bibliographiques

395, rue Wellington
Ottawa ON K1A 0N4
Canada

Your file Votre référence

Our file Notre référence

The author has granted a non-exclusive licence allowing the National Library of Canada to reproduce, loan, distribute or sell copies of this thesis in microform, paper or electronic formats.

L'auteur a accordé une licence non exclusive permettant à la Bibliothèque nationale du Canada de reproduire, prêter, distribuer ou vendre des copies de cette thèse sous la forme de microfiche/film, de reproduction sur papier ou sur format électronique.

The author retains ownership of the copyright in this thesis. Neither the thesis nor substantial extracts from it may be printed or otherwise reproduced without the author's permission.

L'auteur conserve la propriété du droit d'auteur qui protège cette thèse. Ni la thèse ni des extraits substantiels de celle-ci ne doivent être imprimés ou autrement reproduits sans son autorisation.

0-612-81179-4

Canada

University of Alberta

Library Release Form

Name of Author: Wesley Hugh DeHaan

Title of Thesis: Mouth–Throat Deposition With Non-ballistic Pharmaceutical Aerosol Inhalation Devices

Degree: Doctor of Philosophy

Year this Degree Granted: 2002

Permission is hereby granted to the University of Alberta Library to reproduce single copies of this thesis and to lend or sell such copies for private, scholarly or scientific research purposes only.

The author reserves all other publication and other rights in association with the copyright in the thesis, and except as herein before provided, neither the thesis nor any substantial portion thereof may be printed or otherwise reproduced in any material form whatever without the author's prior written permission.

Wesley Hugh DeHaan
20 Jackson Road
Belmont, MA
USA 02478

Date: Aug. 27, 2002

"Your attitude should be the same as that of Christ Jesus:
Who, being in very nature God, did not consider equality with
God something to be grasped, but made himself nothing, taking
the very nature of a servant, being made in human likeness.
And being found in appearance as a man, he humbled himself and
became obedient to death – even death on a cross!
Therefore God exalted him to the highest place and gave him the
name that is above every name, that at the name of Jesus every
knee should bow, in heaven and on earth and under the earth,
and every tongue confess that Jesus Christ is Lord, to the glory of
God the Father."

Philippians 2:6-11, NIV

University of Alberta

Faculty of Graduate Studies and Research

The undersigned certify that they have read, and recommend to the Faculty of Graduate Studies and Research for acceptance, a thesis entitled **Mouth–Throat Deposition With Non-ballistic Pharmaceutical Aerosol Inhalation Devices** submitted by Wesley Hugh DeHaan in partial fulfillment of the requirements for the degree of **Doctor of Philosophy**.

Warren Finlay (Supervisor)

LWK

Beth L. Laube (External)

Carlos F. Lange

Carlos F. Lange

Larry W. Kostiuk

J N McMullin

James N. McMullin

Date: Aug 27, 2002

To my wife Joy, my life,
and to my daughter Lauren, my inspiration

Acknowledgements

I would like to thank Dr. Warren Finlay without whose guidance and support I could not have completed this thesis. I would also like to acknowledge all the members of the aerosol research lab during my time here for their much needed help. I would especially like to thank Dr. Carlos Lange for his ideas and friendship, Biljana Grgic for her help with the radioactive tests, Dr. Edgar Matida for his extensive help with the CFD work and Helena Orzanska for all her laboratory assistance and boundless energy.

In addition, the talents of everyone in the machine shop were a real benefit for compiling the data in this thesis. In particular I would like to thank Ian Butter, Albert Yuen and Don Fuhr.

Thanks to the Alberta Heritage Foundation for Medical Research and the National Science and Engineering Council for providing funding for this research.

Abstract

In this thesis, the enhancement of aerosol deposition in the mouth–throat region by non-ballistic pharmaceutical aerosol devices is investigated and a model to predict the extrathoracic deposition is developed.

In vitro tests were performed in a realistic, idealized mouth and throat geometry using monodisperse aerosols entering through various inlets. It was found that the two dry powder inhalers used as inlets caused elevated deposition in the geometry for a large range of flow rates and particle diameters compared to the other tested inlets.

The in vitro tests were repeated at one flow rate and particle diameter with a radioactively labelled aerosol in order to determine the location of the elevated deposition. It was found that the oral cavity was the primary site of the increase in aerosol deposition relative to the straight tube inlet case.

In order to test the effect of varying the velocity and turbulence intensity at the inlet of the region, monodisperse aerosol deposition was measured in an oral cavity model after entry through a number of straight tubes and contracting nozzles with various outlet diameters. Aerosol deposition was found to be a function of the particle Stokes number based on the inlet diameter and the predicted velocity near the impaction location. Although increased inlet turbulence intensity was found to increase deposition, it was found to be a secondary effect after the Stokes number effect.

In order to investigate the flow field in the oral cavity caused by the confined turbulent jets, a commercial computational fluid dynamics (CFD) package combined with an in-house particle tracking code was employed to predict the flow fields and aerosol deposition within the region. The CFD simulation predicted fluid jet structures in the oral cavity for all inlets less than 17mm in diameter with elevated deposition near the point of jet impingement on the upper, rear wall of the oral cavity. This deposition pattern agreed well with the qualitative deposition patterns observed experimentally. The total deposition predicted in the oral cavity by the in-house particle tracking code showed good agreement with the experimental data, although some overprediction of the

deposition for small particle diameters and underprediction of the deposition for large particle diameters was observed.

A model was developed to predict the aerosol deposition in the oral cavity based on the straight tube and contraction nozzle tests. Extrapolation of this model to inlets that resembled commercially available dry powder inhalers was then tested for monodisperse aerosols. This was achieved by assuming that the dry powder inhalers could be modelled as straight tube inlets with equivalent diameters based on the cross sectional area of the dry powder inhaler mouthpiece. The model was found to give much closer estimates of oral cavity deposition than previous extrathoracic deposition models available in the literature. A small systematic underprediction of the oral cavity deposition for entry through dry powder inhaler geometries was observed.

Finally, a simple model was developed for predicting dry powder inhaler aerosol deposition by extrapolating the oral cavity model to polydisperse aerosols and combining it with the model of Stahlhofen *et al.* for pharynx, larynx and trachea deposition. Results were validated against published in vivo studies with a number of dry powder inhalers. The model was found to improve predictions of the total extrathoracic deposition and to significantly shift the deposition location within the extrathoracic region from the larynx to the oral cavity as is observed in vivo.

Contents

1 Introduction **1**
- 1.1 Introduction to Pharmaceutical Aerosols 1
- 1.2 Commercial Delivery Techniques for Pharmaceutical Aerosols . 3
  - 1.2.1 Nebulizers 3
  - 1.2.2 Propellant (Pressurized) Metered Dose Inhalers (pMDI) 5
  - 1.2.3 Dry Powder Inhalers (DPI) 5
- 1.3 Importance of Prediction 6
- 1.4 Outline of Thesis 7

2 Present State of Knowledge **9**
- 2.1 Introduction 9
- 2.2 Aerosol Deposition Modelling 9
- 2.3 Particle Momentum Equation 12
- 2.4 Sedimentation 16
- 2.5 Diffusion 20
- 2.6 Inertial Impaction 23
- 2.7 Aerosol Deposition in Fully Developed Pipe Flow 29
- 2.8 Lung Deposition Models 36
- 2.9 Extrathoracic Deposition Models 40
  - 2.9.1 Nasal Deposition 40
  - 2.9.2 Oral Deposition 41

3 Total Extrathoracic Deposition Tests [1] **49**
- 3.1 Introduction 49
- 3.2 Experimental Setup 51
  - 3.2.1 Aerosol Generation and Size Verification 53
  - 3.2.2 Tested Devices 55
  - 3.2.3 Mouth and Throat Models 56
  - 3.2.4 Assay 59
- 3.3 Results 60
- 3.4 Discussion 62

4 Regional Extrathoracic Deposition Tests **66**
- 4.1 Experimental Setup 66
  - 4.1.1 Tested Device Connections 70

4.1.2 Radioactivity Measurements 71
4.2 Results and Discussion 75

5 Oral Cavity Deposition Tests 97
5.1 Oral Cavity Geometry 97
5.2 Contraction Nozzle Inlets 100
5.2.1 Experimental Setup 100
5.2.2 Results and Discussion 104
5.2.2.1 Impaction Parameter 106
5.2.2.2 Stokes Number at Nozzle 111
5.2.2.3 Limit of Oral Cavity Jet Effects 113
5.2.2.4 Stokes Number Based on Free Jet Theory . . 121
5.3 Fully Developed Pipe Flow Inlets 126
5.3.1 Experimental Setup 129
5.3.1.1 Aerosol Deposition Tests 129
5.3.2 Inlet Conditions from Turbulent Pipe Flow 130
5.3.3 Results and Discussion 133
5.4 Enhanced Inlet Turbulence Levels 136
5.4.1 Experimental Setup 138
5.4.1.1 Aerosol Deposition Tests 138
5.4.1.2 Velocity Measurement Tests 141
5.4.2 Results and Discussion 145
5.4.2.1 Velocity and Turbulence Results 145
5.4.2.2 Aerosol Deposition Results 146

6 Computational Fluid Dynamics in the Oral Cavity 156
6.1 Introduction 156
6.2 Calculation of Particle Trajectories 161
6.3 Turbulence Models 165
6.4 Geometry and Grid 166
6.5 Boundary Conditions 171
6.6 Iterative Convergence 171
6.7 Results 173
6.7.1 Fluid Flow Fields 173
6.7.2 LDA Comparison 185
6.7.3 Particle Tracking 187
6.7.3.1 Total Deposition in Oral Cavity 187
6.7.3.2 Three Dimensional Deposition Pattern 192

7 Prediction of Extrathoracic Deposition After Dry Power Inhalers 197
7.1 Monodisperse Oral Cavity Deposition Tests with Pharmaceutical Device Inlets 197
7.1.1 Experimental Setup 197
7.1.1.1 Tested Dry Powder Inhalers 198

7.1.1.2 Aerosol Monodispersity 199
7.1.2 Results 200
7.2 Extension of Model to Predict DPI Deposition In Vivo 208
7.2.1 Extension to Polydisperse Aerosols 208
7.2.2 Extension to Total Extrathoracic Deposition 209

8 Conclusions and Recommendations for Future Work 217
8.1 Conclusions 217
8.2 Future Work 219

Bibliography 221

List of Figures

2.1 Wall deposition from fully developed turbulent pipe flow in vertical tubes 31
2.2 In vivo extrathoracic deposition data in literature 45
2.3 Empirical models of extrathoracic deposition 46

3.1 Experimental setup of total extrathoracic deposition tests . . . 52
3.2 Idealized geometry of extrathoracic region in a healthy adult male 57
3.3 Extrathoracic deposition after entry through pharmaceutical inhalers 61
3.4 Comparison of straight tube in vitro extrathoracic deposition data and in vivo data 63

4.1 Experimental setup for radioactive deposition tests 67
4.2 Collimater form for positioning during radioactive deposition tests 73
4.3 Region definition for radioactive deposition tests 74
4.4 Total deposition in extrathoracic region for gamma scintigraphy tests 78
4.5 Averaged total deposition in extrathoracic region for gamma scintigraphy tests 79
4.6 Total extrathoracic deposition for 17 mm inlet pipe 80
4.7 Averaged regional deposition in extrathoracic region for gamma scintigraphy tests 81
4.8 Regional deposition in extrathoracic geometry after 17 mm pipe inlet 82
4.9 Regional deposition in extrathoracic geometry after unvented jet nebulizer 83
4.10 Regional deposition in extrathoracic geometry after pMDI with attached holding chamber 84
4.11 Regional deposition in extrathoracic geometry after Diskus DPI 85
4.12 Regional deposition in extrathoracic geometry after Turbuhaler DPI 86
4.13 Regional deposition of aerosol exiting oral cavity for all devices 87
4.14 Regional deposition in extrathoracic geometry only for all devices 88
4.15 Deposition in oral cavity for all inlet devices 89

4.16 Schematic of Turbuhaler inhaler (AstraZeneca, Sweden) 92
4.17 Schematic of Diskus inhaler (GlaxoSmithKline,UK) 93
4.18 Deposition in pharynx, larynx and trachea for all inlet devices 94
4.19 Deposition on exit filters for all inlet devices 95

5.1 Oral cavity geometry for gravimetric deposition tests 98
5.2 Effect of truncating extrathoracic region 99
5.3 Experimental setup for contraction nozzle inlets 101
5.4 Schematic of phase doppler anemometer 103
5.5 Oral cavity deposition with impaction parameter for contraction nozzle inlets 107
5.6 Typical oral cavity deposition pattern for 3 to 14 mm inlets . 110
5.7 Oral cavity deposition with Stokes number at the contraction nozzle exit 112
5.8 Typical oral cavity deposition pattern for 17 mm inlet 116
5.9 Extrathoracic deposition for 3 different diameter inlets – Stokes number at inlet 118
5.10 Extrathoracic deposition for 3 different diameter inlets – Impaction parameter 119
5.11 Extrathoracic deposition for 3 different diameter inlets – Stokes number in larynx 120
5.12 Contraction nozzle entry oral cavity deposition from free jet theory Stokes number, all nozzles 125
5.13 Contraction nozzle entry oral cavity deposition from free jet theory Stokes number 127
5.14 Experimental setup for turbulent pipe flow inlets 129
5.15 Oral cavity deposition from pipe entries 133
5.16 Oral cavity deposition from pipe and contraction nozzle entries 135
5.17 Best fit curve for oral cavity deposition from pipe and contraction nozzle entries 137
5.18 Experimental setup for enhanced turbulence pipe flow inlets . 139
5.19 Setup of turbulence generator 140
5.20 Experimental setup for velocity measurements inside oral cavity 142
5.21 Oral cavity geometry for velocity measurements 143
5.22 Laser Doppler Anemometer fringe patterns 144
5.23 Contraction nozzle entry oral cavity deposition from free jet theory Stokes number 145
5.24 Oral cavity deposition from highly turbulent inlets 147
5.25 Oral cavity deposition from highly turbulent inlets, pipe flows and contraction nozzles 149
5.26 Oral cavity deposition from highly turbulent inlets, pipe flows and contraction nozzles with modified Stokes number 153
5.27 Prediction of oral cavity deposition for turbulent jet inlets . . 155

6.1 Surface grid of base grid for 8.13 mm inlet 167

6.2 Cross section of base grid through symmetry plane 168
6.3 CFD grid convergence effects on air velocity distribution . . . 169
6.4 CFD grid convergence effects on particle deposition 170
6.5 Convergence of particle deposition predictions 173
6.6 Mean flow field parameters for 10.9 mm inlet 174
6.7 Flow field turbulence parameters for 10.9 mm inlet 177
6.8 Velocity and speed in oral cavity for 3.18 mm inlet 179
6.9 Velocity and speed in oral cavity for 4.95 mm inlet 181
6.10 Velocity and speed in oral cavity for 8.13 mm inlet 182
6.11 Velocity and speed in oral cavity for 10.9 mm inlet 183
6.12 Velocity and speed in oral cavity for 17.1 mm inlet 184
6.13 Air speed in oral cavity for all five inlets 185
6.14 Air velocity in the oral cavity measured and calculated 186
6.15 CFD particle deposition predictions with 3.18 mm inlet 187
6.16 CFD particle deposition predictions with 8.13 mm inlet 188
6.17 CFD particle deposition predictions with 17.1 mm inlet 189
6.18 Aerosol deposition in oral cavity predicted by CFD and experiments 191
6.19 Three dimensional deposition pattern from CFD for large inlets 193
6.20 Three dimensional deposition pattern from CFD for medium inlets 194
6.21 Three dimensional deposition pattern from CFD for small inlets 195

7.1 Experimental setup for dry powder inhaler inlets 198
7.2 Deposition in oral cavity for DPIs as a function of the impaction parameter 201
7.3 Deposition in oral cavity for DPIs compared to Chapter 5 tests 204
7.4 Deposition in oral cavity for DPIs for various turbulence intensities 205
7.5 Predicted and measured oral cavity deposition for 5 DPIs . . . 207
7.6 Predictions of extrathoracic deposition for polydisperse drug formulations from DPIs 212
7.7 Predicted oral cavity and laryngeal deposition for polydisperse drug formulations from DPIs 213
7.8 Predicted extrathoracic deposition for polydisperse drug formulations from Clickhaler 215

List of Tables

2.1 Settling velocities of tested monodisperse aerosols 16
2.2 Equations for aerosol deposition by impaction in lung bifurcation 27

4.1 As tested impaction parameter values for gamma scintigraphy tests 77

5.1 Diameter of aerosol flow path at exit of a sample of dry powder inhalers 105
5.2 Turbulence measurements at pipe centerline 131
5.3 Centerline conditions for turbulent pipe flow jets 132
5.4 Centerline mean and turbulence measurements in oral cavity after enhanced turbulence inlets 146

6.1 Inlet boundary conditions for the CFD tests simulating experimental measurements from section 5.3 171
6.2 Mass and momentum balances for CFD tests simulating experimental measurements from section 5.3 172

7.1 Measured mouthpiece exit dimensions for tested dry powder inhalers 199
7.2 Multiple ANOVA output for tested DPIs 202
7.3 Particle size distributions and extrathoracic deposition for polydisperse aerosols from DPIs 210

Chapter 1

Introduction

1.1 Introduction to Pharmaceutical Aerosols

Aerosols are a part of our environment. Whether the aerosols encountered in everyday life are from natural sources like pollens, mists and sneezes, or are induced by human activity such as cigarette smoke, automobile exhaust and household dust, our bodies are regularly inhaling solid and liquid airborne particles. Because of this, the human body has many defensive mechanisms in place to protect against potentially harmful aerosol particles entering the body through the respiratory tract.

In fact, there exists in the lower 10 km of the atmosphere a background level of particulate matter ranging from 10^2 to 10^6 particles per milliliter.[114] Most of these particles range in size from 0.1 to 1.0 micrometers in diameter and are constantly being inhaled. However, the design of the human body is such that particles in this size range have the least likelihood of depositing in the body. With normal respiration levels and lung characteristics, these particles have too little mass to deposit via inertial impaction or sedimentation, and are too large to deposit by diffusion. This allows the particles to be exhaled without significant effects.

The introduction of industrial processes has greatly altered the concentration and size distribution of aerosols available for inhalation. The presence of airborne particles in size ranges capable of penetrating and depositing deep in the lungs where delicate tissues and close proximity to blood streams may enhance their effects on the body, has led to strong concerns about pollution and much research into its effects on the human body.

In addition to concerns about potentially harmful particles entering the body through the respiratory tract, research in the area of aerosol deposition has also been motivated by the desire to deliver beneficial substances to the body by inhalation. Pharmaceutical aerosols for treating lung diseases like asthma, cystic fibrosis and COPD (chronic obstructive pulmonary disease) have been in use for a number of decades. Recent widespread recognition of the benefits of the inhalation route for delivering various drugs for systemic use such as insulin for diabetes, human growth hormone and vaccines has also stimulated rapid growth in the medical aerosol field.

As the human body is well designed to protect itself against foreign aerosols in the ambient atmosphere, intentionally depositing aerosols into the body requires designing around the body's natural defense mechanisms. As will be discussed in this work, the fluid dynamics in the respiratory tract combined with the forces acting on a particle entering the tract determine if and where a particle will deposit in the body. The design of the human body is such that there is only a small window of particle sizes that will penetrate deep into the lungs and deposit.

For typical respiration profiles and lung geometries, particles with diameters of a few micrometers tend to deposit in the conducting airways and are quickly cleared from the lungs by muco-ciliary transport. Thin layers of mucus overlay the walls of the conducting airways. Many particles that deposit here travel with the mucus which is propelled out of the respiratory tract by rows of tiny cilia beating in rhythm between the cell walls and the layer.

Larger particles tend to deposit in the mouth and throat region and are cleared by either coughing or by swallowing and passing through the digestive tract. Particles with diameters of tenths to hundredths of micrometers tend be exhaled without depositing because they have too little mass to be affected by inertial or gravitational forces but too much mass to be significantly affected by diffusional forces over the course of a respiratory cycle. Finally, particles smaller than 0.01μm encounter increased deposition due to diffusional forces, but have so little mass that their numbers must be extremely high before they have clinical significance since the body typically responds to the mass of drug delivered.

1.2 Commercial Delivery Techniques for Pharmaceutical Aerosols

There are in general three techniques used for producing pharmaceutical aerosols: nebulizers, propellant (pressurized) metered dose inhalers (pMDI), and dry powder inhalers (DPI).

1.2.1 Nebulizers

In nebulizers, the drug is dissolved or suspended colloidally in a bulk liquid, typically an isotonic saline solution or pure water. Energy must be supplied to break up the bulk liquid into small droplets. The two main types of nebulizers are classified based on the way that this energy is supplied to the bulk liquid. Jet nebulizers use a high velocity air jet blowing across a liquid surface to break up the surface into droplets while ultrasonic nebulizers use ultrasonic waves to generate droplets at the liquid surface.

Jet nebulizers are a subset of the more general twin-fluid atomizers and part of the air-assist/airblast class of atomizers discussed by Lefebvre.[93] While traditional atomizers of this type use high pressure liquid feed systems, medical nebulizers do not due to safety, portability and cost constraints. A detailed consideration of the mechanics of jet nebulizers is beyond the scope of this manuscript and the reader is referred to the chapter on jet nebulizers by Finlay.[48]

The basic idea is that a high pressure gas (typically air) is supplied to the nebulizer from a compressor or a compressed air source. The air is accelerated through a venturi or orifice, causing both high air velocity and low static air pressure as the air exits the nozzle. This low pressure location causes the liquid from the bulk liquid reservoir to be drawn upwards to the nozzle exit typically through thin channels. When it comes into contact with the high speed air jet, the liquid surface is broken up into droplets which are entrained in the jet. The jet impinges on a primary baffle and large droplets splash off the baffle causing the formation of smaller secondary droplets. A system of secondary baffles causes large droplets to impact inside the nebulizer and be recycled into the fluid reservoir while smaller droplets are allowed to exit the nebulizer, creating a continuous mist of fine, water based aerosol particles. Some modifications of the basic jet nebulizer design include vented nebulizers which divert the exhaled air away from the production zone, thereby decreasing the loss of aerosol during exhalation, and breath enhanced nebulizers which draw the dilution air in through the nebulizer body, thus increasing the efficiency of the secondary baffles and decreasing the output particle sizes at higher inhalation flow rates.

Ultrasonic nebulizers utilize piezoelectric crystals excited at high frequencies (typically 1-3 MHz) to provide the energy required to break up the fluid surface into droplets. The vibrations of the crystal are transmitted through the liquid, forming standing waves in the bulk fluid reservoir. These standing waves cause a fountain of liquid to be formed in the nebulizer chamber.[111] Similar to the jet nebulizers, baffles are used to prevent large droplets from escaping the nebulizer, so that a mist of small droplets is produced. Some ultrasonic nebulizers incorporate breath actuation of the piezoelectric crystal to limit production of aerosol to inhalation cycles.

1.2.2 Propellant (Pressurized) Metered Dose Inhalers (pMDI)

This type of device for delivering pharmaceutical aerosols has the drug dissolved or in suspension with a volatile propellant and excipients in a small canister.[48] When the valve on the canister is triggered, a precisely metered volume of the mixture is released. The propellant rapidly expands, sending a bolus of volatile droplets out of the device. The aerosol plume develops over an initial region as the particle sizes decrease due to evaporation of the propellant and the velocity of the bolus decreases as the jet expands into the generally slower moving surrounding air. pMDIs are quite common due to their portability and low cost. However, concerns over difficulties in properly timing the inhalation and actuation has led to the development of spacers and holding chambers to both reduce the timing difficulties and to allow the plume to develop prior to inhalation.

1.2.3 Dry Powder Inhalers (DPI)

Rather than being in solution or suspension, the drug is stored in powder form in dry powder inhalers. It is often protected from ambient humidity since exposure can adversely affect powder dispersion. The powder may be contained in blister packs, in capsules, as loose powder or as tablets and is usually combined with a carrier such as lactose to increase powder uptake and ease dose filling during manufacture. An action is usually required prior to inhalation to expose the powder such as tearing open a blister, puncturing a capsule, scooping a measured amount of powder, or scraping a tablet.

Once the device has been primed, most DPIs (known as passive DPIs) use the force of the inhalation air flow to aerosolize and disagglomerate the drug particles although some (known as active DPIs) use mechanical means such as compressed air or battery powered impellers to disperse or disagglomerate the powder. Dunbar *et al.* give a more detailed discussion of the operating principles of many DPIs.[37] The devices are similar in size, portability, and cost to MDIs. While the powder format lends itself more easily to storing and delivering aerosols of proteins and peptides, many of the passive DPIs have minimum inhalation force and flow rate requirements for effective deposition in the lungs which may be difficult for some children or patients with severe respiratory ailments.

1.3 Importance of Prediction

As new and more expensive drugs such as insulin, human growth hormone, and vaccines are being introduced for inhalation, targeting of the drug delivery to specific regions of the respiratory tract is becoming more important. Designing for and predicting deposition in the various regions such as the nasal cavity, the oral cavity, the tracheo-bronchial region, and the alveolar region is crucial as both effectiveness and side effects are directly related to the mass of substance depositing in a specific region.

With a flood of new devices entering the market and under development recently, it is important to be able to predict the deposition of an aerosol exiting any given device. In order to accurately predict the aerosol deposition, the particle properties exiting the device must be known (for example: size distribution, particle density, number concentration, electric charge, hygroscopicity and particle shape). What is not yet well studied is the effect that the device's presence may have on the aerosol deposition, independent of the particle properties it produces. This manuscript attempts to quantify and predict the change in aerosol deposition that results due to the presence of a medical device at the entrance of the oral cavity.

1.4 Outline of Thesis

In Chapter 2, previous work on the possible mechanisms of aerosol deposition in the region is explored including inertial impaction, enhanced diffusion and deposition due to turbulence and sedimentation. The modelling techniques that have been employed to predict deposition of inhaled aerosols in the respiratory tract are considered. The chapter then focuses on modelling in the extrathoracic region, one of the least understood sections of the respiratory tract and the primary objective of the research presented in this manuscript.

An experimental setup was designed to measure the total deposition of monodisperse aerosols depositing in a realistic, idealized mouth and throat geometry after the aerosol entered through a variety of medical devices or a straight tube. The setup, results and discussion of these tests along with comparison to empirical formulas based on in vivo tests are contained in Chapter 3.

In Chapter 4, tests to measure the regional distribution of aerosol deposition in the extrathoracic airways were performed using radioactively labelled aerosol particles and planar gamma scintigraphy. Again various medical devices were used as inlets.

After finding the oral cavity to be a location of major differences in deposition between devices in Chapter 4, a realistic, idealized oral cavity model was constructed. The results of deposition tests using a large number of entrance conditions including various diameter contraction nozzles, straight pipes and pipes with enhanced turbulence are discussed in Chapter 5. Included in this section is the development of a model to predict the oral cavity deposition of monodisperse aerosols based on the entrance conditions for the region.

In Chapter 6, computational fluid dynamics is used as a tool to investigate the fluid flow inside the oral cavity. The purposes of these tests are to validate the length and velocity scales used in the deposition model from Chapter 5 and to quantify the regional deposition pattern in the oral cavity which was only qualitatively observed in the experiments performed.

The oral cavity deposition model from Chapter 5 is extended in Chapter 7 to predict deposition first for monodisperse aerosols entering the oral cavity through complex geometries similar to commercially available dry powder inhalers. The model predications are validated against experimental data. The model is then combined with the model for laryngeal deposition of Stahlhofen *et al.*[148] and further extended to polydisperse aerosols to predict total extrathoracic deposition entering through dry powder inhalers. This is validated against published in vivo data for polydisperse aerosol deposition from a variety of dry powder inhalers.

Chapter 2

Present State of Knowledge

2.1 Introduction

In this chapter the present state of knowledge in the modelling of extrathoracic deposition will be reviewed. The chapter begins by reviewing the general mechanisms of aerosol deposition. It then discusses modelling techniques for the whole respiratory tract and finally narrows to experimental and computational studies of the extrathoracic region and empirical deposition models proposed.

2.2 Aerosol Deposition Modelling

The behaviour of aerosols, solid and liquid particles entrained in gas flows, is actually a specific application of the more general multiphase flow. Multiphase flow deals with the concurrent motion of at least two phases, where the phases under consideration are solid, liquid and gas. Examples of multiphase flows include bubbles in soda pop, cavitation in pumps, sediment motion in rivers and oceans, dust storms, spray coatings, fluidized beds, and ambient and medical aerosols. Crowe *et al.*[28] gives a good introduction to multiphase flow with particles and droplets, including experimental methods and numerical models.

The equations governing the behaviour of a particle phase dispersed in a gas phase are well known. The mass, momentum and energy of the individual phases are transported with the phase and exchanges between phases and the surroundings are possible. The governing equations for a single particle phase (as is often the case in pharmaceutical aerosols) and the gas carrier phase include the continuity, momentum and energy equations for gas and for the particles. A set of equations for the mixture can also be derived. For example, Lixing[101] gives the differential form of the gas phase equations in indicial notation as:

Gas phase continuity

$$\frac{\partial \rho}{\partial t} + \frac{\partial}{\partial x_j}(\rho v_j) = S \tag{2.1}$$

where S is a mass source of the gas phase. For the aerosols studied here, no particulate matter is converted to gas and $S = 0$.

Gas phase momentum

$$\frac{\partial}{\partial t}(\rho v_i) + \frac{\partial}{\partial x_j}(\rho v_j v_i) = -\frac{\partial p}{\partial x_i} + \frac{\partial \tau_{ji}}{\partial x_j} + f_{bi} \tag{2.2}$$

where f_{bi} is the net body force on the gas phase. For example, f_{bi} may be given by:

$$f_{bi} = \Delta \rho g_i + \frac{\rho_p}{\tau_{rp}}(v_{pi} - v_i) + v_i S + F_{Mi} \tag{2.3}$$

where the first term is the gravitational force including buoyancy effects and the last three terms are forces on the gas phase as a result of the interaction with the particles. The second term includes the drag and lift force, the third term is the effect of the mass source on the momentum (which will be zero for our case) and the final term is the Magnus force.

Equation 2.2 as written is true for any fluid and any concentration of the particle phase. However, it is nearly impossible to solve in its present form for all but the simplest of cases. It is known that for dilute aerosols with volume fractions of aerosol to gas less than 10^{-6}, the particle phase will have negligible influence on the fluid phase.[29,41] Although this is not always the case for pharmaceutical aerosols, the tests performed in this work had volume fractions less than 10^{-6}, allowing the final three terms of equation 2.3 to be neglected in the fluid momentum equation. This leads to a one-way coupling of the momentum equations, with the gas velocity field affecting the particle motion, but the particles not affecting the air velocity field.

For Newtonian fluids (such as room air) the stress tensor (τ_{ji}) is linearly related to the strain tensor (S_{ji}) and the gas momentum equation becomes:

$$\frac{\partial}{\partial t}(\rho v_i) + \frac{\partial}{\partial x_j}(\rho v_j v_i) = -\frac{\partial p}{\partial x_i} + \frac{\partial}{\partial x_j}[\mu(2S_{ji} - \frac{2}{3}\delta_{ji}S_{kk}) + \xi\delta_{ji}S_{kk}] + f_{bi} \quad (2.4)$$

where δ_{ji} is the Kronecker delta function, μ is the usual fluid viscosity (shear viscosity), ξ is the bulk coefficient of viscosity and f_{bi} does not involve any of the particle interaction forces.

The bulk viscosity term $\xi\delta_{ji}S_{kk}$ represents the pure expansion or contraction of a control volume due to shearing. For incompressible fluids, this term will be zero. The final form of the stress tensor for incompressible, Newtonian fluids is then given by:

$$\tau_{ji} = 2\mu S_{ji} - \frac{2}{3}\mu\delta_{ji}S_{kk} \quad (2.5)$$

which is true for monotonic gases and a reasonable approximation for air in all engineering situations.[121] Then substituting equation 2.5 into equation 2.2 gives:

$$\frac{\partial}{\partial t}(\rho v_i) + \frac{\partial}{\partial x_j}(\rho v_j v_i) = \rho\frac{Dv_i}{Dt} = -\frac{\partial p}{\partial x_i} + \frac{\partial}{\partial x_i}\left(2\mu S_{ji} - \frac{2}{3}\mu\delta_{ji}S_{kk}\right) + f_{bi} \quad (2.6)$$

Inclusion of the definition of the strain tensor:

$$S_{ji} = \frac{1}{2}\left(\frac{\partial v_j}{\partial x_i} + \frac{\partial v_i}{\partial x_j}\right) \quad (2.7)$$

yields the Navier-Stokes equations which apply to incompressible, Newtonian fluids as:

$$\rho\frac{Dv_i}{Dt} = -\frac{\partial p}{\partial x_i} + \frac{\partial}{\partial x_j}\left(\mu\frac{\partial v_j}{\partial x_i}\right) + f_{bi} \quad (2.8)$$

If μ is assumed to be independent of position in the flow as is usually done since for air, μ is only moderately dependent on the fluid temperature and pressure, then the Navier-Stokes equations reduce to the commonly seen form:

$$\rho\frac{Dv_i}{Dt} = -\frac{\partial p}{\partial x_i} + \mu\frac{\partial^2 v_j}{\partial x_j \partial x_i} + f_{bi} \tag{2.9}$$

which in vector notation is:

$$\rho\frac{D\vec{v}}{Dt} = -\vec{\nabla}P + \mu\nabla^2\vec{v} + \vec{f_b} \tag{2.10}$$

Since the air is assumed to be an incompressible fluid and the viscosity is assumed to be independent of temperature variations within the area of interest, the Navier-Stokes equation is de-coupled from the gas energy equation and the energy equation need only be considered if the temperature field is of interest. Since the aerosols considered in this work are stable over a range of temperatures near room temperature, the energy equation did not need to be considered for either the air flow or the particle phase.

In the following section, the momentum equation for the particle phase is considered.

2.3 Particle Momentum Equation

Since a particle has inertia and is acted on by different forces than the fluid, its motion is governed by the particle momentum equation and its path will not necessarily be the same as that of adjacent fluid elements. It is because of this different path that particles are able to cross fluid streamlines and deposit on the walls of airways and alveoli in the respiratory tract.

Hinze explains that the equations of motion for a rigid sphere in a stationary fluid were derived by Basset, Boussinesq and Oseen, extended to the case of a moving fluid with unsteady velocity by Tchen.[71] They have also been discussed recently by Maxey and Riley.[108]

The equation for a spherical particle travelling in a continuous fluid (not including the lift force, Magnus force and Faxen corrections) is:

$$\frac{\pi}{6}d_p^3\rho_p\frac{dv_p}{dt} = 3\pi\mu d_p(v_f - v_p) + \frac{\pi}{6}d_p^3\rho_f\frac{dv_f}{dt} + \frac{\pi}{12}d_p^3\rho_f\left(\frac{dv_f}{dt} - \frac{dv_p}{dt}\right)$$
$$+\frac{3}{2}d_p^2\sqrt{\pi\rho_f\mu}\int_{t_o}^{t}\frac{\frac{dv_f}{dt'} - \frac{dv_p}{dt'}}{\sqrt{t-t'}}dt' + F_e \qquad (2.11)$$

where the subscript f refers to the fluid and p refers to the particle. The term on the left side of the equation is the force required to accelerate the particle due to its inertia. On the right side of the equation, the first term is the Stokes drag force on the particle, the second is the force on the particle due to the pressure gradient in the fluid surrounding the particle caused by the acceleration of the fluid, the third term is the force required to accelerate the virtual,“added mass” of the particle relative to the fluid, the fourth term is the Bassett history term which is an unsteady correction to the Stokes drag, and the final term is the sum of the external forces on the particle (eg. gravity, buoyancy, electrostatic, etc.)

Since most medical aerosol particles (and the monodisperse aerosols investigated in this work) have densities significantly higher than that of air (eg. $\rho_w = 1000$ kg/m^3 for water while $\rho_a = 1.2$ kg/m^3 for air), many of the forces acting on the particle such as the buoyancy force, Magnus force, Saffman force, Basset force, pressure force, Faxon correction and virtual mass force are much smaller than the drag force and the gravitational force and may all be neglected.[28]

Newton's second law for the aerosol particle can then be written as:

$$m_p\frac{d\vec{v}}{dt} = \vec{F} = m_p\vec{g} + \vec{F_{drag}} \qquad (2.12)$$

where m_p is the mass of the particle, $\vec{v}$ is the particle velocity, $\vec{g}$ is the gravitational vector and F_{drag} is the drag force on the particle caused by relative motion of the air and particle. Since the working fluid for most pharmaceutical aerosols and all the aerosols in the present work is air, we can substitute the subscript a for air for the general fluid subscript f.

For a spherical particle the drag force is well known to be given by:

$$\vec{F}_{drag} = C_D \frac{1}{2} \rho_a v_{rel}^2 A \hat{v}_{rel} \tag{2.13}$$

where ρ_a is the air density, $A = \pi d_p^2/4$ is the cross sectional area of the particle, $\hat{v}_{rel}$ is a unit vector in the direction of the relative velocity between the fluid and the particle (ie. $\vec{v}_{rel} = \vec{v}_a - \vec{v}_p$) while v_{rel} is the magnitude of the vector $\vec{v}_{rel}$. The drag coefficient C_D is a function of the particle Reynolds number Re_p given by:

$$Re_p = \frac{\rho_a d_p v_{rel}}{\mu_a} \tag{2.14}$$

where μ_a is the dynamic viscosity of air. For $Re_p \ll 1$ and $d_p/2 \gg \lambda$ (where λ is the mean free path of molecules in air and $\lambda = 0.067\mu$m at room conditions [48]) the Stoke's Law assumption can be made and

$$C_D = \frac{24}{Re_p} \tag{2.15}$$

For most pharmaceutical aerosols, which have diameters in the range of 1μm to 10μm and follow the flow streamlines fairly well, thus having low relative velocities, the Reynolds number assumption of Stokes drag is generally fulfilled. However, for particles with $d_p < 2\mu$m, the second assumption becomes questionable and the drag coefficient must be modified:

$$C_D = \frac{24}{C_c Re_p} \tag{2.16}$$

to include the Cunningham slip coefficient, C_c, an empirically determined parameter to compensate for the molecular nature of the fluid at these small scales (no longer can the air be assumed to be a continuum). For $d_p > 0.1\mu$m, Willeke *et al.*[163] gives:

$$C_c = 1 + 2.5 \frac{\lambda}{d_p} \tag{2.17}$$

Thus the equation of motion for the spherical particle reduces to:

$$\frac{\pi}{6}d_p^3\rho_p\frac{d\vec{v}}{dt} = \frac{\pi}{6}d_p^3\rho_p\vec{g} + \frac{3\pi}{C_c}\mu_a d_p\vec{v}_{rel} \tag{2.18}$$

If this equation is nondimensionalized in terms of U, a characteristic velocity scale of the fluid and D, a characteristic length scale of the flow, it takes the form:

$$\frac{U}{D/U}\frac{d(\vec{v}/U)}{d(t/(D/U))} = \vec{g} + \frac{18\mu_a U}{\rho_p d_p^2 C_c}\left(\frac{\vec{v}_{rel}}{U}\right) \tag{2.19}$$

Introducing the dimensionless variables:

$$\vec{v}' = \frac{\vec{v}}{U} \tag{2.20}$$

$$\vec{v}'_{rel} = \frac{\vec{v}_{rel}}{U} \tag{2.21}$$

$$\hat{g} = \frac{\vec{g}}{g} \tag{2.22}$$

$$t' = \frac{t}{D/U} \tag{2.23}$$

gives the final form of the particle momentum equation as:

$$Stk\frac{d\vec{v}'}{dt'} = \frac{v_{settle}}{U}\hat{g} + \vec{v}'_{rel} \tag{2.24}$$

where the Stokes number (Stk) is given by:

$$Stk = \frac{U\rho_p d_p^2 C_c}{18\mu_a D} \tag{2.25}$$

and the particle settling velocity (v_{settle}) is:

$$v_{settle} = \frac{C_c\rho_p d_p^2 g}{18\mu_a} \tag{2.26}$$

Geometric Diameter (μm)	Material	Settling Velocity ($\frac{mm}{s}$)
1	dl-α tocopheryl acetate	0.033
1	Di-2-ethylhexyl-sebecate (DEHS)	0.032
2.5	dl-α tocopheryl acetate	0.190
2.5	DEHS	0.182
3.8	dl-α tocopheryl acetate	0.430
3.8	DEHS	0.412
5	dl-α tocopheryl acetate	0.737
5	DEHS	0.706
7.5	dl-α tocopheryl acetate	1.64
7.5	DEHS	1.57

Table 2.1: Settling velocities of tested monodisperse aerosols

2.4 Sedimentation

Sedimentation is aerosol deposition caused by the effect of gravitational forces on aerosol particles. Consider first the case of a spherical particle suspended in stationary air. After a transitional period during which the particle accelerates from rest, the particle will reach its terminal velocity (the maximum velocity at which it may fall) where the downward gravitational force is balanced by the upward oriented drag force.

Since the velocity of the particle is no longer changing, the derivative on the left hand side of equation 2.24 is equal to zero and since the fluid velocity is also equal to zero, the equation reduces to:

$$\vec{v} = v_{settle}\hat{g} = \frac{C_c \rho_p d_p^2 g}{18\mu_a}\hat{g} \tag{2.27}$$

Table 2.1 gives a listing of the settling velocities for monodisperse aerosols with material properties and size ranges tested in this work calculated using equations 2.26 and 2.17.

Since the air in the respiratory tract (and especially in the extrathoracic region) is typically not stationary, but is flowing through conduits, the amount of aerosol that deposits due to sedimentation is dependant on both the settling velocity of the particles and the residence time of the aerosol in the conduit.

For monodisperse aerosols in tubes with all fluid velocities parallel to the tube walls, all particles fall vertically through the fluid at the same speed and there are no particle-particle collisions since no particle can catch up to any other.

The sedimentation of monodisperse particles from fully developed laminar flow in circular tubes has been well studied. For horizontal tubes, Fuchs[57] gives the fraction of aerosol depositing in the tube (P_s) as:

$$P_s = \frac{2}{\pi}[2\kappa\sqrt{1-\kappa^{2/3}} - \kappa^{1/3}\sqrt{1-\kappa^{2/3}} + \arcsin(\kappa^{1/3})] \tag{2.28}$$

where

$\kappa = \frac{3v_{settle}L}{8DU} \equiv$ sedimentation parameter
$v_{settle} =$ particle settling velocity
$L =$ tube length
$D =$ tube diameter
$U =$ average flow velocity

Heyder and Gebhart[68] found that for tubes inclined an angle θ from the horizontal, with the assumption that $v_{settle}\sin\theta \ll U$, P_s is given by the same expression as equation 2.28 but with κ defined by:

$$\kappa = \frac{3v_{settle}L}{8DU}\cos\theta \tag{2.29}$$

Heyder analyzed the case of laminar plug flow in the tube rather than fully developed laminar flow,[66] and the fraction of aerosol depositing in the tube is:

$$P_s = 1 - \frac{2}{\pi}\left[\arccos\left(\frac{4}{3}\kappa\right) - \frac{4}{3}\kappa\sqrt{1-\left(\frac{4}{3}\kappa\right)^2}\right] \tag{2.30}$$

where κ is given by equation 2.29.

The flow in the extrathoracic region is not expected to be laminar for inhalation through mouthpieces due in part to moderately high Reynolds numbers, the presence of free shear layers and complex geometry as discussed further in section 6.1. The presence of turbulence and secondary flows in the region would tend to enhance the aerosol mixing in the region. Finlay [48] considers the case of well mixed laminar plug flow in an inclined tube and derives the following equation for the fraction of aerosol depositing from the flow:

$$P_s = 1 - \exp\left[-\frac{4}{\pi}\frac{v_{settle}\cos\theta}{(U + v_{settle}\sin\theta)}\frac{L}{D}\right], \tag{2.31}$$

which for the case of $v_{settle}\sin\theta \ll U$ reduces to the expression given by other authors for horizontal tubes:[57,115]

$$P_s = 1 - \exp\left(-\frac{16}{3\pi}\kappa\right) \tag{2.32}$$

where κ is given by equation 2.29.

Brockmann [13] discusses sedimentation of aerosols from turbulent pipe flows and finds that for flows with $\kappa < 0.5$, (κ given by equation 2.29) the deposition does not differ significantly from that seen in laminar flows.

The drag force on an aerosol particle and thus the settling velocity, can be affected by internal flows inside a liquid droplet and by the presence of other particles' wakes. Hadamard [65] and Rybczynski [135] independently found that drag force on a liquid particle with internal recirculation can be given by:

$$F_{drag} = 3\pi\mu_a d_p v_{rel}\left\{\frac{1 + 2\mu_a/3\mu_p}{1 + \mu_a/\mu_p}\right\} = F_{Stokes\ drag}\left\{\frac{1 + 2\mu_a/3\mu_p}{1 + \mu_a/\mu_p}\right\} \tag{2.33}$$

For dense clouds, the settling velocity of an aerosol particle is lower than that of a single particle in isolation and is often referred to as 'hindered settling'. Empirical correlations for hindered settling are given by Crowe *et al.*[28] and Di Felice [44] which give for $Re_p \ll 1$:

$$F_{drag} = 3\pi\mu_a d_p v_{rel}/\alpha^{3.7} = F_{Stokes\ drag}/\alpha^{3.7} \tag{2.34}$$

where α is the volume fraction of the continuous phase given by:

$$\alpha = \frac{\text{volume of air}}{\text{volume of air} + \text{volume of particles}} \tag{2.35}$$

The volume fraction of the particle phase, β is given by:

$$\beta = \frac{\text{volume of particles}}{\text{volume of air} + \text{volume of particles}} \tag{2.36}$$

In the tests performed in this work, typical volume fractions of the particle phase were $\beta \simeq 1 \times 10^{-6}$ which corresponds to $\alpha = 0.999999$ and from equation 2.35, a change in the Stokes drag force of $< 0.0004\%$. Clearly, hindered settling is insignificant for our tests.

For the Di-2-ethylhexyl-sebecate (DEHS) and dl-α tocopheryl acetate aerosols, the viscosities of the bulk liqiuds are unknown. However, my observation suggests both have viscosities considerably higher than water, similar to room temperature liquid honey ($\mu = 9$ Pa·s) for dl-α tocopheryl acetate and heated liquid honey ($\mu = 0.26$ Pa·s at 70°C) for DEHS. From equation 2.33 these viscosities cause effects on the drag force of 0.00007% and 0.0023% respectively. Again, this is a negligible effect. Even for viscosities as low as that of room temperature water($\mu = 0.00096$ Pa·s at 22°C), the effect on the Stokes drag force is less than 0.7%.

In order to estimate the importance of sedimentation as a mechanism for aerosol deposition in the extrathoracic region, consider flow in a tube with dimesions similar to the oral cavity region. Sedimentation in the pharynx, larynx and trachea are expected to be negligible since the flow is predominantly vertical, with the settling velocity aligned with the average flow velocity. Consider a tube with diameter $D = 0.025$m, length $L = 0.065$m. Sedimentation will have the most effect for large particle sizes and small flow rates, so consider the case of a 7.5 μm diameter monodisperse aerosol of dl-α tocopheryl acetate with an inhalation flow rate of 15 L/min. This gives a mean velocity in the tube of 0.51 m/s and from equation 2.29, a value for the sedimentation parameter of $\kappa = 0.0063$ which is $\ll 0.5$ so that turbulent effects on settling velocity should be negligible. For fully developed laminar flow in the tube, equation 2.28 predicts a deposition fraction of $P_s = 1.055\%$ while laminar plug flow in the tube from equation 2.30 gives $P_s = 1.066\%$ and well mixed laminar plug flow gives $P_s = 1.060\%$.

If the particle diameter is reduced to 5 micrometers, the sedimentation parameter drops to $\kappa = 0.0028$ and the deposition fraction becomes $P_s = 0.48\%$. Sedimentation is therefore only significant for the largest particle diameter and lowest flow rate tested in this work and is expected to be negligible for the rest of tested cases.

2.5 Diffusion

Brownian diffusion is an important deposition mechanism for aerosol particles with diameters less than approximately 1 μm. As the smallest aerosol particle diameter tested in the current work is 2.5 μm, diffusion is not expected to be significant, but is included here for completeness.

Very small particles ($d_p \ll 1\mu$m) have so little inertia that collisions with moving air molecules cause the particles to readily move in a nondeterministic random walk known as Brownian motion. For an isolated particle diffusing in a stationary fluid, the actual path of the particle cannot be determined. However, the result developed by Einstein in 1905 can be used for time scales much larger than the time between molecular collisions so that the root mean square displacement of the particle (x_d) is given by:

$$x_d = \sqrt{2D_d t} \tag{2.37}$$

where D_d is the particle diffusion coefficient given by:

$$D_d = \frac{kTC_c}{3\pi\mu d_p} \tag{2.38}$$

In this equation $k = 1.38 \times 10^{-23}$J K^{-1} is Boltzmann's constant, T is the temperature in Kelvin, C_c is the Cunningham slip coefficient from equation 2.17, μ is the fluid viscosity and d_p is the particle diameter.

As a first estimate of the importance of diffusion in the extrathoracic region, consider the case of a low flow rate of 15 L/min and an extrathoracic region volume of 50 mL as quoted by Rudolf *et al.*[132] which gives an average residence time in the extrathoracic region of 0.2 seconds. From equation 2.37 a 2.5 μm particle will have a root mean square displacement of 2.0×10^{-6} m, or less than one particle diameter. Clearly, with length scales in the extrathoracic region on the order of 10 mm, diffusion in this region is unlikely to be a significant deposition mechanism for particles 2.5 micrometers in diameter and greater.

However, the air is not stationary in the respiratory tract and a more rigorous estimate of diffusional deposition should include the solution to the Navier-Stokes equations and the solution to the particle momentum equation with Brownian motion superimposed on the particle trajectory. Alternatively, a convective-diffusive equation for the particle concentration n of the form:

$$\frac{\partial n}{\partial t} + \nabla \cdot (n\vec{v}) = D_d \nabla^2 n \tag{2.39}$$

can be solved.[57] Here $n = 0$ at the wall and $\vec{v}$ is the bulk velocity field of the particulate phase which is often assumed equal to the fluid velocity field obtained from the solution of the Navier-Stokes equations.

The solution of these equations in complex geometries is clearly very difficult and approximations for flows in tubes have been developed. For fully developed laminar flow (Poiseuille flow) in a tube, Ingham[79] gives the probability of deposition due to diffusion (P_d) as:

$$P_d = 1 - 0.819e^{-14.63\triangle} - 0.0976e^{-89.22\triangle} - 0.0325e^{-228\triangle} - 0.0509e^{-125.9\triangle^{2/3}} \tag{2.40}$$

where the diffusion parameter $\triangle$ is given by:

$$\triangle = D_d \frac{L}{U} \frac{1}{4R^2} \tag{2.41}$$

and D_d is as defined in equation 2.38, L is the tube length, U is the mean velocity in the tube and R is the tube radius.

For the case of laminar plug flow, there are no radial or axial velocity gradients in the flow and the second term in equation 2.39 goes to zero. This reduces the solution to one identical to the case of a stationary aerosol residing in a cylindrical tube for a time of $t = L/U$. An analytical solution to this problem is available and is given by Fuchs[57] as:

$$P_d = 1 - 4 \sum \frac{1}{\lambda_m^2} e^{-4\lambda_m^2 \triangle} \tag{2.42}$$

where λ_m is the mth zero of the zero-order Bessel function J_o. Unfortunately, the infinite series is slow to converge for small values of $\triangle$ so that at least tens of thousands of terms are required to reduce the error to tolerable levels for values of $\triangle$ on the order of 10^{-9}. To reduce the computational load of such long summations, empirical approximations of the solution have been proposed. Finlay[48] gives:

$$\begin{aligned} P_d = \;& 0.164385\triangle^{1.15217} \exp[3.94325e^{-\triangle} + 0.219155(\ln\triangle)^2 + .0346876(\ln\triangle)^3 \\ & +.00282789(\ln\triangle)^4 + .000114505(\ln\triangle)^5 + 1.81798 \times 10^{-6}(\ln\triangle)^6] \\ & \text{if } \triangle \leq 0.16853 \\ P_d = \;& 1 \text{ if } \triangle > 0.16853 \end{aligned} \tag{2.43}$$

which differs from the exact solution by less than 2% over the range of $10^{-9} < \triangle < 0.3$.

In order to check the importance of diffusion as a deposition mechanism for the conditions tested in this work, consider a monodisperse 2.5 micrometer aerosol diffusing in a tube with dimensions similar to that of the oral cavity model used in Chapter 5. For a tube 0.025m in diameter and 0.060m in length where the air flow rate is 15 L/min at 25°C, from equation 2.41, the diffusion parameter is $\triangle = 2.113 \times 10^{-9}$. If the flow is laminar Poisseuille flow, equation 2.40 gives the deposition due to Brownian diffusion as $P_d = 0.091\%$. For a laminar plug flow profile in the tube, the deposition is found to be

$P_d = 0.024\%$ from equation 2.43. Although the flow in the oral airways is expected to be more complex than laminar flow in a straight tube, Brownian diffusion is not likely to be an important parameter in the deposition of aerosols 2.5 micrometers in diameter and greater in the extrathoracic region.

2.6 Inertial Impaction

A third mechanism which can cause deposition of inhaled aerosols in the respiratory tract is inertial impaction. Since particles have inertia, they cannot respond instantaneously to changes in fluid motion and their trajectories differ from that of nearby fluid molecules when the fluid streamlines curve. The amount that a particle will overshoot the curved path of a fluid streamline depends on the inertia of that particle. When fluid streamlines turn because of the presence of a nearby wall, particles which overshoot the streamline significantly may collide with the wall and are then said to have deposited due to inertial impaction.

Since impaction is driven by a sudden change in the path of the fluid streamlines, the consideration of simple flows like Poisseuille flow or laminar plug flow in a tube are not helpful in gaining understanding of how an aerosol will impact in the extrathoracic region. The flow geometry of the extrathoracic region is complex, including bends, expansions, sharp corners and contractions where the fluid streamlines may change direction. In order to develop a model that might predict the ability of the aerosol to follow the curved streamlines in the flow, we must have a velocity field that duplicates the curved nature of the air streamlines in the oral airways.

So it is necessary to use a reasonably complex flow as a model, solve the Navier-Stokes equations for this flow to give the velocity field and then apply the particle momentum equation to the flow field (assuming that the aerosol is dilute enough to not affect the fluid phase) in order to determine the effect of inertial impaction on the aerosol. Considerable work may be expended on this simplified flow model with only limited applicability of the results to the full complex geometry and velocity field of interest.

Instead of considering inertial impaction in a simplified flow to predict its importance, non-dimensional parameters are often used to predict the relative importance of impaction. From equation 2.24 the coefficients of the dimensionless particle momentum equation should denote the relative importance of the terms in the equations. If the nondimensionalization has been performed correctly, the variables $d\vec{v}'/dt'$, $\hat{g}$, and $\vec{v}'_{rel}$ should all be no greater than order 1 (ie. O(1)). For pharmaceutical aerosols, gravitational effects are often negligible, leading to a small value of the coefficient in the first term of the right hand side of equation 2.24, v_{settle}/U. For example, a 5 micrometer diameter monodisperse DEHS aerosol flowing at 15 L/min in a 25 mm diameter tube has a settling velocity of 0.0007 m/s (see Table 2.1) while the mean velocity in the tube is $U = 0.51m/s$. This gives a value of the leading coefficient for the gravitational term of $0.0014 \ll 1$ and generally negligible. In this case, equation 2.24 reduces to:

$$Stk\frac{d\vec{v}'}{dt'} \simeq \vec{v}'_{rel} \tag{2.44}$$

From this equation it can be seen that if the particle Stokes number goes to zero (due to small particle diameters or small density of the aerosol material) for the given flow geometry, then $\vec{v}'_{rel} \rightarrow 0$. And if $\vec{v}'_{rel} \rightarrow 0$, then $\vec{v}_{rel} \rightarrow 0$ since the fluid velocity scale U is finite which implies that $\vec{v}_a = \vec{v}_p$. If the fluid (air) and particle velocities are equal, then the particle must follow curved fluid streamlines and so the particle is not likely to impact on nearby walls. Conversely, if the particle Stokes number is large, then the relative velocity ($\vec{v}_{rel}$) must also be large, implying that the particle does not follow fluid streamlines well and so would overshoot curved streamlines near a wall and have a relatively high probability of depositing via inertial impaction.

For very large particle Stokes numbers however, the assumption of negligible gravitational effects becomes invalid and this simple analysis breaks down.

It should be emphasized that the choice of the relevant length and velocity scales D and U can greatly affect the value of the particle Stokes number and are application specific. For example, the accepted length scale D for fibrous filtration is the diameter of the fiber [8] while for inertial impactors D should be the radius of the impactor nozzle [103] and for flow in a lung bifurcation Finlay [48] gives D as the diameter of the parent airway and U as the average velocity in the parent airway. A logical choice of the relevant length and velocity scales for the flow being considered is important in order to accurately predict the inertial impaction behaviour of an aerosol by the particle Stokes number. Choices of length and velocity scales in the extrathoracic region studied in this work are explored in Chapter 5.

In addition to the particle Stokes number, parameters that may influence the inertial impaction of an aerosol include the flow Reynolds number and geometry factors. For example, Marple found that although the deposition in a laminar jet impactor was predominantly a function of the Stokes number, it was also affected by the Reynolds number of the flow for $Re < 500$ in the nozzle and was affected by the dimensionless jet-to-plate distance while the dimensionless throat length had negligible effects [102] (nondimensionalization was done in terms of the nozzle diameter for the geometric factors). Numerous experimental and numerical studies of particle deposition in airway replicas and casts of lung bifurcations have been performed and Finlay reports that for Reynolds numbers and in regions where impaction is important, inertial impaction is only weakly dependent on the flow Reynolds number and on the various geometric parameters.[48]

Since the original study of the cascade impactor by May,[109] inertial impaction in cascade impactors has been studied both experimentally and numerically for laminar jets issuing from both round and rectangular nozzles.[102,104,128] Rader *et al.*[128] found that for moderate values of the Reynolds number, the impactor systems could be adequately characterized using only the particle Stokes number. However, at both extremes of high and low Reynolds numbers, an additional parameter was required in order to characterize the particle-fluid interactions.

Determining the relationship between the particle Stokes number and the aerosol deposition in respiratory tract requires reproducing the curvature of the streamlines seen in the respiratory tract. Numerous experimental and numerical studies have been performed of aerosol deposition by impaction in lung bifurcation models and casts ranging in complexity from simple bent tubes to single generation bifurcations to multi-generation bifurcations with trachea and larynx attached. Finlay[48] has summarized the resulting empirical equations for aerosol deposition as a function of the Stokes number in the parent generation and the diameter ratio ($DR = D_d/D_p$ where DR is the diameter ratio, D_d is the diameter of the daughter generation and D_p is the diameter of the parent generation). The equations summarized by Finlay are given in Table 2.2. The large variability in the equation predictions is expected to be mainly due to the inability to accurately reproduce the curved streamlines of flow in a lung bifurcation because of the variation in complexity of the models used and because of the large inter-personal variation in airway geometry preventing the definition of the "true" bifurcation geometry.

In the extrathoracic region, inertial impaction is believed to dominate over sedimentation and diffusion for aerosols in the range of aerosol diameters tested in this work (2.5μm to 7.5μm).[148] The experimental and numerical work done on predicting inertial impaction in the nasal region reviewed in section 2.9.1, while that done in the oral airways is reviewed in section 2.9.2.

It is typical for deposition data in the extrathoracic region to be plotted

Formula	Source
$P_i = 0$ if $Stk < 0.02$, otherwise: $= -0.0394 + 3.7417(2\ Stk\ DR^3)^{1.16}$ for $DR = 0.8 - 1.0$	Kim *et al.*[86]
$P_i = -0.1299 + 1.5714(2\ Stk\ DR^3)^{0.62}$ for $DR = 0.64$	Kim *et al.*[86]
$P_i = a\ Stk$ where $a = f(\varphi, DR)$ and $a = 1.53473$ for Poiseuille flow, branching angle of $\varphi = 35^o$ and $DR = 0.7853$	Cai and Yu [16]
$P_i = b\ Stk/(1 + b\ Stk)$ where $b = 4\ DR^3 \sin\varphi$ and $b = 1.1111$ for $\varphi = 35^o$, $DR = 0.7853$	Landahl [90]
$P_i = 1 - \frac{2}{\pi}\arccos(\varphi\ Stk) + \frac{1}{\pi}[2\arccos(\varphi\ Stk)]$ where $\varphi = 0.568977$ for 32.6^o average branching angle	Yeh and Schum [166]
$P_i = 1.606\ Stk + 0.0023$	Chan and Lippmann [17]
$P_i = 1.3(Stk - 0.001)$	Taulbee and Yu [155]
$P_i = 6.4\ Stk^{1.43}$ generations 1-3 $= 1.78\ Stk^{1.25}$ generations 4-5	ICRP [120]
$P_i = 0$ if $Stk < 0.1$, otherwise $= 4(Stk - 0.1)/(Stk + 1)$	Ferron [46]

Table 2.2: Variety of equations for inertial impaction found in the literature as summarized by Finlay.[48] Stk is based on the daughter airway and $DR = D_d/D_p$ where DR is the diameter ratio between the daughter airway (D_d) and the parent airway (D_p).

against a dimensional parameter commonly known as the impaction parameter ($\rho_p d_p^2 Q$ or $d_{ae}^2 Q$) rather than against the Stokes number. Here, ρ_p is the density of the particle in g/cm^3, d_p is the diameter of the particle in μm, Q is the volume flow rate of the mixture in cm^3/s, and d_{ae} is the aerodynamic diameter of the particle in μm which is the diameter of a drop of unit density (such as water at standard conditions) with the same mass as the particle. The aerodynamic diameter is related to the geometric diameter of the particle by the formula:

$$d_{ae} = \sqrt{\frac{\rho_p}{\rho_{H2O}}} d_p \tag{2.45}$$

Since water at standard conditions has a density of 1 g/cm^3, substituting $d_{ae}^2 = \rho_p d_p^2$ with the set of units defined above yields the two forms of the impaction parameter used interchangeably in the literature. The two forms:

$\rho_p d_p^2 Q$ or $d_{ae}^2 Q$ have the same numerical value but different units due to not including the constant 1 g/cm^3 density in the second form of the parameter.

This impaction parameter can be seen to be proportional to the Stokes number for flow inside a conduit. The Stokes number is defined in equation 2.25 as:

$$Stk = \frac{U \rho_p d_p^2 C_c}{18 \mu_a D}$$

If we define the velocity scale U of the flow as the mean velocity over the cross sectional area A of the conduit so that $U = Q/A$ where Q is the volume flow rate, and the length scale D of the flow as the area equivalent diameter so that $D = D_{eq} = \sqrt{\frac{4A}{\pi}}$, then the Stokes number becomes:

$$Stk = \frac{Q \rho_p d_p^2 C_c}{18 A \mu_a D_{eq}} \tag{2.46}$$

Substituting in for A gives:

$$Stk = \frac{4 C_c}{18 \pi \mu_a D_{eq}^3} \, \rho_p \, d_p^2 \, Q \tag{2.47}$$

For a set flow geometry (as in the case of a respiratory tract cast) the length scale D_{eq}, though varying along the flow path, will be fixed at any streamwise location. Additionally, the Cunningham slip coefficient, C_c, can be expected to be nearly constant for cases where inertial impaction is important since it only becomes significantly large for small particles which is where impaction becomes less important. For example, at room conditions where the mean free path in air has a value of $\lambda = 0.067\mu$m,[48] the slip coefficient varies by only 6.2% with a significant change in particle diameter from 2μm to 10μm. So it is seen that for a fixed geometry, the Stokes number is proportional to the impaction parameter $\rho_p d_p^2 Q$ as:

$$Stk = C_1 \, \rho_p \, d_p^2 \, Q \tag{2.48}$$

where C_1 is a constant with respect to $\rho_p d_p^2 Q$ and:

$$C_1 = \frac{4C_c}{18\pi\mu_a D_{eq}^3} \tag{2.49}$$

Alternatively, consider the case of in vivo measurement of aerosol deposition in the extrathoracic region. The relevant length scale for monodisperse aerosols inhaled through large bore tubes is expected to be the larynx opening (known as the glottis) since the larynx is the primary location of aerosol deposition.[148] However, the larynx can vary significantly in diameter both between persons and for the same person throughout a breathing manoeuver. Since the length scale and so the particle Stokes number is therefore unknown throughout the breathing cycle, many authors resort to the use of the impaction parameter $\rho_p d_p^2 Q$ since it is composed of measurable quantities and should be proportional to the Stokes number. This works if the variations in the length scale are random in nature, for example due to inter-subject variability. However, additional scatter in the data may result if the length scale is correlated with the impaction parameter. This is not unreasonable since the area of the laryngeal opening is known to be a function of the inhalation flow rate.[12]

It is therefore not surprising that Rudolf *et al.*[133] found a reduction in data scatter when plotting the extrathoracic deposition against a parameter which incorporates the tidal volume of the individual patient during the test and not just the impaction parameter $\rho_p d_p^2 Q$.

2.7 Aerosol Deposition in Fully Developed Pipe Flow

An additional parameter unmentioned so far which may have an effect on the inertial impaction of aerosol particles is the presence of turbulence in the fluid phase. In the following section, the present state of knowledge on the wall deposition of an aerosol particle due to turbulence in fully developed pipe and channel flow will be reviewed.

It has been known for more than 45 years that the deposition of small particles from gas flow in a pipe is enhanced by the presence of turbulence. The problem of predicting the deposition rate has occupied researchers for just as long partly due to the practical relevance of the problem and also due to challenge imposed by the inability of any theory to provide a satisfying physical explanation of the observed phenomena.[168]

Due to the broad application of this area of research and the long time it has been under investigation, the amount of information in the archival literature is immense. This section is not meant to be a comprehensive overview of the field, but is intended to highlight the ability of turbulence to affect wall deposition of aerosol particles and to summarize some of the theories for predicting this effect.

The most widely quoted experimental data for aerosol deposition from fully developed, isothermal turbulent pipe flow are those of: Liu & Agarwal,[100] Friedlander & Johnston,[55] Wells & Chamberlain,[161] Sehmel,[144] and Schwendiman & Postma.[141] The deposition data from these studies is plotted in figure 2.1 using the standard dimensionless variables:

$$V_{dep+} = \frac{N_o}{C_{av} u_*} \tag{2.50}$$

and:

$$\tau_{p+} = \frac{\tau_p u_*^2}{\nu_a} \tag{2.51}$$

where V_{dep+} is the dimensionless particle deposition velocity, N_o is the flux of particles to the wall in units of # (or moles) of particles / $(m^2 s)$, C_{av} is the average particle concentration in the pipe cross section in # (or moles) / m^3, u_* is the friction velocity calculated from the wall shear stress τ_w and the

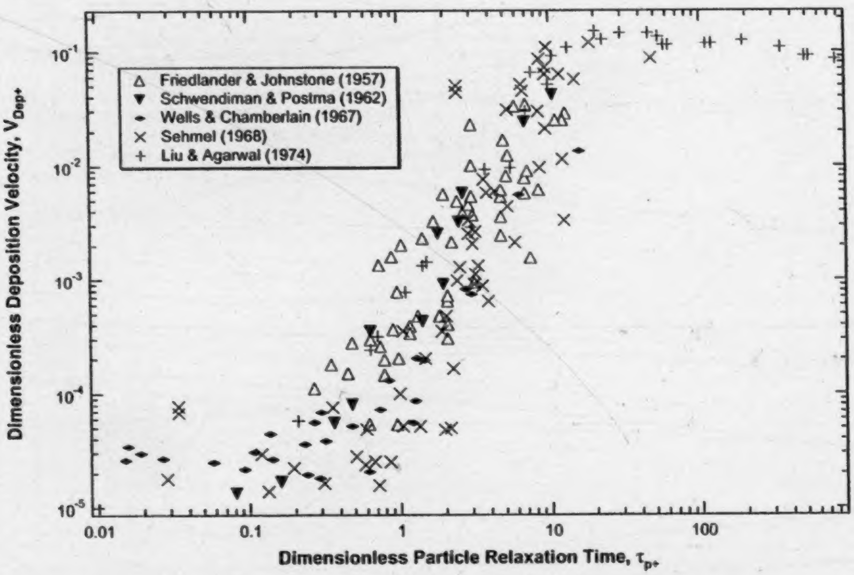

Figure 2.1: Wall deposition of aerosol particles from fully developed turbulent pipe flow. A summary of experimental data in literature.

air density ρ_a as $u_* = \tau_w/\rho_a$, ν_a is the kinematic viscosity of the air, τ_{p+} is the dimensionless particle relaxation time, and τ_p is the dimensional particle relaxation time given by:

$$\tau_p = \frac{\rho_p d_p^2 C_c}{18\mu_a} \tag{2.52}$$

The plot of figure 2.1 is generally split into three sections for analysis. In the first section ($\tau_{p+} < 0.3$) known as the diffusional deposition regime, the deposition velocity is a monotonically decreasing function of τ_{p+} and strongly depends on the particle Schmidt number, Sc given by:

$$Sc = \frac{\nu_a}{D_d} \tag{2.53}$$

where D_d is the standard Brownian particle diffusion coefficient given by equation 2.38. In this regime, the particle deposition is well modelled by a gradient diffusion model, ie. turbulent diffusion in the core of the flow and Brownian diffusion in a thin layer adjacent to the wall.

The middle section ($0.3 \leq \tau_{p+} \leq 20$), often referred to as the diffusion-impaction regime, is the most interesting and the most difficult region to model as the deposition velocity of the particles increases dramatically for small changes in the particle diameter (ie. an increase in particle diameter of 4 times causes an increase in the deposition velocity of greater than two orders of magnitude). This dramatic increase is usually attributed to the interaction of turbulent eddies with particles that have sufficient mass so that they are transported by gradient diffusion from the turbulent core into the boundary layer and then traverse the viscous sublayer by mechanisms other than Brownian diffusion, often assumed to be particle inertia. More details on the mechanisms of deposition in this region will follow.

In the third region, known as the inertia-moderated regime, particles deposit directly due to their inertia. Particles interact with the large eddies in the turbulent core and achieve sufficient momentum to coast through the boundary layer and deposit on the wall directly. In this region deposition velocity is seen to decrease slightly with increasing diameter due to the fact that increasing the inertia of the particles tends to decrease their response to the turbulence.

Early attempts to predict the deposition of small particles from turbulent pipe flows in the inertia-diffusion regime can be grouped under the heading of 'stopping distance' or 'free flight' models. Particles are assumed to be transported by turbulent gradient diffusion from the turbulent core of the pipe to one stopping distance from the wall and from there the particle makes a 'free flight' to the wall.[100] Examples of these models include those developed by Friedlander and Johnstone,[55] Kneen and Strauss,[88] Beal,[10] Sehmel,[143] Liu and Agarwal,[100] and Im and Chung.[78] The stopping distance (S) for spherical particles is typically defined as:

$$S = \frac{\rho_p \, {d_p}^2}{18\mu_a} v_{proj} \tag{2.54}$$

where v_{proj} is the velocity at which the particle is projected towards the wall at the beginning of the 'free flight'. Projection velocities are often taken to be equal to $v_{proj} = 0.9u_*$ where u_* is the friction velocity of the gas phase.[55,88]

The free flight models offer an attractive physical explanation of how particles impact on the wall, but they have some drawbacks. They lack rigor in their derivation. A solution to the particle continuity equation is matched to a free flight model to obtain the deposition flux with no analysis of the particle momentum equation. Yet only the particle momentum equation offers a means of calculating the convective velocity of the particles towards the wall generated by the turbulence. Brownian diffusion is generally assumed to be negligible (which is shown to be reasonable for $\tau_+ > 0.3$[100]) and the turbulent diffusivity of the particles is often taken to be equal to the fluid eddy diffusivity.

However, the most serious drawback of the 'free flight' theories is the need to assume projection velocities for the particles much higher than is realistic. In order to enable the theory to match experimental values, a projection velocity nearly equal to the friction velocity must be assumed for the particles at the point where the free flight begins. However, at locations between $y^+ = 1$ to 10, where y^+ is the dimensionless distance from the wall:

$$y^+ = \frac{y \rho_a u_*}{\mu_a} \tag{2.55}$$

the R.M.S. value of the fluctuations of the gas velocity normal to the wall are known to be much smaller than the friction velocity.[168] For example, Friedlander and Johnstone state that the R.M.S. value of the fluctuating component of velocity normal to the wall increases from zero at the wall to approximately

$0.9u_*$ at $y^+ = 80$. They then assume that the particle begins its free flight with a velocity equal to $0.9u_*$ and calculate the stopping distance locations as less than $y^+ = 5$ for nearly all cases. In fact, a more rigorous analysis of the free flight model by Davies[33] which uses a projection velocity equal to 1/2 the R.M.S. value of the fluctuations of the gas velocity normal to the wall at one stopping distance from the wall, gives particle deposition velocities roughly 2 orders of magnitude lower than experimental values.

More recent work in the area of wall deposition from turbulent pipe flows outlined below, tends to try to predict the particle deposition from the solution of the particle momentum equation coupled to the solution for the Navier-Stokes equations.

Sublayer models use the 2D or 3D coherent vortical structure of near wall turbulence to predict the flow field that interacts with the particles. Particle trajectories in this flow field are explored by solving the particle momentum equations including such external forces as the drag force, Saffmann lift force and gravitational force. For example, Fan and Ahmadi[43] proposed a sublayer model incorporating surface roughness effects as well which showed reasonable agreement with experimental data. The results of a recent direct numerical simulation by Zhang and Ahmadi[172] supports the theory that sublayer structure plays an important role in the particle deposition process as the initial location of depositing particles were observed to form periodic bands which corresponded to bands where high fluid streams towards the wall were formed.

Solution of the Reynolds averaged Navier-Stokes equations with the use of gradient transport terms to model the turbulence quantities is also a fairly common technique to get a fluid flow solution from which the particle momentum equation can be solved to obtain particle trajectories and deposition velocities. For example, Abuzeid *et al.*[1] used a two-equation $k - \varepsilon$ model to simulate the fluid flow field and used a Lagrangian particle tracking technique to predict the particle deposition on the walls.

Young and Leeming[168] used the Reynolds averaged version of the particle momentum equation to determine the relative importance of the various forces on the particle as it approached the wall. They found that the amount of information about the gas turbulence required to solve the particle momentum equation for the particle deposition was minimal, only requiring the radial distributions of the eddy diffusivity, the turbulent Schmidt number and the radial velocity fluctuation correlation $(\overline{u'_r u'_r})$. Empirical models were used for these quantities and a model for predicting particle deposition was developed. They found that particle motion was dominated by different effects in different layers of the boundary layer. The turbophoretic force (a force which tends to accelerate particles down gradients in $\overline{v'_{y+} v'_{y+}}$ where v'_{y+} is the component of the particle fluctuations normal to the pipe wall) given by:

$$(F_+)_{turbo} = -\frac{d}{dy_+}\left(\overline{v'_{y+} v'_{y+}}\right) \tag{2.56}$$

tends to accelerate particles towards the wall for distances $y^+ < 40$ and reaches a maximum at $y^+ = 20$. This is not a small correction and when combined with the Saffman lift force, dominates the particle transport in the region of $20 < y_+ < 40$. Particles propelled by the turbophoretic force towards the wall tend to have higher axial velocities than the fluid near the wall. This relative motion of the particle to the fluid combined with the velocity gradient in the radial direction of the axial component of the fluid velocity causes a lift force directed towards the wall to act on the particle. The combination of this lift force and the turbophoretic force tends to accelerate the particles towards the wall. However, for all but very large particles ($\tau_{p+} > 50$), the turbophoretic and lift forces drop dramatically as the particle nears the wall ($y_+ < 20$) and the viscous drag force decelerates the particle, preventing it from coasting to the wall. A high concentration of particles builds up in the region right near the wall ($y_+ < 3$ for $\tau_{p+} < 10$)[14] and the high concentration gradient near the wall causes diffusion to be the dominating mechanism to transport the particles across the final part of the viscous sublayer until they deposit when they reach one radius from the wall.

A similar technique of Reynolds averaging the particle momentum equations to obtain terms for the particle flux to the wall which correspond to the distinct physical phenomena of Brownian diffusion, thermophoresis, turbophoresis, lift force and electrostatic force is used by Guha[64] who also accounts for surface roughness effects.

Numerical techniques such as LES (Large Eddy Simulation) and DNS (Direct Numerical Simulation) have been employed to predict the particle deposition by numerically releasing particles in the flow solution and tracking their motion over time.[14,156,158,172] The results of these works tend to predict intermediate sized particles having insufficient inertia to coast through the viscous sublayer and building up in concentration very close to the wall, followed by an increase in Brownian diffusion to the wall due to the high concentration gradients.

From this discussion, it can be seen that there is a great deal of uncertainty about the basic mechanisms of aerosol deposition in the relatively simple case of fully developed turbulent flow in a vertical tube or channel. It is therefore not surprising that our knowledge of how aerosols deposit in a complex geometry and flow field like the respiratory tract is far from complete.

2.8 Lung Deposition Models

In order to calculate the amount and location of aerosol particles depositing in the respiratory tract for even the simplified case of dilute aerosols (which can be treated as single particles not affecting each other or the air flow field), the particle momentum equation (in three dimensions) needs to be solved. However, as the particle's momentum is significantly affected by the air's velocity field, this requires the complete solution of the Navier-Stokes equations (an already simplified version of the gas phase momentum equations) to give the air velocity field for the whole time-dependent, three dimensional geometry.

This is very discouraging because the geometry of the respiratory tract is essentially unknown from an engineering perspective. Due to the small nature of the particles and the relative importance of small scale events, the lung geometry must be resolved down to very fine details. For example, one of the major parameters of interest is whether a particle will deposit or not upon reaching an alveolus. In order to predict this, the velocity field within the alveolus must be resolved. However, in a normal adult lung Finlay reports there are approximately 300 million alveoli[48] and in the simplified lung geometry model proposed by Finlay *et al.*[49] nearly 95% of the lung volume is contained in generations with diameters less than 1mm. Not only is there a huge amount of fine detail that needs to be resolved in the geometry, but the geometry also varies dramatically with time. With a typical total lung capacity in adults of approximately 6 liters and a vital capacity (the maximum volume an individual can inhale in a single breath) of about 4 liters, during a very deep breath, the volume contained in the respiratory tract can nearly triple, vastly changing the geometry of the air flow field during the course of a breath. Furthermore, the air flow rate drawn into the lungs and the change in geometry are coupled to the solid mechanics problem of muscles with finite strength expanding the rib cage to inflate the lungs. The final complexity which prevents the solution of the three dimensional air velocity field in the respiratory tract is the variation of lung geometry between people. Inter-person variability persists not only in the fine details of the alveoli locations, but right up to the lengths, diameters and branching locations of the large bronchiole airways. The effects of airway diseases on the geometry of the tract is also known only in general terms and so knowledge of the fine details of diseased lungs is poor at best. Clearly, with our present lack of knowledge of the essential flow geometry and current limitations of computing power, solving the relevant three dimensional gas phase momentum equations is impractical if not impossible.

As a result of this difficulty in solving the complete problem, two main types of lung deposition models have developed: empirical models and dynamical models. Empirical models are curve fits based on experimental data or on data from more complex dynamical models. Dynamical models predict particle deposition based on the equations of motion for the fluid and particle phases (although drastic simplifications are often employed).

There are a wealth of models in the literature for predicting the deposition of aerosols in the respiratory tract. Heyder and Rudolf[70] review the aerosol deposition models for the human respiratory tract and list 27 different deposition models published prior to 1984 with the original work being that of Findeisen in 1935.[47]

Empirical models are the simplest and generally require the least computational time. As they are typically empirical fits to a set of experimental, in vivo deposition data, they form a set of algebraic equations and so are easily implemented. They do not explicitly differentiate between the mechanisms causing the deposition and so do not allow for easy extrapolation beyond the parameters tested in the data set they are based upon which may limit their applicability. Examples of empirical models include those of Davies[34] and Heyder *et al.*[67] whose models give the total deposition the respiratory tract as a function of particle diameter and breathing parameters. Multi-compartmental models such as those of Rudolf *et al.*,[132,133] Yu *et al.*[170] and the ICRP (International Commission on Radiological Protection)[120] predict regional aerosol deposition in a few regions, for example Rudolf's model[133] gives deposition predictions for four regions: extrathoracic, bronchial, bronchiolar and alveolar.

Dynamical models base their predictions of aerosol deposition on the equations of motion for the particle and gas phases, using the available experimental data for validation of the deposition model. Dynamical models can be further categorized based on the reference frame of the equations into Lagrangian models where the aerosol is analyzed in a frame that travels with an individual particle and Eulerian models where the aerosol is analyzed from a stationary reference frame.

The current Lagrangian models in the literature form the next step up in computational complexity from empirical models. Langrangian dynamical models published since Heyder's 1984 review[70] include those by: Finlay and Stapleton,[50] Darquenne and Paiva,[32] Persons *et al.*,[123] Ferron *et al.*,[45,46] and Koblinger and Hofmann.[89] They are typically one dimensional, following an aerosol as it proceeds along the dimension of depth into the lung. The fluid flow in the lung is assumed to be either plug flow or Poiseuille flow in each generation. Deposition probabilities are calculated for each generation based on deposition mechanisms like sedimentation, diffusion and inertial impaction similar to those derived in sections 2.4, 2.5, and 2.6. Typically idealized, symmetrical lung geometries are used, although asymmetrical geometries have been considered.[89]

Eulerian models which have been published since 1984 include those of: Edwards,[39] Egan and Nixon,[40] and Scott and Taulbee.[142] All present Eulerian models are one dimensional, similar to Lagrangian models, with depth into the lung forming the dimension of interest. The general idea of the models is to solve a convective-diffusive equation for the aerosol in an idealized lung geometry. The aerosol is both convected through the lung by the air motion and diffuses by Brownian motion relative to the air. The probability of aerosol deposition in a given airway is again predicted using equations similar to those of sections 2.4, 2.5, and 2.6. These deposition probabilities enter the convective-diffusive equation for the aerosol motion via the terms for the decrease in aerosol concentration due to flux of particles through the sides of the control volume (ie. the airway walls).

Eulerian and Lagrangian dynamical models have their respective tradeoffs. Lagrangian models allow for easy incorporation of one-way and two-way coupled hygroscopic effects but have difficulty incorporating the axial diffusion of an aerosol bolus during a breath and any flow rates and aerosol concentrations that vary during a breath. However, Eulerian models are able to handle time-dependance and bolus dispersion much more easily but generally have difficulty with two-way coupled hygroscopic effects.[48]

2.9 Extrathoracic Deposition Models

Although much of the respiratory tract can be reasonably modelled as a series of cylinders, bifurcations and spheres, greatly simplifying the solution of the necessary equations, the geometry of the extrathoracic region is much more complex and cannot be reduced to such simple geometric shapes. Although the definition of the extrathoracic region varies slightly in the literature, it is generally taken to include the nasal passages, oral (or buccal) cavity, pharynx, larynx and upper part of the trachea.[145,147]

2.9.1 Nasal Deposition

Deposition in nasal passages has been measured experimentally using monodisperse micrometer sized aerosol particles by numerous investigators. Pattle, Fry, and Hounam *et al.* evaluated nasal deposition by measuring the change in aerosol concentration when an aerosol is drawn in through the nasal passages and out through the oral passages while volunteers hold their breath.[56,75,122] External detection of deposited activity after inhaling radioactive labelled particles was used to evaluate nasal, tracheobronchial and alveolar deposition by Lippmann.[98] Giacomelli *et al.* and Heyder *et al.* evaluated nasal deposition during more realistic breathing patterns by assuming oral cavity deposition to be negligible when breathing through large tubes and comparing the change in aerosol concentration for nose-in, mouth-out to mouth-in, mouth-out breathing.[60,69] Heyder also extended this technique to mouth-in, nose-out breathing and showed that nasal deposition for inhalation was different than nasal deposition for exhalation. Equations to predict the deposition efficiency of the nasal passages based on this experimental data have been proposed.[148,169] Cheng *et al.* and Swift *et al.* have investigated the deposition of particles less than 0.5μm in diameter in casts of the nasal passages[20–22,154] and developed a model based on the data.[23] Martonen and Zhang summarized nasal deposition data and developed an empirical formula to predict nasal deposition over a size range of 0.005μm to 7μm.[106] Recent work has also used computational fluid dynamics to predict particle deposition in a model of the nasal passages,[139] though the numerical simulations were found to overpredict deposition for small particles (0.5μm and 1μm) and underpredict particles for larger particles (5μm).

2.9.2 Oral Deposition

Although aerosol deposition in the nasal passages during tidal breathing is important when considering such issues as nasal sprays, drug delivery via face masks, and the effects of pollution or second-hand cigarette smoke on a person, the majority of pharmaceutical aerosols use the oral route for administering drug to the respiratory tract. The oral route generally causes far less aerosol deposition than the nasal route. When plotted against the impaction parameter described in section 2.6, the data presented by such researchers as Yu *et al.*,[169] Lippmann[99] and Stahlhofen *et al.*[148] show significant nasal deposition beginning at values of the impaction parameter at least an order of magnitude lower for nasal inspiration than for mouth inspiration.

Due to the complex geometry in the oral airways, the time varying nature of the geometry and the large inter-subject variability, deposition modelling in this region has proceeded primarily by means of empirical formulas based on experimental data, similar to the modelling in the nasal cavity.

While not as plentiful as the nasal deposition data, a variety of in vivo tests using monodisperse aerosol particles have been done in the oral airways. In a series of papers Lippmann, Chan and Albert [17,97,99] did extensive in vivo testing to investigate the deposition of spherical, monodisperse particles of iron oxide tagged with ^{198}Au, ^{51}Cr or ^{99m}Tc ranging in size from 0.2 to 7.9 μm in diameter. Deposition in the extrathoracic region was quantified by measuring the radioactive counts in the head region and comparing to the radioactive counts in the thoracic region. Unfortunately, their stomach detector could not provide quantification of the amounts cleared to the stomach from the oral airways prior to the head measurements as can occur even when the subject tries to avoid it.[97,145] As well, Gebhart *et al.*[59] found iron oxide to be mildly hygroscopic with possible large effects if care was not taken to thoroughly dialyze the iron oxide colloid. The ICRP model [120] proposes a method for predicting a time dependent aerodynamic diameter for the particles. Stapleton [149] corrected their data for hygroscopic growth in the tracheo-bronchial region, but not in the extrathoracic region.

Emmett *et al.*[42] measured the regional deposition of radioactively labelled, monodisperse polystyrene particles in vivo with aerodynamic diameters ranging from 3.5 μm to 10.0 μm. They found the majority of extrathoracic deposition was located in the throat (larynx and trachea) and the percentage increased with increasing particle diameter.

Foord *et al.*[52] performed in vivo tests measuring the total and mouth deposition of a radioactively labelled, monodisperse polystyrene aerosol. They used a 10 mm diameter inlet and inserted it typically 60 mm into the oral cavity. Mouth deposition was quantified by having the subject gargle three times and measuring the amount of radioactivity in each of the three washings. The authors recognized that laryngeal deposition might not have been removed by mouth washings and the need for standardized methods for in vivo deposition tests through mouthpieces.

Stahlhofen *et al.* performed tests on volunteers measuring the regional deposition of radioactively labelled aerosols made of iron oxide or di-2-ethylhexyl sebecate.[145–147] The flow rate that the subjects inhaled at was carefully monitored and controlled to be uniform over most of the inhalation time. The volunteers inhaled through a 16 mm ID mouthpiece and regional deposition was determined by measuring radioactive counts in the various regions of the body after inhalation. Tissue attenuation factors were generated using human shaped phantoms constructed of polyethylene and polyurethane and interference factors between extrathoracic and chest as well as chest and stomach regions. In this way extrathoracic deposition including any aerosol cleared to the stomach prior to counting was accurately determined.

Svartengren *et al.*[151] measured the deposition of monodisperse Teflon particles with aerodynamic diameters of 3.6 μm in asthmatic subjects. They found considerable scatter in the data but were able to correlate some of the high mouth and throat deposition values to qualitative measures of constriction of the pharynx and larynx during inhalation. There are concerns raised by the author about the accuracy of the extrathoracic deposition measurements because of the possibility of swallowing between measurements causing aerosol to be measured twice. As well, the mouth and throat deposition amount is a combination of 3 separate measurements, leading to extra error. No indication of the mouthpiece used or inlet conditions for the aerosol is given, nor were tests verifying the size distribution of the particles prior to inhalation reported to ensure adequate drying of surfactant and water mixture from the surface of the Teflon particles.

Bowes and Swift[77] studied monodisperse aerosol deposition in the oral airways in vivo. The majority of tests were done without a mouthpiece, but a few tests were performed with two mouthpieces, a 25 mm diameter tube or a rubber mouthpiece. They observed that aerosol deposition in the mouth was lower for either mouthpiece than for no mouthpiece. They also observed that during oral nasal breathing with no mouthpiece, the aerosol deposition pattern was reasonably uniform throughout the oral regions, but with the addition of a mouthpiece or when the mouth opened widely, the deposition was reduced and the pattern changed.

Significant variation in the extrathoracic deposition data is seen when the data from a number of these tests are plotted in figure 2.2. As is common practice in the above references, the deposition data is plotted against the impaction parameter $\rho_p d_p^2 Q$ (or equivalently $d_{ae}^2 Q$) described in sections 2.6 and 5.2.2.1.

Based on various portions of this data set of in vivo measurements, numerous empirical fits have been proposed by various authors.[17,52,99,105,112,148,165,169] In figure 2.3 a number of these empirical fits are plotted along with the raw data from figure 2.2. The deposition models in this section are typically linear and non-linear regression fits to the sections of the total data set that the author considers. As such, all predict extrathoracic deposition as a single function of the impaction parameter $\rho_p d_p^2 Q$.

Rudolf *et al.*[131–134,148] have developed an algebraic model for predicting the deposition of aerosol particles in various sections of the respiratory tract including the extrathoracic region. Their model has been adopted by the Task Group of the International Commission on Radiological Protection (ICRP) [80,120,134] and treats each region of the respiratory tract as a filter with a pre-

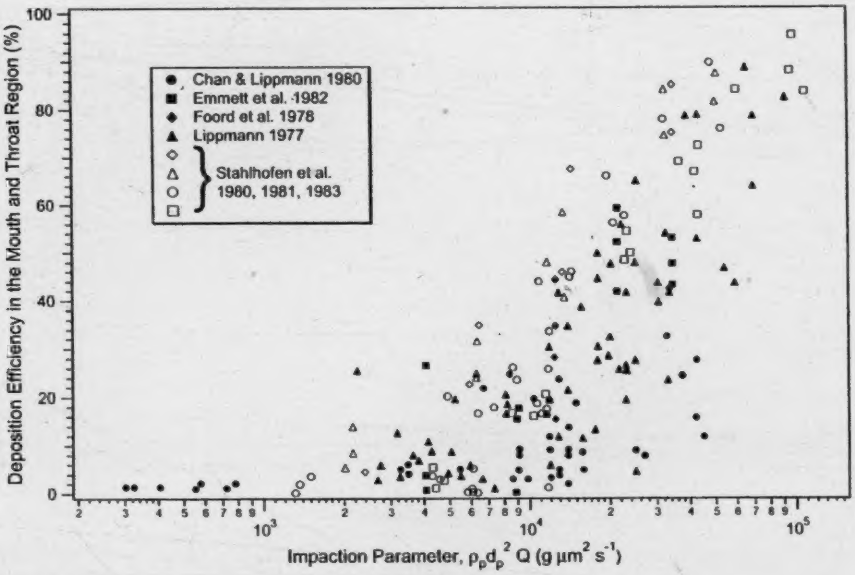

Figure 2.2: Extrathoracic deposition data from archival literature. Deposition plotted as a function of the impaction parameter $\rho_p d_p^2 Q$.

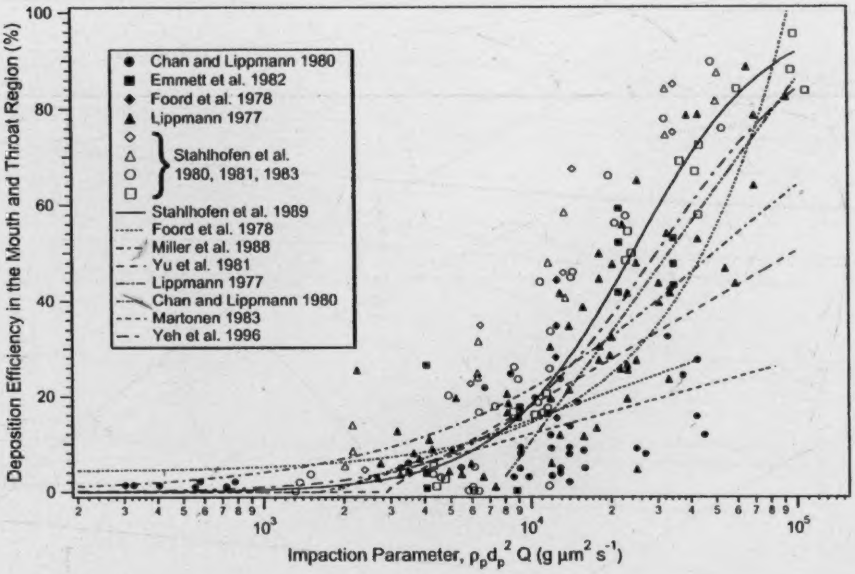

Figure 2.3: Empirical models of extrathoracic deposition presented in the literature along with the deposition data from figure 2.2 upon which most are based.

dictable efficiency at removing aerosol particles for given flow rates, volumes and particle diameters. Rather than plotting extrathoracic deposition versus the impaction parameter, Rudolf argues that oral cavity and pharyngeal deposition are negligible relative to laryngeal deposition and since the opening of the target organ, the larynx, changes with increasing flow rate, the relevant parameter for impaction in the extrathoracic region is $\rho_p d_p^2 Q^{0.6} V^{-0.2}$, not $\rho_p d_p^2 Q$. This leads to a slight decrease in the scatter of the data of Stahlhofen *et al.*[145–147] where the breathing patterns are carefully controlled and documented, but no decrease in the scatter for the data of other researchers who did not document the tidal volume for all patients. Since the curve fits for their models are based on data from many researchers, only marginal improvement in the data scatter is visible by using this new form of an impaction parameter. A major drawback of this model for application to in vitro tests such as those performed in this manuscript is that the parameter tends to zero for large tidal volumes. So it is unclear what tidal volume to use when comparing to tests at steady (non-cyclic) flow rates.

In order to avoid the problem of incorporating tidal volume into a non-cyclic flow pattern and because the larynx in the extrathoracic geometry tested does not have a cross sectional area that varies with flow rate and due to the limited improvement in data collapse afforded by these models, the deposition tests reported here are compared to models based on the original impaction parameter definition, $\rho_p d_p^2 Q$.

Recent work in the oral airways with micrometer sized particles includes deposition testing in vitro using casts of the oral airways. Cheng *et al.*[24] investigated deposition in a cast based on dental impressions of a volunteer connected to a cast from a cadaver. A range of particle diameters and flow rates were investigated for a single 22 mm diameter inlet. Results showed deposition efficiency to be an increasing function of the particle Stokes number calculated based on the minimum hydraulic diameter and the velocity calculated from the mean flow rate and the mean cross sectional area in the region. Their data exhibits far less data scatter than the in vivo tests described above as is expected due to the fixed geometry. However, the effects of inlet conditions were not investigated.

A recent paper by Lin *et al.*[96] investigated the effect of mouthpiece diameter on the deposition in the extrathoracic region during oral breathing. They investigated three particle sizes, four flow rates and three different inlets with internal diameters of 14 mm, 19 mm and 26 mm. They found lower deposition for the larger diameter inlets in certain impaction parameter ranges. However, the geometry of the oral airways was also different with each different inlet and the velocity profile at the inlet was not characterized. Although the tested flow rates were chosen based on high flow rates often seen with dry powder inhalers, the inlet diameters do not cover the range of small inlet diameters often seen with these devices. This work is also discussed in detail in section 5.2.2.3.

To the author's knowledge, there currently exists no data on the in vivo deposition of ultrafine particles (with $d_p < 0.1\ \mu$m) in the oropharyngeal region. However measurements in oral casts have been made [19–21] and relatively high deposition of the ultrafine particles has been observed with Cheng *et al.* reporting 48% to 78% deposition in the oral airway of particles between 1.2 and 1.7 nm in diameter. The dominant mechanism for ultrafine aerosol deposition in the oral airways is believed to be diffusion and deposition data is generally plotted against a diffusional parameter of the form $Q^{-a}D^{b}$ where Q is the volume flow rate and D is the particle diffusion coefficent.

Chapter 3

Total Extrathoracic Deposition Tests [1]

3.1 Introduction

Determination of the dose of drug delivered to a patient by means of an inhaled aerosol is difficult. While the dose of drug placed in a medical device may be directly measured, the actual dose that the patient receives depends both on the efficiency of the device in aerosolizing the drug and on the subsequent deposition of the aerosol. Many parameters affect the location and efficiency of aerosol deposition in the human respiratory tract.[48] Properties of the aerosol material (e.g. density and shape) and characteristics of the aerosol cloud (e.g. particle size distribution, number density and charge) combine with patient variables (e.g. lung morphology, breathing pattern and ambient conditions) to determine the quantity of drug delivered to the lung in a particular setting.

In vivo testing using radioactively labelled aerosols has been shown to be effective for measuring the total and regional deposition of aerosols in humans.[42] However, besides being expensive, labour intensive and time consuming, in vivo tests are intrinsically reactive. They give information on the deposition patterns only for the specific parameter setting tested. Extrapolation of the data and empirical models developed from the data to different parameter settings is difficult since only limited information on the mechanisms which govern the deposition can be inferred from the data. There are many additional variables which cannot be controlled in the in vivo setting and it is generally not feasible to test for the effects of all of them. In order to predict what would happen with a slightly different set of parameters, in vivo tests must be combined with predictive mathematical models.

---

[1] A version of this chapter has been published. DeHaan and Finlay 2001. Journal of Aerosol Medicine. 14,3:361-368

In vitro aerosol tests have been used to determine important aerosol characteristics such as particle size distributions, static charge and number density necessary to describe their behaviour.[152] A predictive tool results when these aerosol parameters are used in combination with computer modelling of aerosol behaviour once the aerosol enters a simulated human respiratory tract. The accuracy of this predictive method may then be validated against in vivo deposition data.

The physics governing aerosol behaviour in the bronchial and alveolar regions of healthy patients is well established. However, theoretical modeling of the aerosol behaviour in the extrathoracic region based on physical laws is difficult due to the complex and time varying geometry of the region and due to the presence of turbulent and transitional flows. Instead, deposition modeling in this region has been based on empirical correlations derived from in vivo test data. Empirical equations have been proposed by various investigators for industrial hygiene applications.[112,133,148,169] In general, the deposition data on which the empirical correlations are based has been gathered by subjects inhaling radioactively labelled monodisperse aerosol particles through large bore tubes as discussed in section 2.9.2.

Clark and Egan[25] suggest that the application of these empirical correlations to pharmaceutical aerosols is based on two assumptions: that the correlations may be extrapolated to higher flow rates of up to 120 L/min and that the geometry of the mouthpiece does not significantly affect the deposition in the extrathoracic region.

Recently, Clark *et al.*[27] compared reported oropharyngeal deposition from seven gamma camera deposition studies (for subjects inhaling through various inhalers) with that predicted by the empirical oropharyngeal deposition equation proposed by Rudolf et al.[133] for polydisperse aerosols. They found experimental oropharyngeal deposition to be 60% to 70% higher than that predicted by the empirical equation, a difference that may be attributable to differences in the fluid motion when inhaling through an inhaler versus a straight tube. In the present work, the effect of mouthpiece geometry on the deposition of aerosols in the mouth and throat region is examined. Variations due to patient dependent parameters were removed by testing the deposition in vitro with identical, realistic mouth and throat geometries at controlled inhalation flow rates. Monodisperse aerosols were used for the tests in order to control aerosol characteristics that affect deposition. Only the inlet flow conditions of the aerosol at the mouth and throat region were varied by having the aerosol enter through a variety of pharmaceutical devices. In this manner, variations in the deposition in the mouth-throat region could be attributed to the different flow patterns set up in the mouth and throat downstream of the mouthpiece geometry.

3.2 Experimental Setup

In order to test the effect of the fluid entry conditions generated by various medical devices on the deposition of aerosol particles in the mouth and throat region, the experimental system illustrated in Figure 3.1 was assembled.

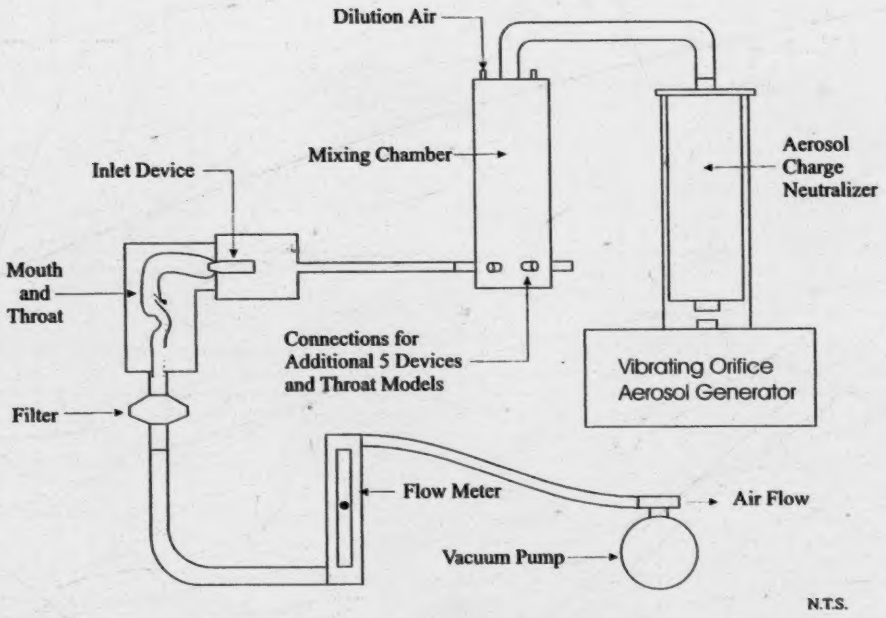
Dilution Air
Mixing Chamber
Aerosol
Charge
Neutralizer
Inlet Device
Mouth
and
Throat
Connections for
Additional 5 Devices
and Throat Models
Vibrating Orifice
Aerosol Generator
Filter
Flow Meter
Air Flow
Vacuum Pump
N.T.S.

Figure 3.1: Experimental setup of total extrathoracic deposition tests for monodisperse aerosols entering through a variety of pharmaceutical inhalers.

3.2.1 Aerosol Generation and Size Verification

Monodisperse aerosol particles of dl-α tocopheryl acetate were generated using a vibrating orifice aerosol generator (VOAG) (Model 345001; TSI Incorporated, St. Paul, MN). The residual charge on the particles was neutralized using a radioactive charge neutralizer (Model 3454; TSI Incorporated, St. Paul, Minnesota). Dl-α tocopheryl acetate was used because it is a non-volatile liquid at room conditions, visible to UV spectroscopy, inert to plastic surfaces, and soluble in a large number of solvents including methanol, isopropyl alcohol and heptane.

The operating principle of the VOAG is well known and relatively simple.[11,18] A solution is created with a known concentration of the aerosol material (in our case dl-α tocopheryl acetate) as the solute and a volatile solvent (in our case isopropyl alcohol). The solution is placed in a syringe and the syringe is uniformly advanced using a stepping motor. The liquid at high pressure is forced through a small diameter orifice to form a thin liquid jet. The orifice is connected to a piezoelectric crystal in order to disturb the jet at a high frequency, breaking it into uniform sized droplets. The size of the primary droplets can be controlled by adjusting the liquid feed rate (which is calibrated in situ) and the oscillatory frequency of the orifice according to the equation given by Berglund and Liu:[11]

$$d_{droplet} = 10^4 \left(\frac{Q}{10\pi f} \right)^{1/3} \tag{3.1}$$

where Q is the liquid feed rate in cm^3/min and f is the vibrating frequency in Hz.

The stream of primary droplets is then mixed with dilution air, allowing the volatile solvent to evaporate until only the solute remains. The final diameter of the solute aerosol can then be calculated from the primary droplet diameter and the solution concentration by volume (including impurities in the solvent) via:

$$d_p = (C + I)^{1/3} d_{droplet} \tag{3.2}$$

The aerosol particles tend to be highly charged due to triboelectric charging effects as they pass through the orifice and need to be brought back to charge equilibrium. The radioactive charge neutralizer used for this purpose contains Krypton-85 which ionizes the air in order to bring the surface charge on the particles back into equilibrium.

The size distribution of the aerosol was verified using a time-of-flight particle measurement system (Aerosizer Mach II; TSI Incorporated, Particle Instruments / Amherst, Amherst, MA). A small sample stream allowed continuous monitoring of the aerosol particle size distribution during all tests. The three tested aerosol particle sizes had calculated mass median diameters of 2.5, 5, and 7 micrometers. They were verified as monodisperse with a measured geometric standard deviation of 1.07 +/- 0.03 (Mean +/- Standard deviation) and a density of 953 kg/m^3.

The operating principle of the Aerosizer is based on the original work of Dahneke *et al.*[30,31] and is reviewed by Baron *et al.*[8]

Briefly, a sample of the aerosol is drawn into an inner capillary tube and particle free sheath air forms an annulus around the tube. The air and the particle streams are accelerated through a convergent nozzle with a 15^o half-angle into a partially evacuated chamber. The pressure in the chamber is maintained sufficiently low by means of a diaphragm vacuum pump to ensure that the flow through the nozzle reaches sonic velocity. As the flow exits the nozzle, the air continues to expand into the chamber and a supersonic free-jet is formed. The particle reaches a terminal velocity shortly after exiting the nozzle.[31] This terminal velocity is obtained by measuring the time it takes for a particle to cross two laser beams with a known separation. Two laser beams from a 5mW He-Ne laser are spaced about 1 mm apart and two separate photomultiplier tubes are used to detect particles passing through each beam. With knowledge of the particle shape and the density of the aerosol material, the particle's geometric diameter can be obtained from the measured time of flight.

3.2.2 Tested Devices

The tested devices included two dry powder inhalers: a Turbuhaler® (Astra Pharma Inc., Mississauga, Ontario) and a Diskus® (GlaxoWellcome Inc., Mississauga, Ontario), one pressurized metered dose inhaler (Ventolin®, GlaxoWellcome Inc., Mississauga, Ontario) with an attached holding chamber (Aerochamber®, Trudell Medical, London Ontario), one vented, valved jet nebulizer (Pari LC STAR®; Pari Respiratory Equipment, Starnberg, Germany), one unvented nebulizer (Hudson T Up-Draft II®; Hudson Respiratory Care, Temecula, California), and a straight aluminum tube with an inner diameter of 1.7 cm.

The tested devices were connected to the idealized mouth and throat geometry by sealing them to small individually manufactured adapters. In all cases, the entire medical device was used for the tests. No pieces were discarded. The adapters were sealed to the end of the device mouthpiece proximal to the oral cavity and then bolted to the front of the throat models. This ensured that the only air entering the mouth and throat models was that which exited the device. It also ensured that the exit of all devices was located in the same plane perpendicular to the direction of mean air velocity. Since the monodisperse aerosol was well mixed with the dilution air and passed through the whole device prior to entering the throat model, it was deemed important to maintain realistic entrance conditions for the aerosol entering the devices as well. This was achieved by containing the dilution air entrances to the device within large diameter cylinders (9 cm inner diameter). For the dry powder inhalers, this implied that the whole device was contained in the cylinder (see Fig. 3.1) while for the nebulizers and metered dose inhaler only the entrance to the device was inserted into the cylinder.

In order to diminish variations caused by slight fluctuations in the generated aerosol's size distribution and environmental conditions, it was desirable to test all six devices simultaneously. Therefore a system was designed to dilute the generated aerosol with ambient air and split the resulting flow into six separate streams (see Figure 3.1). Connecting one stream to each device allowed all six devices to be tested simultaneously.

3.2.3 Mouth and Throat Models

The geometry of the mouth and throat region used for testing was based on the work of Stapleton et al.[150] They generated an idealized geometrical model based on computed tomography scans (CT), magnetic resonance scans (MRI), information available in the archival literature and direct observation of healthy, living subjects. This geometry was replicated into six identical mouth and throat models using three-dimensional computer assisted drafting (CAD) and stereolithography (FDM 8000, Stratasys, Eden Prairie, MN). Each model consisted of two halves, which could be firmly connected along the sagittal plane (Figure 3.2). The resultant models were surface coated with an airtight epoxy layer which was found to have high chemical and physical resistivity to washing with heptane. In order to reduce inter-model variability, the tested device connected to each mouth and throat model was systematically varied between runs.

The geometry of the mouth and throat used in these tests and throughout this thesis was not coated with any liquid for simulating the saliva and mucous layers as is often done when testing dry powder or polystyrene microsphere aerosols. The presence of a liquid layer on the surface of the throat could affect

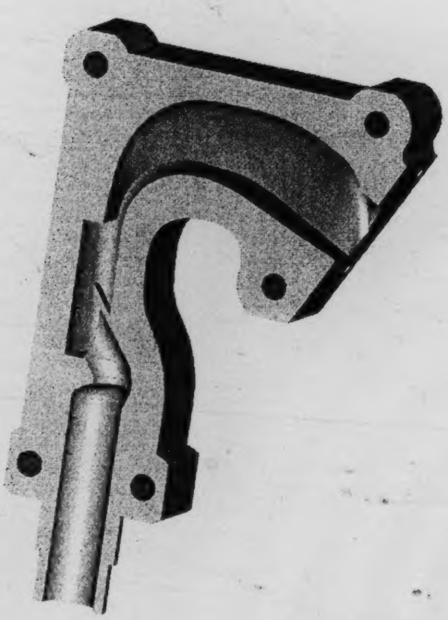

Figure 3.2: Idealized geometry of extrathoracic region in a healthy adult male. Geometry split along sagittal, symmetry plane.

the deposition in the oral airways in one of three ways. If the layer is moving on the surface of the mouth and throat, the air flow field no longer has a no slip condition at its boundary, the liquid surface. This will affect the velocity profile at the wall and may affect the curvature or the magnitude of the mean streamlines. Additionally, the presence of saliva and mucus in the region will narrow the cross sectional area for the air flow and so increase the air velocity in the region and therefore affect particle deposition. Finally, the surface of the liquid layer will alter the surface roughness seen by the air flow, making it smoother if the liquid is calm and rougher if surface waves are present. None of these three effects are expected to be significant for the deposition tests performed in this thesis for the following reasons.

The liquid layer is not expected to flow along the wall as a result of an inhalation. Physiology dictates that the saliva and mucous mixture should not flow into the tracheobronchial airways during an inhalation otherwise foreign matter would be presented to the lungs. In fact, the cilia in the conducting airways continuously move the mucous layers there up and out of the thoracic region. If the high air speeds in the larynx then do not cause significant motion of the liquid layers (and this is borne out by feel at high flow rate inhalations), then the lower velocity air in the rest of the extrathoracic region will not cause significant liquid motion and the no slip condition at the wall is still a good assumption.

In the extrathoracic region, the presence of a thin liquid layer on the surface of the geometry will not significantly affect the cross sectional area of the flow. In the oral cavity, Schroeder[140] gives the maximum thickness of the whole epithelium as 580 μm with the outermost fluid layer (the stratum corneum) having a typical thickness of only 15 μm. In our model, typical cross sectional areas and perimeters for the oral cavity are on the order of 4 cm^2 and 8 cm respectively. The addition of a 15 μm layer would cause a decrease in cross section area of 0.012 cm^2 or 0.3 % which will cause negligible effects on the velocity in the region.

Finally, the surface roughness changes could cause variations in the particle deposition if the deposition was dominated by surface effects, such as is the case in fully developed pipe flow tests where the predominant mechanism for depositing moderately sized aerosol particles is the turbulent eddies generated in the turbulent boundary layer. As will be seen in the remainder of this thesis, the deposition in the oral cavity and extrathoracic region is dominated by inertial impaction due to the curvature of the mean flow streamlines near the wall. Since the length scales of the jet flows and curvature of the soft palate are so much larger than the changes in surface roughness, it will not have any significant effect on the mean streamlines and so will not affect the particle deposition in the extrathoracic region.

The aerosol mass which passed through each mouth and throat model was collected on a bacterial / viral filter (Respirgard - II®; Marquest Medical Products, Englewood, CO). As illustrated in Figure 3.1, a vacuum pump was used to drive the air flow through the entire system. A bank of rotameters (Omega, Stamford, CT) was calibrated and used to both measure and regulate the steady flow rate through the individual mouth and throat models.

3.2.4 Assay

After the completion of a run, the mouth and throat models were disassembled to allow for assaying. The total mass of aerosol that deposited in the model was determined using UV spectroscopy (HP 8452A, Hewlett Packard, Waldbronn, Germany). The halves were washed with a measured volume of heptane. A clean throat model was washed in an identical manner to determine the spectral absorption of the matrix. The concentration of the test heptane solution was calculated by comparison with standard solutions of dl-α

tocopheryl acetate in heptane. From this concentration and the volume of the wash solution, the mass of dl-α tocopheryl acetate that deposited in a given mouth and throat model was determined.

The mass of aerosol that passed through the model and deposited on the downstream filter was also determined using UV spectroscopy. The filters were washed with measured volumes of methanol. Blank solutions were made by washing unexposed filters with methanol. Again the mass of dl-α tocopheryl acetate was determined from the volume of the wash solution and comparison of the UV absorption with standard solutions. Statistical analysis was performed using multivariate ANOVA and Student's t tests.

3.3 Results

The percentage of aerosol mass that deposited in the mouth and throat region is shown in Figure 3.3. Data points in the figure represent mean values of five tests for the 5 and 7 micrometer aerosols and three tests for the 2.5 micrometer aerosols. Error bars refer to standard error of the tests. Since the major deposition mechanism believed to be at work in these tests is that of inertial impaction, the deposition has been plotted as a function of a parameter ($\rho_p d_p^2 Q$) proportional to the Stoke's number, where ρ_p is the particle mass density, d is the particle geometric diameter and Q is the volume flow rate of the aerosol.

No significant differences ($p>0.10$) in mouth-throat deposition were found at any of the flow rates and particle sizes for either nebulizer when compared to the straight tube. As well, comparison of the nebulizers to each other also yielded no significant differences in mouth-throat deposition ($p>0.10$) at any of the test conditions.

Compared to the straight tube, the metered dose inhaler with attached spacer was found to have a significantly higher deposition ($p<0.05$) for only

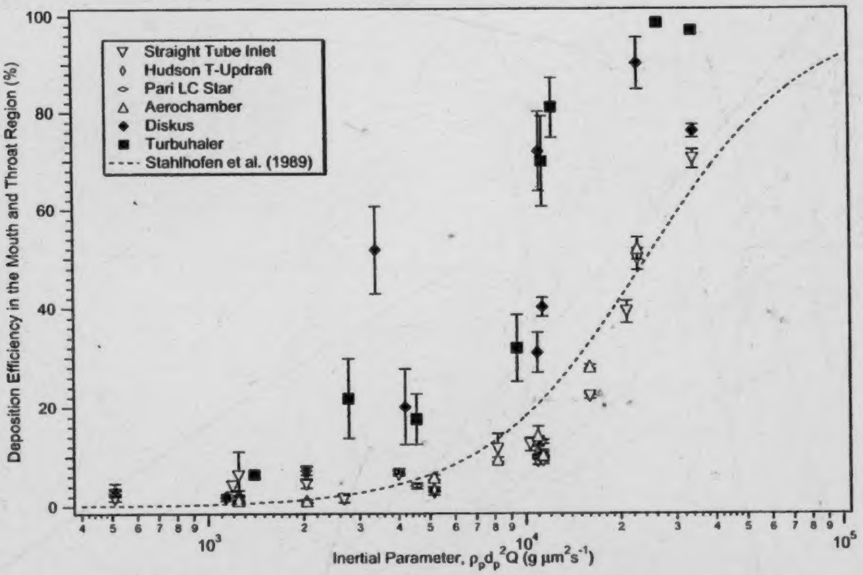

Figure 3.3: Total deposition of monodisperse aerosols in an idealized extrathoracic geometry after entry through different pharmaceutical inhalers.

one case with the 5 micrometer diameter aerosol and one case with the 7 micrometer diameter aerosol, but was not significantly different for any of the other cases. Considering the two dry powder inhalers, the Diskus® was found to cause deposition in the mouth and throat region that was significantly different ($p<0.05$) from that occurring with the straight tube for all cases except two of the 2.5 micrometer particle cases at low $\rho_p d_p^2 Q$ = 1137 and 4190. The Turbuhaler® was found to have significantly different deposition ($p<0.05$) from the straight tube for all cases of the 7 micrometer particles, all but the lowest flow rate test with 5 micrometer particles, but not for either flow rate with the 2.5 micrometer aerosol. The significant difference in deposition ($p<0.05$) for the dry powder inhalers as compared with all the other tested devices for values of $\rho_p d_p^2 Q > 9000$ is quite apparent in Figure 3.3. It can also be seen from Figure 3.3 that the dry powder inhalers begin to deviate dramatically from the straight tube data at lower values of $\rho_p d_p^2 Q$ than the other devices. For the Diskus®, all tests with $\rho_p d_p^2 Q \geq 10954$ and one set at $\rho_p d_p^2 Q = 3399$ showed significantly higher deposition ($p<0.05$) than the straight tube, while for the Turbuhaler® all tests with $\rho_p d_p^2 Q \geq 9435$ yielded higher deposition than the straight tube ($p<0.05$). However, the MDI with attached holding chamber showed significantly higher deposition ($p<0.05$) only at two discrete values of $\rho_p d_p^2 Q$ while the jet nebulizers never showed any significant differences compared to the straight tube over their entire tested range of $590 \leq \rho_p d_p^2 Q \leq 11375$.

3.4 Discussion

Inertial impaction has been cited as the dominant mechanism for deposition in the mouth and throat[112,133,148,169] and hence parameters of the form $\rho_p d_p^2 Q$ have been used to plot the deposition data from in vivo studies breathing through large bore tubes. Recently Cheng *et al.*[24] tested deposition in an airway replica with monodisperse aerosol particles entering through a large tube. They also found impaction to be the dominant deposition mechanism since the deposition efficiency was a unique function of Stokes number.

The model proposed by Stahlhofen *et al.*[148] and the data on which it is based are displayed in Figure 3.4. Our data for deposition in the throat when inhaling through the straight tube is also plotted in figure 3.4 and shows good agreement with both the model of Stahlhofen *et al.* and the data that it is based upon. The correlation of deposition with the parameter $\rho_p d_p^2 Q$ strengthens the claim that impaction is the dominant mechanism in the straight tube tests.

The deposition data from the nebulizers and the pMDI with attached holding chamber also appear to follow well an increasing function of $\rho_p d_p^2 Q$ as seen in Figure 3.3, and appear to be dominated by inertial impaction as well. How-

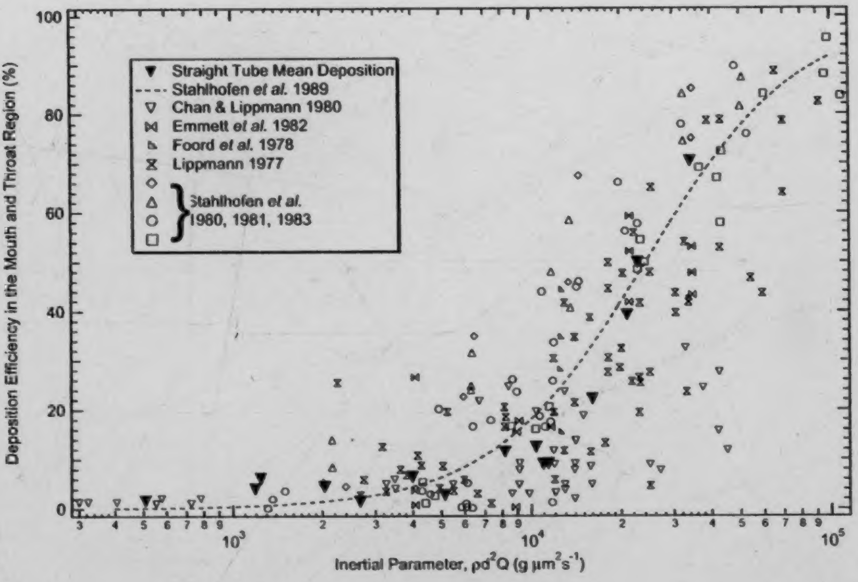

Figure 3.4: Comparison of straight tube extrathoracic deposition data from current tests and the model of Stahlhofen *et al.*[148] along with the in vivo, straight tube inlet data on which it is based.

ever, the dry powder inhaler deposition data is much more scattered and does not follow the parameter $\rho_p d_p^2 Q$ as obviously as the other devices. This variation is due to the presence of an additional important deposition mechanism independent of the impaction parameter $\rho_p d_p^2 Q$.

This mechanism was initially believed to be associated with turbulence, since the dry powder inhalers were expected to generate elevated turbulence levels to increase powder deagglomeration. The work done with deposition in an oral cavity using various diameter inlets described in Chapter 5 has shown that similar elevated levels of deposition can be obtained by the generation of a high speed jet in the oral cavity, independent of the turbulence levels at the inlet of the region. However, increasing the inlet turbulence was also tested in Chapter 5 and found to increase the deposition in the oral cavity, despite being a smaller effect than the inlet diameter change. It is therefore likely that the increased deposition seen in these tests for the dry powder inhalers is due to the combination of high velocities impinging on the walls of the oral airways and elevated turbulence levels at the exit of the devices. However, without reference to the underlying mechanisms, it is clear from our data that the deposition with the tested dry powder inhalers was both elevated and more poorly correlated with $\rho_p d_p^2 Q$ than that with a straight tube entrance.

From the above results, it is seen that caution is needed before using deposition data from straight tube breathing to predict mouth-throat deposition during inhalation from some pharmaceutical aerosol inhalation devices, particularly the dry powder inhalers investigated here.

It should be noted that the data presented deals with the special case of stable monodisperse liquid aerosols flowing through medical devices and depositing in an idealized replica of the mouth and throat region. This was intentionally done in order to highlight the effect of the device geometry on the air flow and hence on the deposition of aerosol in the mouth and throat region. Clearly the case of a patient inhaling a medical aerosol is more complex than the conditions tested here. Factors such as aerosol polydispersity, shape factors, hygroscopicity, bolus effects, Stefan flow conditions, and dense cloud interactions as well as dynamic patient related variables such as breathing patterns and time varying respiratory tract geometries may all come into play in finally delivering pharmaceutical aerosols to patients. However, this work clearly demonstrates that the geometry of the device that the pharmaceutical aerosol is inhaled from may have a significant effect on the deposition of the aerosol in the mouth and throat region. When predicting the extrathoracic deposition from a medical device, care must be taken to choose a model based on data collected from inhaling through similar devices.

Chapter 4

Regional Extrathoracic Deposition Tests

As discussed in Chapter 3, the total deposition of aerosol particles in the extrathoracic region was found to be elevated by the presence of some medical devices. In particular, two dry powder inhalers were found to cause significantly higher deposition than the other inlets in a large number of cases. In this chapter, the two dimensional deposition pattern in the extrathoracic region was quantified using gamma scintigraphy for radioactively labelled aerosol particles for five of the devices. The goal of these tests was to determine the location in the oral airways where the deposition was elevated for the dry powder inhalers in order to determine the dominant mechanisms causing this observed increase in deposition.

4.1 Experimental Setup

A diagram of the experimental setup for this set of tests is illustrated in figure 4.1. The monodisperse aerosol is generated using a condensation monodisperse aerosol generator (TSI Model 3475). The basic operating principle of the generator is as follows. Compressed nitrogen is fed through an atomiser containing a dilute (20 mg/L) saline solution. The polydisperse aerosol produced is passed slowly through a drying tube filled with desecant in order to

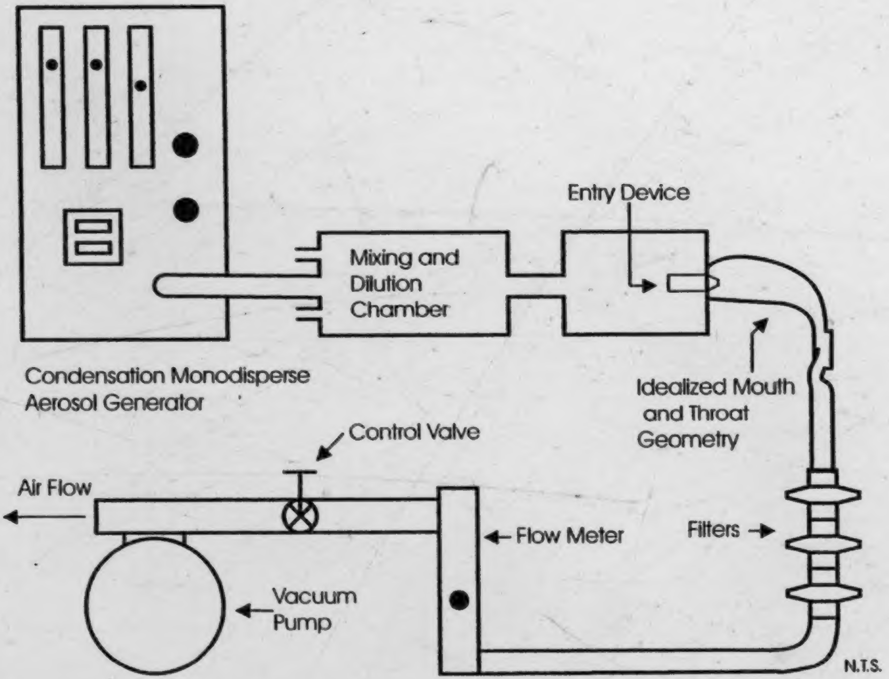
Entry Device
Mixing and Dilution Chamber
Condensation Monodisperse Aerosol Generator
Idealized Mouth and Throat Geometry
Control Valve
Air Flow
Flow Meter
Filters
Vacuum Pump
N.T.S.

Figure 4.1: Experimental setup for quantitative, regional, radioactively labelled monodisperse aerosol deposition tests.

evaporate all the water and leave only sodium chloride crystals. Concurrently, nitrogen is bubbled through a reservoir of Di-2-ethylhexyl-sebecate (DEHS) which is being heated by a temperature controlled heater. The vapour laden flow is mixed with the salt crystal laden flow and reheated to vapourize all liquid DEHS present. The mixture is then allowed to cool in a laminar flow, causing condensation of DEHS onto the salt nuclei. This results in the production of particles composed primarily of sebecate oil with a nearly uniform particle size.

For these tests, radioactive ^{99}Tc was mixed with the dilute saline solution to form the condensation nuclei for use with the generator. In this way, the radioactivity was associated with the condensation nuclei which formed the core of the final DEHS aerosol, giving good association between the radioactivity and the particle. With an identical aerosol generation and conditioning system, Grgic found good agreement between the aerosol deposition measured using gamma scintigraphy and that measured using gravimetry.[63] The ratio of measured aerosol deposition on two filters in series was found to differ by an average of 7.8% for the two measurement techniques.

The radioactively labelled aerosol was diluted with ambient air in a 30.6 cm long 7.8 cm diameter mixing chamber. From the mixing chamber a sample stream was taken to an Amherst Aerosizer where it was continuously monitored before and during the tests. The operating principle of the Aerosizer is given in section 3.2.1. The remainder of the aerosol was drawn into a chamber 15 cm long and 9 cm in diameter. This chamber served to decelerate the particles and allow them to enter the dilution air of the tested device with conditions similar to air inhaled through the device from stationary room air.

The dilution air entrances for each device were inserted well into the chamber at the end opposite of aerosol entry as illustrated in figure 4.1. The exit of the device was connected to the front face of the extrathoracic geometry via four small bolts and a rubber o-ring to ensure an airtight seal.

A new model of the extrathoracic region was created using a three dimensional CAD (Computer Aided Drafting) program and stereolithography. The internal geometry of the extrathoracic geometry was identical to that described in section 3.2.3 but the wall thickness was set to 6 mm throughout except for the inlet flange which was 50 mm by 50 mm and 7 mm thick. The purpose of the uniform wall thickness was to decrease the effects of signal attenuation by the walls. Again the region was built as two halves split along the sagittal plane. Three acrylic pins were placed in the wall of the oral airways to allow alignment of the two halves, one in the plane of the inlet flange, the second 4 mm above the entrance to the pharynx and a third 8 mm above the base of the trachea. During tests, the halves were sealed and wrapped with parafilm and the inlet device bolted onto the inlet flange. Three disposable filters (Respirgard - II®; Marquest Medical Products, Englewood, CO) were connected in series immediately downstream of the trachea. The flow rate through the system was driven by a vacuum pump, adjusted by a control valve and monitored by a field calibrated rotameter as illustrated in figure 4.1. An absolute filter (Model CC05LGH13, Pall, Covina, California) was situated upstream of the rotameter to prevent any aerosol from being vented to the room both prior to testing while the particle size was stabilizing and during the tests.

Due to the surface characteristics of the ABS plastic extrathoracic geometry and the DEHS, depositing aerosol was found to rapidly wet the surface, spreading in seconds along all exposed surfaces. In order to prevent this, the throat model was coated with Fluorad Conformal Coating FC-725 (3M, St. Paul, MN) which both created an airtight surface and caused the DEHS to bead on the surface. The gravimetric tests of section 5.2 found that the DEHS remained beaded on the surface for concentrations up to 13 g/m^2 which was adequate for these tests. As the coating fluoresces under ultraviolet light, the surface integrity was verified prior to each test.

It was necessary to verify that the particle size distribution exiting the pharmaceutical devices was the same as the distribution upstream of the devices where it was monitored during the tests. A sample port was drilled into the oral cavity 20 mm from the inlet flange face and 13 mm above the tongue upper surface. This location was chosen as it was found in the tests to be in the region of the majority of oral cavity deposition caused by the dry powder inhalers. A sample stream was measured with the Aerosizer Mach II and the particle size distribution recorded over the course of the 8 minute tests used with the devices. Prior and after this 8 minute interval the particle size distribution was measured upstream of the dry powder inhaler. The mass median diameter (MMD) of the particle size distributions measured inside the oral cavity and upstream of the DPI were 4.44 ± 0.06 μm and 4.50 ± 0.06 μm respectively for the Turbuhaler and 4.63 ± 0.04 μm and 4.64 ± 0.05 μm for the Diskus. The geometric standard deviations (GSD) of the distributions were 1.123 ± 0.012 inside the oral cavity and 1.053 ± 0.005 upstream of the device for the Turbuhaler and 1.147 ± 0.023 and 1.055 ± 0.006 respectively for the Diskus. The slight broadening of the distribution in the oral cavity is probably due to a limited number of particle-particle collisions in the device and at the exit due to the high velocity gradients expected in the flow. However, the maximum measured GSD of 1.16 inside the oral cavity is still within the range defined by Fuchs as monodisperse (GSD<1.22).[58] So it can be seen that after exiting the dry powder inhalers, the aerosol is still monodisperse with essentially the same mass median diameter as measured upstream of the devices.

These measurements also show that while deposition of the aerosol was observed in the dry powder inhalers, no significant re-entrainment of the liquid is occurring during the complete test time.

4.1.1 Tested Device Connections

The five devices tested included a Turbuhaler, a Diskus, a Hudson Updraft II jet nebulizer, a pMDI with attached Aerochamber and a 17 mm ID straight tube. The devices were emptied of drug and the test aerosol entered through the dilution air of the device, exiting through the mouthpiece of the device. No modifications were made to either the Turbuhaler or the Diskus except that the entire device was mounted onto the center of a disk to connect the reservoir chamber to the oral cavity. The connection between the dry powder inhaler and the disk was air tight so that the only passage for airflow into the oral cavity was out the mouthpiece of the device. Using this technique, the exit plane of the device mouthpiece was located parallel and mated to the front face of the inlet flange on the extrathoracic geometry. The center of each mouthpiece was located at the same point in the plane. Prior to testing, both dry powder inhalers were actuated once and the drug tapped out and disposed of. Air at 90 L/min was blown through the devices for half an hour to ensure no residual drug remained. For the nebulizer, the reservoir was left empty, but a compressor (PulmoAid, model # 5650D, DeVilbiss, Somerset, PA) was connected and allowed to run throughout the test to replicate the mixing conditions of normal use in the "T" section upstream of the mouthpiece. The aerosol was again introduced through the dilution air. For the pMDI and attached holding chamber, the body of the pMDI protruded into the reservoir chamber while the Aerochamber was sealed to the pMDI externally using silicone sealant. The high flow whistle was also sealed to prevent accidental venting of radioactive aerosol into the room which was deemed to be a minor modification of the airflow pattern in the device at the 32 L/min flow rate tested. The drug canister was in place during the tests but was not actuated.

Due to time constraints, only two repeat experiments were performed for each device with the exception of the Turbuhaler where three repeats were performed.

4.1.2 Radioactivity Measurements

The aerosol deposition test time was set iteratively for each device, allowing sufficient time for measurable quantities of the radioactively labelled aerosol to deposit in the extrathoracic region, but limited by overloading any site of deposition in the region which would cause the DEHS to drip or run within the model. Test times ranged between 5 and 9 minutes during which the particle size and flow rate was held constant and measured throughout.

Upon completion of the test time, the extrathoracic region was disconnected from the device, unwrapped, unsealed, split in half along the sagittal plane and carefully laid into a styrofoam form. The form was 375 mm by 375 mm and 35 mm thick and had been carved to hold the two halves level, with the surface formed by the split plane 3 mm above the top surface of the form. Three holes near the top of the form were used to insert the three disposable filters with their filter media held level and 10 mm above the top surface of the form. A sketch of the form is shown in figure 4.2. The purpose of the form was to ensure precise location of all the deposition surfaces on the collimater face during imaging. Alignment marks on the collimater face and the form allowed repeatable positioning of all 5 parts to within 1 mm. This was necessary as identical regions of interest were applied to all images during analysis and the analysis software did not allow for easy movement of the regions of interest in an image. Proper positioning was verified during data analysis for all tests.

The imaging of the filters and throat halves was performed using a single photon emission gamma camera (Prism Axis 2000, Picker, Cleveland, OH) with low energy high resolution collimation with appropriate background and uniformity corrections. Typically tests were performed in the late afternoon and imaging was allowed to run overnight to ensure adequate radioactive counts to minimize counting errors. Typical imaging times ranged from 5 to 12 hours. Tests of the uniformity of response across the camera's surface were performed daily by imaging a uniformity standard and all data was corrected for non-uniformities based on the calibration of the testing day. Background levels were measured simultaneously by specifying 15 circular regions of interest scattered around the image sufficiently far from all edges and radiation sources to prevent elevated readings due to scattering of the photons. The location of the background regions in the image can be seen in figure 4.3. The counts from the 15 background regions were first corrected for the camera's non-uniformity based on that day's calibration and then averaged to give the

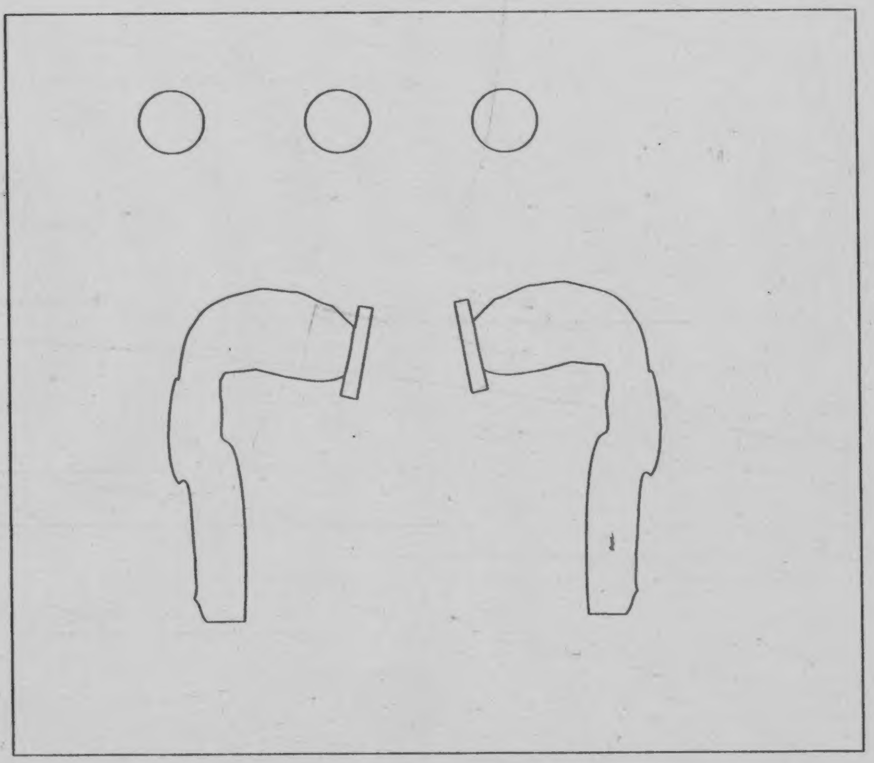

Figure 4.2: Form for repeatable location of filters and throat halves on collimater surface for radioactively labelled monodisperse aerosol deposition tests.

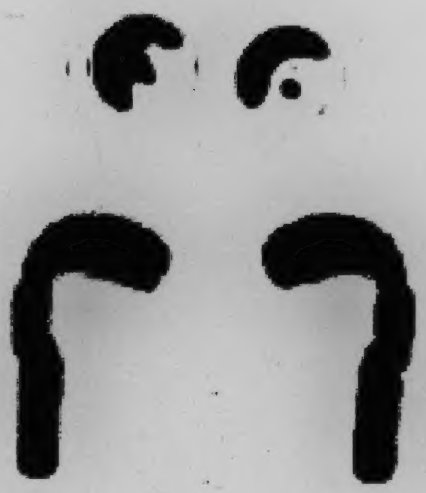

Figure 4.3: Definition of regions of interest for radioactive aerosol deposition tests.

mean background count per pixel.

The standard deviation of the measured counts per pixel in the 15 regions was taken as a measure of the error resulting from subtracting off the background counts per pixel for all the oral airway and filter regions. Other error sources which were quantified in the analysis were: the error caused by the statistical nature of radioactive sources emitting photons which is commonly estimated as equal to the square root of the total number of counts observed, the error caused by the non-uniformity of the camera in each region, and the error caused by overlap of regions in their definition. The error due to region overlap was found to be $< 1.5\%$ for all tests.

Since all components for each test were imaged simultaneously by the same camera, only relative measurements of the radioactive counts in each region were required. No calculations of the actual amount of radioactive material deposited were necessary, thus drastically simplifying the procedure and improving the accuracy of the measurements.

Once the radioactive counts in each region were corrected for camera non-uniformity and background levels, the percentage of aerosol depositing in any given region could be directly calculated from the percentage of corrected counts in that region.

4.2 Results and Discussion

The main results of this series of tests are a series of images which give both a qualitative and a quantitative picture of the aerosol deposition pattern for each of the five tested devices.

In order to accurately define the boundaries of the filters and the oral airways, the halves of the model were placed in the styrofoam form, the inlet and outlet were sealed with tape and the regions were filled with a dilute saline solution mixed with ^{99}Tc. The solution was also administered to the three filters using a syringe until the surface of the filter media was fully covered. The form was carefully located on the collimater surface and imaged. The outer boundary of the mouth and throat halves and of the filters were sketched based on the image. The image used to define the region boundaries is seen in figure 4.3 where the intensity of the dark regions is proportional to the counts per pixel at each pixel and the blue lines show the regions sketched during the analysis. The filters were located right to left in the image with the filter immediately after the exit of the trachea placed in the furthest right location, the second filter placed in the middle location and the third filter placed in the location furthest left. As we ran low on the radioactive mixture and had to dilute it further in order to cover the third filter surface, the count intensity of the third filter is significantly lower than that of the other filters and is quite visible when the intensity scale is turned way up. The throat halves were further subdivided into smaller regions for analysis. The oral cavity was divided into 5 regions on either side, showing the upper surface of the tongue, the anterior section of the hard palette, two middle sections of the hard palette and the posterior section of the oral cavity. The pharynx is divided into two sections on each side, the upper pharynx and lower pharynx (sometimes called the oropharynx and hypopharynx respectively.[153]) The larynx region is not further subdivided. The trachea is subdivided into 3 sections on either side, proximal, mid and distal to the mouth. The 15 background regions are also indicated in figure 4.3.

This template was applied to each of the tested devices and the radioactive counts in each of the regions were recorded and analyzed. The deposition in the oral airways was calculated for the total deposition in the extrathoracic region, for the deposition in the major regions (oral cavity, pharynx, larynx and trachea) and for the deposition in the sub regions listed above.

A plot of the total deposition in the extrathoracic region is given in figure 4.4. Each bar represents one test and the error bars represent the measurement uncertainty in determining the deposition percentage from an error analysis based on the errors discussed in section 4.1.2. The small error bars in this figure (having a maximum value of 1.1% of the total deposition) illustrate that for a given test condition (actual flow rate and particle size), the accuracy of the measurement of the deposition is quite good. The data is re-plotted in figure 4.5 where each bar is the mean deposition for all tests with the given device and the error bars represent one standard deviation. While the nominal

Inlet Device	Run Number	Impaction Parameter (g $\mu m^2 s^{-1}$)	Extrathoracic Deposition (%)
17 mm Tube	1	11194	8.9
17 mm Tube	2	10880	6.9
Hudson Updraft II Nebulizer	1	11835	12.4
Hudson Updraft II Nebulizer	2	11104	10.7
pMDI with Aerochamber	1	11059	11.6
pMDI with Aerochamber	1	12162	14.3
Diskus DPI	1	11149	81.5
Diskus DPI	2	11742	83.1
Turbuhaler DPI	1	11330	91.3
Turbuhaler DPI	2	11239	96.8
Turbuhaler DPI	3	11421	93.5

Table 4.1: As tested impaction parameter values for gamma scintigraphy tests

impaction parameter for all tests was 11 375, the actual test conditions caused the impaction parameter to vary between 10 880 and 12 162. The actual test impaction paramter and the deposition for each run is given in table 4.1.

Similar to the results of Chapter 3, slight increases in the extrathoracic deposition from the 17 mm inlet case are seen for the nebulizer, and pMDI with attached holding chamber while the dry powder inhalers show significantly ($p < 0.05$) higher total deposition.

Plotting the total deposition measured for the straight tube inlet against the impaction parameter in figure 4.6 shows good agreement between the total deposition measurement for this set of tests, for the total deposition tests of Chapter 3 with the 17 mm pipe inlet and the empirical fit of in vivo data from Stahlhofen *et al.*[148] The regional deposition pattern for the straight tube inlet seen in figure 4.8 also shows qualitative agreement with the results of Stahlhofen.[148] They reported that the bulk of the extrathoracic deposition for mouth breathing through a tube occurs in the larynx and our results show deposition primarily centered around the larynx with some deposition slightly upstream and downstream of it.

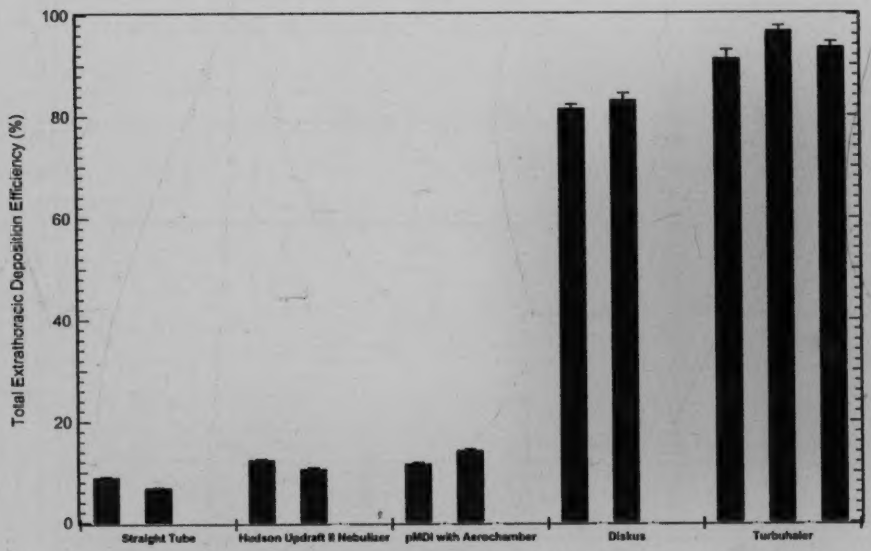

Figure 4.4: Total deposition of aerosol particles in the extrathoracic region for all radioactive aerosol deposition tests. Bars are measured values, error bars are experimental error estimates which include counting errors, background compensation errors, and camera uniformity compensation errors. All tests were at $Q = 30$ L/min, $d_p = 5$ μm and $\rho_p = 9.1$ g/cm^3

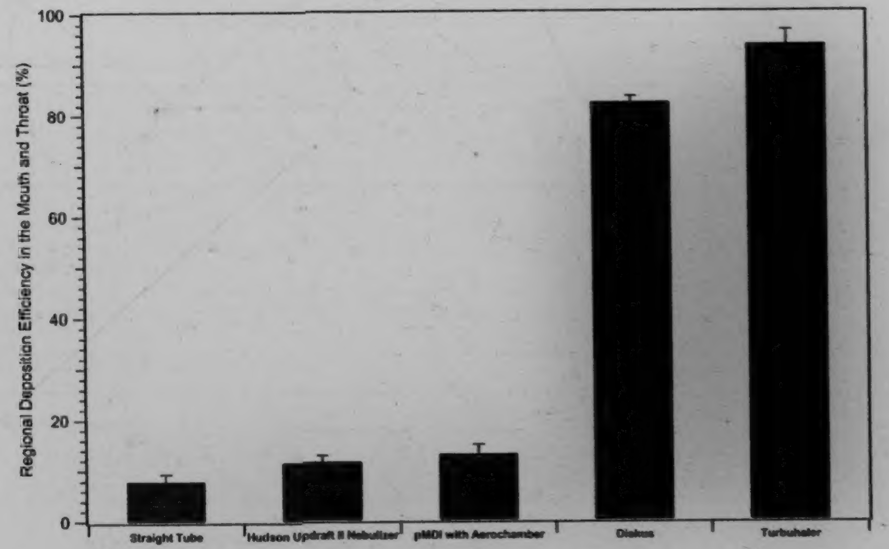

Figure 4.5: Total deposition of aerosol particles in the extrathoracic region for radioactive aerosol deposition tests. Bars are mean values, error bars are standard deviation.

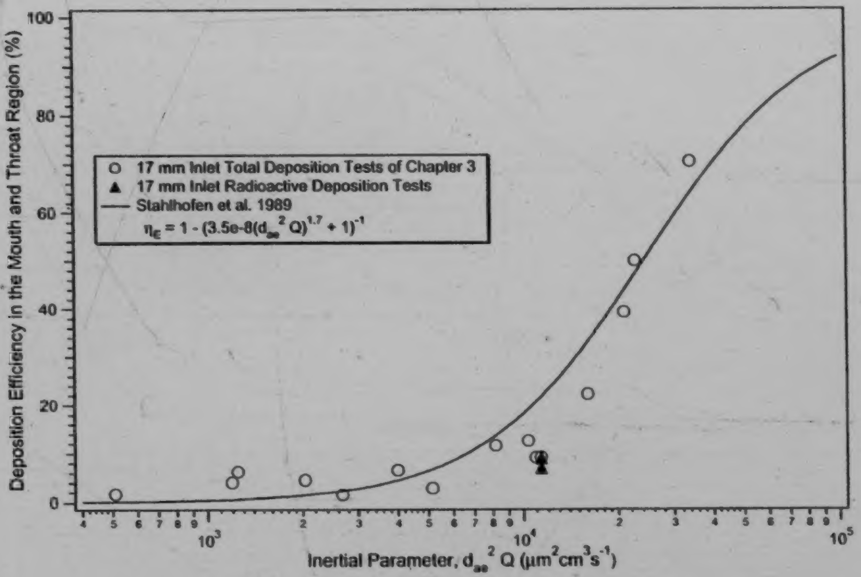

Figure 4.6: Total deposition of aerosol particles in the extrathoracic region for radioactive aerosol deposition tests with tube inlet, tests from Chapter 3 with tube inlet and empirical model of Stahlhofen *et al.*[148]

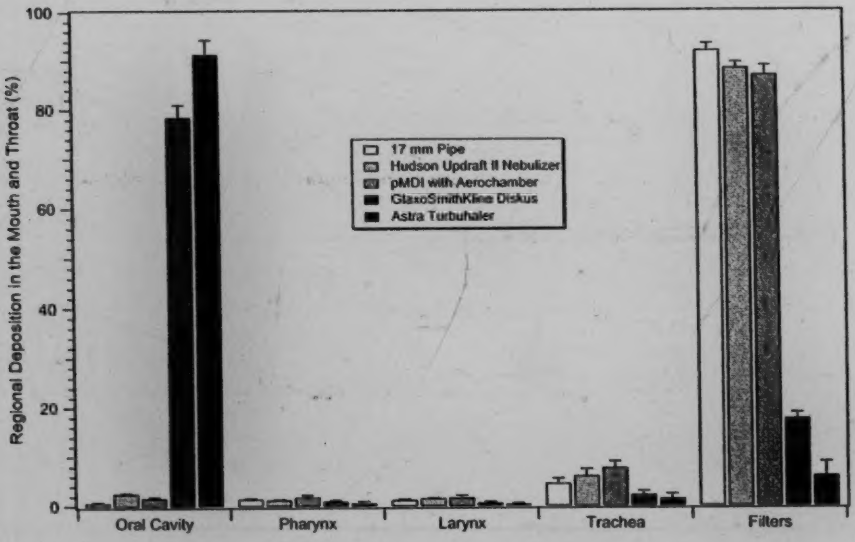

Figure 4.7: Regional deposition of aerosol particles in the oral cavity, pharynx, larynx and trachea for radioactive aerosol deposition tests. Bars are mean values, error bars are standard deviation.

The regional deposition data for the major regions of the oral cavity, pharynx, larynx and trachea are shown in figure 4.7. Bars indicate the mean deposition in the region for the tests performed and error bars indicate one standard deviation of the tests. From this figure it is clear that the major differences between the dry powder inhaler extrathoracic deposition and the extrathoracic deposition from the other devices is due to elevated deposition in the oral cavity with the dry powder inhalers.

Qualitatively, the shift in major deposition from the filter to the oral cavity is seen in figures 4.8 to 4.12 where a representative image from the gamma camera is shown. The slight enhancement in oral cavity deposition with the nebulizer and pMDI with holding chamber are also visible in figures 4.9 and 4.10.

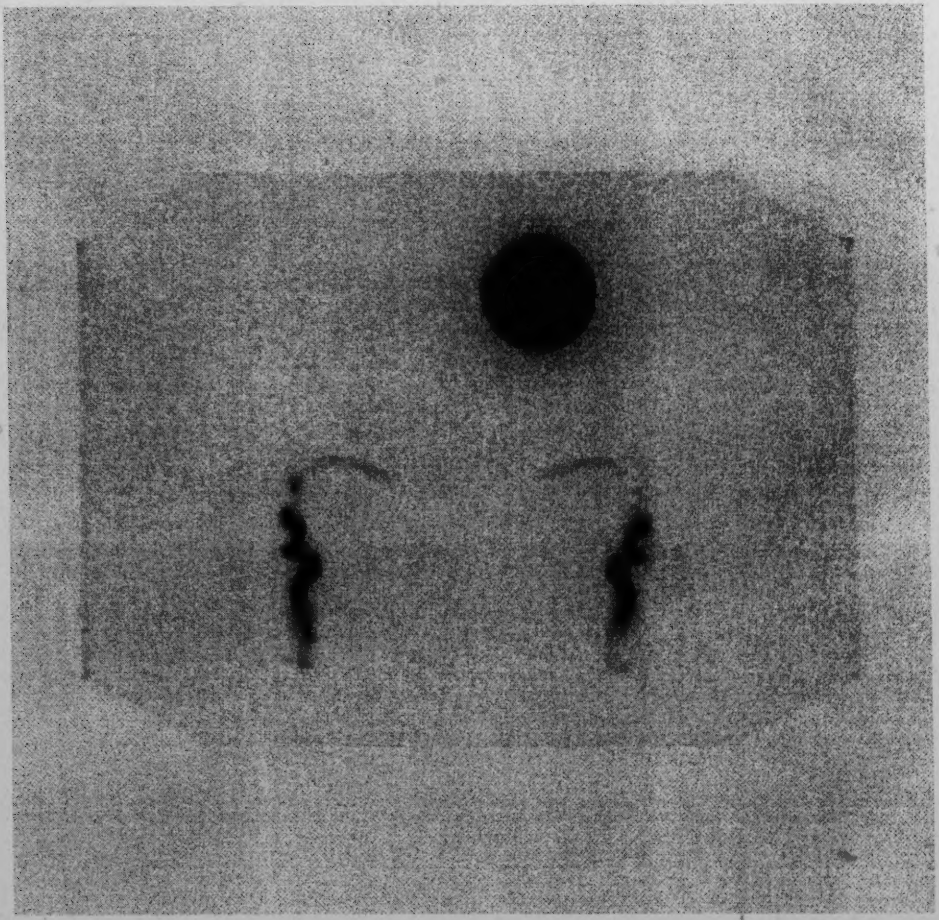

Figure 4.8: Regional deposition of 5 μm monodisperse aerosol particles in the extrathoracic region and after filters after entry through a 17 mm inner diameter pipe.

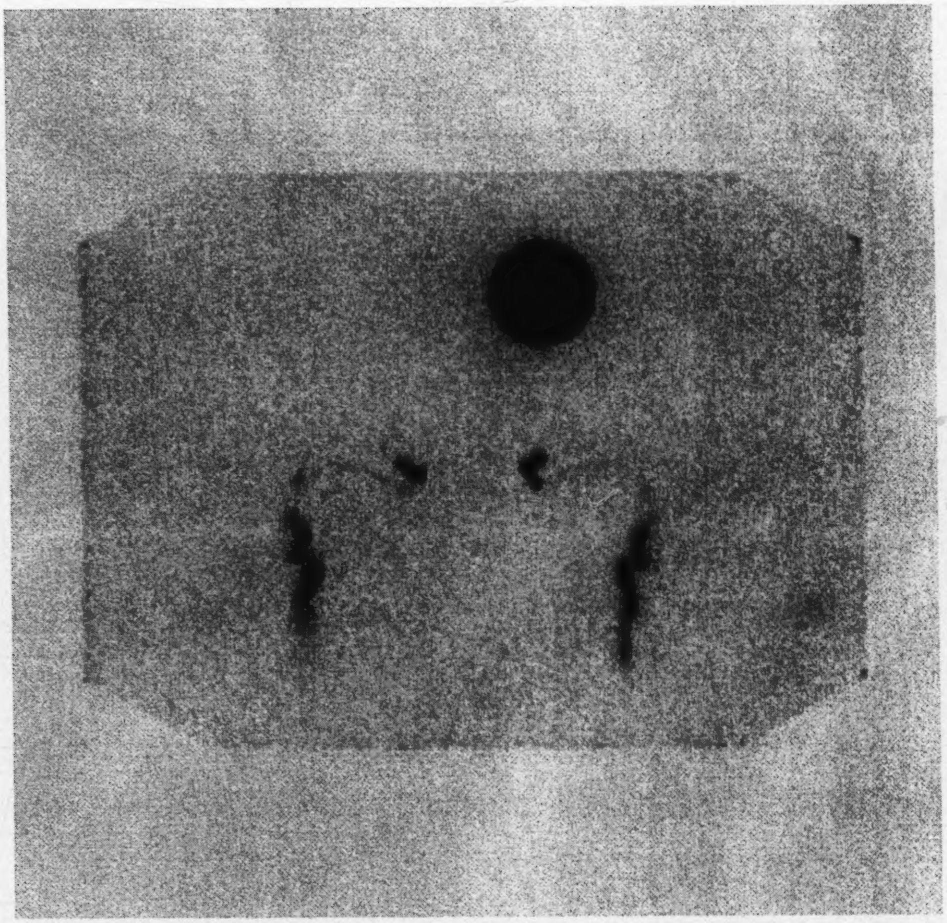

Figure 4.9: Regional deposition of 5 μm monodisperse aerosol particles in the extrathoracic region and after filters after entry through an unvented jet nebulizer.

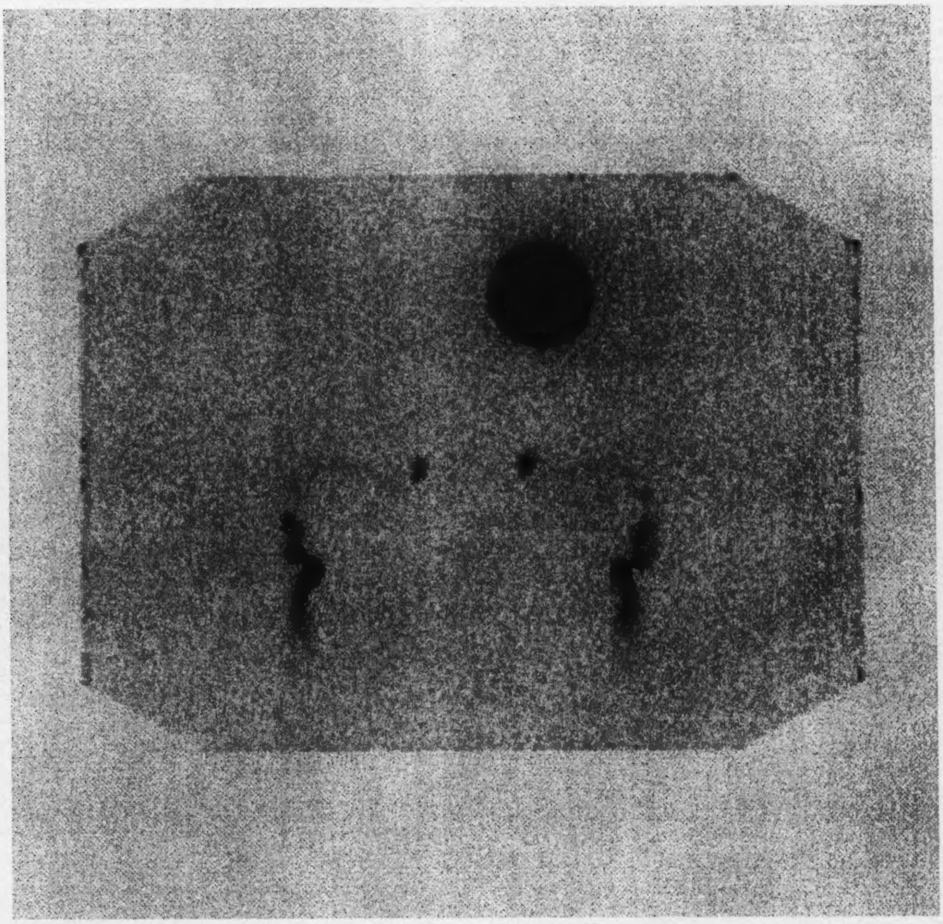

Figure 4.10: Regional deposition of 5 μm monodisperse aerosol particles in the extrathoracic region and after filters after entry through a pMDI with attached holding chamber.

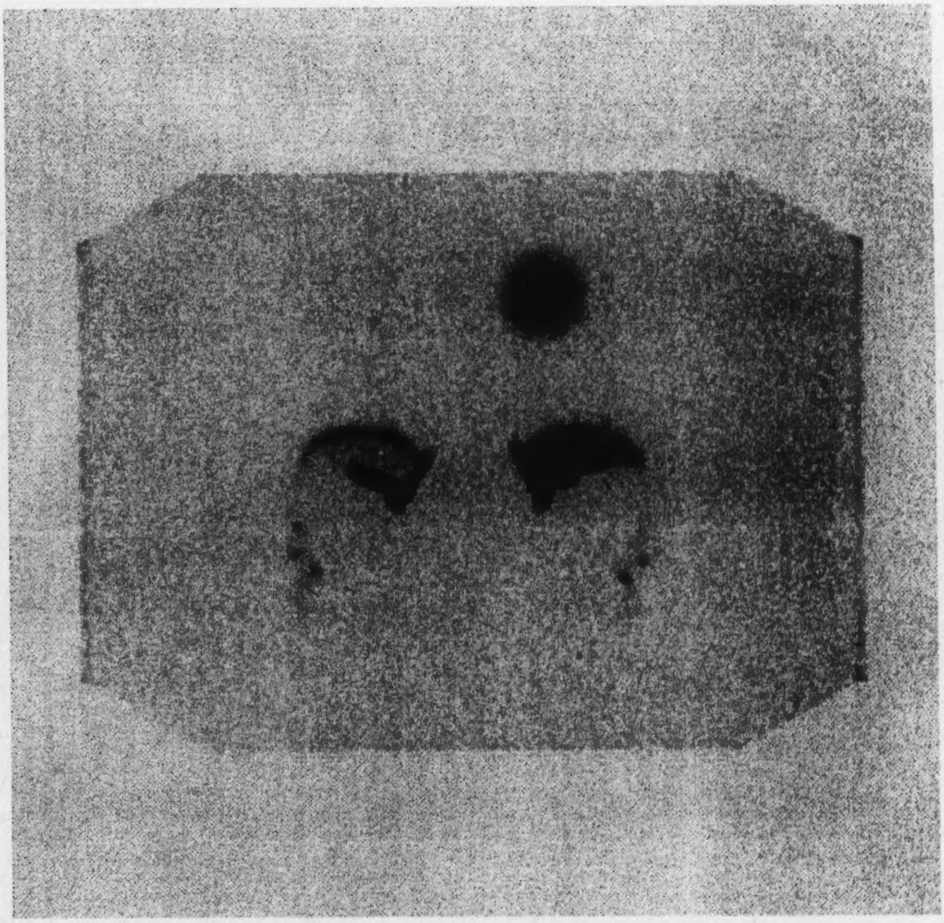

Figure 4.11: Regional deposition of 5 μm monodisperse aerosol particles in the extrathoracic region and after filters after entry through a Diskus dry powder inhaler.

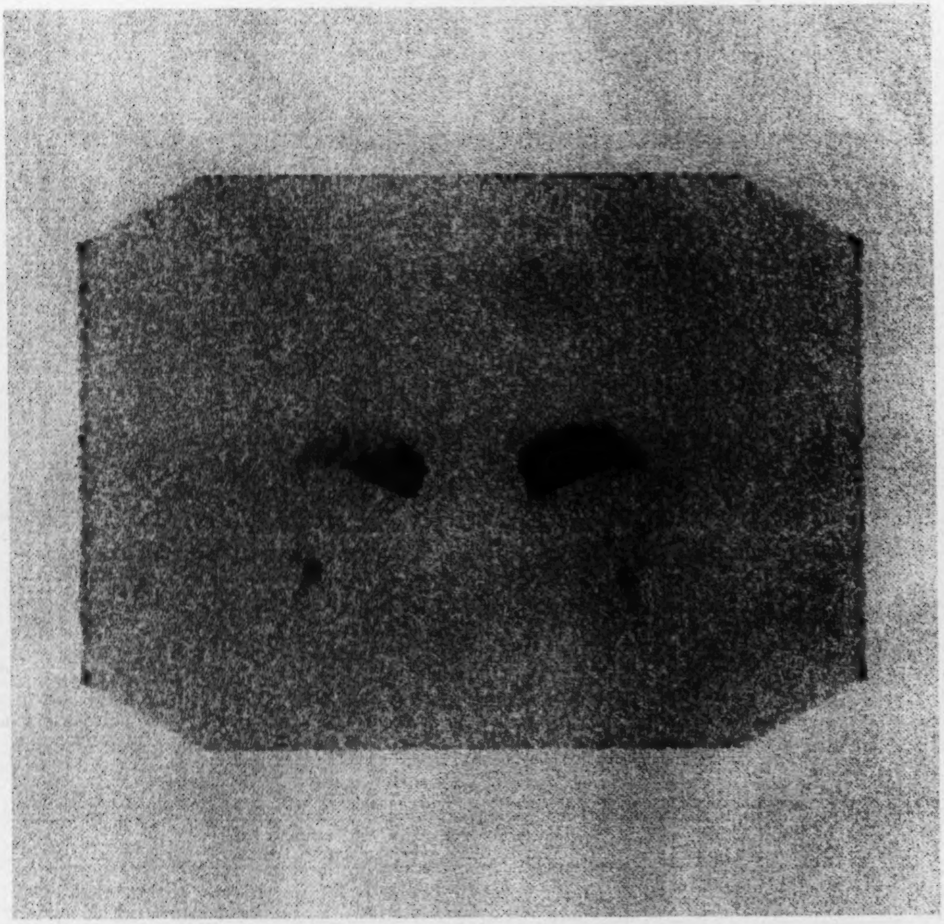

Figure 4.12: Regional deposition of 5 μm monodisperse aerosol particles in the extrathoracic region and after filters after entry through a Turbuhaler dry powder inhaler.

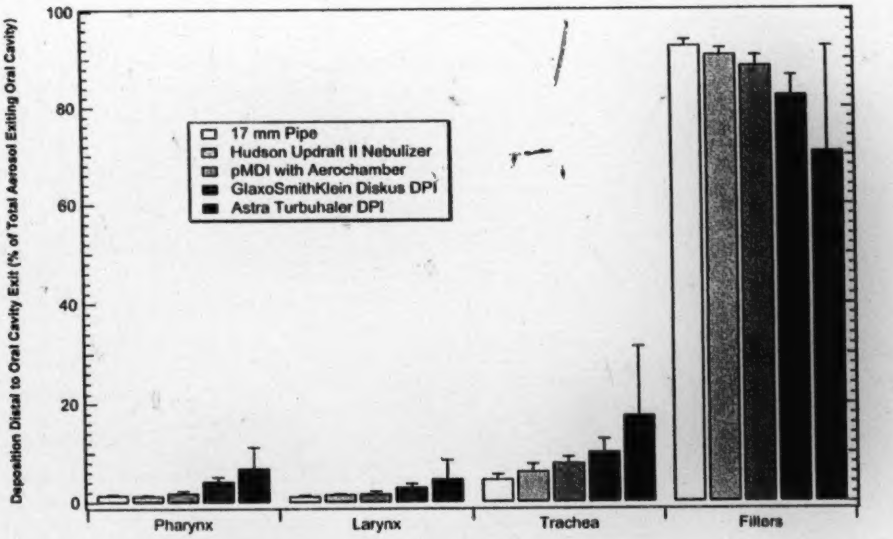

Figure 4.13: Regional deposition of 5 μm monodisperse aerosol particles in the extrathoracic regions after exiting the oral cavity for all 5 different devices.

In order to compare the deposition pattern in the extrathoracic region qualitatively, the deposition patterns are indicated in figure 4.14 for all of the tested devices without the filters. The dry powder inhalers' deposition is centered in the front of the oral cavity with little aerosol and radioactivity penetrating through the oral cavity to deposit in the larynx and trachea. Analysis of the deposition in the regions downstream of the oral cavity appears to show slightly elevated deposition in the pharynx, larynx and trachea for the dry powder inhalers as well (see figure 4.13), however the low radioactive counts in these regions make the measurement uncertainty relatively large and the results inconclusive.

As previously discussed, the oral cavity, pharynx and trachea were divided into subregions in order to quantitatively consider the deposition pattern within the regions. The oral cavity was split into 5 regions and the measured

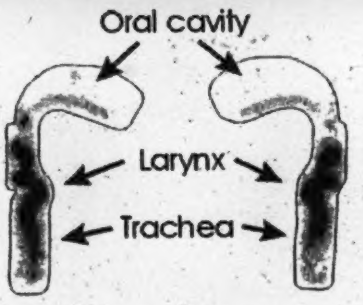
Oral cavity
Larynx
Trachea

17 mm straight tube inlet

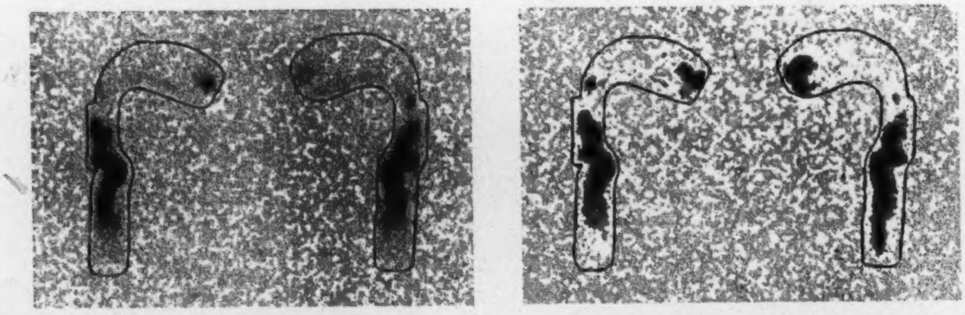

MDI + Aerochamber inlet

Hudson T-Updraft nebulizer inlet

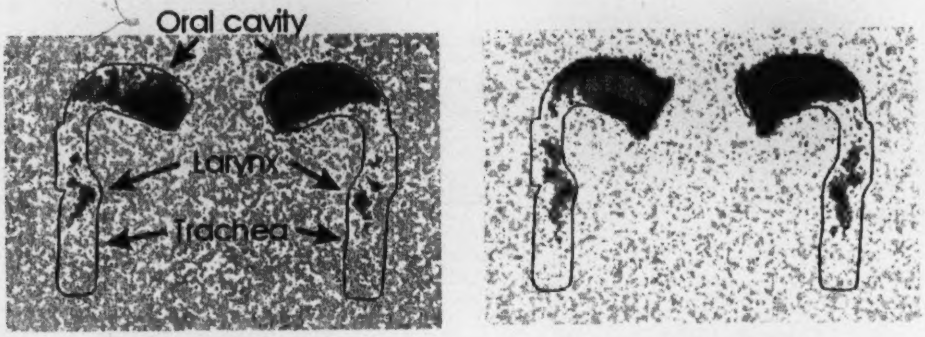
Oral cavity
Larynx
Trachea

Turbuhaler inlet

Diskus inhaler inlet

Figure 4.14: Regional deposition of 5 μm monodisperse aerosol particles in the extrathoracic region after entry through all 5 different devices.

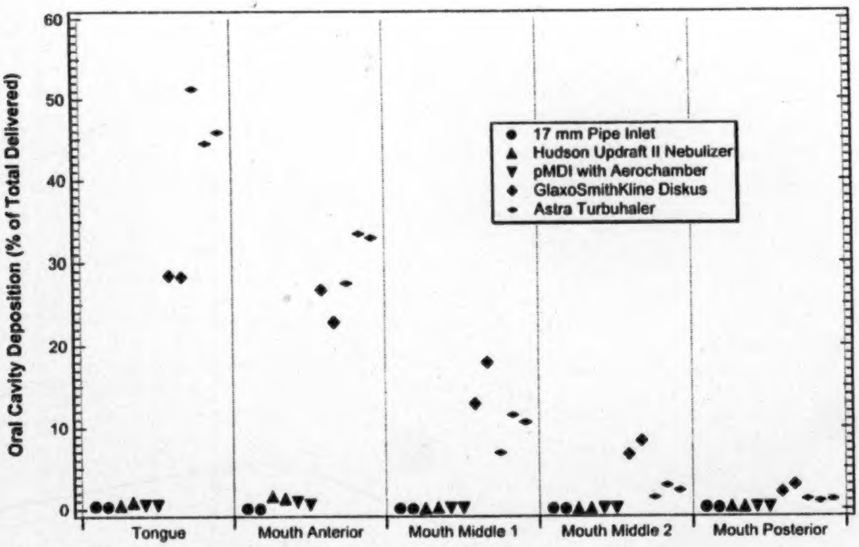

Figure 4.15: Deposition of 5 μm monodisperse aerosol particles in the five subregions of the oral cavity after entry through all 5 devices.

aerosol deposition for each of the five inlets is shown in figure 4.15. Each plotted deposition value is the sum of the deposition for the right and left sides and is given as a percentage of the total aerosol delivered to the extrathoracic region and the filters.

As can be seen in figure 4.15, oral cavity deposition is very low for the straight tube, nebulizer and pMDI with holding chamber. However, slight enhancement of deposition is seen for the nebulizer and pMDI with holding chamber in the anterior region of the oral cavity. This forms the primary difference between the deposition patterns of the three entrances in the extrathoracic region as can be seen qualitatively from figure 4.14. While the deposition in the anterior of the oral cavity is relatively low in all three cases, the deposition in this region with the nebulizer is significantly higher ($\alpha < 0.01$) than the deposition with the straight tube inlet. Similarly, the deposition with the Aerochamber inlet is significantly ($\alpha < 0.01$) higher than the straight tube inlet. The deposition in the region with the nebulizer inlet is also significantly ($\alpha < 0.05$) higher than that of the Aerochamber, although with slightly less confidence. The location of the aerosol deposition in the anterior of the oral cavity for these three inlets was observed, both from figure 4.14 and visibly during the tests to be predominantly on the side wall of the oral cavity, immediately distal to the exit plane of the mouthpieces and centered around the horizontal symmetry plane of the mouthpieces. It is likely that this deposition was then a result of the larger width of the nebulizer mouthpiece (26 mm) and the Aerochamber mouthpiece (25 mm) which brings the issuing aerosol into close proximity with the side wall of the oral cavity. Impaction of the aerosol on the side wall is expected to be enhanced for the aerosol exiting the nebulizer mouthpiece due to the expanding width of the mouthpiece as the aerosol proceeds through it. This expansion causes a component of velocity towards the wall.

The majority of the deposition after the dry powder inhalers is in the oral cavity (ranging between 77% and 93%) while only a small amount (ranging between 0.5% and 0.8%) is deposited in the oral cavity with the straight tube inlet. As a result, the deposition in all 5 oral cavity regions is significantly higher ($\alpha < 0.05$) for the dry powder inhaler inlets compared to the straight tube inlets.

From figure 4.15 it can be seen that in general the deposition for the dry powder inhalers decreases with increasing distance from the inhaler exit. Large amounts of aerosol deposit in the anterior and tongue regions of the oral cavity with decreasing amounts in the middle and posterior regions. The Turbuhaler showed more pronounced decrease in deposition with distance than the Diskus as seen from the figure. This decrease in deposition is expected to be a result of a combination of factors including: decaying turbulence intensity levels downstream of the inhaler exit, deceleration and breakup of high speed fluid structures such as jets and swirling flow by the fluid viscosity and decreasing aerosol concentration entering each subsequent region due to the deposition in the previous region. Although the fluid velocities inside the oral cavity were not investigated in this set of tests, an inspection of the inhaler mouthpieces show that the flow will be complex and three dimensional. Schematics of the Turbuhaler and Diskus are illustrated in figures 4.16 and 4.17 respectively. The Diskus outlet includes a central jet issuing from a 6 mm hole and two intersecting, impinging jets from 1.5 mm holes. The Turbuhaler outlet includes a 2.3 mm central hole surrounded by a 10 mm double helix. Both mouthpieces are expected to cause exit velocities with large radial (and in the case of the Turbuhaler circumferential) components of velocity. The tests of Chapter 5 investigate the effect of inlet nozzle diameter and inlet turbulence intensity for flows entering the oral cavity with no mean radial or circumferential velocities and show the majority of deposition in the posterior of the oral cavity. However, in the current tests with the Turbuhaler and Diskus, the flow is not likely to form a single turbulent jet inside the oral cavity, but a complex, three dimensional flow with high radial and circumferential velocities which appear to cause high levels of mixing and impaction beginning right at the anterior of the oral cavity.

The deposition pattern through the pharynx, larynx and trachea is quantified in figure 4.18. The general pattern for all devices is that there is moderate deposition in both regions of the pharynx followed by an increase in the deposition in the larynx, a further increase in deposition in the anterior portion of the trachea and then a rapid decrease in deposition further downstream in the trachea. This trend is visible for all the tested devices including the dry powder inhalers. However, in the cases of the dry powder inhalers, so much of the aerosol is deposited in the oral cavity that little is left to deposit in the

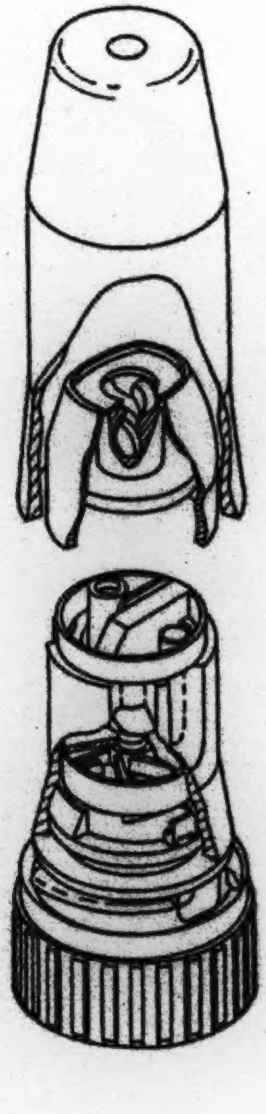

Figure 4.16: Schematic of Turbuhaler inhaler (AstraZeneca, Sweden) from de Koning[35] used with permission.

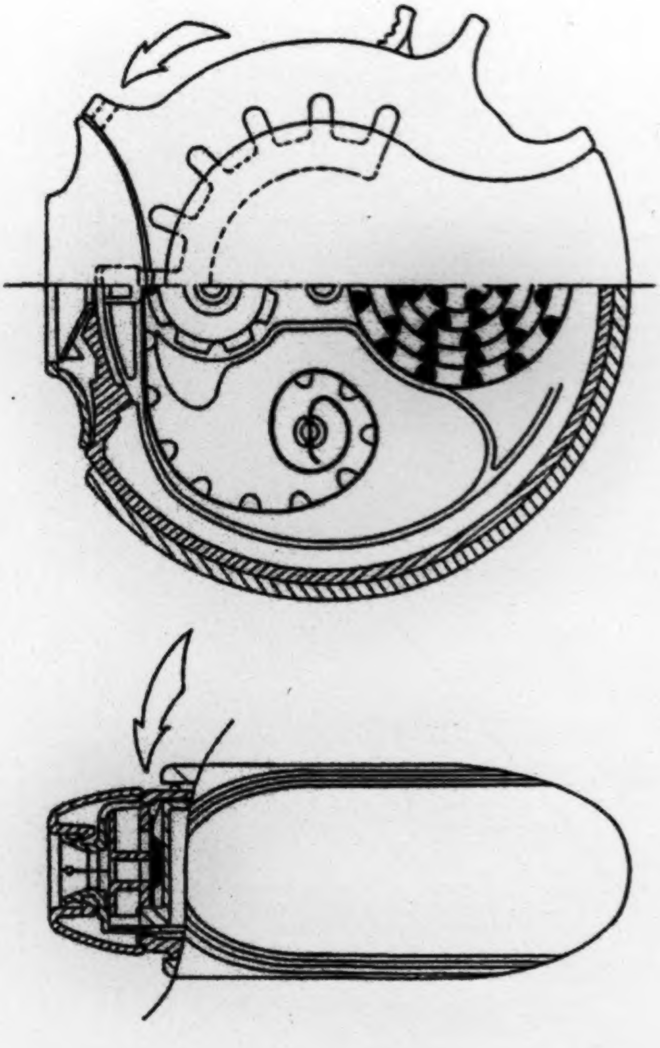

Figure 4.17: Schematic of Diskus inhaler (GlaxoSmithKline,UK) from de Koning[35] used with permission.

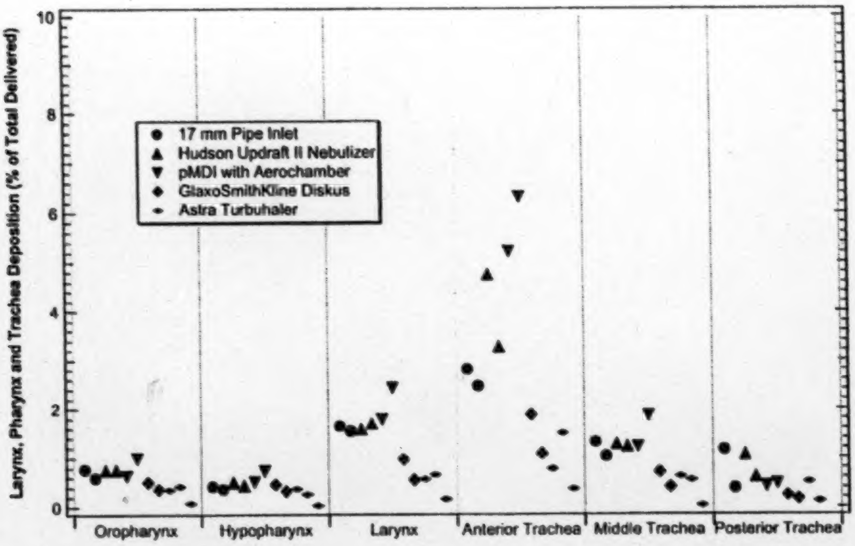

Figure 4.18: Deposition of 5 μm monodisperse aerosol particles in the subregions of the pharynx, larynx and trachea after entry through all 5 devices.

later regions, causing greatly decreased deposition percentages in these regions and high experimental uncertainties because of the few radioactive counts in the regions.

The deposition on the three filters placed in series at the exit of the extrathoracic geometry is shown in figure 4.19 for all 5 inlet devices. From this plot it can be seen that essentially all the aerosol exiting the mouth-throat region was collected on the first filter. Essentially no aerosol passed through the first filter to deposit on the subsequent two filters.

In summary, the experimental procedure for the radioactively labelled aerosol deposition tests was validated by comparing the total deposition in the extrathoracic region to that measured in the independent tests of Chapter 3. Agreement between the tests was good as seen in figure 4.6 and the deposition pattern agrees well with the mainly laryngeal deposition reported

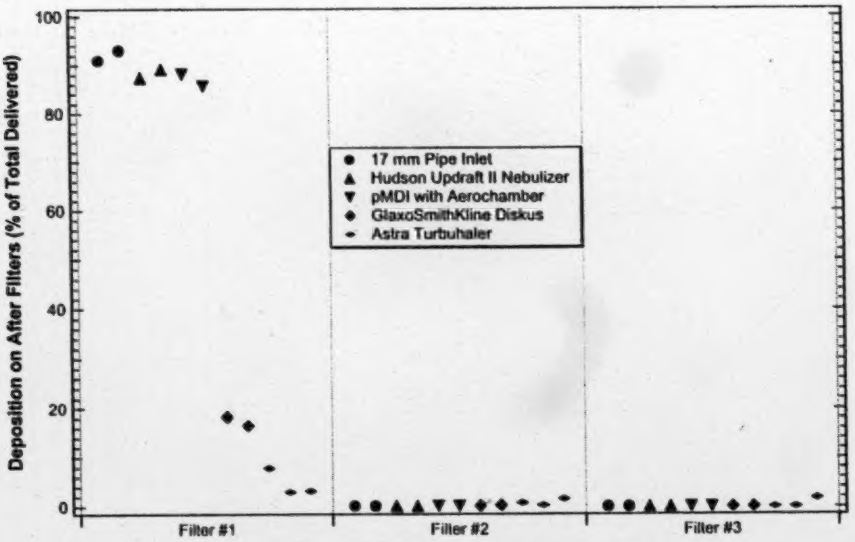

Figure 4.19: Deposition of 5 μm monodisperse aerosol particles on the exit filters after mouth entry through all 5 devices.

by Stahlhofen *et al.*[148] Deposition results with an unvented jet nebulizer and a pMDI with attached holding chamber showed slightly elevated total deposition, located predominantly in the anterior of the oral cavity. Deposition results with two dry powder inhalers showed dramatically different extrathoracic total deposition and regional distribution of the deposition. The majority of aerosol deposition (78.5 % for the Diskus and 91.4 % for the Turbuhaler) occurred in the oral cavity.

From these results it can be seen that further research on predicting deposition in the oral cavity is crucial to understanding deposition from dry powder inhalers. Stahlhofen *et al.* highlighted the fact that the in vivo deposition tests from section 2.9.2 give estimates primarily of laryngeal deposition and little is known about mouth deposition.

As a result, the remainder of this work focuses on deposition in the mouth region alone. Experiments with a variety of inlet conditions including contraction nozzles, pipe flows, enhanced turbulence pipe flows are investigated in Chapter 5. Chapter 6 investigates the flow field and particle deposition patterns inside the oral cavity using computational fluid dynamics and finally in Chapter 7 a model for predicting the extrathoracic deposition after dry powder inhaler inlets is proposed and validated.

Chapter 5

Oral Cavity Deposition Tests

As discussed in Chapter 3, the total deposition of aerosol particles in the extrathoracic region was found to be elevated by the presence of some medical devices. In particular, two dry powder inhalers were found to cause significantly elevated deposition in a large number of cases. In Chapter 4, the two dimensional deposition pattern in the region was quantified using gamma scintigraphy for radiolabelled aerosols after five of the devices. The images clearly showed that the major difference in the deposition pattern between the dry powder inhalers and the other inlets was the deposition in the oral cavity. Because of these results, deposition tests were performed in a model of the oral cavity to determine the major mechanisms at work in this region.

5.1 Oral Cavity Geometry

A model of an adult oral cavity was constructed for these tests. The geometry previously described in section 3.2.3 was truncated 9 mm above the entrance to the pharynx and a short (14 mm) connector length was added to allow direct connection of the disposable filters. One side of the completed geometry can be seen in figure 5.1. Two acrylic pins 2 mm in diameter were added to ensure proper alignment of the halves when assembled. The first pin was located on the upper surface (hard palette) and 3 mm from the mouthpiece connection

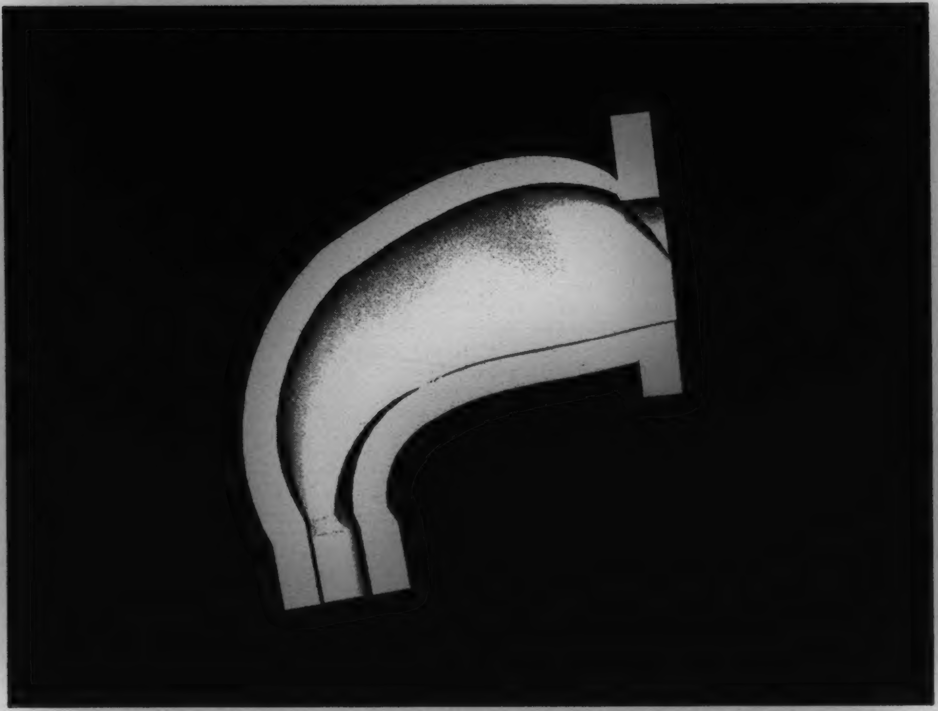

Figure 5.1: Oral cavity geometry used for deposition tests. Only half of geometry is illustrated, split down the symmetry, sagittal plane.

plane. The second pin was located 48 mm from the mouthpiece connection plane and on the lower surface of the model (upper surface of the tongue). Prior to all tests, the halves were assembled, the seam between them was sealed with wax and then a parafilm wrap was applied to prevent any wax from coming off during the course of the test.

Data from section 4.2 for the oral cavity deposition of a 5 micrometer diameter aerosol drawn from a 17 mm inlet through the complete extrathoracic model at 30 L/min was compared to the results of equivalent gravimetric tests

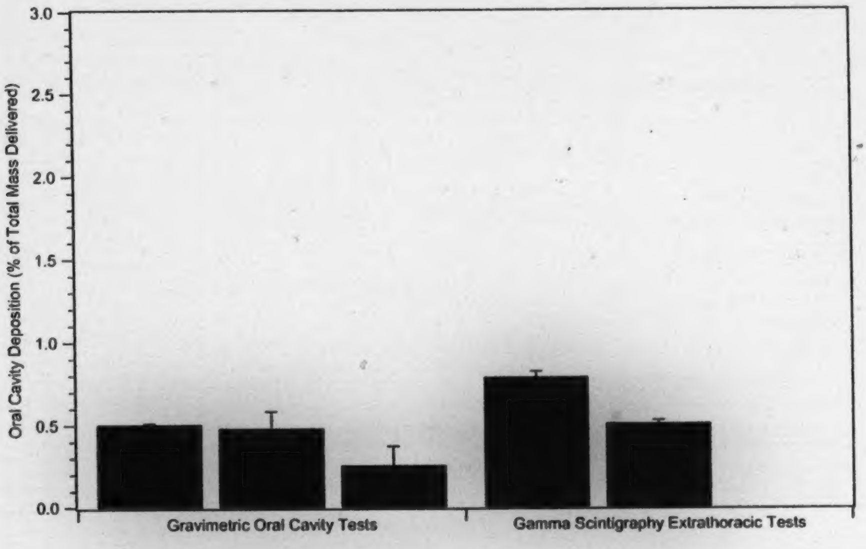

Figure 5.2: Effect of truncating the extrathoracic region on the oral cavity deposition for a 17 mm inlet, 5 micrometer diameter aerosol at 30 L/min. Gravimetric tests were performed with the truncated model (oral cavity only) while gamma scintigraphy tests were performed with the full extrathoracic model and the oral cavity deposition calculated as part of the total extrathoracic deposition. Error bars are experimental uncertainty in the calculated deposition value based on an uncertainty analysis.

using this truncated model (only the oral cavity). The data points are plotted in figure 5.2 where the error bars correspond to the uncertainty in the measured deposition reading calculated from an uncertainty analysis. A student-t test was performed and no significant difference (t > 0.1) was found between the deposition measured in the oral cavity when it was part of the complete extrathoracic model and the deposition measured in the oral cavity when it was connected directly to the exit filters. Therefore, the aerosol deposition in the oral cavity model alone is seen to be equivalent to the oral cavity deposition in the complete extrathoracic model and the truncation of the model has not significantly affected aerosol deposition.

As with the total extrathoracic model, no substances were applied to the inner surface of the oral cavity model to simulate mucous or saliva in the region. As was explained in section 3.2.3, no substance is needed since the presence of a thin liquid layer will not affect the mean streamlines in the region. Since the deposition in the region is dominated by inertial impaction (which will be illustrated in the remainder of the thesis), particle deposition will not be affected by very subtle changes near the wall which do not affect the mean streamlines of the flow.

5.2 Contraction Nozzle Inlets

In this series of tests, the aerosol entered the oral cavity through contraction nozzles in order to generate top hat inlet velocity profiles with very uniform inlet velocity and very low inlet turbulence intensities. Six different contraction nozzles were constructed having outlet diameters of 17.1, 14.4, 10.9, 8.13, 4.95 and 3.18 mm. The contraction nozzles were designed as matched cubic arcs based on the work of Morel.[113] The nozzles have contraction ratios between 5 and 60 and have calculated outlet velocity non-uniformities of $< 2\%$ based on the design charts presented in Morel's work.

5.2.1 Experimental Setup

The experimental setup used for these tests is illustrated in figure 5.3. The monodisperse aerosol is generated by the TSI Model 3475 Condensation Monodisperse Aerosol Generator. The basic operating principle of the generator is given in section 4.1. Measurements using an Amherst Aerosizer Mach II showed particle size distributions with typical geometric standard deviations (GSD) of < 1.06. By controlling the temperature of the reservoir, the flow rate of nitrogen to the reservoir, and the number concentration of condensation nuclei (set by varying the proportion of the salt crystal aerosol which

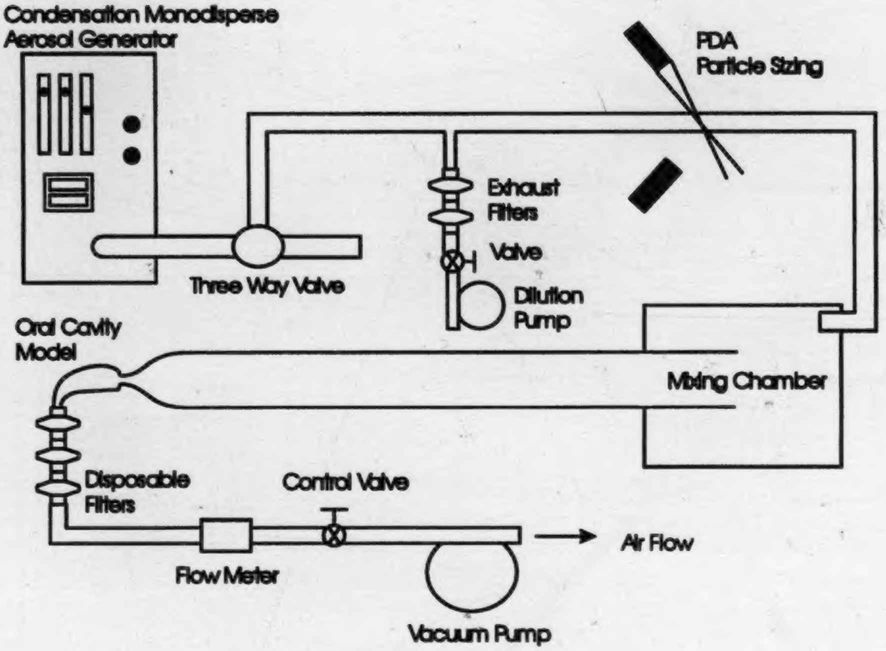
Condensation Monodisperse
Aerosol Generator
PDA
Particle Sizing
Exhaust
Filters
Valve
Dilution
Pump
Three Way Valve
Oral Cavity
Model
Mixing Chamber
Disposable
Filters
Control Valve
Air Flow
Flow Meter
Vacuum Pump

Figure 5.3: Experimental setup for monodisperse aerosol deposition tests in the oral cavity with contraction nozzle inlets.

passed through a filter to remove the crystals from the flow), the size distribution could be shifted from smaller to larger particle sizes. For the tests in this section, particle diameters were varied between 2.5 and 5.0 micrometers.

Immediately downstream of the aerosol generator is a large-bore three way valve. It is used to vent unwanted aerosol. This allows time for the generator to stabilize prior to the test and allows for clear definition of test start and end times.

Since the aerosol generator provides a set mass flow rate of aerosol droplets suspended in approximately 4 L/min of nitrogen, the test aerosol concentration is set by drawing room air through the vent line to mix with the flow from the generator. In order for the presence of the particle phase to have negligible effects on the turbulence in the gas phase, the volume fraction of liquid droplets to the combined volume of liquid and gas must be less than 10^{-6}.[29,41] As the output of the generator often produced higher concentrations of aerosol than this, a dilution pump was connected to the system to decrease the aerosol concentration at the test location. A tee was placed after the three way valve and the dilution pump and filters connected to the arm normal to the main flow direction. Turning on the dilution vacuum pump causes additional air to be drawn through the vent line and mixed with the generator output thus decreasing the concentration of the aerosol. A measured volume flow rate of this dilute aerosol is then drawn to the test section while the remainder is diverted to the dilution filters and pump.

Once the aerosol stream has passed by the dilution pump, the size distribution of the particles is measured using a phase doppler anemometer or PDA (Dantec Dynamics, Skovlunde, Denmark). The operating principle of the phase doppler anemometer has been previously described.[3,9,36,38,136] Briefly, the diameter of a spherical particle of known refractive index can be calculated from the phase shift in scattered light incident on two photodetectors located at different angles to the plane created by the intersection of two laser beams when the particle passes through the intersection volume (see figure 5.4). A linear relationship between the phase shift and the particle diameter occurs when one mode dominates the observed scattered light at the photodetector location. In our case the major mode is second order refraction of light by the particles with the photodetectors located at 73.5^o which is near the Brewster angle of 69.6^o for DEHS with a refractive index of 1.41 at room conditions. Other modes of light scattering include first order refraction, diffraction, and reflection. A previously described optical attachment[149] was used to allow non-obtrusive, online measurement of particle size distributions with high data rates (typically 1-5kHz) during sampling. The PDA calibration was verified by measuring polystyrene microspheres of known diameter and by

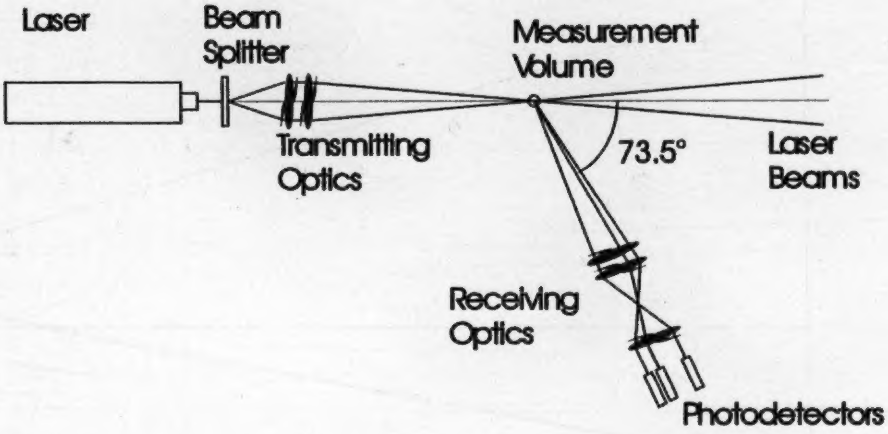

Figure 5.4: Schematic of the operation of a phase doppler anemometer.

comparison with online measurements using the Amherst Aerosizer Mach II which had been previously calibrated with the vibrating orifice aerosol generator described in section 3.2.1 with a DEHS aerosol.

After exiting the PDA's measurement volume, the aerosol enters a parallelepiped mixing chamber with inside dimensions of 295 mm by 305 mm by 305 mm. The aerosol is then drawn out of this chamber through a long, large bore copper pipe. The pipe was designed to keep the Reynolds number of the gas phase based on the pipe inner diameter to be less than 2000 and so to cause the flow in the pipe to be laminar. For flow rates of 30 L/min and below, a 920 mm long pipe with an inner diameter of 26 mm was used while for flow rates between 30 and 90 L/min, a 1860 mm long pipe with an inner diameter of 74.5 mm was used. The pipes were designed to smoothly connect to the entrance of the various contraction nozzles used in these tests.

The air flow rate entering the oral cavity was controlled by a vacuum pump (Model LR 22132, DOERR, Cedarburg, WI, USA) connected to a control valve as indicated in figure 5.3. The flow rate during the test was measured using a pneumotachometer (Series 4719, Hans Rudolph, Inc, Kansas City, MO) connected to a pressure transducer (Model DP45-16; Validyne Engineering Corp., Northridge, CA) and then recorded using a data acquisition system. Deposition was measured for flow rates ranging between 15 and 90 L/min which covers the range of flow rates typically seen with pharmaceutical inhalers.

The halves of the oral cavity were coated with Fluorad Conformal Coating FC-725 (3M St. Paul,MN) to allow much higher deposition on the oral cavity surfaces prior to the DEHS beginning to flow. Wax was used to create an airtight seal between the halves and then the model was wrapped in parafilm to prevent any mass loss from the wax during the test. The total aerosol deposition in the oral cavity and on the filters was determined gravimetrically by weighing the components before and after the tests. A balance (Sartorius GMBH, Germany) with a resolution of 0.0001 grams was used for the measurements. Since the tests are performed at steady flow rates, the test times were set to allow sufficient aerosol deposition to cause measurable changes in the mass of the oral cavity.

The deposition efficiency of the oral cavity with the tested contraction nozzle mouthpiece was calculated as follows:

$$Deposition\ Efficiency = \frac{\Delta m_{Oral\ Cavity}}{\Delta m_{Oral\ Cavity} + \Delta m_{filters}} * 100 \qquad (5.1)$$

Qualitative deposition patterns in the oral cavity were obtained by blotting the inner surface of the halves with Kimwipes after disassembly of the oral cavity.

5.2.2 Results and Discussion

The flow rate range tested in this set of experiments ranging from 15 L/min to 90 L/min is typical of the inhalation flow rates observed for many dry powder inhalers. The range of nozzle exit diameters from 3 mm to 17 mm also spans

Dry Powder Inhaler	Company	Exit Diameter (mm)
Easyhaler	Orion	5.4
Inhalator (Single Dose)	Boehringer Ingelheim	5.9
Inhalator (Multiple Dose)	Boehringer Ingelheim	7.9
Aerolizer	Novartis	10.7
Diskhaler	GlaxoSmithKlein	12.0

Table 5.1: Diameter of aerosol flow path at exit of a sample of dry powder inhalers

much of the range of exit sizes seen in dry powder inhalers. A small sample of commercially available dry powder inhalers and the measured diameter the aerosol flow exits the device through is shown in Table 5.1. For non-circular exits, the diameter listed is that of a circular exit with the same cross-sectional area as the device exit.

At each test parameter location (nozzle diameter, aerosol diameter, and flow rate) a minimum of three measurements were taken to ensure repeatability of the data.

The contraction nozzles were used as inlets for the oral cavity in order to test the effect of high velocity jets expected at the outlet of many dry powder inhalers without the complication of turbulent inlet velocity profiles. In this way, the effects of high mean inlet velocities and varying turbulence intensities could be tested for independently. The effect of varying levels of turbulence intensity being advected into the oral cavity is explored in section 5.4. Turbulence is expected to be produced by the shear layer between the jet and the slow moving fluid in the oral cavity for all the tested entry nozzle diameters since the Reynolds numbers for the jets based on the nozzle diameters range from 2608 to 14494, but the contraction nozzles ensure that very little turbulence is initially in the flow as it enters the oral cavity.

For the particle diameters tested (nominally 2.5, 3.8 and 5.0 micrometers), diffusion and sedimentation of the particles is expected to be negligible in the oral cavity. Because of the small settling velocities of the particles listed in Table 2.1, the relatively large vertical distances involved and the relatively short residence time of the fluid, deposition due to gravitational settling should be negligible. For example, from Table 2.1 the highest settling velocity occurs for the 5.0 micrometer DEHS particle and is 0.706 mm/s. Since the oral cavity has a volume of 49.2 mL and the lowest flow rate tested was 15 L/min or 250 mL/s, the shortest average residence time is expected to be 0.2 seconds during which the 5 micrometer particle would settle 0.14 mm. However, the height of the roof of the oral cavity above the tongue ranges from 22 mm to 29 mm in the idealized geometry, so only particles which are first transported very close to the bottom surface will deposit due to gravity. Similarly, for the smallest particles (2.5 micrometers) the root mean square displacement of the particle caused by Brownian diffusion from equation 2.37 is expected to be 2.0×10^{-6} m. Again comparing this to the large distances in the oral cavity, deposition due to diffusion is expected to be very low, found in section 2.5 to be on the order of 0.09%.

5.2.2.1 Impaction Parameter

Inertial impaction was hypothesized to be the major mechanism for particle deposition in the oral cavity for these tests. Whether the impaction was caused by high mean fluid velocities, large secondary flows and vortices or high turbulent transport in the region was unclear. However, if impaction is the dominating mechanism, then the Stokes number should be the governing non-dimensional number. Since the oral cavity geometry is the same for all tests, if the velocity and length scales in the Stokes number are taken to be set by the flow rate and the flow geometry in the oral cavity, then the Stokes number should be proportional to the impaction parameter $\rho d_p^2 Q$ used to plot in vivo deposition tests by many authors[17,52,99,105,112,148,165,169] and used in sections

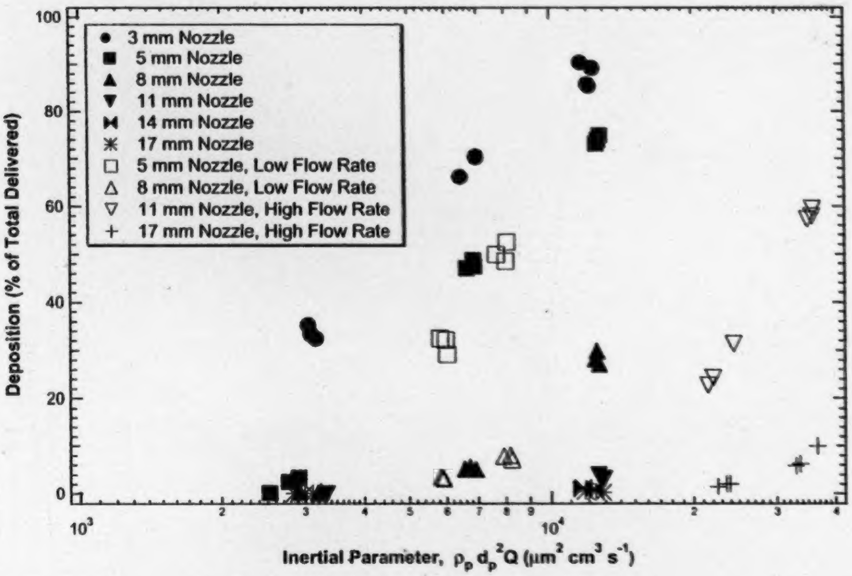

Figure 5.5: Variation of monodisperse aerosol particle deposition in the oral cavity entering through contraction nozzles with the impaction parameter $\rho_p d_p^2 Q$.

2.9.2 and 3.3 to plot total extrathoracic deposition. The oral cavity deposition results of all the contraction nozzle deposition tests are plotted against the impaction parameter $\rho d_p^2 Q$ in figure 5.5.

It can be seen from the figure that aerosol deposition in the oral cavity is not a unique function of the impaction parameter. The deposition does appear to be a monotonically increasing function of the impaction parameter for each individual inlet nozzle, but the slope of the function is dramatically different between nozzles, with the smallest diameter nozzles having the steepest slopes. The clear trend of increasing deposition with increasing impaction parameter for a given inlet nozzle does indicate that inertial impaction is the major mechanism of aerosol deposition. However, no consideration has been given to the effect of the nozzles on the flow in the oral cavity. By plotting the impaction parameter, all flows which have the same particle diameter and flow rate will be predicted to have the same deposition, regardless of the size of the inlet. Clearly from figure 5.5 this is not true.

The trouble comes from using the dimensional impaction parameter rather than the non-dimensional Stokes number. Whether or not a particle will have sufficient momentum to deposit as it nears a wall can be calculated from the particle momentum equation (Equation 2.24) if the full solution of the air flow field and the particles initial velocity is known. Otherwise the probability of the particle depositing can be estimated from the particle's Stokes number since the Stokes number may be interpreted as the non-dimensional distance or time it would need to stop after the fluid makes a sudden turn (such as at a solid barrier or wall). For flow inside a pipe, the typical length and velocity scales used for the Stokes number are the pipe diameter and the average velocity in the pipe. For example the Stokes number is often calculated for each generation of a lung model based on the predicted airway diameter and average velocity in generation. The Stokes number formulated in this manner is then used to predict the deposition due to impaction in that generation.[16,17,46,86,90,120,155,166]

When considering the extrathoracic region, an added complication is the varying cross sectional area throughout the region. Trying to calculate the Stokes number for this region as if it were a pipe of varying cross section for a set volume flow rate and particle size leads to a different particle Stokes number at every different cross section in the region, making prediction of deposition very difficult. The impaction parameter avoids this problem by dropping the length and velocity scales completely. This leads to only one value of the parameter throughout the region for a given particle size and flow rate. Thus the need for the local cross sectional area throughout the region is eliminated and allowing comparison of data despite the inter- and intra-person variability of the geometry. This works well if the impaction is dominated by an effect based on the mean flow within the tube. For example deposition in a pipe caused by a bend in a pipe (such as the curve in the path between the oral cavity and the pharynx) or deposition caused by a constriction in the pipe (such as the larynx) will all be well modelled using the impaction parameter since the Stokes number that should be used is based on the average velocity in the region (in the curve or in the larynx) and the equivalent diameter of the region (diameter of the conduit or diameter of the larynx). However, if the aerosol impaction is caused by a flow structure inside the region and not dependant on the overall diameter of the region itself at the impaction location, then the impaction parameter cannot account for the substructure and so does not necessarily predict deposition.

This is believed to be the problem in these tests. The aerosol flow is entering the oral cavity through relatively small diameter nozzles. These nozzles cause a high velocity jet to form inside the cavity and the aerosol tends to deposit where the jet impinges on the walls and due to flows within the cavity set up by the presence of the jet. This means that the aerosol impaction is dominated not by the average flow through the whole region, but by the substructure. The length and velocity scales of interest for the particle Stokes number are then not the cross sectionally averaged velocity and equivalent diameter of the region, but are the diameter and velocity of the jet. When the jet impinges on a wall, the particle will see a change in the fluid velocity on the order the jet velocity (since it goes to zero at the wall) in a distance which is of the order of the jet diameter.

The deposition pattern observed for nearly all the cases with the exception of the 17 mm inlet support this idea. A typical deposition pattern for the 3-14 mm nozzles is shown in figure 5.6. No deposition is visible in the first 35-40 mm distal to the nozzle outlet. The deposition is then seen to be located on

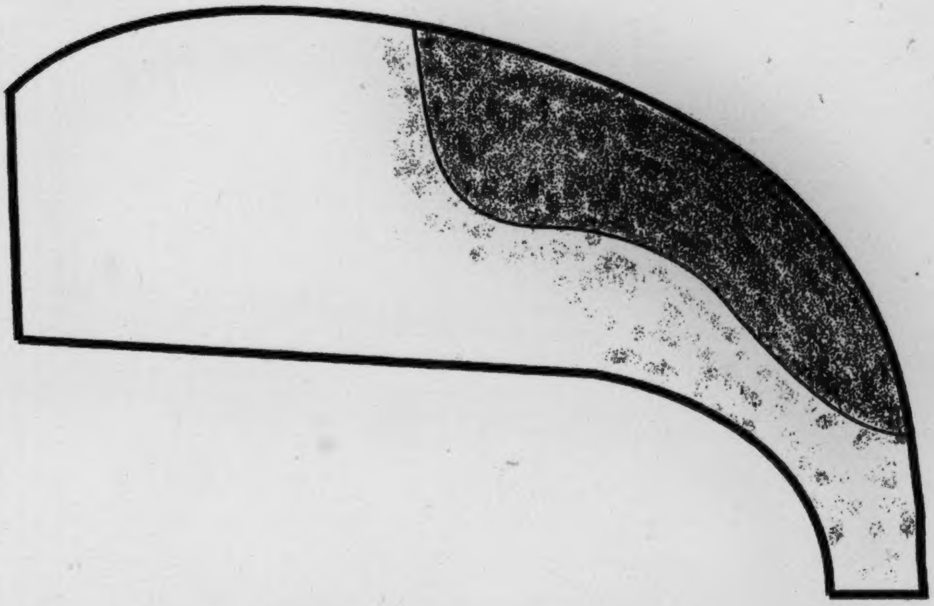

Figure 5.6: Typical deposition pattern observed through blotting of oral cavity after deposition test for inlets ranging from 3 to 14 mm in diameter.

the upper surface of the oral cavity, centered about the location 60 mm distal to the nozzle exit, where the oral cavity curves down towards the pharynx, forming the back wall of the region. Additional deposition tailing off around the corner is probably due to centrifugal effects as the high speed jet rounds the corner. The jet is expected to be nearly adhered to the back wall, causing inertial impaction of the particles due to the rapid change in direction of the fluid.

5.2.2.2 Stokes Number at Nozzle

If the elevated deposition in the oral cavity is caused by an impinging jet for the small inlet nozzles, then the Stokes number based on the jet velocity and diameter should collapse all the deposition tests onto a single curve. A difficulty occurs in calculating the Stokes number since the the velocity and length scales to be used should be indicative of the velocity and length scales of the flow 'near' the impaction site. Since the impaction site is located well inside the oral cavity, it is not obvious how to predict the velocity and length scales of the turbulent jets inside the region. In the tested oral cavity geometry, the predicted impaction site was chosen on the rear wall of the cavity where wall crosses the nozzle axis. This was measured to be 60 mm from the outlet of the nozzle. Since the nozzle diameters range from 3-17 mm, the impaction location is anywhere from 3.5 to 19 nozzle diameters downstream of the nozzle exit. As a first approximation, the length and velocity scales for the particle Stokes number were taken as the average velocity at the nozzle outlet and the nozzle diameter respectively. The deposition data is plotted against the Stokes number based on the velocity and diameter at the nozzle exit in figure 5.7.

Comparing figures 5.5 and figure 5.7, it can be seen that the data collapses much better when plotted against the Stokes number at the nozzle exit. As expected, the data does not collapse exactly onto a single curve since the velocity and length scales at the nozzle exit may be quite different from the scales at the impaction sites for the small diameter nozzles due to their distance from the site of up to 19 diameters. The deposition curves for the smaller diameter nozzles appear to be shifted to the right of the larger diameter nozzle curves. This would indicate an over-prediction of the velocity scale or an under-prediction of the length scale for the small nozzles. This agrees with the above theory as the jet leaving the small nozzles is expected to be gradually

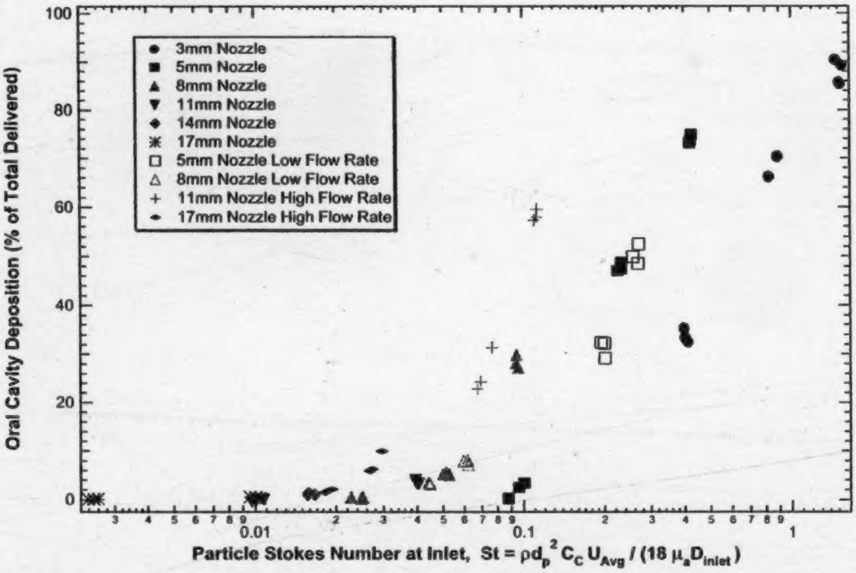

Figure 5.7: Variation of monodisperse aerosol particle deposition in the oral cavity entering through contraction nozzles with the Stokes number based on average inlet velocity and nozzle exit diameter.

decelerated by the surrounding fluid and widened out by the entrainment of air. This idea will be investigated further in section 5.2.2.4.

One major advantage of calculating the Stokes number based on the flow conditions at the inlet of the region is that no information about the location of the impaction site or the geometry of the oral cavity was required. The geometry of the oral cavity varies significantly from person to person. Orientation of the inhalation device may also vary between people and between uses, all of which result in a change in the location of the jet impingement site. For designers of inhalation devices, the location of the jet impingement site and the oral cavity geometry may only be roughly known. However, the exit diameter and exit velocity of the aerosol flow as it leaves a pharmaceutical device can be easily determined. The reasonably good collapse of the deposition data based on only the particle Stokes number at the exit of the contraction nozzles is encouraging and may be quite useful for determining rough deposition predictions when designing new devices. However, caution must be given before applying the results of figure 5.7 directly to medical devices. The data presented is for dilute monodisperse aerosols entering an idealized geometry with uniform, top hat velocity profiles. While the effect of higher turbulence intensity at the nozzle exit is examined in section 5.4, and the applicability to polydisperse aerosols is investigated in section 7.2.1, the effects of higher volume fractions of aerosols, variations of oral cavity geometry and variations of inlet orientation are necessary but lie beyond the scope of the present work.

5.2.2.3 Limit of Oral Cavity Jet Effects

The case of the 17 mm diameter nozzle has some characteristics that set it apart from the other inlets. The deposition patterns obtained by blotting the oral cavity surface after each test were quite different for this inlet compared to all the smaller diameter nozzle tests. The major location of deposition was no longer at the projected jet impingement location, but was concentrated near the exit of the region where the cross section of the region narrows to its minimum. Traces of aerosol deposition were also visible along the upper surface of the tongue (the bottom surface of the oral cavity) throughout the region. This agrees qualitatively with the deposition pattern measured in the radioactive aerosol tests of Chapter 4. Quantitative deposition amounts also show very good agreement between the oral cavity tests for the 17 mm contraction nozzle at 32 L/min and the radioactive aerosol tests with a 17 mm long tube entrance at 32 L/min. The gravimetric oral cavity tests gave 0.42% ± 0.14% while the radioactive aerosol test gave 0.65% ± 0.20%. As will be discussed in section 5.3, the radioactive tests were expected to show slightly higher deposition in the oral region because the inlet had a fully developed turbulent velocity profile instead of the uniform profile seen with the contraction nozzle. From the radioactive tests, the hot spot at the back of the oral cavity accounted for approximately half of the oral cavity deposition with the majority of the rest being on the upper surface of the tongue. This would indicate that particles are impacting in the back of the oral cavity due to the acceleration of the fluid into the narrowing flow channel and gravitationally settling onto the tongue surface. The computational fluid dynamics solution of the flow field in the oral cavity for the 17 mm inlet in section 6.7.1 indicates that the flow near the tongue surface is moving very slowly, allowing particles which reach this region to have long enough residence times for measurable amounts (approximately 0.2% of the aerosol entering the oral cavity) to deposit by sedimentation for the 5 micrometer, 32 L/min case.

The evidence that the aerosol depositing from the curve at the back of the oral cavity is due to inertial impaction caused by the mean fluid flow (and not an inlet jet effect) comes from a number of sources. First, the deposition is in the wrong location for it to be caused by a high speed jet due to the entrance condition. For all of the other contraction nozzles, the major aerosol deposition was centered around the nozzle axis on the upper, rear surface of the oral cavity. The deposition with the 17 mm nozzle was located nearly 30 mm below the predicted jet impingement location as illustrated in figure 5.8 and was roughly uniformly distributed around the perimeter at that location. Second, as the flow rate was increased from 32 to 60 and then to 90 L/min, the deposition on the upper surface of the tongue was no longer visible as much shorter test times were required to obtain measurable quantities of aerosol depositing in the region and deposition in the narrow base of the oral cavity became more pronounced. Thus the deposition at the base of the oral cavity must be due to impaction since at higher flow rates and shorter test times the amount depositing there increased. If the deposition was due to diffusion or sedimentation, the amount depositing would have decreased with increased flow rate and decreased test time. Third, the results of the CFD simulation in figure 6.19 shows no indication of deposition due to a high speed jet along the upper rear surface of the oral cavity while the simulations of the other entrance nozzles did. (see figures 6.19, 6.20, and 6.21)

This is important because it indicates an upper limit for the inlet nozzle diameter where high speed jet effects are important. Increasing the diameter of the inlet beyond 17 mm should not significantly reduce the oral cavity deposition for flow rates up to 90 L/min and particle sizes up to 5 micrometers since the deposition was observed to be governed primarily by the mean flow conditions and not a high speed jet phenomena. Therefore the impaction parameter works well for modelling deposition after a 17 mm inlet as was seen in section 4.2 where good agreement was observed with the model of Stahlhofen *et al.*[148] and the deposition should be nearly independent of the inlet conditions. Therefore decreasing the inlet velocity any further is expected to cause only very marginal decreases in deposition in the oral cavity.

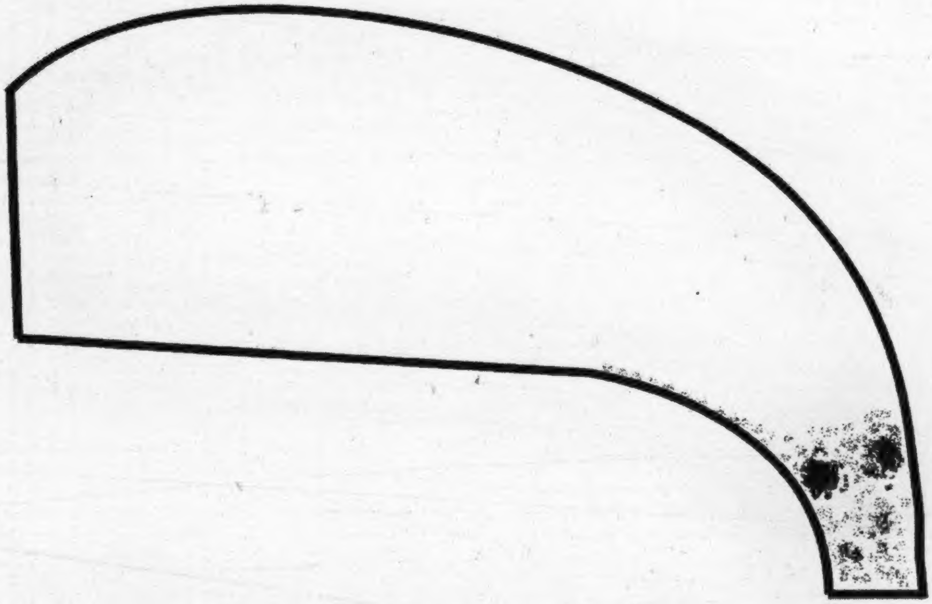

Figure 5.8: Typical deposition pattern observed through blotting of oral cavity after deposition test for 17 mm diameter inlet.

In apparent contrast to this, Lin *et al.* recently found decreased deposition in a cast of the oral cavity, pharynx, larynx and trachea for certain cases of flow rates and particle sizes when changing from inlets with inner diameters of 14, 19 and 26 mm.[96] Unfortunately, no deposition patterns nor details of the primary location of aerosol deposition in the tests are given. The results that they tabulated are plotted in figures 5.9, 5.10 and 5.11 against the particle Stokes number based on nozzle diameter and velocity, the impaction parameter and the Stokes number based on the reported larynx dimensions. From figure 5.9 it can be seen that the deposition does increase with increasing particle Stokes number for each of the three inlets. However, the inability of the Stokes number based on the inlet velocity and diameter to collapse the data onto a single curve does indicate that the major effect is not a jet phenomena in the oral cavity for at least two of the inlets. As shown in figures 5.10 and 5.11, the data collapses much better when plotted against the impaction parameter and the Stokes number based on the conditions in the larynx. This would indicate that the primary deposition location is in the larnyx for the 19 and 26 mm cases. The slight increase in slope of the 14 mm inlet data when plotted against the impaction parameter could be evidence of increased deposition due to a jet in the oral cavity as a similar effect was seen when our data was plotted against the impaction parameter in figure 5.5.

Decreased deposition due to a decrease in jet effects in the oral cavity when moving from the 14 mm inlet to the 19 mm inlet in Lin *et al.*'s data agrees with the results obtained here as elevated deposition due to jet effects in the oral cavity were observed in an 14.4 mm inlet. However, the decrease in deposition from a 19 mm inlet to a 26 mm inlet is surprising, even if only for a limited number of particle size and flow rate cases. There are a number of possible reasons for this observed decrease in deposition. The first is that the oral cavity geometry was not identical for the different diameter inlets. Three

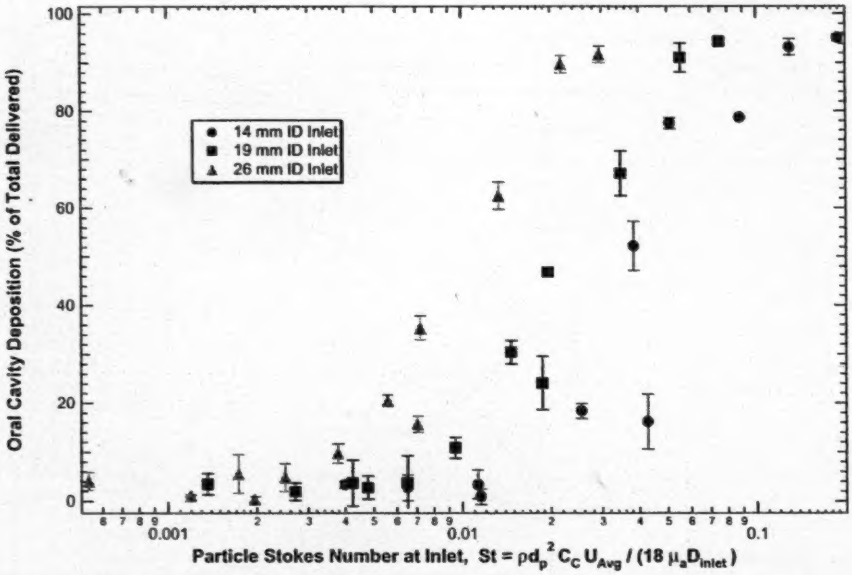

Figure 5.9: Effect of inlet diameter and mouth opening on particle deposition in the extrathoracic region. Plotted against particle Stokes number at the exit of the inlet tube. Data from Lin *et al.*[96] Error bars are standard error.

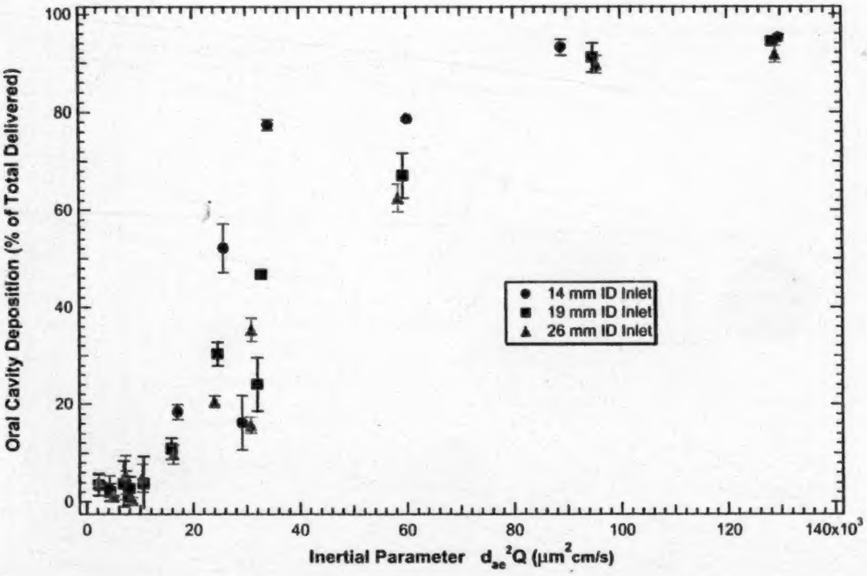

Figure 5.10: Effect of inlet diameter and mouth opening on particle deposition in the extrathoracic region. Plotted against impaction parameter $\rho d_p^2 Q$. Data from Lin *et al.*[96] Error bars are standard error.

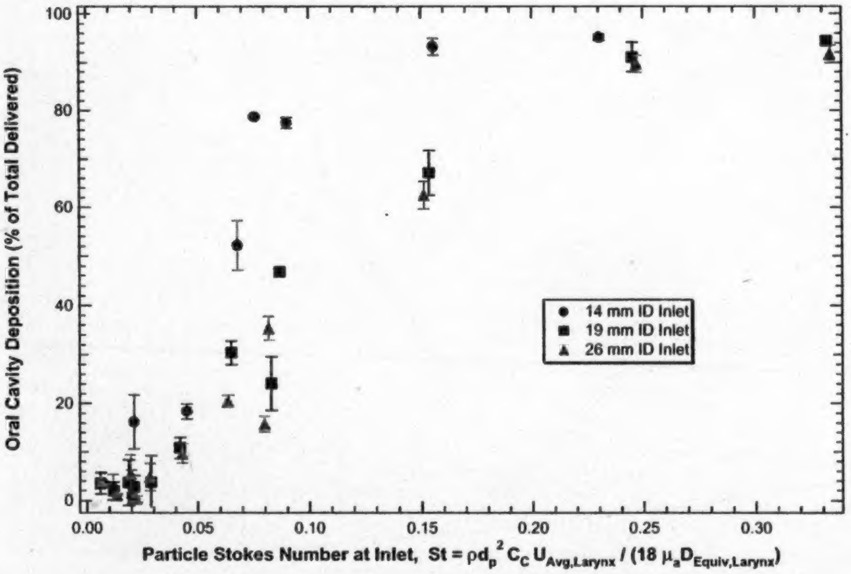

Figure 5.11: Effect of inlet diameter and mouth opening on particle deposition in the extrathoracic region. Plotted against the particle Stokes number based on mean velocity and equivalent diameter in the larynx. Data from Lin *et al.*[96] Error bars are standard error.

different casts of the subjects oral cavity were made. For the larger inlets, the subjects mouth was open further, presumably increasing the oral cavity dimensions well into the region, possibly decreasing the oral cavity deposition. Second, the connection between the oral cavity cast and the separate cast of the pharynx to trachea is not well defined. In our tests with both the 17 inlet in the oral cavity and in the radioactive deposition tests, this region held significant amounts of the oral cavity deposition and the way that the wax connection between the regions was formed for each of the three inlets may have affected deposition here. Third, the entrance length of the inlets is very short at only 13 mm, less than one inlet diameter in all cases. The effect of inlet turbulence, though discussed, was not measured. Apparent step changes from their air inlet piece to the mouthpiece less than one diameter upstream from the inlet may have significant effects on the velocity profile at the mouth inlet and so on the deposition as will be seen in sections 5.3 and 5.4.

5.2.2.4 Stokes Number Based on Free Jet Theory

In order to refine the predictions of aerosol deposition for the 3-14 mm cases, the length and velocity scales in the Stokes number need to be refined. In order to precisely define them, the behaviour of turbulent jets in the confined three dimensional geometry would have to be analyzed. An analytical solution of this problem is nearly impossible due to the random nature of turbulence and our limited understanding of turbulent flows. In section 6.7.1 an approximate solution of the flow field for the 32 L/min cases is calculated numerically using by solving the Reynolds averaged Navier-Stokes equations with a k-ε model for the turbulence. This solution is still only approximate and requires significant computational time and power to achieve.

A simpler method of predicting the velocity and length scale of the flow near the impaction location is to neglect the presence of the confining walls and consider the deceleration of a turbulent free jet. Although the assumption of the walls not influencing the jet is probably not valid for the larger diameter entrances where the oral cavity has an equivalent diameter of approximately two times the jet diameter, for the small diameter jets (3-5 mm) it may be a valid assumption. Since the major discrepancies were seen for the 3 and 5 mm nozzles using the Stokes number at the mouthpiece, this free jet assumption appears reasonable.

The classical theory and experiments for single phase round free jets issuing into either a still fluid or into a secondary stream is reviewed by Hinze.[71] The jet structure can be split into three components. In the initial region, turbulent mixing between the slower fluid outside the jet and the fluid inside the jet causes a mixing layer to form and gradually increase in width with increasing distance from the nozzle exit up to a point x_c where the mixing zone covers the entire jet. For $x < x_c$, a potential core region exists from the jet axis out to the edge of the mixing layer where the fluid velocity is equal to the nozzle discharge velocity U_p. Next comes a transition region where the centerline axial velocity of the jet decreases with increasing distance from the nozzle exit. Finally comes a fully developed region where the jet velocity profile is similar at subsequent axial locations.

The classical theory applies primarily to the fully developed region far enough from the jet orifice for the jet to be similar. For a jet issuing from a nozzle of diameter D with uniform velocity U_p into a stream with unform velocity U_s, Hinze gives the axial velocity of the jet above the free stream velocity, $\bar{U}_x$, as:

$$\bar{U}_x = U_p \left(\frac{x+a}{D} \right)^p f(\xi_2) \tag{5.2}$$

where

$$\xi_2 = \frac{r/D}{[(x+a)/D]^q} \tag{5.3}$$

and $x = -a$ is the "origin of similarity". For $\bar{U}_x/U_s \gg 1$, the exponents p and q are found to be $p = -1$ and $q = 1$, giving:

$$\bar{U}_x = U_p \left(\frac{x+a}{D} \right) f(\xi_2) \tag{5.4}$$

and

$$\xi_2 = \frac{r/D}{(x+a)/D} \tag{5.5}$$

Therefore the lines of similarity form rays outward from the virtual origin at $r = 0$ and $x = -a$, yielding a jet radius which increases linearly with $x + a$ and a jet velocity which decreases hyperbolically with $x + a$.

Experimental work with gas jets issuing into air in the fully developed region of the jet flow are numerous and reasonably old.[2,130,137,164] They generally support the theory of the jet radius increasing linearly and the velocity decreasing hyperbolically in the fully developed region. Similar results have been found for submerged water jets.[53] Forstall and Shapiro[81,82] did extensive tests on the more general case of jets issuing into a secondary, slower stream, where the assumption $\bar{U}_x/U_s \gg 1$ is not valid. More recently Hussein *et al.* re-examined the far field of turbulent gas jets issuing into large rooms with LDA and found that most earlier works were not free from influences of the surrounding walls and their results differed in level and shape of the profiles, especially for turbulent higher moments and off the center axis.[76] However, as our flow involves relatively close surrounding walls and predictions for mean velocities along the jet centerline, results from the earlier works are deemed adequate for our model.

Measurements by Hinze and Van der Hegge Zijnen[72] give the length of the potential core region as $x_c \simeq 6$ to $8D$ depending on the thickness of the boundary layer at the jet orifice. The boundary layer thickness is expected to be quite thin due to the presence of the contraction nozzles for our test setup so that despite the relatively low Reynolds numbers at the nozzle exit, an estimate of $x_c = 7D$ is believed to be reasonable.

Hinze[71] notes that the transition region is quite short and states that beyond $x = 6$ to $8D$ the velocity distributions were similar. For this reason, in our model of free jet turbulence the transition region will be neglected and the jet will be assumed to switch directly from having a potential core to being fully developed at $x = x_c = 7D$.

In the fully developed region, the centerline (and maximum) axial velocity decreases with distance from $x + a$ as:

$$\frac{\bar{U}_{x,max}}{U_p} = A\frac{D}{x+a} \tag{5.6}$$

where A and a are experimentally determined. The values of A and a vary between investigators and depend on the jet initial conditions and Reynolds number. The results of Hinze and Van der Hegge Zijnen's[72] measurements were used which gave $A = 5.9$ and $a = -0.5D$ since they considered the region $10 < (x+a)/D < 50$ which covers much of the region prior to impaction of the jets we are considering.

Based on the above theory, the velocity scale for the particle Stokes number was chosen to be equal to the predicted centerline velocity of a free jet issuing into stationary air at $x = 60$ mm where x is along the nozzle axis and $x = 0$ is at the exit plane of the nozzle. Therefore if $x = 60$ mm corresponded to $x < 7D$ where D is the nozzle diameter, then a potential core region was assumed to exist and the velocity scale was set equal to the discharge velocity at the exit of the nozzle:

$$U_{C,jet} = U_p \tag{5.7}$$

If $x = 60$ mm corresponded to $x > 7D$, then the velocity scale was set equal to:

$$U_{C,jet} = 5.9\frac{U_p D}{x - 0.5D} \tag{5.8}$$

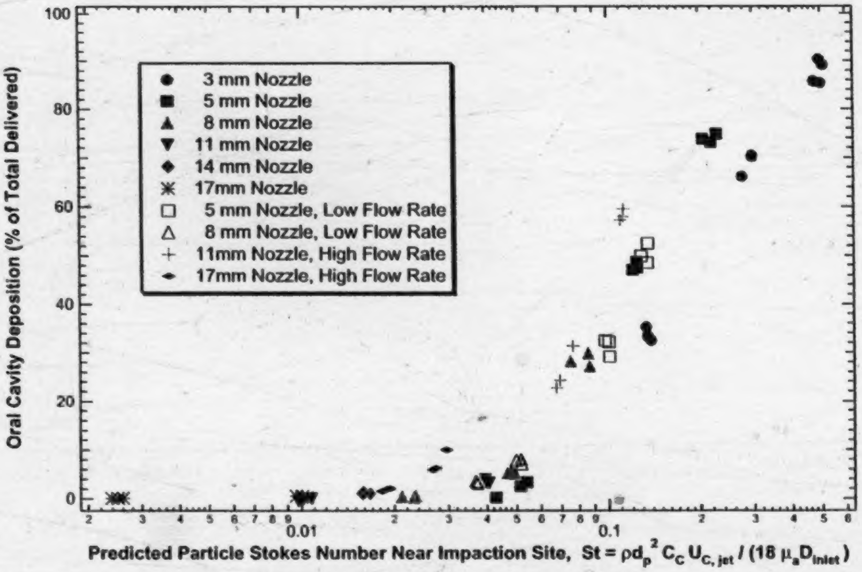

Figure 5.12: Variation of monodisperse aerosol deposition in the oral cavity with the particle Stokes number. Stokes number calculated from the nozzle diameter and the velocity near the impingement location predicted from free jet theory.

Difficulties were encountered using this theory to predict the length scale of the jet at the location $x = 60$ mm. The theory predicts nearly identical diameters of the jet for the 8, 5 and 3 mm nozzles varying from 9.75 mm to 10.15 mm. This is unrealistic for the confined jets as indicated by the CFD flow fields which showed quite different jet diameters for the three cases near $x = 50$ mm in part (c) of figures 6.8, 6.9, and 6.10. Due to the k-ε model's tendency to overestimate the jet diameter as discussed in section 6.7.3.1, the CFD predictions of jet diameter were not used for the Stokes number calculation. Lacking a clear theory from predicting the expansion of the confined turbulent jets, the length scale was left equal to the diameter of the nozzle exit.

The results of plotting the oral cavity deposition against the Stokes number based on the predicted velocity scale from free jet theory are presented in figure 5.12. The results are quite encouraging considering the number of assumptions made in the predictions of velocity and length scales for the various inlets. The collapse of the data for the various inlet nozzles diameters, flow rates and particle sizes gives credence to the theory that for inlet diameters below 17 mm, a high velocity jet can cause significantly elevated deposition in the oral cavity. Based on the discussion of section 5.2.2.3, the data is re-plotted in figure 5.13 without the results from the 17 mm inlet nozzle since the jet effect with this large nozzle is not significant enough to cause elevated deposition at the jet impingement site. This lack of elevated deposition at the jet impingement site was observed both with the qualitative deposition patterns visible in the tests of this chapter and in the deposition results from the CFD analysis of section 6.7.3.2.

Although figure 5.13 shows a much better collapse of the deposition data than simply using the particle Stokes number at the exit of the nozzle, knowledge of the location of the jet impingement site in the oral cavity is required. This may cause difficulties in some cases where the patients oral cavity geometry or inhaler orientation is unknown. However, in cases where orientation and geometry are well known, this free jet theory model greatly reduces the uncertainty in the prediction of oral cavity deposition.

5.3 Fully Developed Pipe Flow Inlets

In the preceding section, the inlet velocity profile was carefully controlled as a uniform, top hat profile by the use of contraction nozzles at the oral cavity inlet. While useful for testing the effect of the inlet diameter and velocity on deposition, this restriction limits the applicability of the data to predict deposition from pharmaceutical devices as commercially available devices do not use top hat velocity profiles or contraction nozzles at their exit.

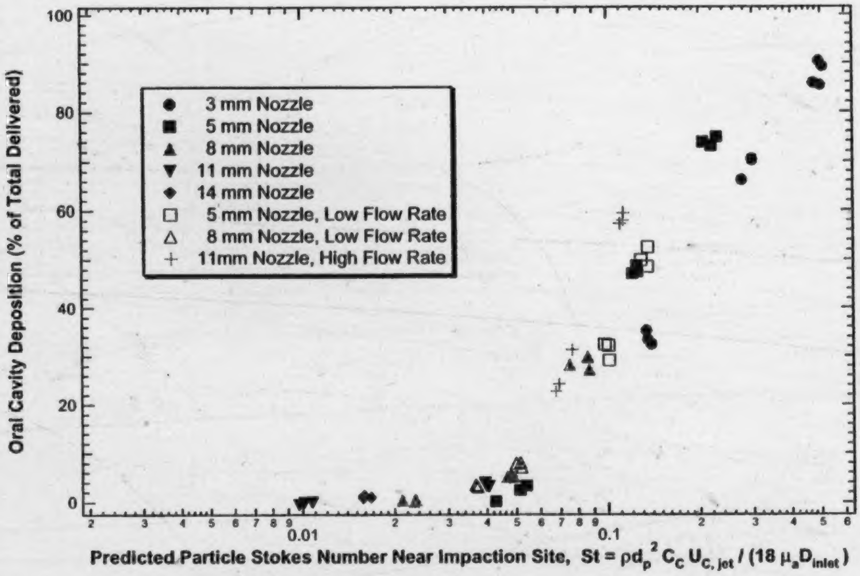

Figure 5.13: Variation of monodisperse aerosol deposition in the oral cavity with the particle Stokes number. Stokes number calculated from the nozzle diameter and the velocity near the impingement location predicted from free jet theory. 17mm inlet nozzles neglected due to lack of jet effects observed.

In order to relax the velocity profile restriction on the predictive model for oral cavity deposition, a series of tests was done testing the effects of a variety of inlet velocity profiles. In this section, the first set of tests is presented. Straight tubes were used as inlets for the oral cavity in order to generate turbulent velocity profiles at the inlet of the oral cavity.

Under normal engineering flow circumstances, transition to turbulence occurs in pipe flows for Reynolds numbers Re $\approx$ 2300[54] where:

$$Re = \frac{\rho_a \bar{V} D}{\mu_a} \tag{5.9}$$

and D is the inner diameter of the pipe, $\bar{V}$ is the average air velocity in the pipe, and ρ_a and μ_a are the density and viscosity of air. For a flow rate of 32 L/min used in this set of tests, this corresponds to D $\lesssim$ 20 mm. Therefore turbulent flow is expected for all the entrance tubes which range in diameter from 3.18 mm to 17.1 mm and have Reynolds numbers which range from 2550 to 13 700.

An entrance length is required in order for the velocity profile in a tube to reach a fully developed state (so that it is unchanging at locations further downstream). For flow entering a tube with an initially uniform velocity profile, Fox *et al.* states that the velocity profile will be fully developed within 25 to 40 diameters from the entrance.[54] In our test setup, the flow enters the inlet tubes from a long (approximately 50 diameters) 19 mm diameter tube where the velocity profile is already a well developed turbulent profile. Because of this, the entrance length required for fully developed turbulent flow is expected to be much shorter and the 20 diameters of inlet tube sufficient to produce a fully developed flow profile at the inlet of the oral cavity.

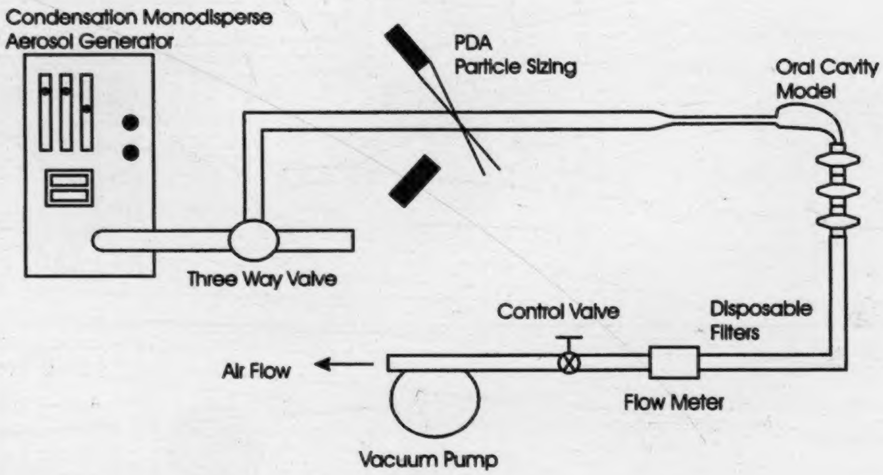
Condensation Monodisperse Aerosol Generator
PDA Particle Sizing
Oral Cavity Model
Three Way Valve
Control Valve
Disposable Filters
Air Flow
Flow Meter
Vacuum Pump

Figure 5.14: Experimental setup for monodisperse aerosol deposition tests in the oral cavity with turbulent pipe flow inlets.

5.3.1 Experimental Setup

5.3.1.1 Aerosol Deposition Tests

The equipment setup for this series of tests with turbulent pipe flow entering the oral cavity is shown in figure 5.14. The setup is similar to that of the contraction nozzles' test setup described in section 5.2.1. The monodisperse aerosol is again generated with the TSI model 3475 Condensation Monodisperse Aerosol Generator although only particles nominally 5 μm in diameter were tested. The aerosol size distribution was again verified using a phase doppler anemometer or PDA (Dantec Dynamics, Skovlunde, Denmark). Flow through the system was driven by a vacuum pump with a pneumotachometer used to measure the flow rate and a control valve used to adjust it.

No mixing chamber was used for these tests. The flow moved directly from the conducting 19 mm diameter tubing into the entrance tubes via a gradual, axis symmetric contraction with a slope of 7^o.

5.3.2 Inlet Conditions from Turbulent Pipe Flow

Hinze[71] has compiled experimental data on mean and turbulent velocity profiles in fully developed pipe flow. The mean velocity profile in a pipe may be characterized as a power law function such that:

$$\frac{\bar{U}_x}{\bar{U}_{x,max}} = \left(\frac{2r}{D}\right)^{1/n} \tag{5.10}$$

where x is the axial direction, r is the radial coordinate measured from the pipe wall towards the center, D is the pipe diameter, $\bar{U}_x$ is the axial velocity at the radial location r, $\bar{U}_{x,max}$ is the maximum axial velocity which occurs at the centerline of the pipe and n is a function of the pipe Reynolds number. Nikuradse[118,119] found that n = 6 at $\mathrm{Re}_D = 4 \times 10^3$, n = 7 at $\mathrm{Re}_D = 10^5$, n $= \simeq 9$ at $\mathrm{Re}_D = 10^6$, and n = 10 at $\mathrm{Re}_D = 3 \times 10^6$. Averaging the velocity profile over the pipe cross-section gives:

$$\bar{U}_{x,avg} = \frac{2n^2}{(n+1)(2n+1)}\bar{U}_{x,max} \tag{5.11}$$

where $\bar{U}_{x,avg}$ is the average velocity across the cross section which is calculated from the measured volume flow rate and the calculated cross sectional area of the pipe.

Extensive measurements of the turbulent quantities in fully developed pipe flow were performed by Laufer[91] in 1954 and since then have been repeated and extended by many authors, see for example Lawn.[92] The turbulence intensity in terms of the maximum axial velocity for the three components at the pipe centerline from Laufer's data are given in table 5.2.

While Laufer's data was collected with a much larger pipe diameter than we are using (247 mm versus our 3-17 mm) and at Reynolds numbers approximately two orders of magnitude higher than seen in our tests, if both flow are fully developed, it should give a reasonable estimate for the turbulent fluctuations in the current setup. From these predictions, the maximum value of the

Investigator	$\frac{u'_x}{U_{x,max}}$	$\frac{u'_r}{U_{x,max}}$	$\frac{u'_\varphi}{U_{x,max}}$	Pipe Diameter (mm)
Laufer	0.0283	0.0249	0.0258	247

Table 5.2: Relative turbulence intensity measurements in pipe flows at pipe centerlines

square root of the turbulent kinetic energy, $k^{1/2}$ which will be used in section 5.4.2 to modify the particle Stokes number for the inlet turbulence, is only 4 % of the average inlet velocity. This means that the particle Stokes number changes by a maximum of 7.5 % with the inclusion of the fully developed pipe flow turbulence levels. With this small of a correction to the Stokes number, the errors introduced by using the data of Laufer to predict the turbulence in our Reynolds number range will be negligible.

In his discussion of experimental results for pipe flows, McComb[110] points out that it is not surprising that the axial component u'_x is the largest at all radial locations since only u'^2_x is produced from the direct conversion of kinetic energy of the mean motion while u'^2_r and u'^2_φ are generated by inertial transfer from u'^2_x. Since the production of u'^2_x occurs primarily near the wall where the Reynolds stress and the mean velocity gradients are large, the turbulent energy is both transported in the radial direction and transferred from u'^2_x to u'^2_r and u'^2_φ. Thus the further from the wall, the more homogeneous is the flow (as the transport of energy nears completion) and the more isotropic (as the transfer of energy nears completion). The data of Laufer is used here to predict the centerline values of the radial and circumferential turbulence intensities for our test conditions. Since our pipes are smaller diameter than those on which Laufer's data is based, it is expected that the prediction for u'^2_x will be a slight underestimate while the predictions for u'^2_r and u'^2_φ will be slight overestimates, such that the turbulent kinetic energy calculated from the three components should still be good. The calculation of the velocity fluctuations is then as

Pipe Diameter (mm)	$U_{x,avg}$ (m/s)	$U_{x,max}$ (m/s)	u'_x (m/s)	u'_r (m/s)	u'_φ (m/s)	Turbulent Kinetic Energy (m^2/s^2)
17.1	2.32	2.93	.0851	.0822	.0807	0.00684
14.4	3.28	4.15	.120	.116	.114	0.0136
10.9	5.72	7.23	.210	.203	.199	0.0415
8.13	10.3	13.1	.379	.366	.359	0.135
4.95	27.8	35.2	1.02	.982	.964	0.976
3.18	66.4	83.6	2.42	2.34	2.30	5.55

Table 5.3: Calculated oral cavity inlet conditions at centerline of turbulent pipe flow jets

follows:

$$\begin{aligned} u'_x &= 0.0283U_{x,max} \\ u'_r &= 0.0249U_{x,max} \\ u'_\varphi &= 0.0258U_{x,max} \end{aligned} \tag{5.12}$$

and the turbulent kinetic energy k is given by:

$$k = \frac{1}{3}(u'^2_x + u'^2_r + u'^2_\varphi) \tag{5.13}$$

Based on the above analysis, the mean axial velocity ($U_{x,max}$), turbulent velocity fluctuations (u'_x, u'_r and u'_φ) and turbulent kinetic energy (k) at the centerline of the pipe prior to exiting into the oral cavity were predicted for all the test conditions. The results based on the pipe diameter and the average flow rate across all tests are listed in table 5.3. Centerline values were chosen as a reasonable indicator of the inlet conditions to the oral cavity since the three types of inlets profiles used (top hat jets, turbulent pipe flow jets and the jets with greatly enhanced turbulence due to the turbulence generator) are expected to have quite different radial distributions of mean and fluctuation velocities.

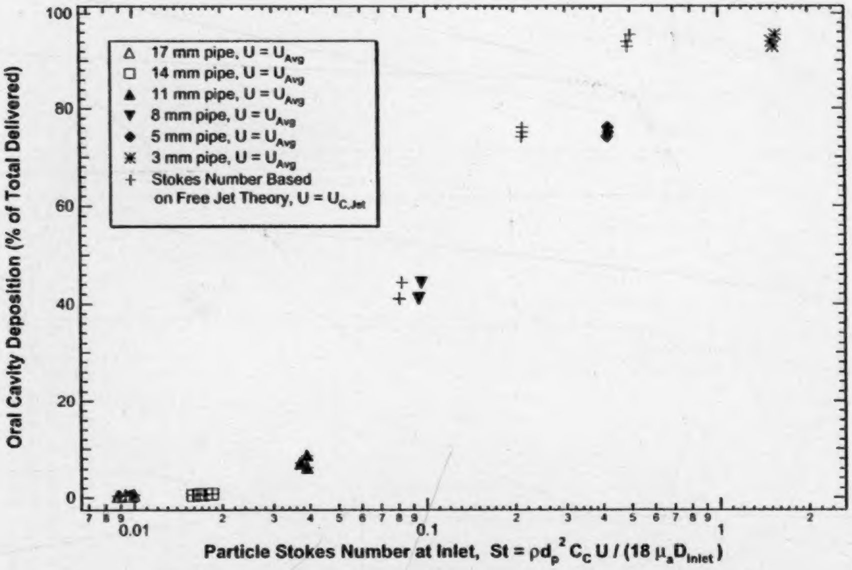

Figure 5.15: Variation of monodisperse aerosol deposition in the oral cavity due to entry from various diameter pipes. Stokes number calculated based on average velocity in pipe or from free jet theory.

5.3.3 Results and Discussion

The deposition in the oral cavity for the six different inlet diameters at a flow rate of 32 L/min and a particle diameter of 5 micrometers is shown in figure 5.15. The deposition increases with decreasing inlet diameter and so shows a monotonic increase with the particle Stokes number calculated based on length and velocity scales at the tube exit or calculated near the impaction site based on predictions from free jet theory as described in section 5.2.2.4.

Again, this demonstrates the dependence of the deposition within the oral cavity on the inlet conditions of the region. The same nominal average flow rate, particle density and particle diameter for all tests gives similar values of the impaction parameter with an average value across the tests of 12166 ± 576 (mean ± standard deviation). Using an empirical deposition model yields a single value for the deposition for each value of the impaction parameter. For the tested range of impaction parameters, the deposition model of Stahlhofen *et al.*[148] gives a range of deposition for the full extrathoracic region to be 22.1% to 25.0% , with oral cavity deposition expected to be negligible. However, these tests show that oral cavity for this parameter value can range from 0.45% ± 0.09% with a 17 mm inlet to 94.1% ± 1.3% with a 3.2 mm inlet. The 17 mm inlet is similar in diameter to those used to collect the data on which Stahlhofen's model is based and the small oral cavity deposition of 0.45% with it supports his assumption of negligible oral cavity deposition. Compared to the predicted average extrathoracic deposition of 23.6%, the oral cavity deposition is less than 2% of the the deposition in the extrathoracic region. However, an oral cavity deposition of up to 94% is clearly no longer negligible and needs to be incorporated into the predictive model for extrathoracic deposition.

The deposition in the oral cavity for the turbulent pipe flow jets is compared to that of the uniform velocity ('top hat') jets from the contraction nozzle tests in figure 5.16 for the tests performed at nominally 32 L/min. It can be seen from the figure that in general the oral cavity deposition is slightly higher for the turbulent pipe flow inlets. Student-T tests with $\alpha = 0.05$ found that the deposition for the turbulent pipe flow entrances was significantly greater than for the contraction nozzle entrances for the 10.9, 8.1 and 3.2 mm inlets. However, compared to the increase in deposition caused by varying the inlet diameter, the effect of small levels of inlet turbulence is relatively minor. The effect of increasing the inlet turbulence levels further is investigated in section 5.4 where a relationship between the deposition and the turbulent kinetic energy per unit mass at the inlet is developed and further discussion of this topic is deferred to there.

Non-linear regression was performed for a large number of function families to determine a functional best fit curve for the data. A functional form similar

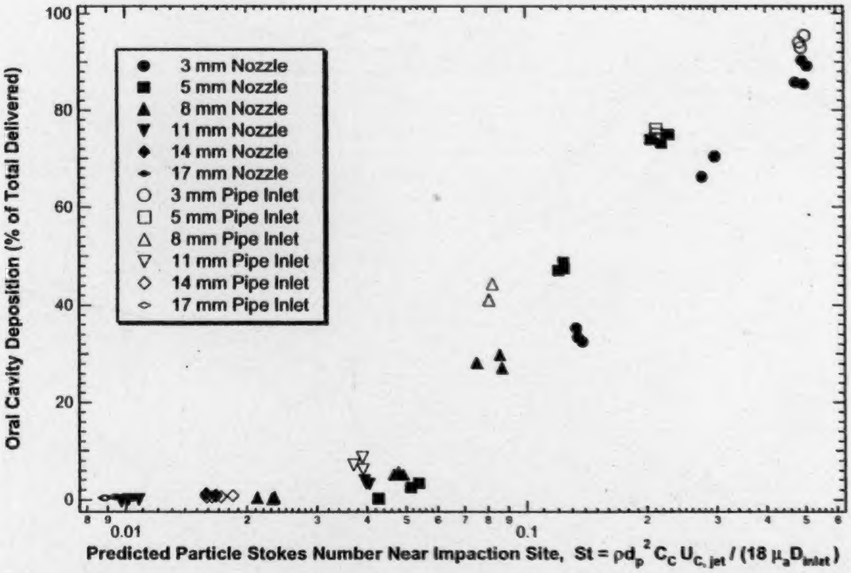

Figure 5.16: Effect of jet type (top hat jet or pipe flow jet) on monodisperse aerosol deposition in the oral cavity. Stokes number calculated based on average velocity in pipe or nozzle exit. Nominal flow rate is 32 L/min for all tests.

to that used by Stahlhofen *et al.*[148] in the extrathoracic region for the impaction parameter was chosen for predicting oral cavity deposition based on the Stokes number. Here the Stokes number is calculated near the impaction location based on free-jet theory as described in section 5.2.2.4. This functional form was chosen both because it gives a good fit for the data ($r^2 = 0.953$) and because it satisfies the limiting conditions of the system which require that the deposition goes to zero as the Stokes number approaches zero and goes to 100% as the Stokes number goes to infinity.

Based on the experimental oral cavity deposition tests of sections 5.2 and 5.3, the following equation was determined for predicting the oral cavity deposition based on the particle Stokes number near the impaction site predicted from the conditions at the exit of the inlets and the free jet theory of section 5.2.2.4:

$$Deposition_{Oral\,Cavity} = 100 - \frac{100}{(45.45St^{1.91} + 1)} \tag{5.14}$$

where $Deposition_{Oral\,Cavity}$ refers to the percentage by mass of the aerosol entering the oral cavity which deposits in the region and the Stokes number, St is calculated from equation 2.25 using the velocity scales from equations 5.7 and 5.8.

The function for predicting oral cavity deposition from contraction nozzle inlets and straight pipe inlets is shown in figure 5.17 along with the data on which it is based. Also shown in the figure are the prediction intervals for 95% confidence.

5.4 Enhanced Inlet Turbulence Levels

In the preceding two sections (5.2 and 5.3) the deposition of aerosol particles in the oral cavity was investigated for inlet conditions of uniform velocity

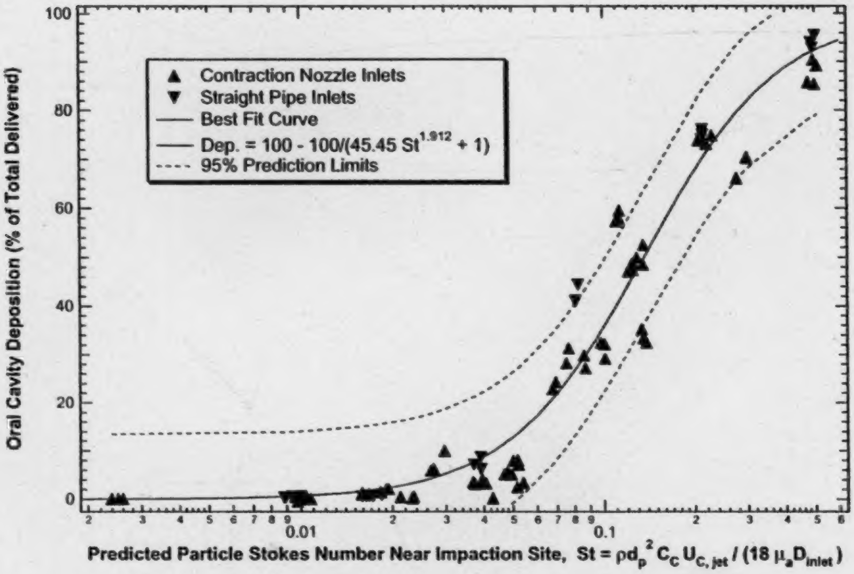

Figure 5.17: Best fit curve of oral cavity deposition data from all contraction nozzle and straight pipe inlets. The Stokes number, *St* is calculated from equation 2.25 using the velocity scales from equations 5.7 and 5.8.

profiles and turbulent pipe flow profiles. However, many dry powder inhalers produce enhanced levels of turbulence in order to deagglomerate the drug containing powder. For example, Voss[157] measured a turbulence velocity u'_x of 1.95 m/s with LDV on the centerline 18 mm downstream of the exit of a Diskhaler® exiting into a 19 mm diameter pyrex tube for a 60 L/min flow rate. As the Diskhaler® has a measured cross sectional area of 133 mm^2, a pipe with the same equivalent diameter and flow rate would have a centerline turbulent velocity of $u'_x = 0.32$ m/s based on the analysis of section 5.3.2. This enhanced turbulence is expected to be due to the presence of a grid located 24 mm upstream of the exit plane and two holes on opposite sides of the mouthpiece causing two high velocity impinging jets 17 mm from the exit plane. Many other dry powder inhalers contain mechanisms which may greatly disturb the fluid velocity levels near the exit of the device such as grids, torturous flow pathways through capsules, swirl generators and impinging jets. The operating principles and methods used for dispersion of powder of a large number of dry powder inhalers are given by Dunbar.[37]

In order to model the deposition of aerosols exiting dry powder inhalers, expansion of the deposition data and prediction model to inlet turbulence levels higher than that seen with simple turbulent pipe flow was required. This section describes a series of tests undertaken using a previously documented turbulence generator[157] to measure the effect of highly elevated inlet turbulence levels on aerosol deposition in the oral cavity.

5.4.1 Experimental Setup

5.4.1.1 Aerosol Deposition Tests

The experimental setup for this series of tests was identical to that of the turbulent pipe flow tests in section 5.3.1 except for the inclusion of the turbulence generator, inserts and related equipment. The full setup is illustrated in figure

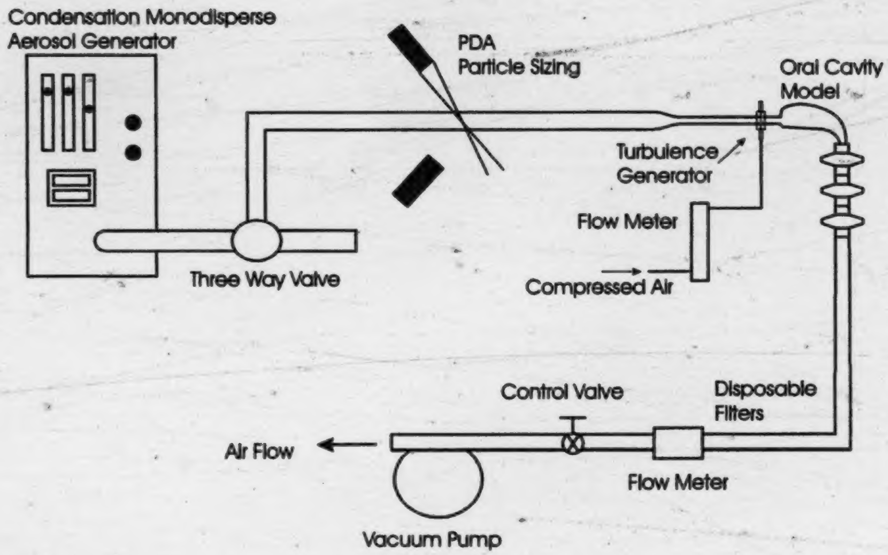
Condensation Monodisperse Aerosol Generator
PDA Particle Sizing
Oral Cavity Model
Turbulence Generator
Flow Meter
Three Way Valve
Compressed Air
Control Valve
Disposable Filters
Air Flow
Flow Meter
Vacuum Pump

Figure 5.18: Experimental setup for monodisperse aerosol deposition tests in the oral cavity with enhanced turbulence pipe flow inlets.

5.18. The monodisperse aerosol is created by the condensation monodisperse aerosol generator (TSI model 3475), particle size is monitored using the phase doppler anemometer (Dantec Dynamics, Skovlunde, Denmark), total flow rate through the system is generated using a vacuum pump and monitored with a pneumotachometer (Series 4719, Hans Rudolf Inc., Kansas City, MO) connected to a data acquisition system.

The main addition to the setup is the turbulence generator described by Voss[157] illustrated in figure 5.19. The generator consists of 4 high speed impinging jets spaced equally around the perimeter of the inlet tube, 37 mm upstream from the entrance into the oral cavity. Filtered compressed air from a wall source was supplied to a rotameter which was used to monitor the flow rate to the jets. A pressure gauge was attached to the discharge of the rotameter to ensure repeatable operation of the system. After leaving the rotameter,

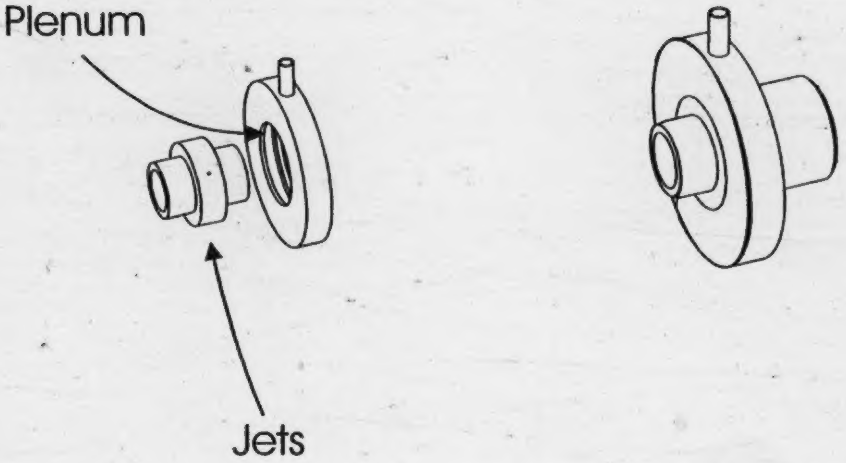

Figure 5.19: Sketch of turbulence generator designed by Voss.[157] The insert contains 4 impinging jets 1.0 mm in diameter.

the compressed air entered an annular plenum from which four tubes separated by 90° led in toward the pipe centerline. The plenum and tube assembly was connected to either a 17.1 mm inner diameter inlet pipe or a 10.9 mm inner diameter inlet pipe. An acrylic sleeve was machined to fit over the outside of the 10.9 mm pipe to connect to the plenum assembly. finally four matching holes of 0.9 mm diameter were drilled through the pipe (pipe and sleeve for the 10.9 mm case) along with a thin groove 1.7 mm by 0.8 mm around the pipe outer perimeter to prevent overpressuring in case of slight misalignment of the plenum assembly.

Oral cavity deposition was determined by gravametric analysis of the sealed oral cavity and the downstream filters before and after each run.

5.4.1.2 Velocity Measurement Tests

Measurements of the mean velocity and turbulent fluctuations in one dimension were performed at the entrance of the oral cavity using Laser Doppler velocimetry. The setup for this part of the tests is shown in figure 5.20. The flow was seeded using 2.5 μm diameter monodisperse particles using the same generator as in section 5.3.1.1, maintaining the volume fraction of particles less than 10^{-6} to prevent the particles presence from affecting the flow field turbulence[29,41] as discussed in section 5.2.1. The measurement volume of the LDA was located along the axis of the entrance pipe, 5 mm into the oral cavity. As illustrated in figure 5.21, an identical copy of the oral cavity geometry was generated using stereolithography with the following modifications: the oral cavity was created as a single piece rather than split into 2 halves along the sagittal plane, a section of the flat lower surface of the oral cavity (the upper surface of the tongue) was removed and replaced with a flat piece of optical glass as illustrated in the figure, and finally the region was painted flat black to decrease reflection of the laser at the wall.

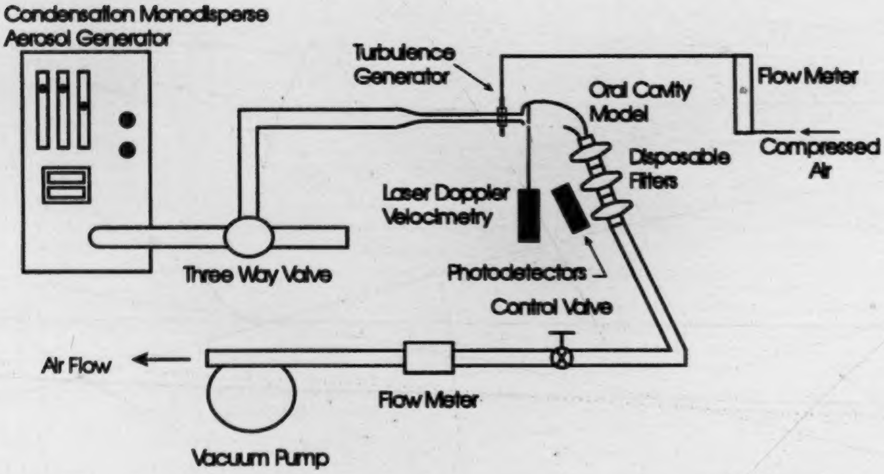
Condensation Monodisperse Aerosol Generator
Turbulence Generator
Flow Meter
Oral Cavity Model
Compressed Air
Disposable Filters
Laser Doppler Velocimetry
Three Way Valve
Photodetectors
Control Valve
Air Flow
Flow Meter
Vacuum Pump

Figure 5.20: Experimental setup for velocity measurements inside the oral cavity model. Two intersecting laser beams lie in the plane indicated by the red line.

The basic technique of laser doppler velocimetry was developed by Yeh and Cummins[167] in 1964 and then expanded to turbulence measurements by Goldstein *et al.*[61] As the technique is quite widely used and well documented, the reader is referred to reviews by Durst *et al.*[38] and Buchhave.[15] The essence of the technique is illustrated in figure 5.22. A continuous laser beam is produced, split into two beams (so that they are in phase with each other) and then the two beams are intersected at small angles (an initial beam separation of 74 mm with a focal length of 310 mm was used in our tests). The measurement volume is formed by the intersection of the two beams. Here, the interference patterns of the beams form a series of bright and dim planes parallel to the bisector of the laser beams and perpendicular to the plane formed by the two beams. The behaviour of particles greater than a few wavelengths of the light can be described using geometric optics and a fringe model of the interference planes. In our tests the laser had a wavelength of 632.8 nm and a Gaussian

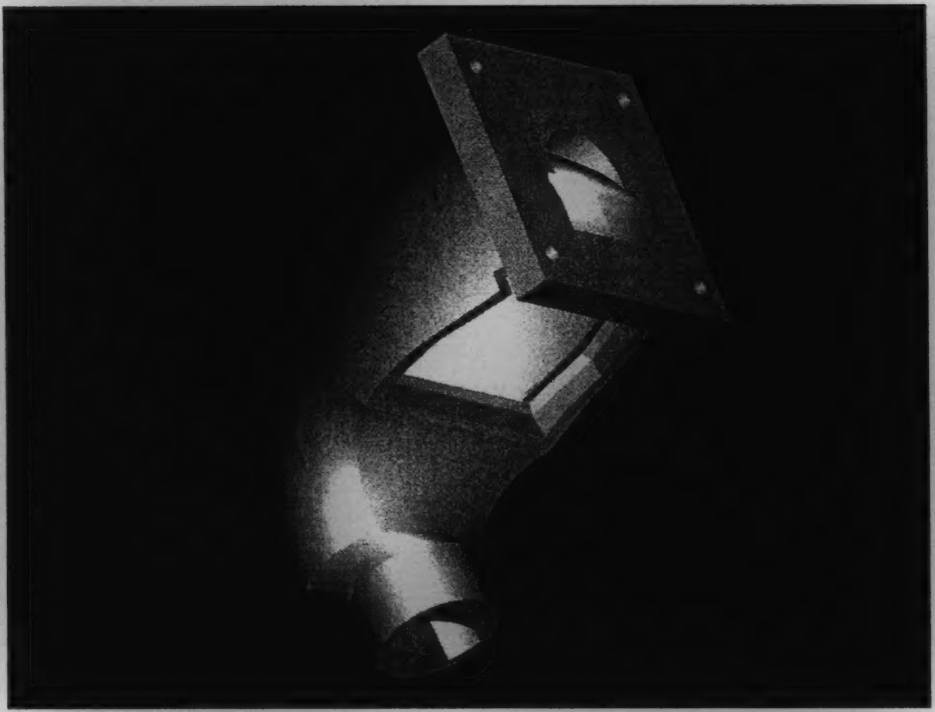

Figure 5.21: Geometry produced by stereo-lithography for velocity measurements inside the oral cavity model.

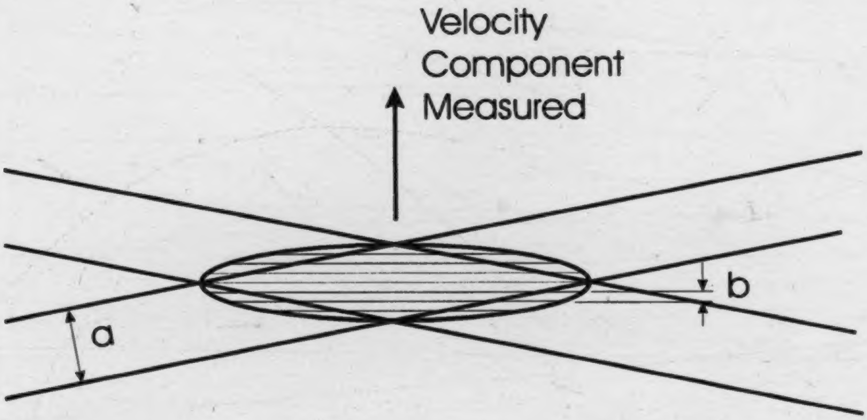

Figure 5.22: Operating principle of the Laser Doppler Anemometer based on geometrical optics. Dimension a is the Gaussian beam diameter while dimension b is the separation between bright interference planes. The ellipse represents the measurement volume (ellipsoid in 3D) formed by the intersection of the two laser beams.

beam diameter of 0.68 mm, giving 75 bright planes spaced 2.67 μm apart in the measurement volume. A photodetector is focused on the measurement volume so that as particles enter, the light they scatter in the direction of the photodetector is recorded. As a particle passes through the bright and dim interference planes, the detector will record a series of flashes. The time between the flashes is proportional to the particle's velocity in the direction perpendicular to the fringes divided by the fringe spacing. In order to remove the ambiguity of which direction the particle is passing through the volume, the frequency of one of the beams is shifted by use of a Bragg cell (in our case by 40 MHz) so that the fringes are moving with a known velocity.

For the velocity measurements, the photodetector was set at 159^o from the forward scatter mode in order to measure light scattering primarily by second order refraction for the DEHS aerosol and to allow both transmitting and receiving optics access through the same planar window.

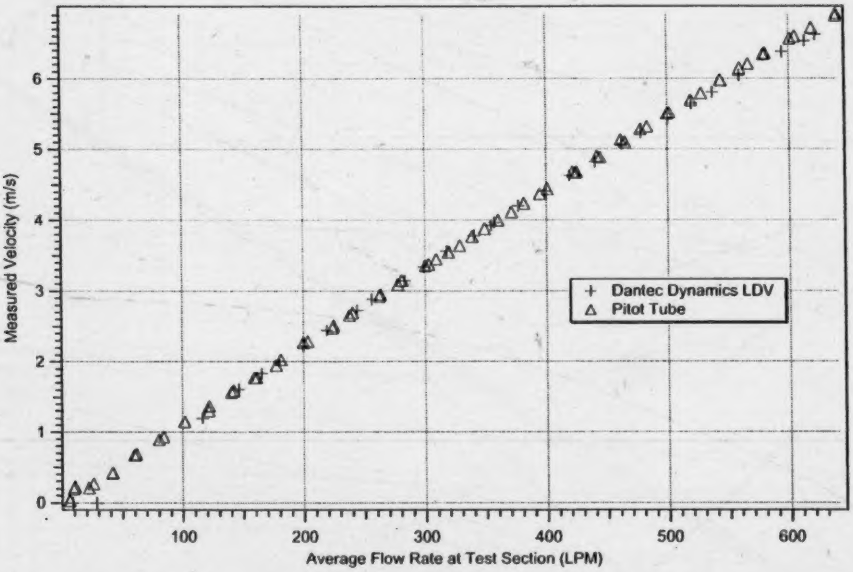

Figure 5.23: Verification of the calibration of the Laser Doppler Anemometer. Comparison to a pitot static tube for centerline velocity measurements in the entrance region of a pipe flow.

The calibration of the LDA was verified by comparing to a pitot static tube in the laminar entrance region of a pyrex tube across the expected range of velocities. The calibration curve is shown in figure 5.23 and agreement was found to be good.

5.4.2 Results and Discussion

5.4.2.1 Velocity and Turbulence Results

The measurements described in section 5.4.1.2 were performed and the resulting centerline mean and turbulent intensities along the pipe axis are presented in table 5.4.

The turbulence intensities present at the inlet of the oral cavity in these tests ranged from 25% to 116%, a large increase from the fully developed pipe flow tests where the predicted centerline turbulence intensity was less than

Inlet Diameter (mm)	Turbulence Generator Level	Total Volume Flow Rate (L/min)	Calculated Avg. Velocity (m/s)	Mean Centerline at Centerline (m/s)± St.Dev.	Turbulence Intensity (%) ± St.Dev.
17.1	High	32.1	2.33	1.50±0.09	115.7±6.2
17.1	High	103.3	7.50	4.00±0.24	45.8±1.9
10.9	High	32.0	5.71	4.04±0.15	44.3±5.1
10.9	Med	32.0	5.71	4.46±0.20	30.7±2.9
10.9	Low	32.2	5.76	4.74±0.10	25.5±1.1

Table 5.4: Centerline mean and turbulence measurements in oral cavity after enhanced turbulence inlets

3%.

5.4.2.2 Aerosol Deposition Results

In general, the results of the deposition tests showed elevated aerosol deposition in the oral cavity for higher turbulence levels at the inlet of the region for a given mouthpiece diameter, aerosol diameter and mean flow rate. The data is plotted in figure 5.24 showing the deposition data for the runs plotted against the particle Stokes number at the pipe outlet based on the average velocity and the pipe diameter. The turbulence generator was run in one of three modes labelled high medium and low in figures 5.24 and 5.25. High refers to 21.5 L/min of clean air entering through the jets, medium refers to 16.1 L/min of air entering through the jets and low refers to 10.7 L/min entering through the jets. The remainder of the total air flow rate drawn through the oral cavity was laden with aerosol particles. The small variation in the Stokes number between runs and between sets of runs is due to the combination of variations in the mean particle diameter, measured flow rate and atmospheric pressure from run to run. This slight variation was neglected in the statistical analysis comparing the different inlet turbulence levels.

In figure 5.25 the highly turbulent inlets are compared to the pipe flow and contraction nozzle inlet tests. All deposition data is plotted against the particle Stokes number based on the free jet theory. As the free jet theory

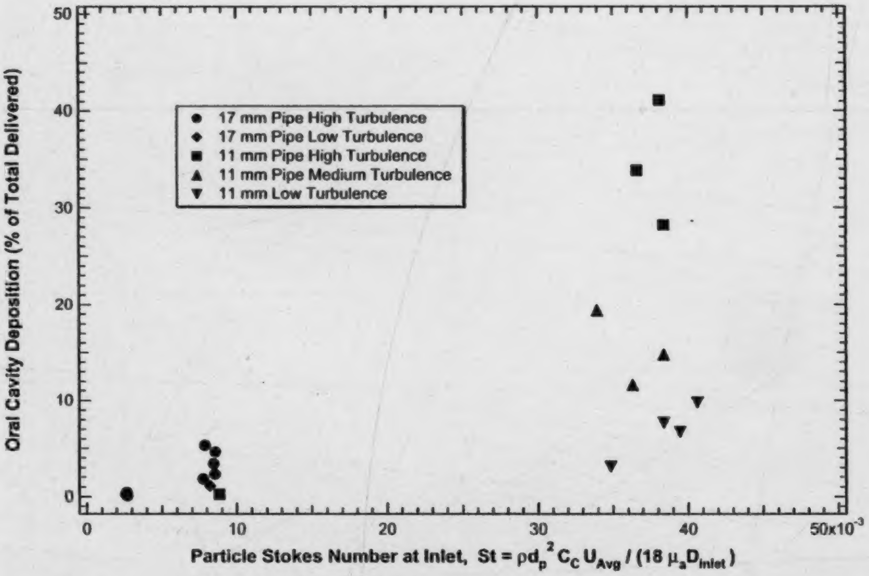

Figure 5.24: Effect of enhanced inlet turbulence levels on monodisperse aerosol deposition in the oral cavity. Stokes number calculated based on average velocity in pipe exit. High, Medium and Low refer to 21.5, 16.1 and 10.7 L/min flow through turbulence generator respectively.

from section 5.2.2.4 only modifies the Stokes number for the inlets 8 mm in diameter and smaller, the Stokes number for the 17 mm and 11 mm inlets plotted is identical to the Stokes number based on the average velocity and diameter at the pipe exit. This is important because the free jet theory assumption that the jet has a potential core is drastically broken by the highly turbulent inlets. Applying the free jet approximations for the deceleration of the centerline velocity without further testing would be questionable. Significant enhancement of the deposition of approximately one order of magnitude is seen between the contraction nozzle test and the highest enhanced turbulence test. For example the 17 mm contraction nozzle at nominally 32 L/min and a 5 micrometer diameter aerosol had an average of 0.41% with the contraction nozzle inlet and an average of 3.43% with the high turbulent setting on the turbulence generator.

Since there are no turbulence parameters in the particle Stokes number based on the average velocity and pipe diameter, the Stokes number alone as formulated is not capable of predicting elevated deposition resulting from higher inlet turbulence levels. Either an additional non-dimensional parameter is required to reflect the turbulence levels, or the Stokes number must be modified to incorporate a turbulence parameter.

In our analysis, the latter option was explored in order to maintain the simplicity of predicting the oral cavity deposition based on only one parameter - a Stokes number. The turbulence was incorporated into the Stokes number by means of the turbulent kinetic energy per unit mass 'k' and the velocity scale of the Stokes number. Since it is again unclear how the presence of the nearby walls will affect the spread of the jet in the oral cavity and whether the enhanced mixing in the core of the jet due to the turbulence throughout will cause a faster spread of the jet into the surroundings or if the lower velocity gradient at the jet boundary with the turbulent case will cause lower shears

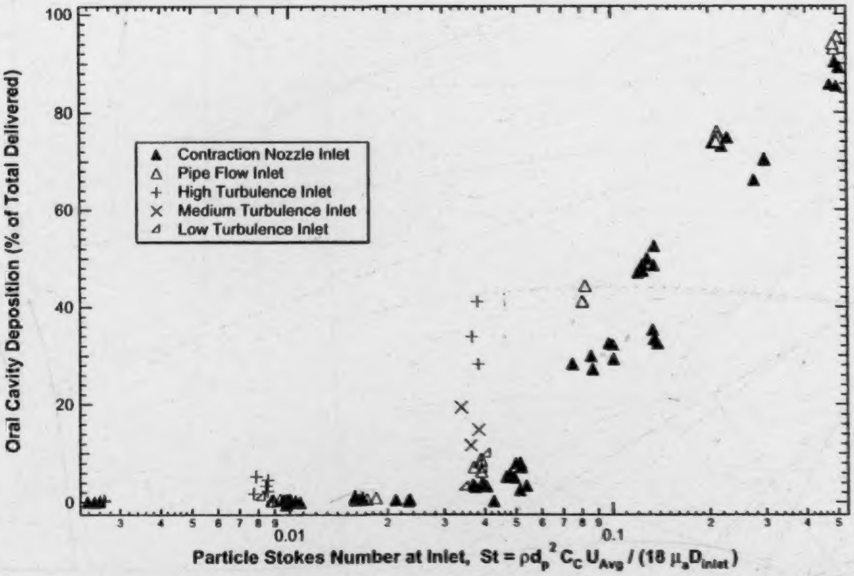

Figure 5.25: Effect of enhanced inlet turbulence levels on monodisperse aerosol deposition in the oral cavity. Comparison to pipe flow and contraction nozzle inlets. Stokes number calculated based on free jet theory. High, Medium and Low refer to 20, 15 and 10 sL/min flow through turbulence generator respectively.

and a slower spread of the jet, as in section 5.2.2.4 it was decided to leave the length scale in the Stokes number fixed and modify only the velocity scale.

Using the procedure devised by Reynolds,[129] the instantaneous velocity at a point can be split into a mean component and a fluctuating component so that:

$$U(\vec{x},t) = \bar{U}(\vec{x},t) + u(\vec{x},t) \tag{5.15}$$

where $\bar{U}$ refers to the mean velocity at the point and u refers to the fluctuation from the mean. The velocity at a point in time and space in a pipe is given by:

$$\begin{aligned} U_x(\vec{x},t) &= \bar{U}_x(\vec{x},t) + u_x(\vec{x},t) \\ U_y(\vec{x},t) &= \bar{U}_y(\vec{x},t) + u_y(\vec{x},t) \\ U_z(\vec{x},t) &= \bar{U}_z(\vec{x},t) + u_z(\vec{x},t) \end{aligned} \tag{5.16}$$

in cartesian coordinates where the subscript x refers to the coordinate along the axis of the pipe and y and z are in the plane of the pipe cross section and the time dependance refers to slow variations compared with the fluctuating components u_x, u_y, and u_z. At the centerline of the inlet pipe for a stationary process this gives:

$$\begin{aligned} U_x &= \bar{U}_x + u_x \\ U_y &= u_y \\ U_z &= u_z \end{aligned} \tag{5.17}$$

since $\bar{U}_y$ and $\bar{U}_z$ are equal to zero as the only mean velocity is directed along the pipe axis. However, there may be random, turbulent fluctuations in all directions.

The kinetic energy per unit mass of the turbulence is then given by:

$$k = \frac{1}{2}(u_x^2 + u_y^2 + u_z^2) \tag{5.18}$$

or equivalently for cylindrical coordinates by:

$$k = \frac{1}{2}(u_x^2 + u_r^2 + u_\varphi^2) \tag{5.19}$$

For the case of the fully developed pipe flow entrances investigated in section 5.3, the values of the turbulent velocities were calculated based on the experimental data of Laufer[91] while for the enhanced turbulent tests of this section, only the root mean square (RMS) value of the axial velocity fluctuation $(u_x^2)^{1/2}$ was measured and isotropy was assumed in order to calculate the other two fluctuating velocity components.

Turbulence is by nature three dimensional even in flows where the mean velocities can be represented as only one or two dimensional in character and all of the fluctuating components u_x, u_y, or u_z can be expected to be nonzero in a turbulent flow. We therefore need a velocity scale related to the turbulence in the flow which captures the three dimensional character of the turbulence to incorporate into the velocity scale of the Stokes number. By this criteria, none of the fluctuating components u_x, u_y, or u_z are appropriate as they only capture the turbulence in a single dimension. Some combination of the three appears to be a logical choice. The commonly used turbulent kinetic energy per unit mass k is such a combination and a connection between the extra energy of the flow due to the turbulence and elevated particle depositions seems logical. However, k is not dimensionally correct to be a velocity scale since it has dimensions of m^2/s^2. If we use instead a velocity scale proportional to the square root of k we get dimensional consistency and dependency on the three dimensional nature of the turbulence so that:

$$U_{turb} \propto \sqrt{k} = a\sqrt{k} \tag{5.20}$$

where a is an unknown constant. If we assume that the velocity scale in the Stokes number is an analytical function of this turbulent velocity scale, then we can represent the Stokes number velocity scale as a power series expansion:

$$V_{Stokes} = f(U_{turb}) = f(a\sqrt{k}) = B_0 + B_1 a\sqrt{k} + B_2(a\sqrt{k})^2 + \ldots \tag{5.21}$$

For the case of the pipe flow jets, the effect of turbulence on the deposition was seen to be only a slight increase in section 5.3 while large effects on the deposition are only seen in figure 5.25 for very high inlet turbulence levels, much higher than expected in commercially available dry powder inhalers. For this reason, truncation of the series after the second term is believed to be reasonable. This gives:

$$V_{Stokes} = f(a\sqrt{k}) \simeq B_0 + B_1 a\sqrt{k} \tag{5.22}$$

The determination of the constant B_0 requires the application of a boundary condition. The relevant condition here is that as the turbulent intensity decreases to zero, we should recover the original Stokes number so that the velocity scale for the Stokes number should go to the value calculated for non-turbulent flows (ie. U_{mean} from section 5.2.2.2). This gives that $B_0 = U_{mean}$ and combining the two coefficients a and B_1 into B yields:

$$V_{Stokes} = U_{mean} + B\sqrt{k} \tag{5.23}$$

where the coefficient was found to have a value of approximately $B = 2$. This value was found to best collapse the turbulence deposition data onto the curve from the contraction nozzle tests.

The data from all oral cavity deposition tests including the contraction nozzle, fully developed pipe flow and enhanced turbulence inlets are plotted in figure 5.26. The turbulence correction from equation 5.23 is applied at the exit plane of the pipe as the flow enters the oral cavity. Therefore it is calculated

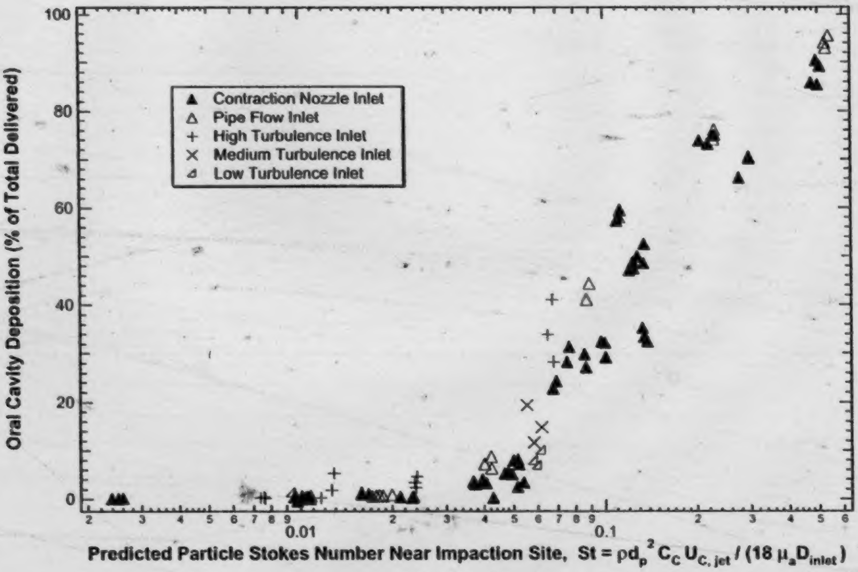

Figure 5.26: Effect of enhanced inlet turbulence levels on monodisperse aerosol deposition in the oral cavity. Comparison to pipe flow and contraction nozzle inlets. Stokes number calculated based on free jet theory modified for inlet turbulence from equations 5.24 and 5.25. High, Medium and Low refer to 21.5, 16.1 and 10.7 L/min flow through turbulence generator respectively.

prior to the application of the free jet theory predictions. The final calculation of the Stokes number is therefore given by:

$$St = \frac{\rho_p d_p^2 C_c}{18 \mu_a D}(U_{avg} + Bk^{1/2}) \tag{5.24}$$

for the cases where the jet is expected to still have a core region near the impaction site (ie. $7D < 60$ mm). For cases beyond this region the Stokes number is calculated as:

$$St = \frac{\rho_p d_p^2 C_c}{18 \mu_a D}(U_{avg} + Bk^{1/2}) A \frac{D}{x + a} \tag{5.25}$$

where the experimental constants have values of $A = 5.9$, $B = 2$ and $a = -0.5D$.

Considering the variety of inlet conditions considered in these tests, the good agreement of the data in figure 5.26 indicates that the theory presented in this chapter adequately describes the major phenomena causing deposition in the oral cavity. Those phenomena being impaction due to the formation of a high velocity jet and enhancement of deposition due to increased kinetic energy for highly turbulent inlets.

As was described in section 5.3.3, non-linear regression was performed to determine a best fit curve for the data. Again a functional form similar to that used by Stahlhofen *et al.*[148] in the extrathoracic region for the impaction parameter was chosen for predicting oral cavity deposition based on the Stokes number. Here the Stokes number is calculated near the impaction location based on free-jet theory as described in section 5.2.2.4 with the inlet turbulence modification described in section 5.4.2. This functional form again gave a good fit for the data ($r^2 = 0.946$) and satisfies the boundary conditions of the system which require that the deposition goes to zero as the Stokes number approaches zero and goes to 100% as the Stokes number goes to infinity.

Based on the experimental oral cavity deposition tests of sections 5.2, 5.3 and 5.4, the following equation was determined for predicting the oral cavity deposition. It is based on the particle Stokes number near the impaction site predicted from the conditions at the exit of the inlets and the free jet theory of section 5.2.2.4 with the turbulence modification of section 5.4.2:

$$Deposition_{Oral\ Cavity} = 100 - \frac{100}{(44.53St^{1.91} + 1)} \tag{5.26}$$

where $Deposition_{Oral\ Cavity}$ refers to the percentage by mass of the aerosol entering the oral cavity which deposits in the region and the Stokes number, St is calculated from equations 5.24 and 5.25.

The plot of equation 5.26 for predicting oral cavity deposition from contraction nozzle inlets, straight pipe inlets and highly tubulent jet inlets is shown in figure 5.27 along with the data on which it is based. Also shown in the figure

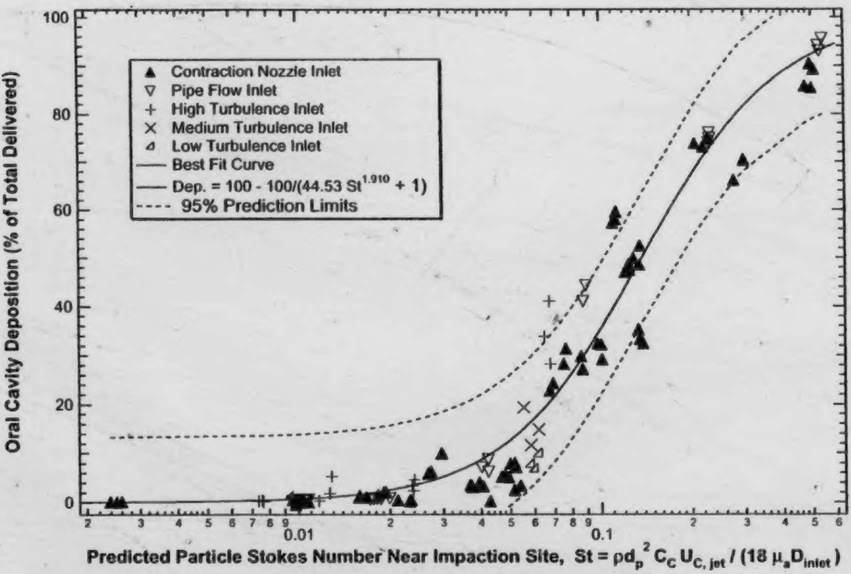

Figure 5.27: Best fit curve of oral cavity deposition data from all contraction nozzle, straight pipe, and enhanced turbulence inlets. The Stokes number, St is calculated from equations 5.24 and 5.25.

are the prediction intervals for 95% confidence.

Chapter 6

Computational Fluid Dynamics in the Oral Cavity

6.1 Introduction

The deposition tests of Chapters 3 and 5 give total deposition of the monodisperse aerosol particles in the tested region, with only qualitative deposition patterns within the region. The radioactive aerosol tests of Chapter 4 give quantitative aerosol deposition patterns, but only as a two dimensional projection onto a plane. It would be beneficial to know the quantitative three dimensional deposition pattern of the aerosol in the extrathoracic region and specifically in the oral cavity to further our understanding of the effect of inlet conditions on the deposition in the regions. Measurements of this 3D deposition pattern are possible with such techniques as PET (Positron Emission Tomography) however, the relatively high cost, long imaging times, low resolution and high radioactivity required made this unfeasible for the present work. Instead, computational fluid dynamics, or CFD, was used as a means to predict the three dimensional deposition pattern of aerosols in the oral cavity for a range of monodisperse aerosols entering through a variety of inlet diameters, similar to the test cases of Chapter 5.

Computational fluid dynamics (CFD) is a popular tool used in many engineering fields. It complements experimental work by providing the ability to vary a large number of parameters individually (eg. inlet mean velocity, inlet turbulence levels, inlet velocity profiles, particle concentration) while eliminating experimental error and fluctuations in control parameters (eg. particle diameter, particle size distribution, ambient air properties, flow rates). CFD refers to the solution of the Navier-Stokes equations (see equation 2.8) by numerical techniques. Typically, the time dependent, transient term is neglected and the steady state solution is sought from CFD. The Navier-Stokes equations are the governing partial differential equations of a single phase Neutonian fluid. By solving the equations numerically on a three dimensional grid, the flow field of a single phase fluid in a complex geometry can be determined. The motion of a second phase such as aerosol particles can then be determined by releasing individual particles at the flow inlet and tracking their motion through the domain by solving the particle momentum equations.

Recently, CFD has become much more accessible as a research and industrial tool due to the development of commercially available CFD packages, user friendly interfaces, robust solvers, inexpensive computers and higher computational speeds. However, CFD is still not mature enough that calculations can be performed without great care to verify and validate the results. A complete discussion of the limitations and issues involved with CFD lies beyond the scope of the present work. The reader is referred to textbooks on CFD such as that of Wilcox[162] for a discussion of the major issues surrounding CFD in general and to Finlay *et al.*[51] for a discussion of the use of CFD in the human respiratory tract.

Some of the major difficulties with CFD stem from the nature of the equations being solved. The Navier-Stokes equations are a three dimensional set of coupled, nonlinear partial differential equations. They contain all the physics for the motion of Neutonian fluids; however, without further simplifying assumptions, they are very difficult to solve. Analytical solutions of the equations are possible only for a very few simple geometries (see for example Panton [121]) and we must quickly resort to numerical techniques. However, with the speed and memory restrictions of today's computers, only the simplest of cases can be solved in reasonable times. It is therefore necessary to model certain aspects of the flow, such as turbulence, in order to make numerical solutions of the Navier-Stokes equations (with simplifying assumptions) possible. Because the equations being solved are non-linear, extrapolation from one geometry to another is very difficult and the solution for one geometry cannot generally be applied to other cases with much certainty.

The purpose of the series of tests described in this chapter is to study the usefulness of CFD for predicting the fluid flow and aerosol deposition in the oral cavity. The two main goals of the section are to test the validity of the velocity and length scales used for calculating the Stokes number based on the free jet theory from section 5.2.2.4 and to obtain quantitative predictions of the three dimensional deposition pattern in the oral cavity for tests similar to those performed in Chapter 5.

A commercially available CFD software package (TASCflow3D, AEA Technology, Waterloo, ON) was used to study the fluid flow and aerosol deposition in an oral cavity geometry described in section 5.1 with 5 different mouthpiece inlet diameters. The software solves the Reynolds averaged Navier-Stokes equations on block-structured, non-orthogonal, body fitted grids with equal order velocity-pressure interpolation.[126]

There are a number of factors which may affect the accuracy of the CFD predictions in the oral cavity. The Reynolds number in the oral cavity is on the order of a few thousand meaning that the flow in the region is probably neither fully laminar, nor fully turbulent, and current turbulence models are known to perform poorly in this case. The expected presence of free shear layers in the oral cavity caused by the turbulent jets formed by the smaller diameter inlets will probably cause a rapid transition to turbulent flow in the downstream region of the oral cavity. This may reduce the effects of expected laminar boundary layers near the mouth transitioning to turbulent boundary layers further downstream. However, since the $k-\varepsilon$ turbulence model, which is used in these tests, is known not to perform well in the presence of recirculating, three-dimensional flows with free shear layers and curved streamlines[51,162] and all of these phenomena are expected to be present in the current tests, the fluid flow solution and especially the turbulence quantities may not be well predicted by the simulation. However, due to budget, computational and time constraints, more advanced techniques which may increase the accuracy of the solution at greater costs such as second-order models which model the correlations in the differential equation for the Reynolds stresses rather than the Reynolds stresses directly, non-linear eddy viscosity models, and large eddy simulation (LES) which resolves the larger eddies and models only the finer eddies were not implemented.

There are a growing number of studies in the literature using computational fluid dynamics to investigate the fluid flow and particle deposition in the respiratory tract but still only a limited number using CFD in the oral airways.

Fluid flow and particle deposition has been studied using CFD in bifurcations corresponding to the 3rd to 5th generation of the Weibel A lung[127] (an idealized lung geometry for predicting airway lengths, diameters and number) by a large number of authors.[4–7,73,74,87,138] Deposition in a human nasal passage has been studied by Sarangapani *et al.*[139] although their results underpredict aerosol deposition for larger particles ($d_p = 5\mu$m) and overpredict deposition for smaller particles ($d_p \leq 1\mu$m).

Yu *et al.* have investigated the fluid flow and particle deposition for ultrafine particles ($d_p \leq 0.01\mu$m) using CFD for a model including the nasal cavity, oral cavity, pharynx, larynx, and the first two generations of the tracheobronchial airways.[171] Their results show reasonable agreement with experimental studies of ultrafine particle deposition. They tested three inlet conditions: nasal breathing only, oral breathing only and nasal and oral breathing. Their oral cavity geometry is based on a person in a relaxed state, breathing slowly with lips open slightly and so their oral cavity has a much smaller opening between the tongue and roof of the mouth than cases based on inhaling through a mouthpiece.

Investigations of the flow in the larynx and trachea have been performed by Katz and Martonen using a commercial CFD software package FIDAP (Fluid Dynamics International, Inc., Evanston IL) which uses a finite element technique for solving the Navier-Stokes equations.[83] In a companion paper, they tracked the motion of massless particles in the flow field[84] and later tracked the deposition of monodisperse aerosol particles (primarily 10 μm diameter but also 0.1 μm diameter).[85] They did not compare their results to experimental work.

Li *et al.* have investigated the oral cavity, pharynx, larynx and trachea using CFD.[94,95] Their analysis focused on determining the flow field, transport properties and particle deaggregation phenomena in the oral cavity rather than only on particle deposition in the region.

Stapleton *et al.* used a commercially available CFD software package (TASCflow3D, Advanced Scientific Computing Ltd., Waterloo ON) to evaluate the flow field and particle deposition within an idealized, realistic adult male extrathoracic model.[150] Their results showed good agreement between the CFD and experimental tests for low flow rates and laminar flow, but the CFD overpredicted the particle deposition for the higher flow rate, turbulent case.

6.2 Calculation of Particle Trajectories

In CFD, particle deposition is often calculated by tracking particles through the flow field. A particle is released into the flow with appropriate inlet conditions and its motion is tracked by solving the particle momentum equation at each step along its path. Once a particle reaches a location of one particle radius from a wall, it is said to have deposited and its location is noted. Releasing a large number of particles into the flow thus allows a statistical description of particle deposition to be obtained.

The particle momentum equation was derived in section 2.3 and for the CFD tests performed, the solved equations took the form of equation 2.18 as:

$$\frac{\pi}{6}d_p^3\rho_p\frac{d\vec{v}}{dt} = \frac{\pi}{6}d_p^3\rho_p\vec{g} + \frac{3\pi}{C_c}\mu_a d_p\vec{v}_{rel}$$

In order to account for the effects of turbulent fluctuations in the fluid velocity field on the particle motion, an eddy interaction model is used. The eddy interaction model is based on the work of Gosman and Ioannides[62] and assumes that it is possible to define a single characteristic eddy for the flow at a given location which has a characteristic fluctuating velocity v'_f, lifetime τ_e and length l_e calculated from the local turbulence properties of the flow.[29] When a particle enters an eddy, the fluctuating component of the fluid velocity (v'_f) is added to the mean component of the fluid velocity at that location to obtain the instantaneous fluid velocity to enter into equation 2.18. The particle remains in the eddy and is exposed to the same fluctuating fluid velocity as long as the particle/eddy interaction time is longer than the eddy lifetime, τ_e and the displacement of the particle within the eddy is smaller than the eddy length scale, l_e. Once these conditions are exceeded, the particle is assumed to enter a different eddy with new characteristics v'_f, τ_e and l_e.

The characteristics of the eddy are obtained from the fluid turbulence quantities by the following formulas:

$$v'_f = \Gamma \left(\frac{2k}{\varepsilon} \right) \tag{6.1}$$

$$l_e = \frac{C_\mu^{3/4} k^{3/4}}{\varepsilon} \tag{6.2}$$

$$\tau_e = \frac{l_\varepsilon}{(2k/3)^{1/2}} \tag{6.3}$$

where k is the local turbulent kinetic energy, ε is the local energy dissipation rate, C_μ is a turbulence constant for the $k - \varepsilon$ model and Γ is a normally distributed random number to account for the randomness of the turbulence.

The particles are tracked through the domain using an explicit Euler technique for a time step of δt,

$$x_i^n = x_i^o + \frac{dx_i^o}{dt} \delta t \tag{6.4}$$

where n refers to the new value, o refers to the old or previous value and $\frac{dx_i}{dt} = v_{p_i}$ is the particle velocity in the ith direction. The particle velocity is calculated using a temporal discretized version of the particle momentum equation (equation 2.18) with the same time step δt.

The time step used for the particle tracking code is independent of the fluid flow solution time step and is limited by three criteria. First, the particle may not travel through a flux element boundary during a time step. Instead the particle will stop at the boundary and begin the next time step on the other side of the boundary. Second, in one time step the particle cannot travel more than 1/5 of the characteristic length of the flux element it is in. And third, the time step cannot be larger than the eddy lifetime and the particle cannot pass out of an eddy during a time step, but will stop at the edge of the eddy and begin the following time step in a new eddy. Time steps continue until the particle either deposits on the wall of the oral cavity or exits the region through the outlet.

Three variations of the particle tracking described above were implemented in our tests. Stapleton *et al.* used a similar procedure to the one described above for a grid based on the complete extrathoracic region tested in Chapter 3.[149,150] They found that the CFD significantly overpredicted the particle deposition in the region. The first method of particle tracking used was the turbulent, eddy-interaction model built into the commercial software as described above. The second method was to track the particles with the eddy interaction model turned off so that the particles were influenced only by the mean fluid velocities and not by the fluid turbulence.

The third particle tracking method has been developed in our lab and involves an eddy-interaction model identical to the one proposed above but with modified values of the turbulent kinetic energy near the walls of the geometry. This particle tracking algorithm is described by Matida *et al.*[107] and is based on the idea that while particle deposition is dominated near the wall by the turbulent fluctuating components in the direction normal to the wall, the primary production of turbulence at the wall is in the direction parallel to the wall. In section 5.3.2 it was noted that for fully developed pipe flow, the axial component of the fluctuations was larger than either the radial or circumferential components across the cross section of the pipe. McComb[110] points out that it is not surprising that the axial fluctuating component is larger than the other two since only the streamwise excitation ($< u_x^2 >$) is produced by the direct conversion of kinetic energy of mean motion. Experimentally, the classic measurements done by Laufer[91] clearly demonstrate that when approaching the wall, the local intensity of the radial and circumferential fluctuations decrease while the local intensity of the axial component increases. For example, in fully developed pipe flow at $y^+ = 20$ (where y^+ is the distance from the wall in the radial direction) Laufer's data gives values for the turbulent intensities as: $u'_r/\bar{U}_x = 0.05$, $u'_\varphi/\bar{U}_x = 0.11$, and $u'_x/\bar{U}_x = 0.21$. Therefore, at $y^+ = 20$ the axial fluctuating component is approximately four times greater in magnitude than the component normal to the wall.

However, despite the majority of the turbulence near the wall being in the axial direction for wall produced turbulence, the original eddy interaction model generates the fluctuations for the turbulent eddy in all three directions based on the same relation, equation 6.1. Therefore it is expected that near the wall, the characteristic eddy generated by the original particle tracking method will have significantly higher radial fluctuations and significantly lower axial fluctuations than are present in the real flow. Because only the radial component of the turbulence near the wall will affect the particle deposition, it is reasonable to expect the particle tracking algorithm to overpredict aerosol particle deposition as was observed by Stapleton *et al.*[149,150]

In order to address this deficiency, Matida proposed using an equivalent turbulent kinetic energy k_{dep} instead of k in the eddy interaction model near the wall for calculating the eddy characteristics. This k_{dep} is calculated so that when it is substituted for k in equation 6.1, the fluctuating velocity components (without the random function Γ) are equal to predicted values of u'_r near the wall. Wang and James[159] introduced modifying functions for calculating the fluctuating components from the turbulent kinetic energy, k approaching the wall as:

$$u'_i = f_i \Gamma \left(\frac{2k}{\varepsilon}\right)^{1/2} \tag{6.5}$$

where f_i is a function of the dimensionless distance from the wall y_+ and the component perpendicular to the wall is:

$$u'_r = f_r \Gamma \left(\frac{2k}{\varepsilon}\right)^{1/2} = [1 - \exp(-0.02 y_+)] \left(\frac{2k}{\varepsilon}\right)^{1/2} \tag{6.6}$$

Although this result is strictly only applicable to fully developed, vertical channel flow where it was derived, it is believed to be a reasonable approximation for other flow geometries, at least better than the assumed isotropy of our earlier model. Using this result then, the value of k_{dep} is calculated as:

$$k_{dep} = \frac{3u_r'^2}{2} = \frac{3}{2}\left[f_r\left(\frac{2k}{3}\right)^{1/2}\right]^2 = f_r^2 k = [1 - \exp(-0.02y_+)]^2 k \tag{6.7}$$

The new values of the eddy fluctuating velocities, eddy length, and eddy life time are found by substituting k_{dep} from equation 6.7 into equations 6.1, 6.2 and 6.3.

6.3 Turbulence Models

When calculating the steady state solution of the Reynolds averaged Navier-Stokes equations, it is necessary to determine whether laminar or turbulent equations should be used. For the 5 inlet diameters used, at a flow rate of 32 L/min which corresponds to the flow rate used in the experimental tests we wish to validate the CFD with from Chapter 5, the Reynolds number of the flow at the inlet varies between 2377 for the 17.1 mm inlet and 12780 for the 3.2 mm inlet. Therefore the Reynolds numbers for all the inlets are higher than the transition to turbulence values of a straight tube of 2300 and turbulence may be expected to be present at the inlet. The flow at the front of the oral cavity is expected to form a jet because of the rapid expansion after the inlet. The presence of the free shear layer at the jet boundary causes instability in the flow and a transition to turbulence at lower Reynolds numbers. Therefore, the assumption of turbulence being present in the oral cavity for all the inlets appears reasonable and the turbulent equations are the proper choice.

Once the presence of turbulence has been established, the choice of a turbulence model is necessary to adequately solve the turbulent equations. TASCflow3D comes equipped with three turbulence models. The first is the standard $k - \varepsilon$ model, the most widely used model in engineering fields which solves two differential transport equations for the turbulent kinetic energy, k and the energy dissipation rate,ε. The second is the $k - \omega$ model which is also a two equation model and solves two differential transport equations but this time for the turbulent kinetic energy, k and the vorticity, ω. The third model is a hybrid of the previous two and solves the standard $k - \varepsilon$ model in the main flow and the $k - \omega$ model near solid boundaries.

For the work presented here, the standard $k - \varepsilon$ model was used for all the tests. The gas flow solution was obtained for one inlet and with one flow rate using the $k - \omega$ model and the particle deposition was calculated for 5 particle diameters with similar results to those obtained with the use of the standard $k - \varepsilon$ model.

It can be shown that when the no slip condition is imposed at the wall and integrated through the viscous sub-layer, two-equation models do not accurately predict the flow velocities near the wall.[162] Instead, the first grid point from the wall should be placed outside of the viscous sublayer ($y_+ > 10$) and an algebraic expression called a wall function is used to calculate the values of k and ε at the first grid point. In this manner, the well known "law of the wall" is forced.

6.4 Geometry and Grid

One base geometry and grid was created for the oral cavity from the computer files used for creating the oral cavity geometry model by stereolithography in Chapter 5. The base grid consisted of 25 blocks with 169,200 grid points. An additional 4 grids were generated by modifying the anterior 5 blocks to incorporate varying diameter inlet regions. The base geometry had an inlet diameter of 8.13 mm while the other grids had inlets of: 3.18 mm, 4.95 mm, 10.9 mm and 17.1 mm. Two additional grids were generated for grid convergence tests which were a coarse, low resolution grid consisting of 84,240 grid points, and a fine, high resolution grid consisting of 336,240 grid points.

The surface grid of the base grid for the 8.13 mm inlet is shown in figure 6.1.

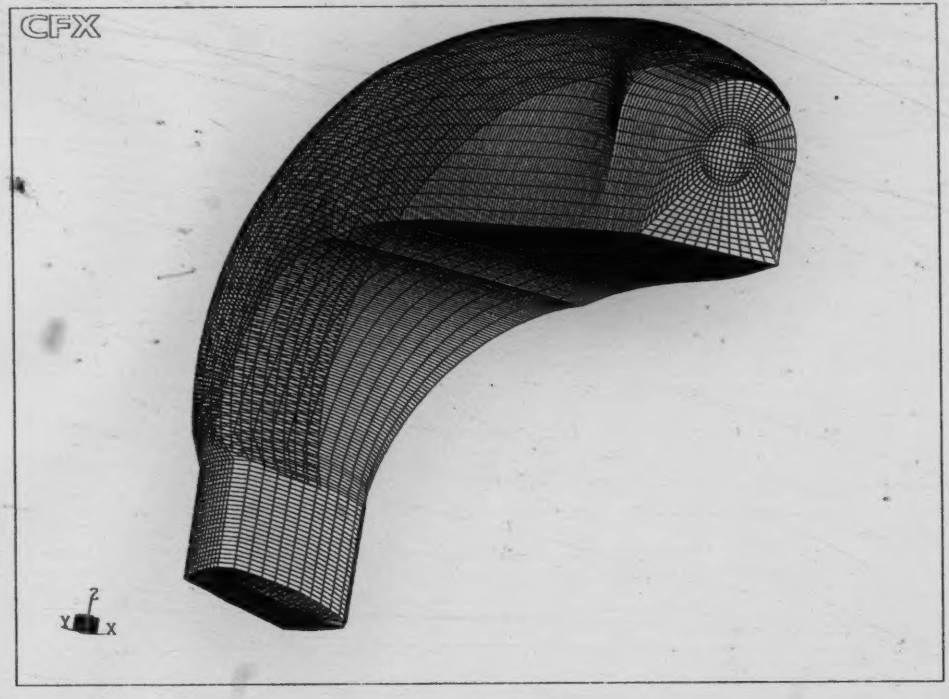

Figure 6.1: View of the surface grid of the base grid for the 8.13 mm inlet.

A cross section through the symmetry plane of the base grid is shown in figure 6.2 with the solution for the 8.13 mm inlet case in that plane superimposed on the grid.

The geometry was slightly modified only in the anterior 8 mm of the region to allow for easier gridding of the region. The side walls were smoothed marginally and the curved region directly posterior to the lower teeth was truncated. Both modifications were expected to have little effect on the particle deposition as no deposition had been observed in these regions during the experimental tests of Chapter 5.

Grid convergence tests were performed to demonstrate that both the fluid flow solution and the particle deposition calculations were independent of the number of grid points. In order to test the convergence of the gas flow solution

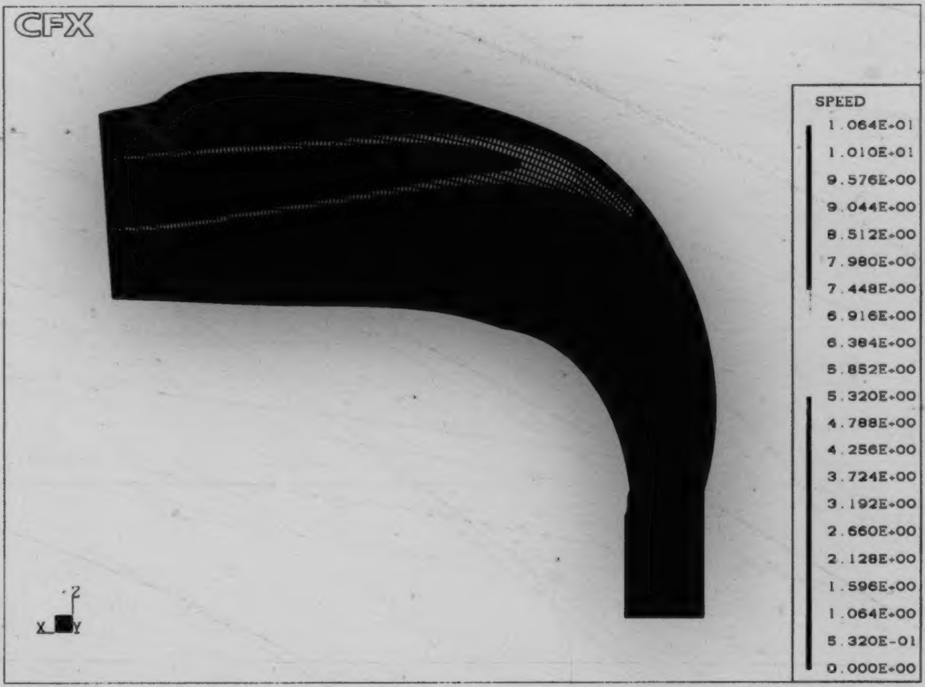

Figure 6.2: Cross sectional view of base grid through the symmetry plane for the 8.13 mm inlet. A fringe plot of the predicted air speed for the case is superimposed over the grid.

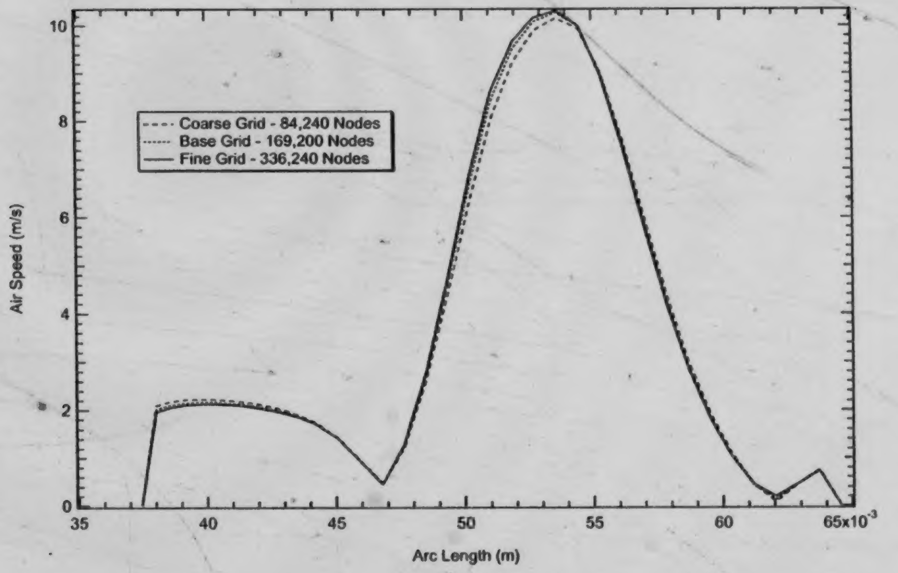

Figure 6.3: Effect on air velocity distribution predictions from CFD with increasing grid refinement. Coarse grid corresponds to 84,240 grid points, base grid corresponds to 169,200 grid points and fine grid corresponds to 336,240 grid points. The arc is a vertical line in the symmetry plane of the region, parallel to the inlet face and 27 mm into the region.

with grid points, the gas speed was plotted along a vertical grid line in the symmetry plane, 27 mm from the plane of the inlet. This grid line was chosen for comparing the three grid densities since it intersected regions of interest in the flow including slow moving flow near the walls, the high velocity gradient free shear layers, and the turbulent jet axis. Figure 6.3 shows the calculated air speed along the grid line for the three grid densities. It can be seen from the figure that negligible improvement in the accuracy of the velocity is obtained with the high resolution grid, demonstrating that the base grid is sufficiently dense for the calculation.

Particle tracking was done using the eddy-interaction model with modified turbulent kinetic energy near the walls described in section 6.2 for the coarse,

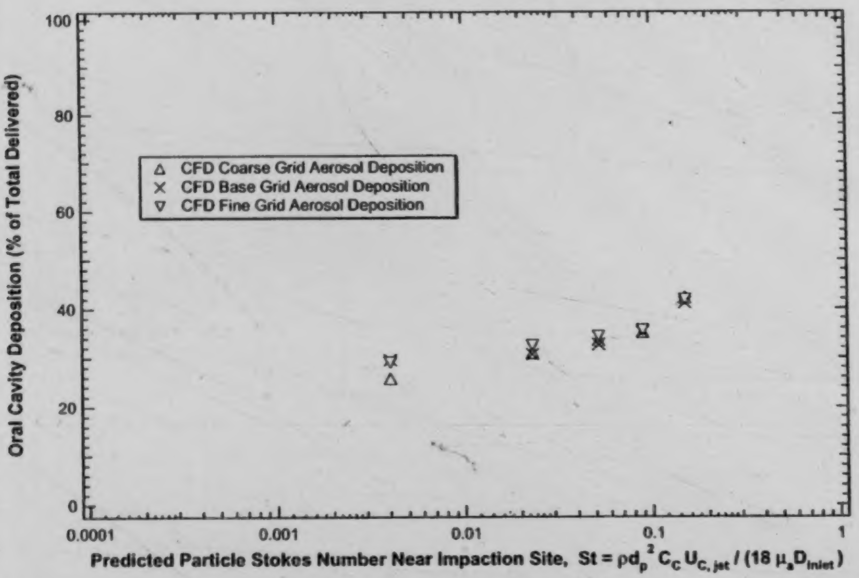

Figure 6.4: Effect on aerosol deposition predictions from CFD with increasing grid refinement. Coarse grid corresponds to 84,240 grid points, base grid corresponds to 169,200 grid points and fine grid corresponds to 336,240 grid points.

base and fine grids using five different particle diameters (1, 2.5, 3.8, 5 and 6.5 micrometers). Figure 6.4 shows the effect on the deposition prediction of increased grid density. From the figure it can be seen that the change in particle deposition with the increased density grid is relatively small. The deposition predicted with the fine grid which had nearly double the number of elements differed from that with the base grid by less than 1% for 3 of the 5 cases and differed by less than 2% for the other two cases. Compared to the expected errors introduced by the use of the $k-\varepsilon$ model for this geometry, the use of wall functions and the approximations of the turbulence modifications in the particle tracking code, the error introduced by the grid resolution is seen to be small.

6.5 Boundary Conditions

The inlet boundary conditions were chosen based on the measured flow rate data from the oral cavity deposition tests in Chapter 5 which these CFD tests were meant to simulate. The inlet velocity profile was set to a plug flow with inlet flow rates of nominally 32 L/min (exact flow rate and velocities for each diameter inlet is listed in table 6.1). The inlet turbulence intensity was set to 0.05 and the eddy length scale was set to 10% of the inlet diameter.

Inlet Diameter (mm)	Volume Flow Rate (L/min)	Inlet Velocity (m/s)
3.18	32.3	67.8
4.95	32.1	27.8
8.13	32.6	10.47
10.9	32.0	5.72
17.1	31.8	2.31

Table 6.1: Inlet boundary conditions for the CFD tests simulating experimental measurements from section 5.3

6.6 Iterative Convergence

Iterative convergence was tested independently for the flow solution and the number of particles released into the flow.

For the solution of the gas flow field, iterative convergence was considered to be achieved when the RMS residuals over the entire flow field were all less than 1×10^{-7}. The number of iterations needed to achieve this level of convergence from a uniform velocity initial condition varied depending on the inlet diameter (with smaller inlets requiring more iterations to achieve iterative convergence) and had a range of 300 to 1000 iterations. For all results given in this chapter, iterative convergence was achieved by ensuring that the dimensionless RMS residuals over the entire flow field were always less than 1×10^{-7}.

TASCflow3D also outputs a report on the overall conservation of mass and momentum equations. A typical sample of the report is shown in table 6.2 for the converged single phase air flow field for the 8.13 mm inlet. The 'Net Flow' reported in the table is a measure of the numerical accuracy of the calculations. The conserved property (for example X-momentum) is calculated for each boundary by summing the property at all the grid points on that boundary. As there are no sources of momentum or mass in the flow field, the total momentum and mass should be conserved so that the summation of all the properties on all the boundaries should equal to zero. The 'Net Flow' is this summation and so is a measure of the numerical errors caused by round-off errors, and inaccuracies from the discretization and the finite differencing scheme. As can be seen in table 6.2 the 'Net Flow' is approximately 4 orders of magnitude less than the property for the X-momentum, Z-momentum and mass. From the mass and momentum flow summaries and the iterative convergence data, the flow solutions were determined to be converged.

Boundary or source	X-momentum	Y-momentum	Z-momentum	Mass
B.C. # 1, WALL	6.112E-03	-2.186E-07	-2.532E-03	0.000E+00
B.C. # 2, INFLOW	-6.090E-03	-7.857E-09	4.253E-04	5.871E-04
B.C. # 3, OUTFLOW	-2.226E-05	2.085E-07	2.107E-03	-5.871E-04
Particle sources	0.000E+00	0.000E+00	0.000E+00	0.000E+00
Net Flow	2.923E-09	-1.796E-08	2.026E-08	2.910E-10

Table 6.2: Mass and momentum balances for CFD tests simulating experimental measurements from section 5.3

The convergence of the particle deposition data was also checked to ensure that a sufficient number of particles were released and tracked. For the deposition tests using the TASCflow3D particle tracking algorithms, 10,000 particles were released for each test. However, the modified particle tracking algorithm required significantly longer time periods to track each particle, limiting the number of particles that could be analyzed. A typical plot of the convergence of particle deposition data is given in figure 6.5. Based on these plots, a min-

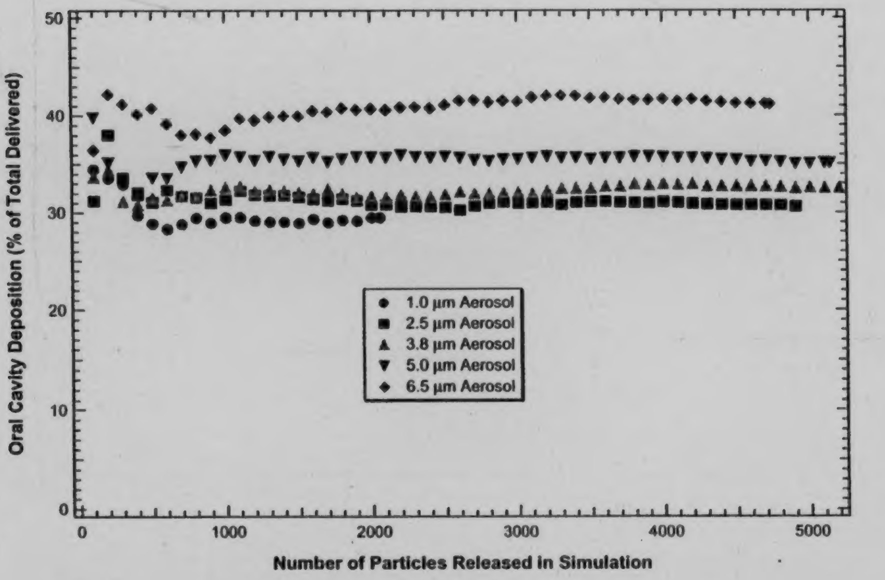

Figure 6.5: Aerosol deposition predictions from CFD with increasing number of particles tracked. The case plotted is the 8.13 mm inlet with the base grid resolution and five different aerosol diameters.

imum number of particles tracked was set at 1500 although typically 5000 particles were tracked except for the 1 and 2.5 micrometer aerosol cases with large diameter inlets.

6.7 Results

6.7.1 Fluid Flow Fields

Once the converged solution for the fluid flow was obtained from the CFD, a wealth of information about the air flow field becomes available. Not only are the distributions of the mean quantities such as velocity, static pressure and total pressure, but also the spatial distributions of the turbulence quantities such as the turbulent kinetic energy, the dissipation rate and the turbulent viscosity are accessible.

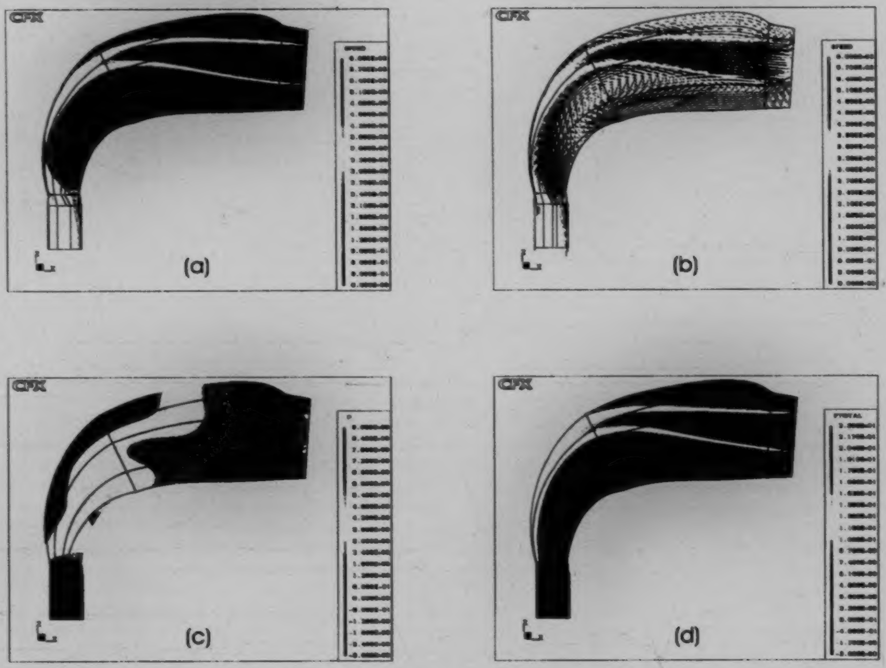

Figure 6.6: Mean flow parameters for 10.9 mm inlet along central, symmetry plane. (a) Air Speed in m/s, (b) Velocity vector plot in m/s, (c) Static pressure in Pa, (d) Total pressure in Pa

In Figure 6.6, the flow field parameters of the 10.9 mm inlet case are examined. The values of the various parameters on the central symmetry plane are plotted using coloured fringe plots to show the distribution of the parameter in the plane. Clearly the three dimensional nature of the distributions of the parameters will not be captured with this view alone. However, the number of views and figures required to show the three dimensional fields of all the parameters for all five of the inlets is prohibitively large. Therefore, for one inlet (the 10.9 mm inlet) the distributions of a large number of relevant parameters will be illustrated along the central plane and the air speed will be considered with multiple views to illustrate the three dimensional field and with the rest of the inlets, only the velocity and speed of the air will be illustrated.

In part a of Figure 6.6, the air speed along the central plane of the oral cavity can be seen. The jet issuing from the inlet is initially uniform with a speed of 5.716 m/s, but immediately begins to gradually decelerate and enlarge in diameter. The structure of a jet flow is clear through most of the oral cavity. The jet lifts slightly towards the roof of the mouth and then appears to impinge and attach to the upper surface of the oral cavity approximately 60 mm from the inlet plane. It then follows the curve of the region along the back wall, still not fully mixed with the rest of the flow as it exits the oral cavity through the outlet.

In part b, a vector plot of the fluid velocity components tangential to the central plane are shown. It was observed that the plot of the total velocity vectors was nearly identical to that shown here. This was expected since the illustrated central plane is a symmetry plane for the region. In addition to the information obtained from part a, the vector plot gives the direction of the fluid velocity at each grid point. For clarity, only every fifth grid point is shown in the figure. One of the major advantages of this plot is its ability to illustrate structures in the flow field. A small recirculation zone can be seen to exist at the front of the oral cavity near the roof of the mouth. A much larger recirculation zone centered above the base of the tongue is also observed and flow can be seen to be flowing back towards the inlet along the upper surface of the tongue and then curve upwards, becoming entrained in the jet. A stagnation point in the flow is observed down and to the left of the large recirculating eddy near the base of the tongue where flow to one side moves back towards the inlet along the bottom surface of the region and flow on the other side of the stagnation point flow towards the exit of the region at the outlet.

In part c the static (or thermodynamic) pressure distribution in the oral cavity is shown. Comparing parts a and c, it can be seen that the highest static pressure point occurs at the location where the jet impinges on the upper, rear wall of the oral cavity. This can be understood when part d, the total pressure distribution is considered. From the fluid momentum equation (equation 2.10) it can be seen that the air momentum is affected by both gradients in static pressure and velocity. For incompressible flow (ie. Mach ≤ 0.3 which is true for our tests), the total pressure is equal to the static pressure plus the dynamic pressure, where the dynamic pressure is the increase in static pressure which would occur if the air was decelerated to a stop given by Fox as:[54]

$$P_{total} = P_{static} + \frac{1}{2}\rho V^2 \tag{6.8}$$

where V is the magnitude of the air velocity (ie. air speed). The increase in static pressure at the impingement site corresponds to a decrease in the dynamic pressure as the air is decelerated so that the total pressure plot of part d of figure 6.6 shows little effect in the region.

Along the bottom surface of the oral cavity, a local static pressure maximum is visible in part c. This location corresponds to the stagnation point observed in part b. An adverse pressure gradient is seen to exist across the height of region which decelerates the air. At the bottom of the oral cavity, air entering the region has low velocities and the pressure gradient is sufficiently strong to reverse the flow of the air and for the 11 mm inlet air is seen to flow back towards the inlet along the tongue surface. On the other side of the pressure maximum, the pressure gradient exerts a force on the air accelerating it towards the outlet of the region.

Characteristics of the turbulence in the flow field are also generated as part of the solution to the CFD problem and are displayed in figure 6.7. In part a, the distribution of the turbulent kinetic energy (k) is illustrated. The core of the jet is seen to be nearly free of turbulent energy (a 5% turbulent intensity was specified across the inlet) while the turbulent energy is rapidly produced

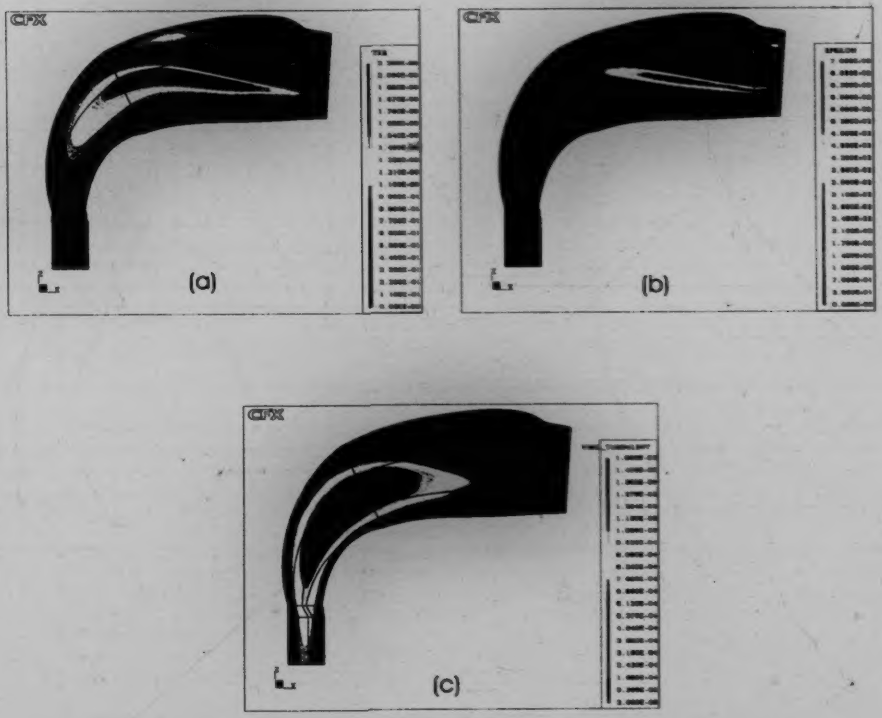

Figure 6.7: Flow turbulence parameters for 10.9 mm inlet along central, symmetry plane. (a) Turbulent Kinetic Energy in m^2/s, (b) Dissipation Rate in m^2/s, (c) Turbulent Viscosity in m^2/s

by the free shear layer between the high speed jet and the low speed flow in the rest of the oral cavity. The maximum turbulent kinetic energy in the flow field occurs in the region where the recirculation bubble intersects with the high speed jet, pushing it up towards the wall. The interface between these two large scale structures causes significant production of turbulent kinetic energy.

The dissipation rate ε is also calculated at every grid point during the solution of the equations. The distribution of the energy dissipation rate looks similar to that of the turbulent kinetic energy, with high dissipation in the shear layer of the jet. In 1935, Taylor showed that for isotropic turbulence, (and because dissipation occurs at very small scales, isotropy is a good assumption for nearly all flows) the dissipation rate ε is proportional to the square of the gradient of the turbulent fluctuating velocities. Since this gradient is the largest in areas of high turbulence, high dissipation rates in these areas are also expected. The distribution will not be identical however, since turbulent energy is produced by large scale motion and the majority of the energy is contained in reasonably large eddies while dissipation occurs at very small scales and it takes time for the energy produced to cascade down to the small scales and be dissipated. During this time, the fluid is in motion so that the turbulent energy produced at one location will be dissipated at a different location which may or may not be close by depending on the mean fluid motion.

The turbulent viscosity ν_{turb} is calculated from the values for k and ε at each grid location. The plot of the turbulent viscosity is shown in part c of figure 6.7. The concept of a viscosity due to turbulence is based on the idea that turbulence will be diffused in the fluid in a way similar to that of molecular diffusion. For molecular diffusion, the important parameter is the gas kinematic viscosity ν and so an analogous viscosity based on the length and time scales of the flow is introduced in order to model the Reynolds stresses in the Reynolds averaged Navier-Stokes equations. This viscosity varies and needs to be calculated at all locations in the flow.

The speed and velocity vector plots on the symmetry plane and the plots of the speed along a number of planes perpendicular to the symmetry plane for all 5 of the inlets considered are shown in figures 6.8 to 6.12.

The velocity field for the 3.18 mm inlet is shown in figure 6.8. A very high speed jet (67.78 m/s at the inlet) is seen to impinge on the upper, rear surface of the oral cavity. Notice that the colour scaling is different from figure 6.6, the maximum velocity in figure 6.8 being $>$ 10 times higher. From parts c and d, it can be seen that the jet increases in diameter somewhat, spreading

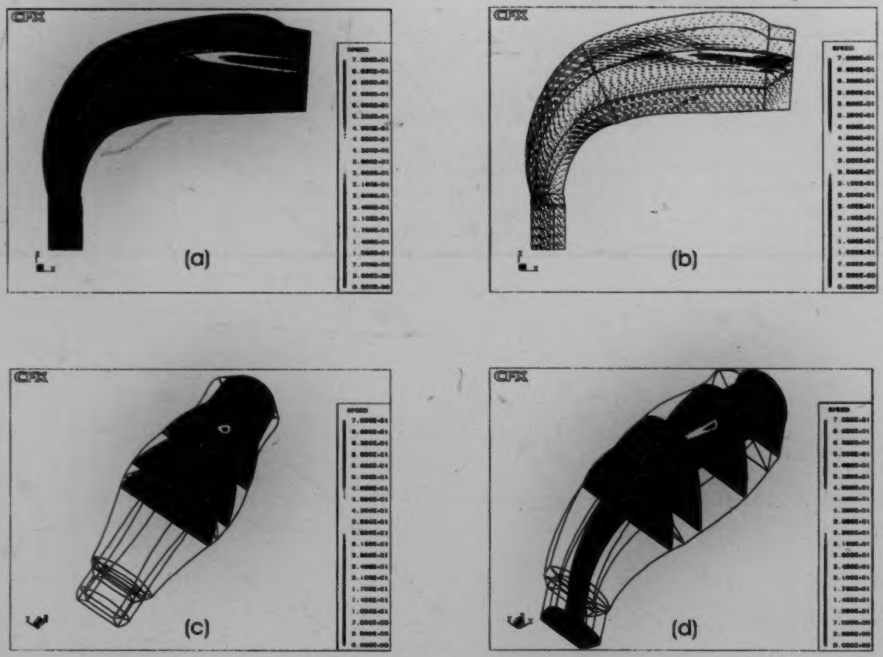

Figure 6.8: Plots of air velocity and speed in oral cavity for 3.18 mm inlet. (a) Air Speed in m/s along symmetry plane, (b) Velocity vector plot in m/s along symmetry plane, (c) Air speed in m/s in planes parallel to inlet plane 0.2, 20, 40, and 50 mm from the inlet, (d) Air speed in m/s for planes from (c), symmetry plane and outlet plane

more in width than in height. The centerline velocity of the jet decreases significantly prior to impinging on the wall. The centerline speed of the jet in a plane 60 mm from the inlet was found to be 16.6 m/s. This is lower than the velocity scale used in the particle Stokes number from in section 5.2.2.4 estimated from free jet theory which was 21.3 m/s. Taking the diameter of the jet to be the height between the points where the jet velocity falls below 50% of its maximum value, then at this same plane, the jet diameter has increased from 3.18 mm to 7.9 mm. It should be noted however, that the steady state solution of the Reynolds averaged Navier-Stokes equations does not show the intermittency so often present in real turbulent flows (especially jet flows). The real jet may be a narrower, higher velocity jet that oscillates around in space and so the CFD diameter predictions should be taken to be a maximum diameter for the jet. As discussed in section 6.7.3.1, the Reynolds averaged equations can be expected to predict a broader jet which decelerates faster than occurs in reality due in part to the introduction of the turbulent viscosity. In this way, the CFD can be seen as giving a lower bound for the fluid velocities near the impaction site. Throughout this section, the CFD is seen to consistently underpredict the maximum speed of the jet relative to the predictions of the free jet theory of section 5.2.2.4.

The flow field for the 4.95 mm inlet is shown in figure 6.9. The jet at the inlet has a velocity of 27.80 m/s. Similar to the 3.18 mm inlet, the velocity is decelerated prior to the flow reaching the wall. At a location 60 mm from the inlet plane, the centerline speed of the jet was found to be 10.1 m/s. The predictions that were used based on free jet theory gave 14.1 m/s as the velocity scale near the impaction site which is again higher than predicted by the CFD here. The measured length scale of the jet based on the 50% heights previously defined is 8.0 mm which implies an increase of 62% from the inlet of the oral cavity. It can be observed from parts c and d of the figure that

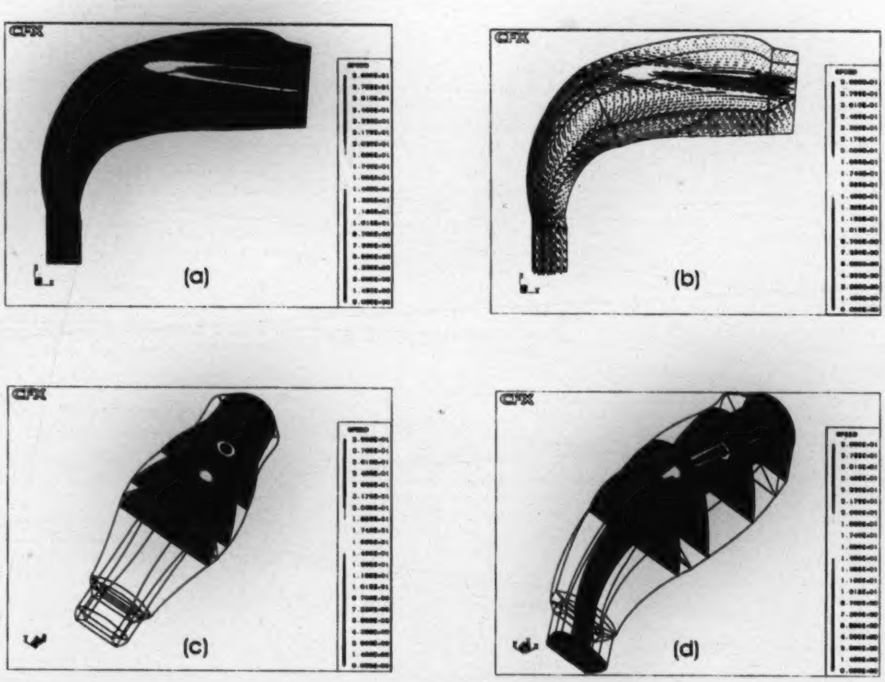

Figure 6.9: Plots of air velocity and speed in oral cavity for 4.95 mm inlet. (a) Air Speed in m/s along symmetry plane, (b) Velocity vector plot in m/s along symmetry plane, (c) Air speed in m/s in planes parallel to inlet plane 0.2, 20, 40, and 50 mm from the inlet, (d) Air speed in m/s for planes from (c), symmetry plane and outlet plane

the jet is expanding more in width than in height, so this diameter is likely an underestimate of the jet diameter. The recirculation zone near the base of the tongue, though slightly smaller than the one for the 3.18 mm inlet, is still quite large and caused reversed flow throughout the bottom, front of the oral cavity.

The cases of the 8.13 mm and the 10.9 mm inlets are shown in figures 6.10 and 6.11. Both are similar in structure to the flow fields for the two smaller diameter inlets already discussed. They all show the jet to be reasonably well defined throughout the front part of the oral cavity and to turn slightly upwards towards the upper, rear surface of the oral cavity (due to the influence

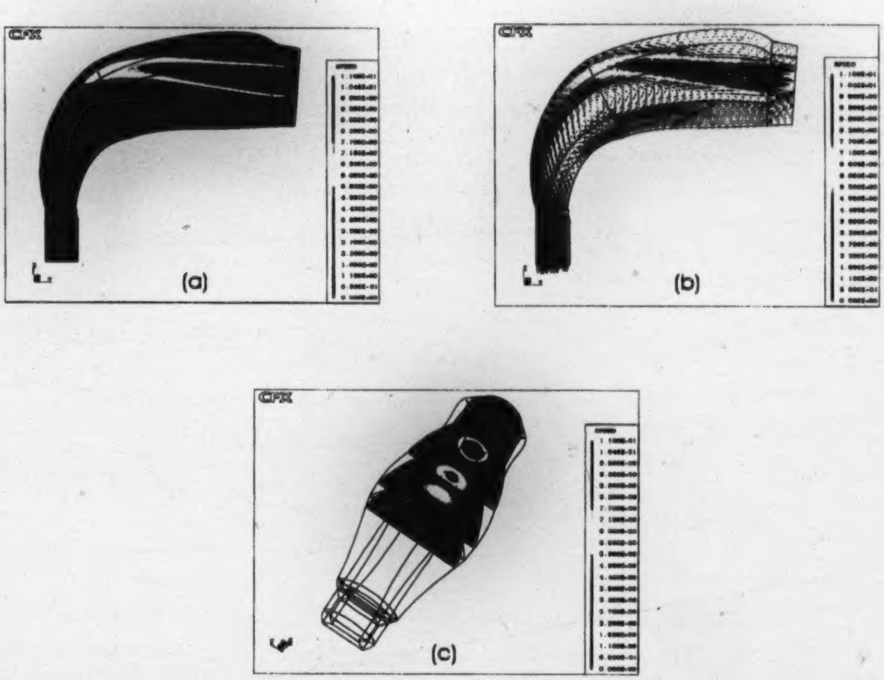

Figure 6.10: Plots of air velocity and speed in oral cavity for 8.13 mm inlet. (a) Air Speed in m/s along symmetry plane, (b) Velocity vector plot in m/s along symmetry plane, (c) Air speed in m/s in planes parallel to inlet plane 0.2, 20, 40, and 50 mm from the inlet, (d) Air speed in m/s for planes from (c), symmetry plane and outlet plane

of the recirculation region) where they impinge on the surface. The jet then appears to follow the curvature of the wall, remaining a defined region of high velocity air right until it exits the region through the outlet. The jet never appears to fully mix with the remainder of the flow in the region tested.

For the 8.13 mm inlet seen in figure 6.10, the maximum velocity of the jet at a location 60 mm from the inlet plane was found to be 5.42 m/s. The predicted value of the velocity near the impaction site based on the free jet theory proposed in section 5.2.2.4 was 8.86 m/s, a difference of 39%. The measured jet diameter from the CFD was 9.5 mm, an increase of 17% from the initial diameter.

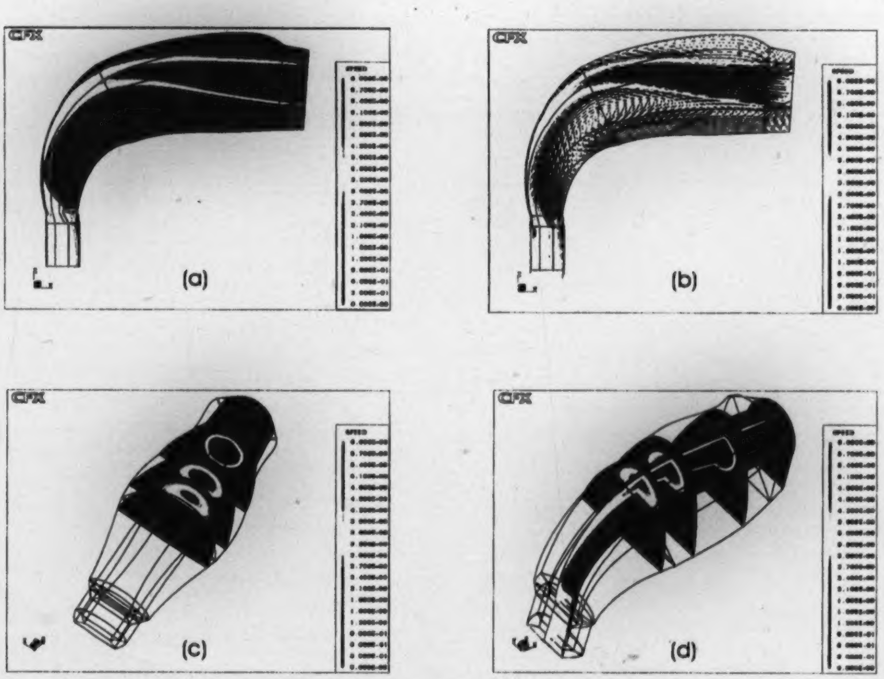

Figure 6.11: Plots of air velocity and speed in oral cavity for 10.9 mm inlet. (a) Air Speed in m/s along symmetry plane, (b) Velocity vector plot in m/s along symmetry plane, (c) Air speed in m/s in planes parallel to inlet plane 0.2, 20, 40, and 50 mm from the inlet, (d) Air speed in m/s for planes from (c), symmetry plane and outlet plane

For the 10.9 mm inlet seen in figure 6.11, the maximum velocity of the jet at a location 60 mm from the inlet plane was found to be 3.61 m/s. The predicted value of the velocity near the impaction site based on the free jet theory proposed in section 5.2.2.4 was 5.72 m/s, a difference of 37%. The measured jet length scale from the CFD was 10.9 mm which is identical to the inlet diameter.

With the 17.1 mm inlet, the flow field appears different. From part b of figure 6.12, the recirculation region is no longer visible. A stagnation point in the flow is still present, however it is closer to the inlet than for the other cases. Part d of the figure shows that the maximum velocity in the oral cavity

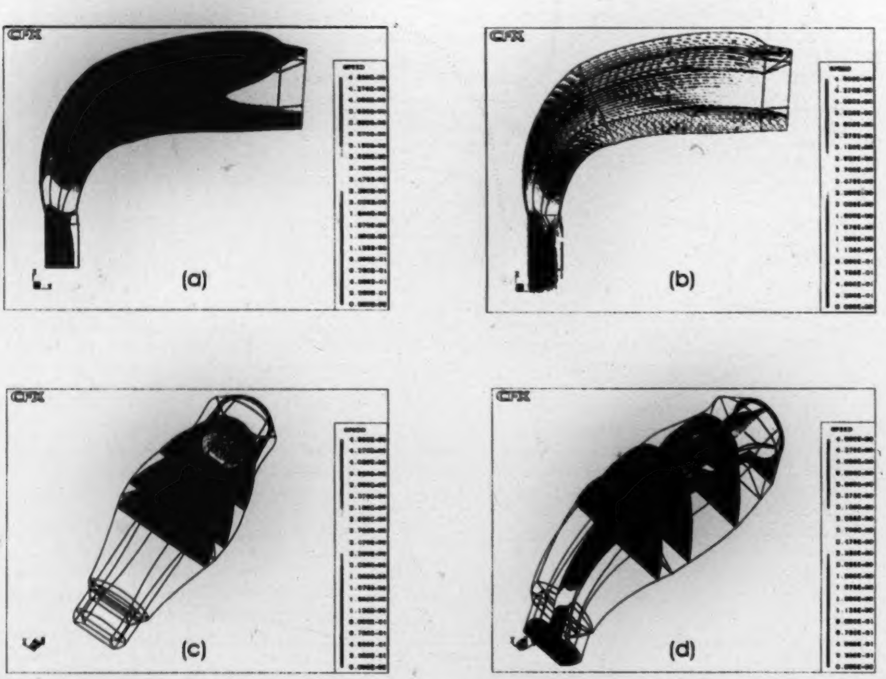

Figure 6.12: Plots of air velocity and speed in oral cavity for 17.1 mm inlet. (a) Air Speed in m/s along symmetry plane, (b) Velocity vector plot in m/s along symmetry plane, (c) Air speed in m/s in planes parallel to inlet plane 0.2, 20, 40, and 50 mm from the inlet, (d) Air speed in m/s for planes from (c), symmetry plane and outlet plane

is no longer in the entrance jet, but is now in the exit region where the cross sectional area decreases.

The final plots of the fluid flow in figure 6.13 show the air speed in the symmetry plane for all 5 of the inlets. All are plotted using the same colour scale to highlight the large differences in jet velocities between the cases studied. Since all five cases correspond to the same nominal flow rate of 32 L/min, the pronounced effects of the inlet diameter on the local velocities in the oral cavity are clearly visible. These effects are seen to penetrate deeply into the region for all but the largest inlet diameter.

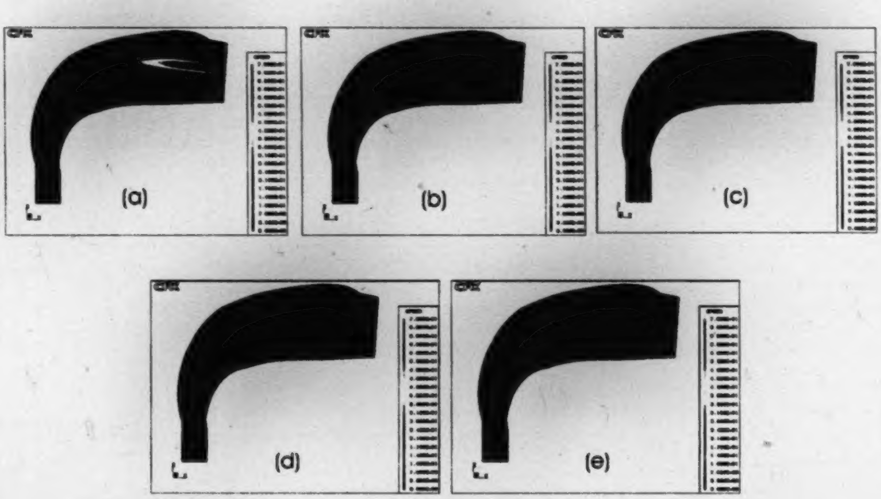

Figure 6.13: Plots of air speed in oral cavity for the five different inlet diameters. The air speed in the symmetry plane is plotted for all inlets with the same colour scale ranging from 0 m/s to 70 m/s. (a) 3.18 mm inlet (b) 4.95 mm inlet (c) 8.13 mm inlet (d) 10.9 mm inlet and (e) 17.1 mm inlet

6.7.2 LDA Comparison

Measurements of the mean velocities were made inside the oral cavity using laser Doppler anemometry in a second order refraction mode. The experimental setup for these tests is described in section 5.4.1.2.

The velocity was measured along the axis of the inlet nozzle, a distance of 5 mm from the plane of the inlet. With the 10.9 mm inlet, the CFD predicted a centerline velocity of 5.774 m/s at this location. The values of the centerline velocity measured with the LDA are illustrated in figure 6.14. The average of the series of 5 measurements was 5.892 m/s with a standard deviation of 0.013 m/s. The difference between the measured and predicted velocity at this point is then 2.0%, which is within the error of the flow meter for controlling the flow rate at the 32 L/min used for these tests.

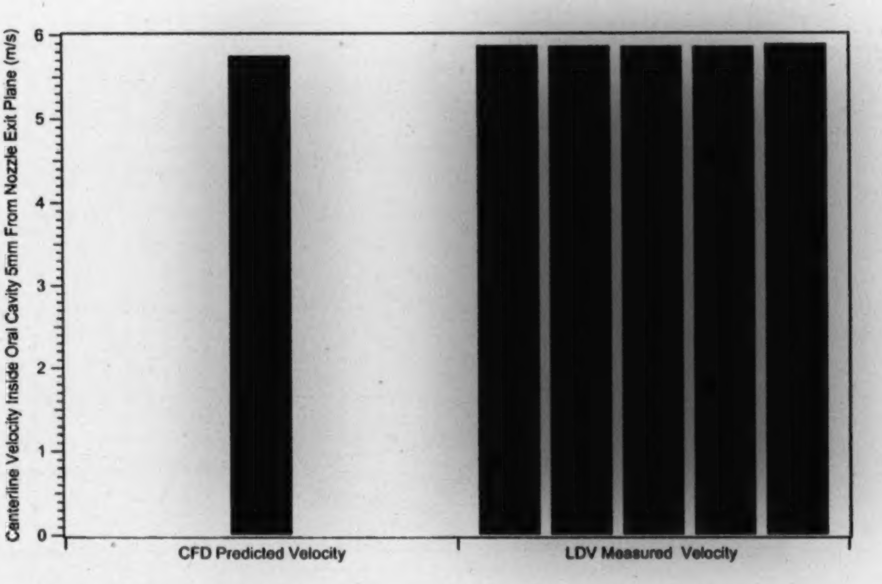

Figure 6.14: Air velocity in the oral cavity 5 mm from the exit plane of the 10.9 mm nozzle along the nozzle centerline. The measured values were taken using the LDA in backscatter mode.

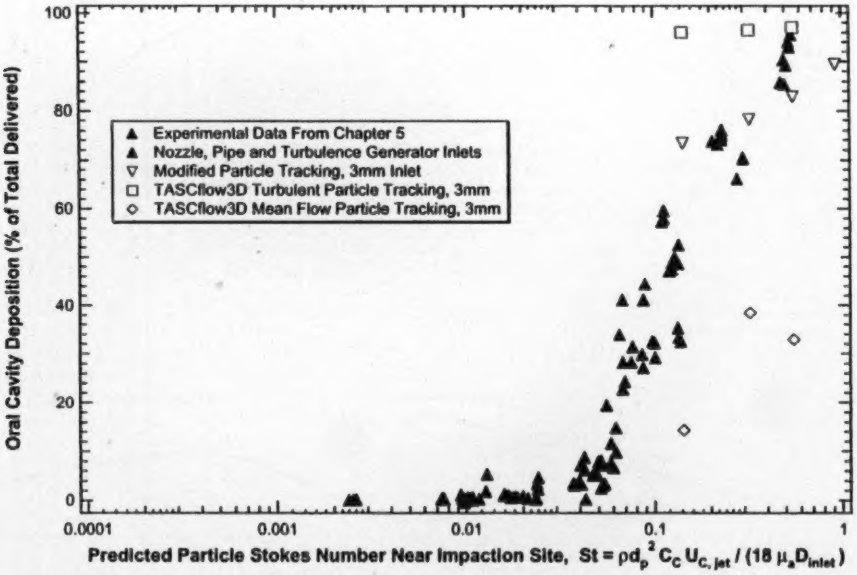

Figure 6.15: CFD particle deposition predictions for the 3.18 mm inlet using the three particle tracking algorithms described in section 6.2. The same converged fluid flow solution was used for all three cases.

6.7.3 Particle Tracking

6.7.3.1 Total Deposition in Oral Cavity

The total deposition of particles in the oral cavity was calculated using the three different particle tracking algorithms described in section 6.2. The total deposition for the three algorithms was tested for the 3.18, 8.13 and 17.1 mm inlets using 2.5, 3.8 and 5 micrometer diameter aerosol particles. The results of the tests are plotted in figures 6.15 to 6.17 and compared to the experimental deposition values from chapter 5.

The particle tracking for the 17.1 mm inlet using the commercial tracking software in either the turbulent or mean flow configurations overpredicts the particle deposition for all three aerosol diameters. The modified turbulent tracking routine overpredicts in this case as well, but it is the lowest and the

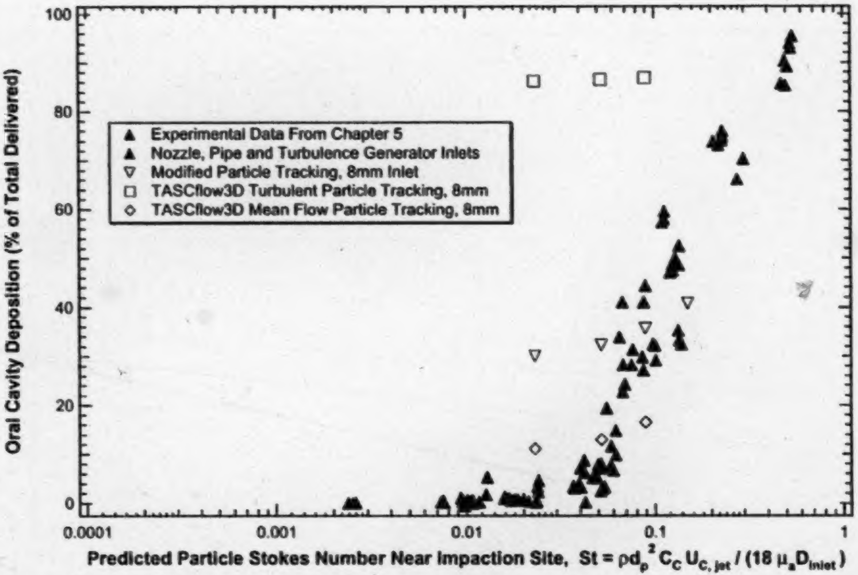

Figure 6.16: CFD particle deposition predictions for the 8.13 mm inlet using the three particle tracking algorithms described in section 6.2. The same converged fluid flow solution was used for all three cases.

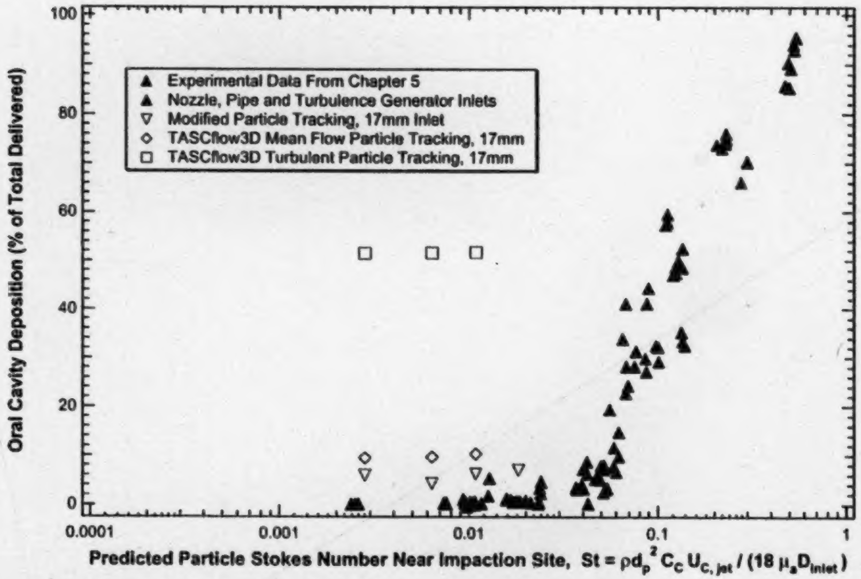

Figure 6.17: CFD particle deposition predictions for the 17.1 mm inlet using the three particle tracking algorithms described in section 6.2. The same converged fluid flow solution was used for all three cases.

best of the three.

For the 8.13 mm inlet, figure 6.16 shows that the turbulent tracking clearly overpredicts the deposition, while both the modified turbulent tracking and the mean flow tracking give results that agree with the experimental values for some of the particle diameters, but not all. Finally, the 3.18 mm inlet tests shown in figure 6.15 were found to be overpredicted by the turbulent tracking and significantly underpredicted by the mean flow tracking. In this case, the modified turbulent tracking algorithm performed the best. Based on these results, the modified turbulent tracking algorithm appears to be the most accurate of the three tested and gives relatively good agreement with experimental data.

The results of all the particle tracking tests using the modified eddy-interaction model described in section 6.2 are shown in figure 6.18. The total deposition of the particles is calculated and compared with the experimental values of the tests from Chapter 5.

All tests were performed at 32 L/min and 4 particle diameters are plotted for each inlet in the figure. Good agreement is seen between the CFD predictions and the experimental values.

It can be seen from the figure that though the agreement with experimental values is good, there is a trend for the large particles to have their deposition underpredicted and the small particles to have their deposition overpredicted. Similar effects have been seen by other authors[139] and are believed to be caused by the use of the Reynolds averaged equations in solving the flow field. The combination of the time averaging of the equations and the introduction of the eddy viscosity tends to make the CFD predict broader and slower flow regions than may occur in reality. In places where there may be high velocity jets fluctuating in space, the CFD will smear out the oscillatory effects. For example, in all the inlet cases, the jet in the oral cavity impinged and then followed the

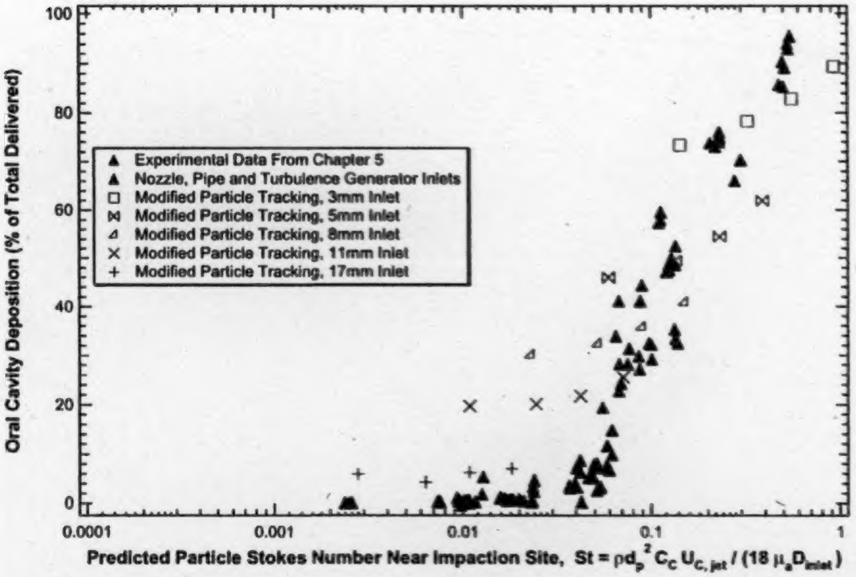

Figure 6.18: Deposition in the oral cavity of monodisperse aerosol particles. Comparison of CFD particle tracking by modified turbulent tracking algorithm to experimental values.

curvature of the upper rear wall of the oral cavity. In a region such as this, the CFD will predict a slightly wider and slower flow along the wall than may really exist since the real flow will have intermittency and oscillations which are not modelled in the CFD. For large particles, this lower mean velocity will mean a decrease in inertial impaction relative to the real case. However, small particles which have their deposition affected by diffusion, will have a longer residence time near the wall in the slower CFD case and so more will be predicted to deposit than do in reality.

6.7.3.2 Three Dimensional Deposition Pattern

The deposition pattern in three dimensions was obtained by recording the coordinates of the location of deposition for all particles tracked. Once sufficient particle numbers have been tracked, particle deposition patterns can be observed by plotting all of the final locations of the aerosol particles.

While the data was plotted and inspected for all deposition tests, only a few examples will be included here in the interests of brevity. In figures 6.19 to 6.21, a number of deposition patterns are presented covering the complete range from the largest inlet diameter (17.1 mm) and smallest particle diameter (1.0 μm) where the least deposition is expected, to the smallest inlet diameter (3.18 mm) and largest aerosol diameter (6.5 μm) where the greatest deposition is expected. In the figures, an orthographic view as well as a projection of the particle deposition locations onto the central plane of the oral cavity are presented for each case in order to allow a three dimensional understanding of the data from the 2D plots.

In general, the CFD deposition patterns matched well with the qualitative patterns obtained from the tests in Chapter 5. For the 3-11 mm inlets, nearly no deposition was present in the first 30 mm of the oral cavity. This was also observed in all the experimental tests of chapter 5 excluding the turbulence

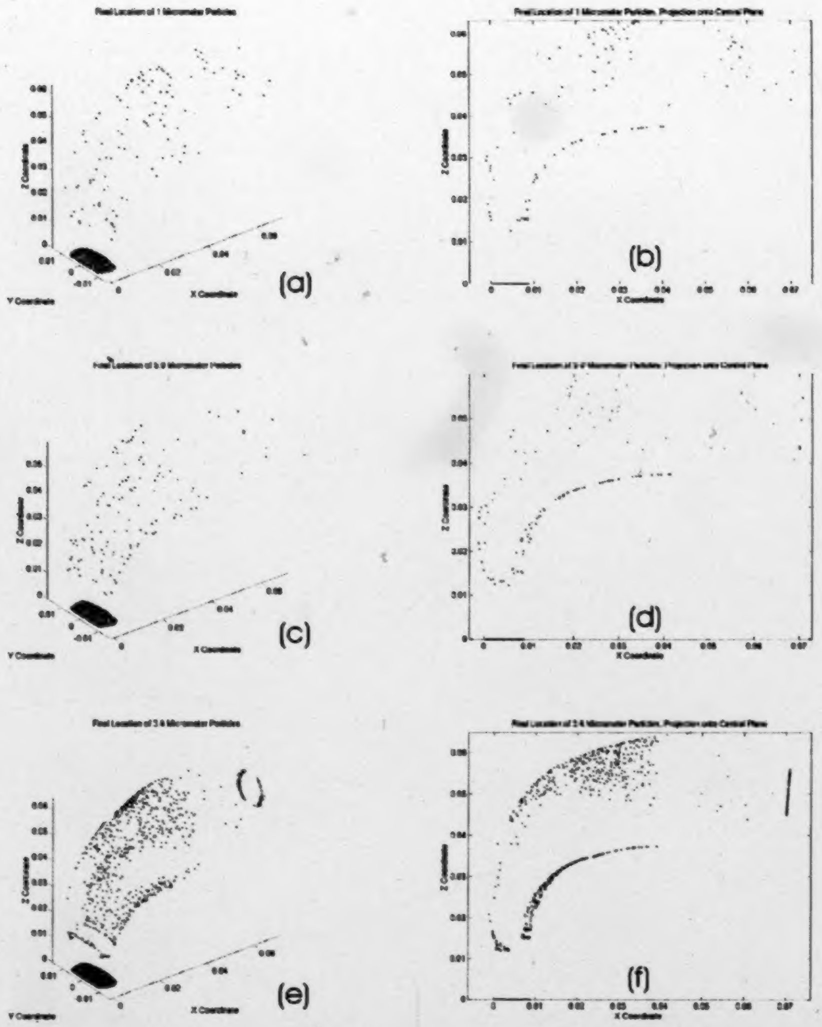

Figure 6.19: Computed deposition patterns in the oral cavity of monodisperse aerosol particles for large inlets. Blue points indicate location of tracked aerosol particle deposition, green points indicate location where tracked aerosol particle exits domain, red points indicate location of stagnant particles neither depositing nor exiting the domain. Graphs on left side show 3D deposition pattern. Graphs on right show projection of particle deposition onto central plane of oral cavity for the same case. Cases plotted: (a) and (b) 17.1 mm inlet, 1.0 μm aerosol; (c) and (d) 17.1 mm inlet, 5.0 μm aerosol; (e) and (f) 10.9 mm inlet, 3.8 μm aerosol

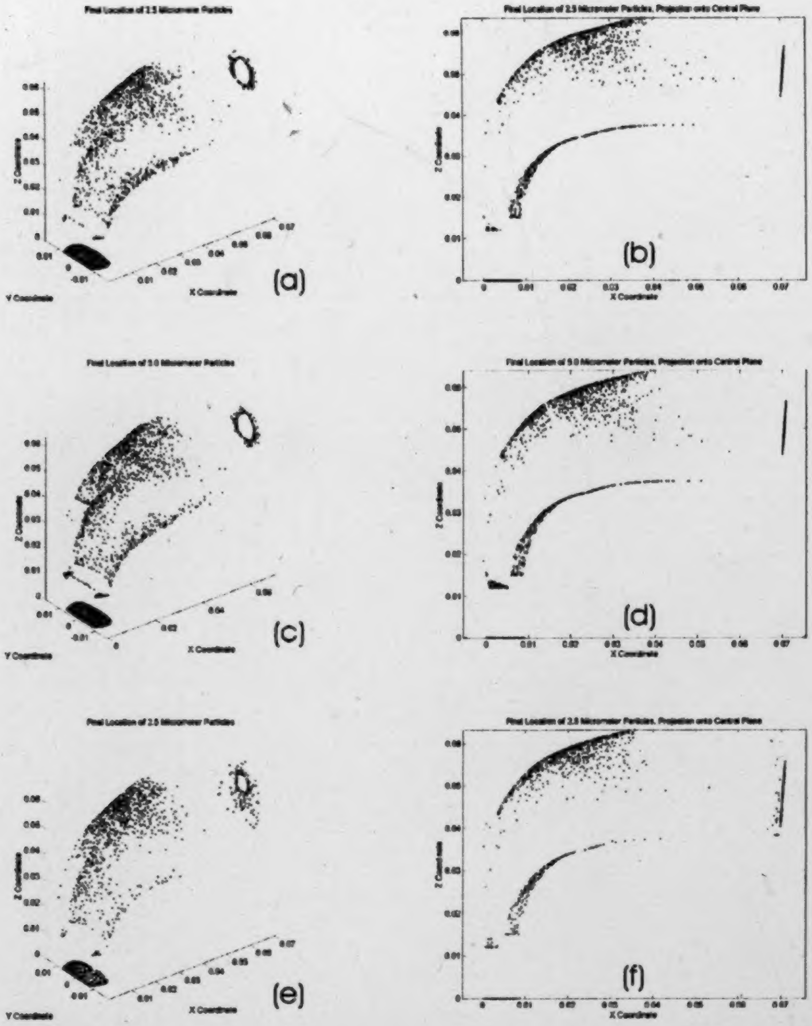

Figure 6.20: Computed deposition patterns in the oral cavity of monodisperse aerosol particles for large inlets. Blue points indicate location of tracked aerosol particle deposition, green points indicate location where tracked aerosol particle exits domain, red points indicate location of stagnant particles neither depositing nor exiting the domain. Graphs on left side show 3D deposition pattern. Graphs on right show projection of particle deposition onto central plane of oral cavity for the same case. Cases plotted: (a) and (b) 8.13 mm inlet, 2.5 μm aerosol; (c) and (d) 8.13 mm inlet, 5.0 μm aerosol; (e) and (f) 4.95 mm inlet, 2.5 μm aerosol

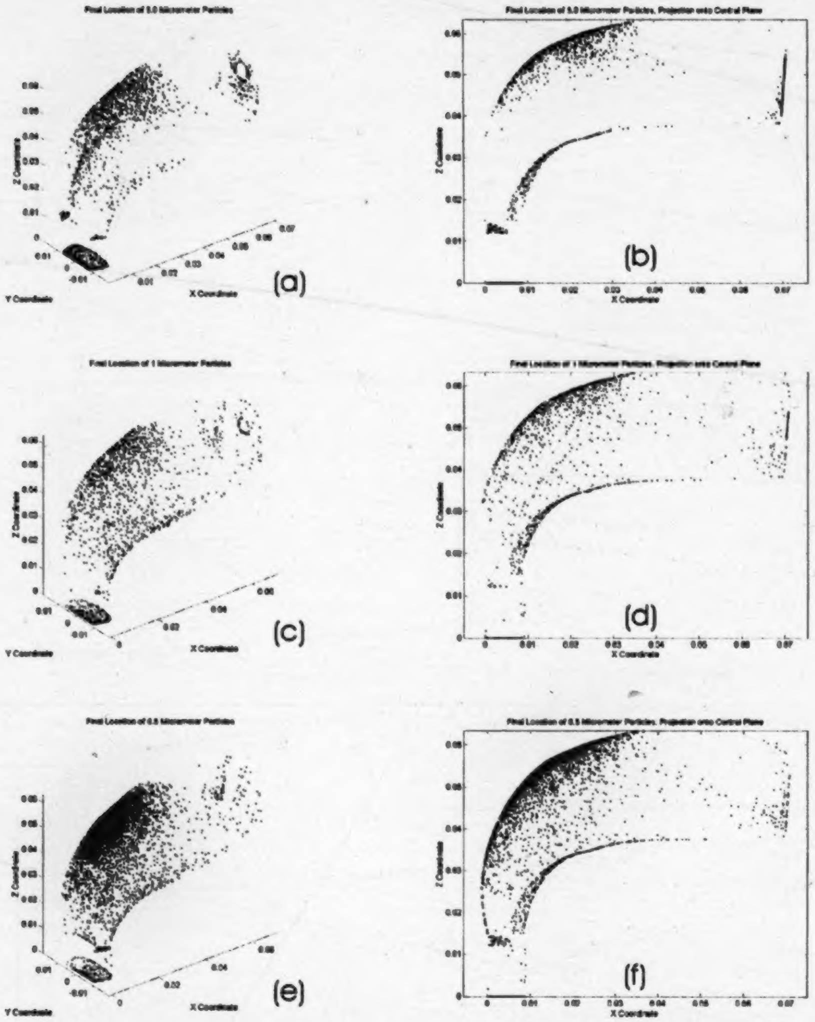

Figure 6.21: Computed deposition patterns in the oral cavity of monodisperse aerosol particles for large inlets. Blue points indicate location of tracked aerosol particle deposition, green points indicate location where tracked aerosol particle exits domain, red points indicate location of stagnant particles neither depositing nor exiting the domain. Graphs on left side show 3D deposition pattern. Graphs on right show projection of particle deposition onto central plane of oral cavity for the same case. Cases plotted: (a) and (b) 4.95 mm inlet, 5.0 μm aerosol; (c) and (d) 3.18 mm inlet, 1.0 μm aerosol; (e) and (f) 3.18 mm inlet, 6.5 μm aerosol

generator tests. The majority of the deposition then was spread from a point on the upper rear surface of the oral cavity down towards the rear of the region. The CFD predicts slightly more deposition than was observed on the upper surface of the tongue. It also predicts a small amount of aerosol depositing on the inlet face while no aerosol was observed to deposit here during the runs.

It is interesting to note that in parts (a) and (b) of figure 6.19, only 8.4% of the 1.0 μm diameter particles deposit in the oral cavity with the 17.1 mm inlet. However, for the same flow rate and particle diameter, with the 3.18 mm inlet, 66.4% are predicted to deposit. In parts (c) and (d) of figure 6.21, the majority of the deposition of the 1.0 micrometer diameter aerosol particles is located along the upper, rear wall of the oral cavity where the high velocity jet was seen to impinge in section 6.7.1. Thus, the major mechanism of the aerosol deposition in this case is inertial impaction, despite the small mass of the 1.0 μm particles.

This result contrasts sharply with the widely held belief in the pharmaceutical aerosol field that particles smaller than 5 μm in diameter will have little to no deposition in the upper airways regardless of the inlet geometry. And this CFD simulation was at the relatively low flow rate of 32 L/min. Typical flow rates for dry powder inhalers can range from 30 to 90 L/min. As was seen in chapter 5, aerosol deposition in the oral cavity will significantly increase at the higher flow rates, making the effect of inlet conditions even more pronounced.

The effects of more complex inlet conditions similar to commercially available dry powder inhalers on aerosol deposition in the oral cavity is explored experimentally in Chapter 7.

Chapter 7

Prediction of Extrathoracic Deposition After Dry Power Inhalers

7.1 Monodisperse Oral Cavity Deposition Tests with Pharmaceutical Device Inlets

7.1.1 Experimental Setup

The empirical predictions of oral cavity deposition from Chapter 5 were derived primarily from the relatively simple inlet conditions of contraction nozzles and pipe flows. While the relatively good agreement of the numerical results of Chapter 6 gives additional evidence of the importance of inlet conditions on the deposition in the extrathoracic region, the extension to more complex inlets such as commercially available pharmaceutical devices requires additional verification.

In order to test the oral cavity deposition for inlet conditions similar to those seen with pharmaceutical aerosol devices, monodisperse aerosols were passed through the dilution air for a variety of dry powder inhalers. The experimental setup for this set of tests is illustrated in figure 7.1. The monodisperse aerosol was produced using a condensation monodisperse aerosol generator (Model 3475; TSI Incorporated, St. Paul, Minnesota). The particle size

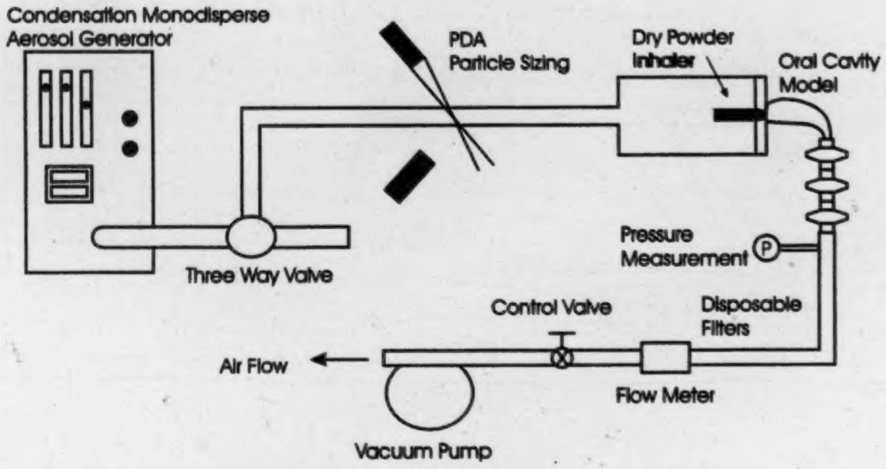
Condensation Monodisperse Aerosol Generator
PDA Particle Sizing
Dry Powder Inhaler
Oral Cavity Model
Pressure Measurement
P
Three Way Valve
Control Valve
Disposable Filters
Air Flow
Flow Meter
Vacuum Pump

Figure 7.1: Experimental setup for monodisperse aerosol deposition tests in the oral cavity with dry powder inhaler inlets.

and monodispersity was monitored using a phase doppler anemometer (Dantec Dynamics, Skovlunde, Denmark), the air flow rate was monitored with a pneumotachometer (Series 4719, Hans Rudolph, Inc, Kansas City, MO), the static pressure just downstream of the oral cavity was monitored with a diaphragm pressure transducer (Validyne Engineering Corp., Northridge, CA) and the flow through the system was driven by a vacuum pump (Model LR 22132, DOERR, Cedarburg, WI, USA).

Similar to the test procedures of Chapter 5, the oral cavity deposition was determined using gravimetry, weighing the model of the oral cavity and the filters before and after each run. All tests were repeated a minimum of three times to ensure repeatability. Tests were performed for all devices with a nominal aerosol diameter of 3.8 micrometers and at a flow rate of 30 L/min.

7.1.1.1 Tested Dry Powder Inhalers

The tested inlets consisted of a Diskhaler (GlaxoSmithKline, Mississauga, Ontario, Canada), an Aerolizer (Novartis Pharmaceuticals, Dorval, Quebec,

Dry Powder Inhaler	Cross Sectional Area (mm^2)	Mouthpiece Diameter (mm)
Diskhaler	113	12.0
Aerolizer	90.3	10.7
Inhalator (Single Dose)	27.3	5.89
Inhalator (Multi-Dose)	49.0	7.90
Easyhaler	22.6	5.37

Table 7.1: Measured mouthpiece exit dimensions for tested dry powder inhalers

Canada), a single dose Inhalator (Boehringer Ingelheim, Ridgefield, Connecticut), a multidose Inhalator (Boehringer Ingelheim, Ridgefield, Connecticut) and an Easyhaler (Orion, Karlsruhe, Finland). All devices were sealed to a disk 8 mm thick, ensuring that the monodisperse aerosol which entered a large chamber 110 mm in length and 90 mm in diameter, passed through the dry powder inhaler via the dilution air pathways and exited the dry powder inhaler through its mouthpiece and into the oral cavity. The capsules were removed from the single and multidose Inhalators and the Aerolizer to prevent excessive deposition of the aerosol inside the devices.

The cross sectional areas of the dry powder inhaler mouthpieces were measured at the exit of the device. Table 7.1 summarizes the cross sectional area and diameter of the dry powder inhalers at their mouthpiece exits. For the Diskhaler which has an elliptic mouthpiece, the diameter presented is the equivalent diameter for a circular mouthpiece with the same cross sectional area.

7.1.1.2 Aerosol Monodispersity

The aerosol particle size distribution was monitored throughout all tests upstream of the dry powder inhalers using a phase Doppler anemometer (Dantec Dynamics, Skovlunde, Denmark).

The particle size distribution was sampled inside the oral cavity for two dry powder inhalers using an Aerosizer Mach II(TSI Incorporated, Particle

Instruments / Amherst, Amherst, MA) to ensure that it was unaffected by the passage through the inhalers. Approximating the particle size distribution as log normal, it was found that the mass median diameter of the aerosol changed by less than 1.8 % while the geometric standard deviation of the particle size distribution remained less than 1.16, indicating that the aerosol exiting the dry powder inhalers was still monodisperse. These tests also demonstrated that no re-entrainment of the aerosol material which deposited in the dry powder inhaler was occurring in the size ranges measurable by the Aerosizer. To ensure that large aggregates beyond the measurable range of the Aerosizer were not building up inside the devices and splattering into the oral cavity, all the inlet devices were thoroughly cleaned between runs and test times were progressively decreased to ensure the measured oral cavity deposition was independent of test run time. Additionally, the dry powder inhalers were visually inspected after each test to ensure that there was no significant buildup of aerosol material inside the device.

7.1.2 Results

The oral cavity deposition for the various inhalers was calculated and plotted against the impaction parameter in figure 7.2. Because all tests were performed at the same nominal particle diameter and flow rate, all the devices have nominally the same impaction parameter. The variations in the parameter from the nominal value are a result of slight variations in controlled parameters, primarily the particle diameter since the iterative nature of the condensation generator prevents exact specification of the aerosol diameter.

From figure 7.2, it is clear that the impaction parameter is not a unique determinant of the aerosol deposition in the oral cavity. This is similar to the results of Chapter 3, where the dry powder inhalers tested there were found to have significantly higher deposition than other inlet conditions in the whole

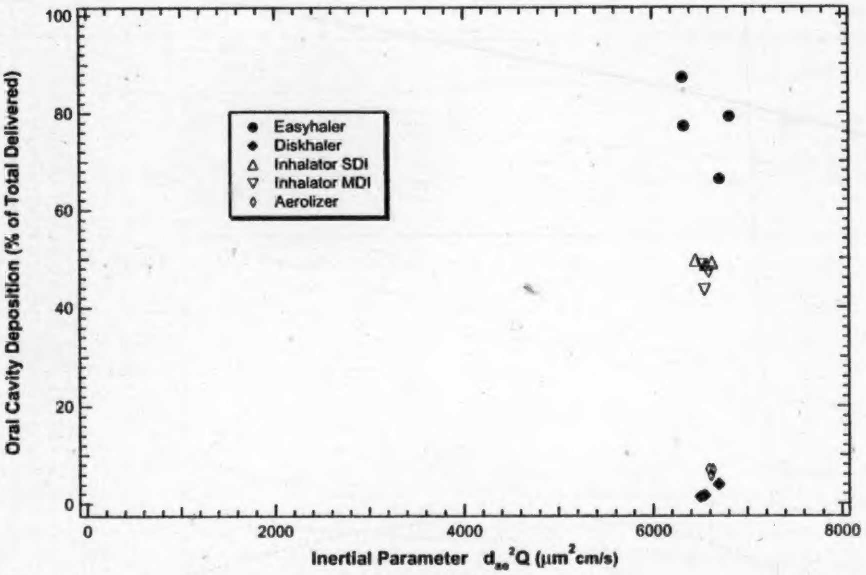

Figure 7.2: Deposition in the oral cavity of monodisperse aerosol particles after entry through commercially available dry powder inhalers as a function of the impaction parameter.

Dry Powder Inhaler	Diskhaler	Aerolizer	Inhalator (Single Dose)	Inhalator (Multi-Dose)	Easyhaler
Diskhaler	1	0.293	9.8×10^{-8}	1.8×10^{-7}	3.0×10^{-10}
Aerolizer	0.293	1	2.6×10^{-7}	5.0×10^{-7}	6.0×10^{-10}
Inhalator (Single Dose)	9.8×10^{-8}	2.6×10^{-7}	1	0.506	7.1×10^{-6}
Inhalator (Multi-Dose)	1.8×10^{-7}	5.0×10^{-7}	0.506	1	3.0×10^{-6}
Easyhaler	3.0×10^{-10}	6.0×10^{-10}	7.1×10^{-6}	3.0×10^{-6}	1

Table 7.2: Comparative p-values for determining statistically significant differences from multiple ANOVA calculation for tested dry powder inhalers. $p < 0.001$ implies statistically significant differences while $p > 0.05$ implies no statistically significant differences

extrathoracic airways. In the present tests, it can be seen that this applies also to deposition in the oral cavity as well. A statistical analysis of the data was performed using a multiple ANOVA with the Tukey HSD analysis. The output table of the calculation showing the p-values for comparing all the devices to eachother is included in table 7.2.

If we take as a measure of statistical significance p-values ≤ 0.01, then from table 7.2 it can be seen that there are significant differences in the oral cavity deposition between many of the devices. The Easyhaler has an oral cavity deposition which is significantly higher than all other devices. The two Inhalator devices have oral cavity depositions which are not statistically different from eachother, but are significantly higher than the Diskhaler or Aerolizer and are significantly lower than the Easyhaler. Similarly, the oral cavity depositions for the Diskhaler and Aerolizer at the test conditions were not statistically different from eachother, but were found to be significantly lower than all the other DPIs.

Clearly, as was demonstrated in Chapter 3, discussed in section 5.2.2.1 and again illustrated with the current data, the impaction parameter is often not an ideal measure of the probability of aerosol deposition. As it is based on cross sectionally averaged values of flow rate and conduit diameter, it cannot predict deposition as a result of high momentum structures such as turbulent jets within the conduit (in our case the oral airways). Predicting extrathoracic deposition for dry powder inhalers based on empirical models like that of Stahlhofen *et al.*[148] which depend only on the impaction parameter, such as recommended by Clark *et al.*[26] can be expected to underpredict the extrathoracic deposition. This type of model would predict that all devices would have identical extrathoracic deposition for the same impaction parameter value, but from figure 7.2 it is clear that this is not likely to be the case. As demonstrated throughout this work, the mouthpiece geometry can have significant effects on the aerosol deposition in the oral cavity. Figure 7.2 shows that dry powder inhaler mouthpiece geometries must be included in the prediction of extrathoracic deposition for inlets typical of commercially available dry powder inhalers.

Instead of plotting the deposition against the impaction parameter, the oral cavity deposition is plotted against the particle Stokes number (modified to near the impaction location as in section 5.2.2.4 and for inlet turbulence as in section 5.4) in figure 7.3. As the inlet turbulence was found in section 5.4 to be a relatively small correction for all but very high levels of turbulence, inlet turbulence levels of 10% were assumed for all dry powder inhalers. In figure 7.4, the oral cavity deposition is re-plotted with error bars indicating the change in the particle Stokes number due to varying the inlet turbulence intensity from 10% down to 0% and up to 20%. It can be seen from the figure that relative to the scatter in the experimental data, the effect on the turbulent particle Stokes number of doubling the turbulence intensity is not large. Based on this, the estimate of an inlet turbulence intensity of 10% for all the dry powder inhalers appears to be reasonable.

The measured oral cavity deposition for the monodisperse 3.8 μm diameter

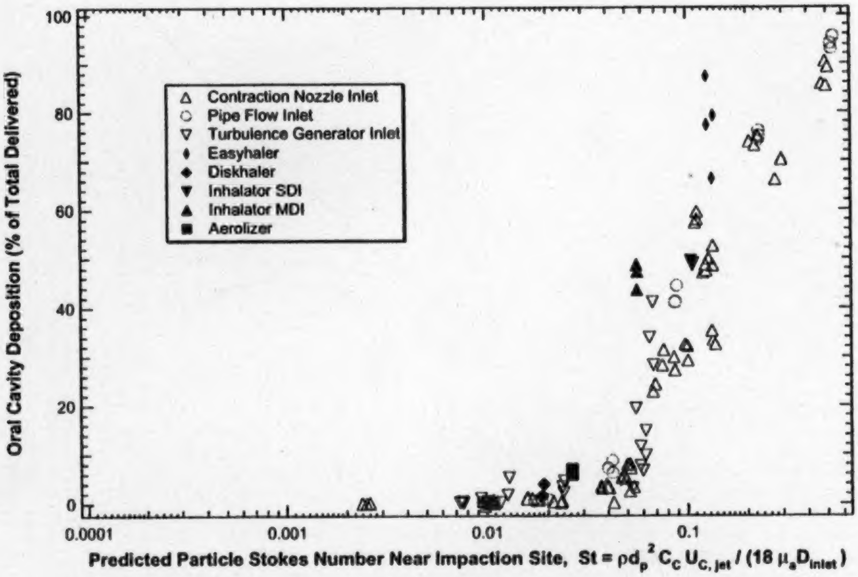

Figure 7.3: Deposition in the oral cavity of monodisperse aerosol particles. Comparison deposition after DPI's to deposition from tests in Chapter 5. Particle Stokes number calculated from equations 5.24 and 5.25.

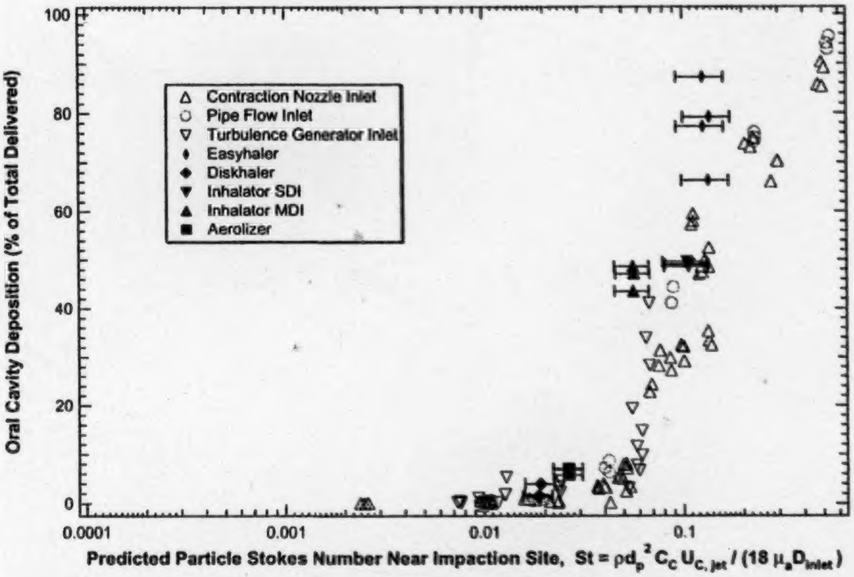

Figure 7.4: Deposition in the oral cavity of monodisperse aerosol particles. Comparison deposition after DPI's to deposition from tests in Chapter 5. Particle Stokes number calculated from equations 5.24 and 5.25. Error bars represent 0% to 20% turbulence intensities at inhaler outlet.

aerosols entering through the dry powder inhalers is compared to the predictions for oral cavity deposition from equation 5.26 in figure 7.5. Also shown in the figure are the predictions for the total extrathoracic deposition from a number of the models in the literature discussed in section 2.9.2. Although oral cavity deposition is not calculated directly in the literature models, it is a part of the extrathoracic deposition along with pharyngeal and laryngeal and tracheal depositions. In this way, the total extrathoracic deposition prediction gives an upper bound for what the models could predict for oral cavity deposition (ie. if all the deposition in the extrathoracic region occurred in the oral cavity). Compared to predicting oral cavity deposition with the archival models, the predictions of equation 5.26 is seen to be quite good. The models are seen to dramatically underpredict the extrathoracic deposition for the smaller inlet DPIs since the laryngeal deposition still needs to be added to the measured oral cavity deposition to get the total extrathoracic deposition. The overestimation of the oral cavity deposition for the larger diameter DPIs is expected since the measured deposition does not include the pharynx, larynx or trachea.

The equation for predicting the oral cavity deposition derived in section 5.4.2 based on contraction nozzle and straight pipe inlets is seen to predict oral cavity reasonably well. Although it underpredicts the oral cavity deposition for all the tested devices, it appears to capture the trend of the data and appears to be a significant improvement over all other published models the author is aware of.

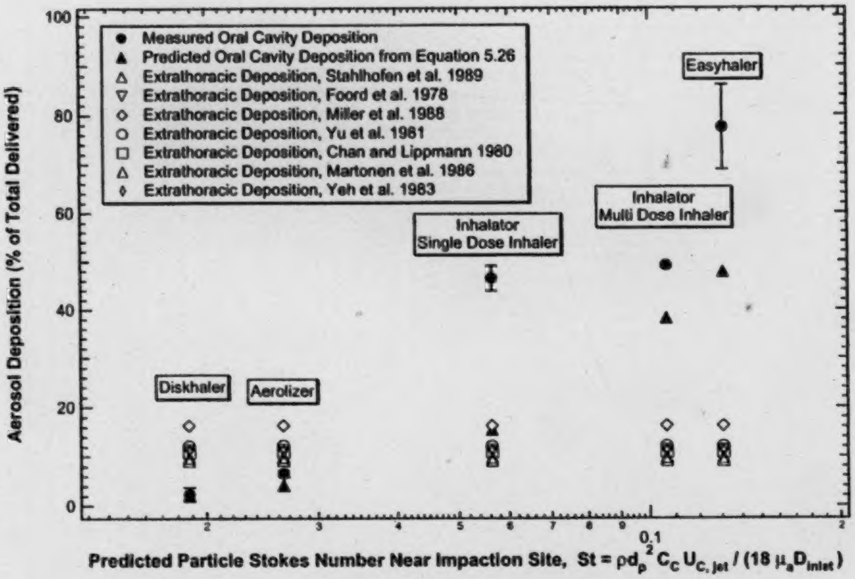

Figure 7.5: Predicted and measured deposition in the oral cavity of monodisperse aerosol particles after entry through 5 different dry powder inhalers. Comparison of deposition prediction using equation 5.26 and total extrathoracic deposition models from the archival literature. Error bars represent one standard deviation for the measured data.

7.2 Extension of Model to Predict DPI Deposition In Vivo

7.2.1 Extension to Polydisperse Aerosols

The extension to polydisperse aerosols for the prediction of first oral cavity and then total extrathoracic deposition is relatively straightforward with a few simplifying assumptions.

The calculation of the oral cavity deposition of polydisperse aerosols can be achieved by discretizing the aerosol distribution into a finite number of bins, determining the deposition probability for each bin and then calculating the resultant deposition probability of the entire distribution. This assumes that the aerosol can be treated as an ensemble of monodisperse aerosols which do not interact with eachother. Some caution is required here as there often may be particle-particle interactions during inhalation with dry powder inhalers, especially when there are large lactose carriers with smaller drug particles still undergoing deaggregation as the aerosol exits the device and enters the oral airways. However, as a first approximation, the distribution is treated as an ensemble of independent monodisperse aerosols.

Also neglected in this analysis is the influence of the particle field on the turbulence levels of the flow field which can become important for high number concentration aerosols seen in some dry powder inhalers.[48] However, it was determined in Chapter 5 that inlet turbulence levels had a much smaller effect on oral cavity deposition than inlet diameter and mean velocities, so this assumption is believed to be reasonable.

A number of other factors such as static charge and hygroscopicity of the particles have been neglected here which may be important for predicting deposition from some dry powder inhalers. Further work is required to extend the current model to include these effects.

7.2.2 Extension to Total Extrathoracic Deposition

In order to calculate the total extrathoracic deposition, an oral cavity prediction model based on equation 5.26 needs to be combined with a prediction model for the rest of the extrathoracic region.

The model of Stahlhofen *et al.*[148]was chosen to represent the deposition in the remainder of the extrathoracic region. As discussed in section 2.9.2, their model is based on a large number of available test data. As it is based on deposition data from patients inhaling through large bore tubes, the deposition in the oral cavity was quite minimal. The authors propose that the oral cavity and pharyngeal deposition are negligible relative to laryngeal deposition for these tests and their model gives an estimate primarily of laryngel deposition. If this is true, then combining the oral cavity deposition prediction from section 5.4.2 with the deposition model Stahlhofen *et al.* for pharyngeal, laryngeal and tracheal deposition should give negligible overlap and should accurately predict the deposition of monodisperse aerosols (or bins of polydisperse aerosols).

The total extrathoracic deposition of a monodisperse aerosol is then given by:

$$\eta_{extrathoracic} = \eta_{oral\ cavity} + (100 - \eta_{oral\ cavity})\eta_{laryngeal} \tag{7.1}$$

where from equation 5.26,

$$\eta_{oral\ cavity} = 100 - \frac{100}{(44.53St^{1.91} + 1)} \tag{7.2}$$

with the Stokes number, St calculated from equations 5.24 and 5.25 and $\eta_{laryngeal}$ is given by:

$$\eta_{laryngeal} = 100 - \frac{100}{(3.5 \times 10^{-8}(\rho_p d_p^2 Q)^{1.7} + 1)} \tag{7.3}$$

Dry Powder Inhaler	Author	MMAD (μm)	GSD	In vivo Extrathoracic Deposition (% of Emitted Dose)
Turbuhaler	Warren *et al.*[160]	16.8	3.43	80.5
Spinhaler	Newman *et al.*[116]	15.4	2.10	90.8
Pulminval	Pitcairn *et al.*[124]	15.3	2.67	84.4
Leiras mDPI	Pitcairn *et al.*[125]	2.93	3.26	56.0
Clickhaler	Warren *et al.*[160]	13.9	3.28	70.9
Easyhaler	Newman *et al.*[117]	19.4	3.73	79.4

Table 7.3: Particle size distribution data measured in vitro and corresponding in vivo extrathoracic deposition data for polydisperse drug aerosols from six dry powder inhalers.

In order to test the usefulness of equation 7.3 for predicting extrathoracic deposition using polydisperse aerosols, the equation was used to predict the deposition for a number of in vivo deposition studies using dry powder inhalers. The reported particle size distribution measured in vitro was used for each device to predict the extrathoracic deposition and was then compared to the reported in vivo extrathoracic deposition of the emitted dose in each study. The dry powder inhalers which were studied are the Turbuhaler® (AstraZeneca, Herts, U.K.), the Spinhaler® (Fisons PLC Markham, Ontario, Canada), the Pulminval® (Chiesi Farmaceutici S.p.A, Italy), the Leiras multidose dry powder inhaler (mDPI) (Leiras Oy, Turku, Finland), the Clickhaler® (Innovata Biomed Ltd., St. Albans, U.K.) and the Easyhaler® (Orion Pharma, Kuopio, Finland). The calculated MMAD and GSD for the emitted doses measured in vitro and the corresponding in vivo extrathoracic depositions are given in table 7.3 for the published studies.

As was noted by Clark *et al.*,[27] current extrathoracic deposition models greatly underpredict the deposition seen with dry powder inhalers. As well, the qualitative deposition patterns are different with much more oral cavity deposition observed with the DPIs than predicted.

Similar to the methods of Clark *et al.*, smooth curves were fit to the cumulative percentage by mass undersize curve calculated from the measured particle size distribution. This fit curve was used to partition the particle size distribution into smaller 0.2 micrometer width bins. This particle distribution was then used to predict the extrathoracic deposition using two different deposition models. The model of Rudolf *et al.*[133] was used to compare with Clark's results and good agreement was found, suggesting that the high resolution particle size distribution was very similar to the one they calculated independently. This model also predicts the deposition to be primarily laryngeal while the in vivo studies showed significant oral cavity deposition.

The tested cases are shown in figure 7.6 where the predictions of Rudolf's model and the predictions based on equation 7.3 are compared to the experimentally measured deposition for the polydisperse aerosols in vivo.

While the new model still underpredicts the in vivo deposition data in some cases, it is no longer the consistent underprediction seen with the predition model of Rudolf *et al.*[133] illustrated in figure 7.6 and observed by Clark *et al.* In figure 7.7, the deposition in the oral cavity and larynx are differentiated for the model based on equation 7.1. Clearly, the primary deposition location has shifted for the DPIs from the larynx as predicted exclusively by Rudolf's model to the oral cavity which agrees more with the deposition patterns observed in vivo.

As is seen in figure 7.6, the predictions of the new model for total extrathoracic deposition are, on average, quite good and a marked improvement over the model of Rudolf *et al.*[133]

However, variability in the accuracy of the predictions is still seen. Besides the accuracy of the model itself, a number of factors significantly impact this variability. While only studies which reported similar flow conditions for the in vitro particle sizing and the in vivo deposition tests were considered here, there were differences between the steady flow rates for the in vitro tests and

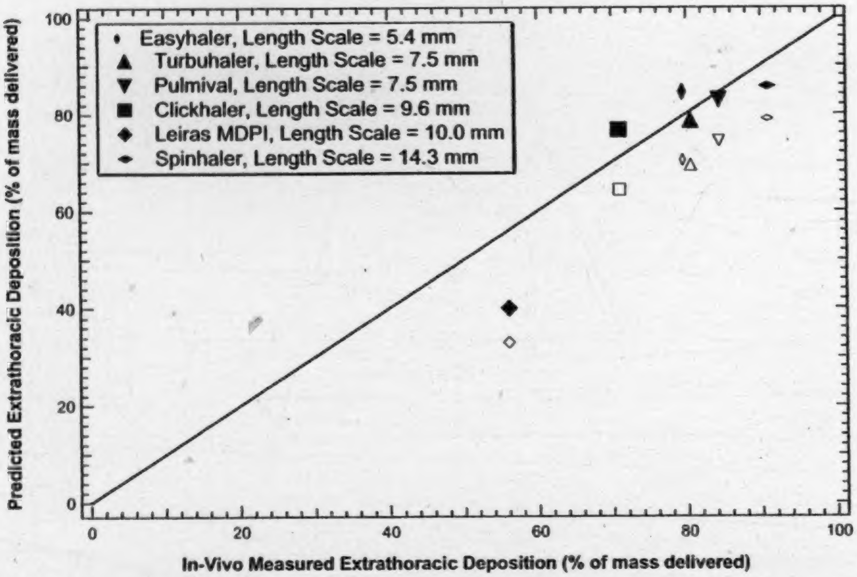

Figure 7.6: Predicted deposition in the extrathoracic region of polydisperse aerosol particles generated by six different dry powder inhalers. Predictions are based on the model of Rudolf *et al.*[133] (hollow symbols) and equation 7.1 (solid symbols) for in vitro measured aerosol distributions using the indicated length scale at mouthpiece for each device. The predictions are compared to in vivo, gamma scintigraphy aerosol deposition measurements from literature sources.

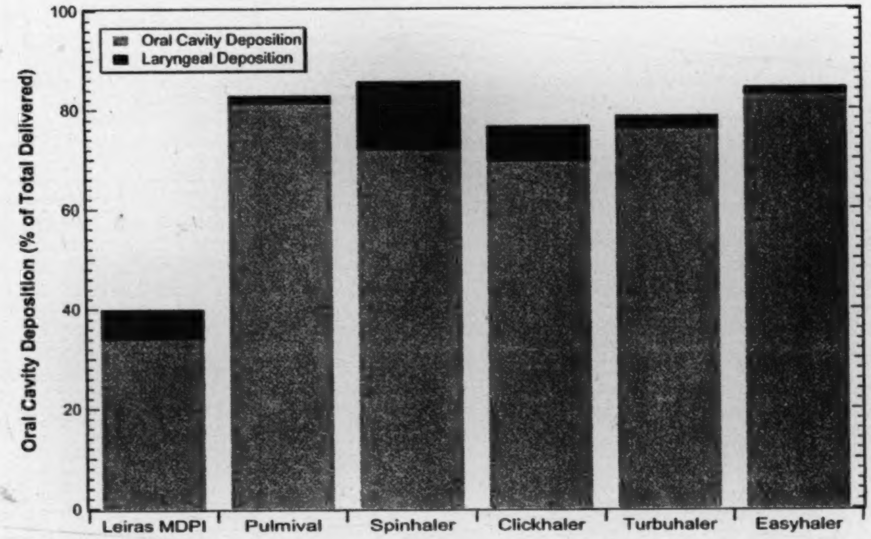

Figure 7.7: Predicted deposition in the oral cavity and larynx for polydisperse aerosol particles generated by three different dry powder inhalers. Predictions are based on equation 7.1 for in vitro measured aerosol distributions.

the time dependent patient driven flow rates in the in vivo tests. Since the dry powder inhalers considered are all passive inhalers, the particle size distribution produced by the device is highly dependent on the patient's breathing pattern. However, the author is not currently aware of any published studies giving in vivo extrathoracic deposition data along with in vitro particle size distributions for identical breathing patterns from dry powder inhalers with polydisperse aerosols. The in vitro particle size distributions with the dry powder inhalers were primarily done using multistage liquid impingers which while allowing imaging of the stages and preventing particle bounce issues, give reasonably coarse measures of the distribution from the inhalers. These factors which cause the particle size distribution entered into the predictive models to be somewhat different from the true particle size distribution being inhaled by the test subjects will lead to variability in the accuracy of the predictive models.

From figure 7.8, the primary advantage of the new model is seen to be an increase in the extrathoracic deposition probability for particles in the 2 to 10 micrometer range. This is significant since it shows that the often quoted fine particle fractions (mass of aerosol particles < 5 μm typically) may not alone be a good indicator of the amount of aerosol which penetrates to the alveoli. As has been reported throughout this work, mouthpiece effects significantly affect the extrathoracic deposition of these intermediate size particles. Particles with aerodynamic diameters less than about 2 micrometers have Stokes numbers that are too low (for typical DPIs) to be much affected by inertial impaction. Particles with aerodynamic diameters greater than approximately 10 micrometers have such large Stokes numbers regardless of the mouthpiece that they can expected to deposit somewhere in the oral airways. If not in the oral cavity due to mouthpiece effects such as was seen in chapter 5, then in the larynx due to the constriction of the airway there.

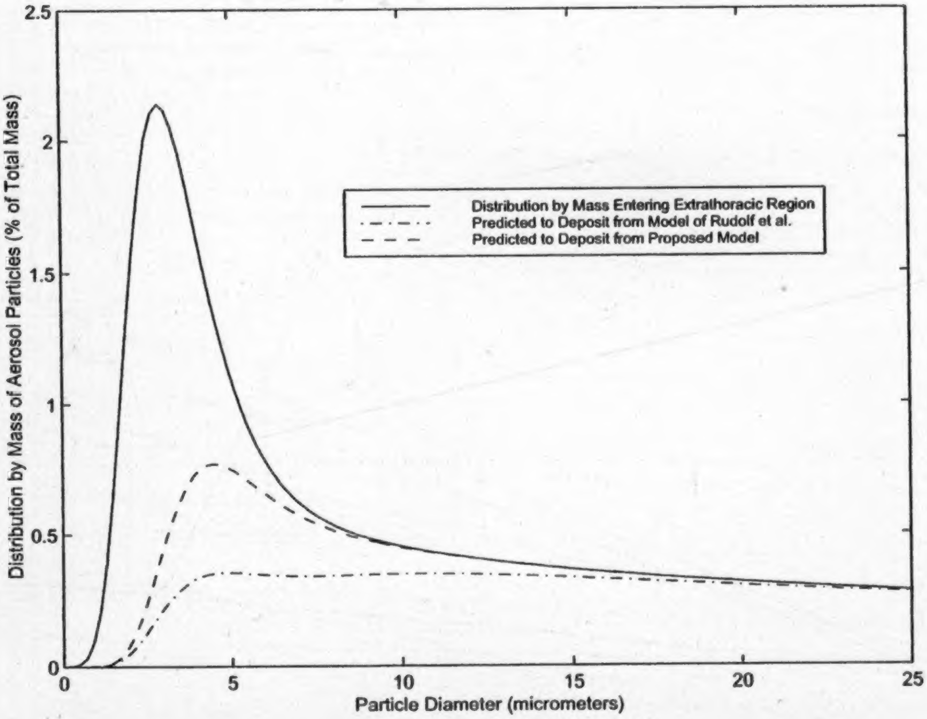

Figure 7.8: Predicted deposition in the extrathoracic region for a polydisperse aerosol distribution generated by the Clickhaler dry powder inhaler. The smooth fit particle size distribution by mass is given along with the distributions by mass of the aerosol predicted to deposit in the extrathoracic region by the model of Rudolf *et al.*[133] and that of equation 7.1.

The deposition model proposed in this section encompasses what is believed to be the primary deposition mechanism in the extrathoracic region: inertial impaction. It has however, neglected a number of other secondary phenomena such as particle number concentration, hygroscopic growth, the presence of an additional inert particle phase (lactose carrier), and static charge effects which may affect aerosol deposition in the region.

In summary, the proposed model for extrathoracic deposition brings the predictions into much closer agreement with in vivo data, both in total deposition in the region and in location of that deposition. Future work to test the importance of number concentration, static charge, hygroscopic growth and particle size distribution changes with patient breathing patterns is required before the model can be confidently implemented in the full in vivo setting.

Chapter 8

Conclusions and Recommendations for Future Work

8.1 Conclusions

In this thesis, the enhancement of aerosol deposition in the mouth–throat region by non-ballistic pharmaceutical aerosol devices has been investigated and a model proposed to predict the extrathoracic deposition.

Total extrathoracic deposition of monodisperse aerosols was measured using a number of pharmaceutical aerosol devices as inlets using a realistic, idealized mouth and throat geometry. In contrast to current extrathoracic deposition modelling techniques, the inlet conditions for the region were found to significantly alter the deposition in the region. Over a range of flow rates and particle diameters, the two dry powder inhalers tested were found to greatly enhance the aerosol deposition while the two nebulizers and the pMDI with attached holding chamber showed little difference from a large diameter tube.

The regional deposition pattern for the monodisperse aerosols entering through the different inhalers was quantified using planar gamma scintigraphy. The data showed a significant shift in the site of aerosol deposition from the larynx and upper trachea for the large diameter inlets to the oral cavity for the DPIs. Again, significantly more total extrathoracic deposition was observed with the DPIs.

Testing was then performed in an model of an adult oral cavity to determine the major mechanisms for the observed elevated deposition with DPIs. It was determined that inertial impaction was the dominant mechanism in the region. Using a large number of inlets, deposition data was generated which spanned the range seen between large diameter inlets and the DPIs from the previous section. This data was found to collapse reasonably well with the particle Stokes number indicating that inertial impaction was the primary deposition mechanism. The data collapse was found to be even better when the Stokes number was formulated using predictions of the flow length and velocity scales near the impaction site, yielding a best fit curve given by equation 5.14.

The presence of turbulence in the flow at the inlet of the region was also found to be a mechanism causing elevated deposition, but was of secondary importance relative to the inertial impaction. By using a formulation of the Stokes number which incorporates the turbulence intensity of the flow at the inlet of the region, it was found that the aerosol deposition in the oral cavity due to both mechanisms could be predicted quite well with equation 5.26.

Computational fluid dynamics with particle tracking algorithms was then employed to investigate the three dimensional flow and deposition patterns inside the oral cavity for the contraction nozzle inlets. The CFD found fluid jet structures in the oral cavity for all inlets less than 17mm in diameter with elevated aerosol deposition near the point of jet impingement on the upper, rear wall of the oral cavity. The match between the CFD predictions and the measurements and observations from the corresponding experiments was good for both the total deposition in the region and the location of that deposition. This lends confidence to the CFD results necessary due to the complexity of the geometry and flow field under investigation.

With the confidence that the two major mechanisms governing aerosol deposition in the region were now adequately captured with our model for straight tube and contraction nozzle inlets and monodisperse aerosols, an extrapolation of the model to predict the deposition for the complex case of commercially available DPIs was undertaken.

In the first phase, the restriction of straight tube inlets was removed. Oral cavity deposition tests performed using DPIs as inlets for monodisperse aerosols showed reasonable agreement with the extrapolated model, although some underprediction of the deposition for the smaller diameter inlets was observed.

In the final phase, the model was extrapolated to the full case of human subjects inhaling polydisperse, multi-component drug formulations from dry powder inhalers. Despite the complexity of this scenario and the relative simplicity of the model given by equation 7.1, marked improvement over the often quoted model of Rudolf *et al.*[133] was seen in predicting the total extrathoracic deposition for 6 different DPIs. As expected, there was some variability in the model's accuracy in predicting deposition in the full, complex case of subjects inhaling from DPIs. However, a significant part of this variability is expected to be due to the uncertainties in the particle size distributions studied due to coarse sizing techniques and differences between in vitro and in vivo flow patterns causing different deaggregation of the powder and not necessarily due to simplifying assumptions of the model presented here.

8.2 Future Work

As a result of the work done in this thesis, the need for additional research in a number of areas has become clear.

1. There is a need for high quality in vivo deposition data that can distin-

guish between oral cavity and laryngeal deposition for aerosols exiting dry powder inhalers for validating the regional predictions of section 7.2.2.

2. Testing the influence of gradually decelerating the aerosol streams exiting the small diameter mouthpieces of some dry powder inhalers prior to entry into the oral cavity on the extrathoracic deposition needs to be done.

3. Hot wire anemometry should be performed in an oral cavity model when dry powder inhalers are used for the flow inlet to get better predictions of the range of turbulence generated by different devices.

4. It would be beneficial to perform experiments to determine the fluid flow field in the oral cavity with the various straight tube inlets in order to verify and improve on the CFD predictions. Particle Image Velocimetry (PIV) would be a good way to determine the large scale structures and mean flows in the region. Hot wire and laser doppler anemometry could be used to traverse the region and obtain good turbulence measurements near aerosol deposition locations.

5. CFD simulations of aerosol deposition and fluid flow fields in the oral cavity can be investigated for a variety of different entry conditions from what was investigated in this work. Specifically testing the influence of radial velocity components at the inlet by using cones rather than straight pipes as inlets and varying the cone angles significantly.

6. PIV experiments to complement the recommended CFD tests using inlets with radial components of velocity at the inlet should be performed.

Bibliography

[1] S. Abuzeid, A. A. Busnaina, and G. Ahmadi. Wall deposition of aerosol particles in a turbulent channel flow. *J. Aerosol Sci.*, 91:43–62, 1991.

[2] M. L. Albertson, Y. B. Dai, A. Jensen, and H. Rousse. Diffusion of submerged jets. *Proc. Amer. Soc. of Civil Engineers*, 74:1571–1596, 1948.

[3] W. D. Bachalo and M. J. Houser. Phase/doppler spray analyzer for simultaneous measurements of drop size and velocity distributions. *Optical Engineering*, 23(5):583–590, 1984.

[4] I. Balásházy, T. Heistracher, and W. Hofmann. Air flow and particle deposition patterns in bronchial airway bifurcations: The effect of different cfd models and bifurcation geometries. *J. Aerosol Med.*, 9(3):287–301, 1996.

[5] I. Balásházy and W. Hofmann. Particle deposition in airway bifurcations – ii. expiratory flow. *J. Aerosol Sci.*, 24(6):773–786, 1993.

[6] I. Balásházy, W. Hofmann, and T. Heistracher. Computation of local enhancement factors for the quantification of particle deposition patterns in airway bifurcations. *J. Aerosol Sci.*, 30(2):185–203, 1998.

[7] I. Balásházy, W. Hofmann, and T. Martonen. Inspiratory particle deposition in airway bifurcation models. *J. Aerosol Sci.*, 22(1):287–301, 1991.

[8] P. A. Baron, M. K. Mazumder, and Y. S. Cheng. Direct-reading techniques using optical particle detection. In K. Willeke and P. A. Baron, editors, *Aerosol Measurement*, chapter 17, pages 381–409. Van Nostrand Reinhold, 1993.

[9] K. Bauckhage and H. H. Floegel. Simultaneous measurement of droplet size and velocity in nozzle sprays. In *Second International Symposium on Applications of Laser Anemometry to Fluid Mechanics, Lisbon*, volume Section 18.1, pages 1–6, 1984.

[10] S. K. Beal. *Nucl. Engng Chem.*, 40:1, 1970.

[11] R. N. Berglund and B. Y. H. Liu. Generation of monodisperse aerosol standards. *Environ. Sci. Technol.*, 7(2):147–153, 1973.

[12] T. Brancatisano, P. W. Collett, and L. A. Engel. Respiratory movements of the vocal cords. *J. Appl. Physiol*, 54:1269–1276, 1983.

[13] J. E. Brockmann. Sampling and tansport of aerosols. In K. Willeke and P. A. Baron, editors, *Aerosol Measurement: Principles, Techniques and Applications*, pages 77–111. Van Nostrand Reinhold, New York, NY, 1993.

[14] J. W. Brooke, T. J. Hanratty, and J. B. McLaughlin. Free-flight mixing and deposition of aerosols. *Phys. Fluids*, 6(10):69–79, 1994.

[15] P. Buchhave, W. K. George Jr., and J. L. Lumley. The measurement of turbulence with the laser-doppler anemometer. *Ann. Rev. Fluid Mech.*, 11:443–503, 1979.

[16] F. S. Cai and C. P. Yu. Inertial and interceptional deposition of spherical particles and fibers in a bifurcating airway. *J. Aerosol Sci.*, 19:679–688, 1988.

[17] T. L. Chan and M. Lippmann. Experimental measurements and empirical modelling of the regional deposition of inhaled particles in humans. *Am. Ind. Hyg. Assoc. J.*, 41:399–409, 1980.

[18] B. T. Chen. Instrument calibration. In K. Willeke and P. A. Baron, editors, *Aerosol Measurement*, chapter 22, pages 493–520. Van Nostrand Reinhold, 1993.

[19] K.-H. Cheng, Y.-S. Cheng, H.-C. Yeh, and D. L. Swift. An experimental method for measuring aerosol deposition efficiency in the human oral airway. *American Industrial Hygiene Association Journal*, 58:207–213, 1997.

[20] Y.-S. Cheng, , Y. Yamada, H.-C. Yeh, and D. L. Swift. Deposition of ultrafine aerosols in a human oral cast. *Aerosol Science and Technology*, 12:1075–1081, 1990.

[21] Y.-S. Cheng, Y.-F. Su, H.-C. Yeh, and D. L. Swift. Deposition of thoron progeny human head airways. *Aerosol Science and Technology*, 18:359–375, 1993.

[22] Y.-S. Cheng, Y. Yamada, H.-C. Yeh, and D. L. Swift. Diffusional deposition of ultrafine aerosols in a human nasal cast. *J. Aerosol Sci.*, 6:741–751, 1988.

[23] Y.-S. Cheng, H.-C. Yeh, and D. L. Swift. Aerosol deposition in human nasal airway for particles 1 nm to 20 μm: a model study. *Radiation Protection Dosimetry*, 38(1):41–47, 1991.

[24] Y.-S. Cheng, Y. Zhou, and B. T. Chen. Particle deposition in a cast of human oral airways. *Aerosol Science and Technology*, 31:238–300, 1999.

[25] A. R. Clark and M. Egan. Modelling the deposition of inhaled powdered drug aerosols. *J. Aerosol Sci.*, 25(1):175–186, 1994.

[26] A. R. Clark and A. M. Hollingworth. The relationship between powder inhaler resistance and peak inspiratory conditions in healthy volunteers – implications for in vitro testing. *J. Aerosol Med.*, 6(2):99–110, 1993.

[27] A. R. Clark, S. P. Newman, and N. Dasovich. Mouth and oropharyngeal deposition of pharmaceutical aerosols. *J. Aerosol Med.*, 11(S1):S116–S120, 1998.

[28] C. Crowe, M. Sommerfield, and Y. Tsuji. *Multiphase flows with droplets and particles.* CRC Press, Boca Raton, 1998.

[29] C. T. Crowe, T. R. Troutt, and J. N. Chung. Numerical models for two-phase turbulent flows. *Ann. Rev. Fluid Mech.*, 28:11–43, 1996.

[30] B. Dahneke. Aerosol beam spectrometry. *Natural Physical Science*, 244:54–55, 1973.

[31] B. Dahneke and Y. S. Cheng. Properties of continuum source particle beams. i. calculation methods and results. *J. Aerosol Sci.*, 10:257–274, 1979.

[32] C. Darquenne and M. Paiva. One-dimensional simulation of aerosol transport and deposition in the human lung. *J. Appl. Physiol.*, 77(6):2889–2898, 1994.

[33] C. N. Davies. Deposition from moving aerosols. In C. N. Davies, editor, *Aerosol Science*, pages 393–446. Acedemic Press, 1966.

[34] C. N. Davies. Deposition of particles in the human lungs as a function of particle size and breathing pattern: an empirical model. *Ann. Occup. Hyg.*, 26:119–135, 1982.

[35] J. P. de Koning. *Dry powder inhalation – technical and physiological aspects, prescribing and use.* PhD thesis, Groningen University Institute for Drug Exploration (GUIDE), 2001. ISBN 90-367-1401-x.

[36] L. E. Drain. Laser anemometry and particle sizing. In *International conference on laser anemometry - advances and application, manchester, UK.*, pages 17–30, 1985.

[37] C. A. Dunbar, A. J. Hickey, and P. Holzner. Dispersion and characterization of pharmaceutical dry powder aerosols. *KONA, Powder and Particle*, 16:7–45, 1998.

[38] F. Durst and M. Zaré. Laser doppler measurements in two-phase flows. In *The Accuracy of Flow Measurements by Laser Doppler Methods : Proceedings of the LDA-Symposium Copenhagen, 1975*, pages 403–429. Proceedings LDA-Symposium Copenhagen 1975, 1976.

[39] D. A. Edwards. The macrotransport of aerosol particles in the lung: aerosol deposition phenomena. *J. Aerosol Sci.*, 26(2):293–317, 1995.

[40] M. J. Egan and W. Nixon. A model of aerosol deposition in the lung for use in inhalation dose assessments. *Radiation Protection Dosimetry*, 11(1):5–17, 1985.

[41] S. Elghobashi. On predicting particle-laden turbulent flows. *Applied Scientific Research*, 52:309–329, 1994.

[42] P. C. Emmett, R. J. Aitken, and W. J. Hannan. Measurements of the total and regional depositionof inhaled particles in the human respiratory tract. *J. Aerosol Sci.*, 13:549–560, 1982.

[43] F. G. Fan and G. Ahmadi. A sublayer model for turbulent deposition of particles in vertical ducts with smooth and rough surfaces. *J. Aerosol Sci.*, 24(1):45–64, 1993.

[44] R. Di Felice. The voidage function for fluid-particle interaction systems. *Int. J. Multiphase Flow*, 20(1):153–159, 1994.

[45] G. A. Ferron, B. Haider, and W. G. Kreyling. Inhalation of salt aerosol particles – I. Estimation of the temperature and relative humidity of the air in the human upper airways. *J. Aerosol Sci.*, 19(3):343–363, 1988.

[46] G. A. Ferron, W. G. Kreyling, and B. Haider. Inhalation of salt aerosol particles – II. Growth and deposition in the human respiratory tract. *J. Aerosol Sci.*, 19(5):611–631, 1988.

[47] W. Findeisen. Über das absetzen kleiner, inderluft suspendierter teilchen in der menschlichen lunge. *Pflüger Arch. F.d. ges. Physiol.*, 236:367–379, 1935.

[48] W. H. Finlay. *The Mechanics of Inhaled Pharmaceutical Aerosols: An Introduction.* Academic Press, London, 2001.

[49] W. H. Finlay, C. F. Lange, M. King, and D. P. Speert. Lung delivery of aerosolized dextran. *Am. J. Respir. Crit. Care Med.*, 161:91–97, 2000.

[50] W. H. Finlay and K. W. Stapleton. The effect on regional lung deposition of coupled heat and mass transfer between hygroscopic droplets and their surrounding phase. *J. Aerosol Sci.*, 26:655–670, 1995.

[51] W. H. Finlay, K. W. Stapleton, and J. Yokota. On the use of computational fluid dynamics for simulating flow and particle deposition in the human respiratory tract. *J. Aerosol Med.*, 9(3):329–341, 1996.

[52] N. Foord, A. Black, and M. Walsh. Regional deposition of 2.5-7.5 μm diameter inhaled particles in healthy male non-smokers. *J. Aerosol Sci.*, 9:343–357, 1978.

[53] W. Forstall and E. W. Gaylord. Momentum and mass transfer in a submerged water jet. *Journal of Applied Mechanics*, 22:161–164, 1955.

[54] R. W. Fox and A. T. McDonald. *Introduction to Fluid Mechanics.* John Wiley & Sons, Inc., fourth edition, 1992.

[55] S. K. Friedlander and H. F. Johnstone. Deposition of suspended particles from turbulent gas streams. *Ind. Eng. Chem.*, 49(7):1151–1156, 1957.

[56] F. A. Fry. Charge distribution on polystyrene aerosols and deposition in the human nose. *Aerosol Science*, 1:135–146, 1970.

[57] N. A. Fuchs. *The Mechanics of Aerosols.* Dover Publications, Inc., New York, 1964.

[58] N. A. Fuchs and A. G. Sutugin. *Aerosol Science*, pages 1–30. Acedemic Press, New York.

[59] J. Gebhart, G. Heigwer, J. Heyder, C. Roth, and W. Stahlhofen. The use of light scattering photometry in aerosol medicine. *J. of Aerosol Med.*, 1(2):89–112, 1988.

[60] G. Giacomelli-Maltoni, C. Melandri, V. Prodi, and G. Tarroni. Deposition efficiency of monodisperse particles in human respiratory tract. *American Industrial Hygiene Association Journal*, pages 603–610, 1972.

[61] R. J. Goldstein and W. F. Hagen. Turbulent flow measurements utilizing the doppler shift of scattered laser radiation. *Physics of Fluids*, 10:1349–1352, 1967.

[62] A. D. Gosman and E. Ioannides. Aspects of computer simulations of liquid-fuelled combustors. *AIAA Pap. 81-0323*, 1981.

[63] B. Grgic. Personal communication. 2000.

[64] A. Guha. A united eulerian theory of turbulent deposition to smooth and rough surfaces. *J. Aerosol Sci.*, 28(8):1517–1537, 1997.

[65] J. S. Hadamard. *C. R. Acad. Sci.*, 152:1735, 1911.

[66] J. Heyder. Gravitational deposition of aerosol particles within a system of randomly oriented tubes. *Aerosol Science*, 6:133–137, 1975.

[67] J. Heyder, L. Armbruster, J. Gebhart, E. Grein, and W. Stahlhofen. Total deposition of aerosol particles in the human respiratory tract for nose and mouth breathing. *J. Aerosol Sci.*, 6:311–328, 1975.

[68] J. Heyder and J. Gebhart. Gravitational deposition of particles from laminar aerosol flow through inclined circular tubes. *J. Aerosol sci.*, 8:289–295, 1977.

[69] J. Heyder and G. Rudolf. Deposition of aerosol particles in the human nose. In W. H. Walton, editor, *Inhaled Particles IV - Proceedings of an International Symposium organized by the British Occupational Hygiene Society, Edinburgh*, number Part 1, pages 107–126. Pergamon Press, 1975.

[70] J. Heyder and G. Rudolf. Mathematical models of particle deposition in the human respiratory tract. In H. Smith and G. Gerber, editors, *Lung Modelling for Radioactive Materials*, EUR 9834 EN, pages 17–38. Commision of the European Communities, Luxembourg, 1984.

[71] J. O. Hinze. *Turbulence.* McGraw-Hill, Inc., second edition, 1975.

[72] J. O. Hinze and B. G. Van Der Hegge Zijnen. Transfer of heat and matter in the turbulent mixing zone of an axially symmetric jet. *Appl. Sci. Res.*, 1A:435–460, 1949.

[73] W. Hofmann and I. Balásházy. Particle deposition patterns within airway bifurcations – solutions of the 3d navier-stokes equations. *Radiation Protection Dosimetry*, 38(1):57–63, 1991.

[74] W. Hofmann, I. Balásházy, T. Heistracher, and L.Koblinger. The significance of particle deposition patterns in bronchial airway bifurcations for extrapolation modeling. *Aerosol Science and Technology*, 25:305–327, 1996.

[75] R. F. Hounam, A. Black, and M. Walsh. The deposition of aerosol particles in the nasopharyngeal region of the human respiratory tract. *Aerosol Science*, 2:47–61, 1971.

[76] H. J. Hussein, S. P. Capp, and W. K. George. Velocity measurements in a high-reynolds-number, momentum-conserving, axisymmetric, turbulent jet. *J. Fluid Mech.*, 258:31–75, 1994.

[77] S. M. Bowes III and D. L. Swift. Deposition of inhaled particles in the oral airway during oronasal breathing. *Aerosol Science and Technology*, 11:157–167, 1989.

[78] K. H. Im and P. M. Chung. Particulate deposition from turbulent parallel streams. *AlChE Journal*, 29(3):498–505, 1983.

[79] D. B. Ingham. Diffusion of aerosols from a stream flowing through a cylindrical tube. *J. Aerosol Sci.*, 6:125–132, 1975.

[80] A. C. James, W. Stahlhofen, G. Rudolf, M. J. Egan, W. Nixon, P. Gehr, and J. K. Briant. The respiratory tract deposition model proposed by the ICRP task group. *Radiation Protection Dosimetry*, 38(1):159–165, 1991.

[81] W. Forstall Jr. and A. H. Shapiro. Momentum and mass transfer in coaxial gas jets. *Journal of Applied Mechanics*, 17:399–408, 1950.

[82] W. Forstall Jr. and A. H. Shapiro. Momentum and mass transfer in coaxial gas jets - discussion. *Journal of Applied Mechanics*, 18:219–220, 1951.

[83] I. M. Katz and T. B. Martonen. Flow patterns in three-dimensional laryngeal models. *J. Aerosol Med.*, 9(4):501–512, 1996.

[84] I. M. Katz and T. B. Martonen. Three-dimensional fluid particle trajectories in the human larynx and trachea. *J. Aerosol Med.*, 9(4):513–520, 1996.

[85] I. M. Katz and T. B. Martonen. A numerical study of particle motion within the human larynx and trachea. *J. Aerosol Sci.*, 30(2):173–183, 1999.

[86] C. S. Kim, D. M. Fischer, D. J. Lutz, and T. R. Gerrity. Particle deposition in bifurcating airway models with varying airway geometry. *J. Aerosol Sci.*, 25:567–581, 1994.

[87] A. A. Kinsara, R. V. Tompson, and S. K. Loyalka. Computational flow and aerosol concentration profiles in lung bifurcations. *Health Physics*, 64(1):13–22, 1993.

[88] T. Kneen and W. Strauss. Deposition of duse from turbulent gas streams. *Atmospheric Environment*, 3:55–67, 1968.

[89] L. Koblinger and W. Hofmann. Monte carlo modeling of aerosol deposition in human lungs. part i: Simulation of particle transport in a stochastic lung structure. *J. Aerosol Sci.*, 21(5):661–674, 1990.

[90] H. D. Landahl. On the removal of air-borne droplets by the human respiratory tract. *Bull. Math. Biophys*, 12:43–56, 1950.

[91] J. Laufer. The structure of turbulence in fully developed pipe flow. *Natl. Advisory Comm. Aeronaut. Tech. Repts. No. 1174*, pages 417–434, 1954.

[92] C. J. Lawn. The determination of the rate of dissipation in turbulent pipe flow. *J. Fluid Mech.*, 48(3):447–505, 1971.

[93] A. H. Lefebvre. *Atomization and Sprays.* Taylor & Francis, Bristol, PA, 1989.

[94] W.-I Li, M. Perzl, G. A. Ferron R. Batycky, J. Heyder, and D. A. Edwards. The macrotransport properties of aerosol particles in the human oral-pharyngeal region. *J. Aerosol Sci.*, 29(8):995–1010, 1998.

[95] W.-I Li, M. Perzl, J. Heyder, R. Langer, J. D. Brain, K. H. Englmeier, R. W. Niven, and D. A. Edwards. Aerodynamic and aerosol particle deagglomeration phenomena in model oral-pharyngeal cavities. *J. Aerosol Sci.*, 27(8):1269–1286, 1996.

[96] T. Lin, P. N. Breysse, B. L. Laube, and D.L. Swift. Mouthpiece diameter affects deposition efficiency in cast models of the human oral airways. *J. Aerosol Med.*, 14(3):335–341, 2001.

[97] M. Lippmann. The effect of particle size on the regional deposition of inhaled aerosols in the human respiratory tract. *Ammerican Industrial Hygiene Association Journal*, pages 257–275, 1969.

[98] M. Lippmann. Deposition and clearance of inhaled particles in the human nose. *Ann. Otol. Rhinol. Laryngol.*, 79:519–528, 1970.

[99] M. Lippmann. *Regional deposition of particles in the human respiratory tract*, chapter 14, pages 213–232. Handbook of Physiology Section 9: Reactions to Environmental Agents. American Physiological Society, Bethesda, MD, 1977.

[100] B. Y. H. Liu and J. K. Agarwal. Experimental observation of aerosol deposition in turbulent flow. *Aerosol Science*, 5:145–155, 1974.

[101] Z. Lixing. *Theory and Numerical Modeling of Turbulent Gas-Particle Flows and Combustion.* CRC Press, Boca Raton, FL, USA, 1993.

[102] V. A. Marple and B. Y. H. Liu. Characteristics of laminar jet impactors. *Environmental Science and Technology*, 8(7):648–654, 1974.

[103] V. A. Marple, K. L. Rubow, and B. A. Olson. *Inertial, gravitational, centrifugal, and thermal collection efficiencies*, chapter 4. In Willeke and Baron,[163] 1993.

[104] V. A. Marple and K. Willeke. Impactor design. *Atmospheric Environment*, 10:891–896, 1976.

[105] T. B. Martonen. Deposition of inhaled particulate matter in the upper respiratory tract, larynx and bronchial airways: a mathematical description. *Journal of Toxicology and Environmental Health*, 12:787–800, 1983.

[106] T. B. Martonen and Z. Zhang. Comments on recent data for particle deposition in human nasal passages. *J. Aerosol Sci.*, 23(6):667–674, 1992.

[107] E. A. Matida, B. Grgic, C. Lange, and W. H. Finlay. Simulation of aerosol deposition in an idealized mouth-throat geometry. *In Press.*

[108] M. R. Maxey and J. J. Riley. Equations of motion for a small rigid sphere in a nonuniform flow. *Phys. Fluids*, 26(4):883–889, 1983.

[109] K. R. May. The cascade impactor: an instrument for sampling coarse aerosols. *J. Sci. Instrm*, 22:187–195, 1945.

[110] W. D. McComb. *The Physics of Fluid Turbulence.* Oxford Engineering Science Series; 25. Oxford University Press, 2000.

[111] T.T. Mercer. Production of therapeutic aerosols, principles and techniques. *Chest*, 6:813–817, 1981.

[112] F. J. Miller, T. B. Martonen, M. G. Ménache, R. C. Graham, D. M. Spektor, and M. Lippmann. Influence of breathing mode and activity level on the regional deposition of inhaled particles and implications for regulatory standards. *Ann. Occup. Hyg.*, 32(Supplement 1):3–10, 1988. Inhaled Particles VI.

[113] T. Morel. Comprehensive design of axisymmetric wind tunnel contractions. *Journal of Fluids Engineering*, 97(2):225–233, 1975.

[114] P. E. Morrow. Aerosol characterization and deposition. *Am. Rev. Respir. Dis.*, 110(6):88–99, 1974.

[115] W. B. Morton. The settling of a suspension flowing along a tube. *Proc. Roy. Irish Acad.*, 43:1, 1935.

[116] S. P. Newman, A. Hollingworth, and A. R. Clark. Effect of different modes of inhalation on drug delivery from a dry powder inhaler. *International Journal of Pharmaceutics*, 102:127–132, 1994.

[117] S. P. Newman, G. R. Pitcairn, D. A. Adkin, M. T. Vidgrin, and M. Silvasti. Comparison of beclomethasone dipropionate delivery by easyhaler dry powder inhaler and pmdi plus large volume spacer. *Journal of Aerosol Medicine*, 14(2):217–225, 2001.

[118] J. Nikuradse. Gesetzmäßigkeiten der turbulenten strömung in glatten rohren. *VDI - Forschungsheft, No. 356*, page 260, 1932.

[119] J. Nikuradse. Strömungsgesetze in rauhen rohren. *VDI - Forschungsheft, No. 361*, page 208, 1933.

[120] ICRP (International Commission on Radiological Protection). Human respiratory tract model for radiological protection. *Annals of the ICRP, ICRP Publication 66*, 24(1–3), 1994.

[121] R. L. Panton. *Incompressible Flow.* John Wiley & Sons, Inc., New York, 1996.

[122] R. E. Pattle. The retention of gases and particles in the human nose. In C. N. Davies, editor, *Inhaled particles and vapours*, pages 302–310. Proceedings of an International Symposium organized by the British Occupational Hygiene Society, Oxford, 1960, Pergamon Press, 1961.

[123] D. D. Persons, G. D. Hess, W. J. Muller, and P. W. Scherer. Airway deposition of hygroscopic heterodispersed aerosols: results of a computer calculation. *J. Appl. Physiol.*, 63(3):1195–1204, 1987.

[124] G. Pitcairn, G. Lunghetti, P. Ventura, and S. Newman. A comparison of the lung deposition of salbutamol inhaled from a new dry powder inhaler, at two inhaled flow rates. *International Journal of Pharmaceutics*, 102:11–18, 1994.

[125] G. R. Pitcairn, T. Lankinen, E. Valkila, and S. P. Newman. Lung deposition of salbutamol from the leiras metered dose powder inhaler. *Journal of Aerosol Medicine*, 8(3):307–311, 1995.

[126] C. Prakash and S. V. Patankar. A control volume-based finite-element method for solving the navier-stokes equations using equal-order velocity-pressure interpolation. *Numerical Heat Transfer*, 8:259–280, 1985.

[127] Weibel E. R. *Morphology of the human lung.* Acedemic Publishers Inc., New York, 1963.

[128] D. J. Rader and V. A. Marple. Effect of ultra-stokesian drag and particle interception on impaction characteristics. *Aerosol Science and Technology*, 4:141–156, 1985.

[129] O. Reynolds. On the dynamical theory of incompressible viscous fluids and the determination of the criterion. *Philosophical Transactions of the Royal Society of London. A*, 186:123–164, 1895.

[130] Von P. Ruden. Turbulente ausbreitungsvorgänge im freistrahl. *Die Naturwissenschaften*, 21:375–378, 1933.

[131] G. Rudolf. A mathematical model for the deposition of aerosol particles in the human respiratory tract. *J. Aerosol Science*, 14:188–192, 1983.

[132] G. Rudolf, J. Gebhart, J. Heyder, Ch. F. Schiller, and W. Stahlhofen. An empirical formula describing aerosol deposition in man for any particle size. *J. Aerosol Science*, 17(3):350–355, 1986.

[133] G. Rudolf, R. Köbrich, and W. Stahlhofen. Modelling and algebraic formulation of regional deposition in man. *J. Aerosol Science*, 21(Suppl. 1):S403–S406, 1990.

[134] G. Rudolf, R. Köbrich, W. Stahlhofen, and A. C. James. Regional aerosol deposition in man - a statistical and algebraic model. *Ann. Occup. Hyg.*, 38(Suppl. 1):1–14, 1994.

[135] W. Rybczynski. *Bull. Int. Acad. Sci. Cracov*, 1911A:40, 1911.

[136] M. Saffman, P. Buchhave, and H. Tanger. Simultaneous measurement of size, concentration and velocity of spherical particles by a laser doppler method. In *The Second International Symposium on Applications of Laser Anemometry to Fluid Mechanics, Lisbon*, Section 8.1, pages 1–8, 1984.

[137] S. Sami. Balance of turbulence energy in the region of jet-flow establishment. *J. Fluid Mech.*, 29(1):81–92, 1967.

[138] R. Sarangapani and A. S. Wexler. Modeling aerosol bolus dispersion in human airways. *J. Aerosol Sci.*, 30(10):1345–1362, 1999.

[139] R. Sarangapani and A. S. Wexler. Modeling particle deposition in extrathoracic airways. *Aerosol Science and Technology*, 32:72–89, 2000.

[140] H. E. Schroeder. *Oral Structural Biology*. Theime Medical Publishers, New York, 4th edition, 1991.

[141] L. C. Schwendiman and A. K. Postma. Turbulent deposition in sampling lines. *Tech. Inf. Div. Rep.*, TID-7628(Book 1, (USAEC)), 1962.

[142] W. R. Scott and B. B. Taulbee. Aerosol deposiiton along the vertical axis of the lung. *J. Aerosol Sci.*, 16(4):323–333, 1985.

[143] G. A. Sehmel. Particle deposition from turbulent air flow. *Journal of Geophysical Research*, 75(9):1766–1781, 1970.

[144] G. A. Sehmel. Aerosol deposition from turbulent airstreams in vertical conduits. Technical Report BNWL-578, Pacific Northwest Laboratory, Richland, Washington, January, 1968.

[145] W. Stahlhofen, J. Gebhart, and J. Heyder. Experimental determination of the regional deposition of aerosol particles in the human respiratory tract. *Am. Ind. Hyg. Assoc. J.*, 41(6):385–398a, 1980.

[146] W. Stahlhofen, J. Gebhart, and J. Heyder. Biological variability of regional deposition of aerosol particles in the human respiratory tract. *Am. Ind. Hyg. Assoc. J.*, 42(5):348–352, 1981.

[147] W. Stahlhofen, J. Gebhart, J. Heyder, and G. Scheuch. New regional deposition data of the human respiratory tract. *J. Aerosol Sci.*, 14:186–188, 1983.

[148] W. Stahlhofen, G. Rudolf, and A. C. James. Intercomparison of experimental regional aerosol deposition data. *J. Aerosol Med.*, 2(3):285–308, 1989.

[149] K. Stapleton and W. Finlay. Deposition of medical aerosols in the respiratory tract. Report MA-1, Department of Mechanical Engineering, University of Alberta, Edmonton, Alberta, 1997.

[150] K. W. Stapleton, E. Guentsch, M. K. Hoskinson, and W. H. Finlay. On the suitability of k-ε turbulence modeling for aerosol deposition in the mouth and throat: a comparison with experiment. *J. Aerosol Sci.*, 31(6):739–749, 2000.

[151] K. Svartengren, P.-Å.Lindestad, M. Svartengren, G. Bylin, K. Philipson, and P. Camner. Deposition of inhaled particles in the mouth and throat of asthmatic subjects. *Eur. Respir. J.*, 7:1467–1473, 1994.

[152] D. L. Swift. Aerosol measurement in the health care field. In K. Willeke and P. A. Baron, editors, *Aerosol Measurement - Principles, Techniques and Applications*, chapter 37, pages 816–832. Van Nostrand Reinhold, New York, 1993.

[153] D. L. Swift. The oral airway – a conduit or collector for pharmaceutical aerosols? In *Respiratory Drug Delivery IV*, Buffalo Grove, IL, 1994. Interpharm Press Inc.

[154] D. L. Swift, N. Montassier, P. K. Hopke, K. Karpen-Hayes, Y.-S. Cheng, Y. F. Su, H. C. Yeh, and J. C. Strong. Inspiratory deposition of ultrafine particles in human nasal replicate cast. *J. Aerosol Sci.*, 23(1):65–72, 1992.

[155] D. B. Taulbee and C. P. Yu. A theory of aerosol deposition in the human respiratory tract. *J. Appl. Physiol.*, 38(1):77–85, 1975.

[156] W. S. Uijttewaal and R. V. A. Oliemans. Particle dispersion and deposition in direct numerical and large eddy simulations of vertical pipe flows. *Phys. Fluids*, 8(10):2590–2604, 1996.

[157] A. P. Voss. Deaggregation of dry powder pharmaceutical aerosols. Master of science, University of Alberta, Edmonton, AB, Canada, 2001.

[158] Q. Wang and K. D. Squires. Large eddy simulation of particle deposition in a vertical turbulent channel flow. *Int. J. Multiphase Flow*, 22(4):667–683, 1996.

[159] Y. Wang and P. W. James. On the effect of anisotropy on the turbulent dispersion and deposition of small particles. *Int. J. Multiphase Flow*, 25:551–558, 1999.

[160] S. Warren, G. Taylor, J. Smith, H. Buck, and M. Parry-Billings. Gamma scintigraphic evaluation of a novel budesonide dry powder inhaler using a validated radiolabeling technique. *Journal of Aerosol Medicine*, 15(1):15–25, 2002.

[161] A. C. Wells and A. C. Chamberlain. Transport of small particles to vertical surfaces. *Brit. J. Appl. Phys.*, 18:1793–1799, 1967.

[162] D. C. Wilcox. *Turbulence Modeling for CFD.* DCW Industries, Inc., La Cañada, California.

[163] K. Willeke and P. A. Baron, editors. *Aerosol Measurement: principles, techniques, and applications.* Van Nostrand Reinhold, New York, 1993.

[164] I. Wygnanski and H. Fiedler. Some measurements in the self-preserving jet. *J. Fluid Mech.*, 38(3):577–612, 1969.

[165] H.-C. Yeh, R. G. Cuddihy, R. F. Phalen, and I.-Y. Chang. Comparisons of calculated respiratory tract deposition of particles based on the proposed ncrp model and the new icrp66 model. *Aerosol Science and Technology*, 25:134–140, 1996.

[166] H.-C. Yeh and G. M. Schum. Models of human lung airways and their application to inhaled particle deposition. *Bull. Math. Biology*, 42:461–480, 1980.

[167] Y. Yeh and H. Z. Cummins. Localized fluid flow measurement with an he-ne laser spectrometer. *Applied Physics Letters*, 4(10):176–178, 1964.

[168] J. Young and A. Leeming. A theory of particle deposition in turbulent pipe flow. *J. Fluid Mech.*, 340:129–159, 1997.

[169] C. P. Yu, C. K. Diu, and T. T. Soong. Statistical analysis of aerosol deposition in the nose and mouth. *American Industrial Hygiene Association Journal*, 42(10):726–733, 1981.

[170] C. P. Yu, L. Zhang, M. H. Becquemin, M. Roy, and A. Bouchikhi. Algebraic modeling of total and regional deposition of inhaled particles in the human lung of various ages. *J. Aerosol Sci.*, 23(1):73–79, 1992.

[171] G. Yu, Z. Zhang, and R. Lessmann. Fluid flow and particle deposition in the human upper respiratory system. *Aerosol Science and Technology*, 28:146–158, 1998.

[172] H. Zhang and G. Ahmadi. Aerosol particle transport and deposition in vertical and horizontal turbulent duct flows. *J. Fluid Mech.*, 406:55–80, 2000.